Hydrographic variability in the Irminger Sea

De hydrografische variabiliteit in de Irmingerzee

(met een samenvatting in het Nederlands)

PROEFSCHRIFT

ter verkrijging van de graad van doctor aan de Universiteit Utrecht
op gezag van de rector magnificus, prof.dr. J.C. Stoof,
ingevolge het besluit van het college voor promoties
in het openbaar te verdedigen op

maandag 18 oktober 2010 des middags om 2.30 uur

door

Marieke Femke de Jong

geboren op 2 januari 1980 te Valkenswaard

Promotor: Prof.dr. J. T. F. Zimmerman
Co-promotor: Dr. H. M. van Aken

Dit proefschrift werd mede mogelijk gemaakt door financiële steun van het project “North Atlantic monitoring and modelling (CS1)” binnen het Klimaat voor Ruimte programma en het programma THOR “Thermohaline Overturning – at Risk?” binnen het 7de Europese Kaderprogramma.

About the cover

The cover of this thesis contains three layers. The lowest layer is a photo of the Irminger Sea during typical weather conditions (fog). The middle layer is a color plot of salinity observations from the first and second deployment of the LOCO 3 mooring. It shows the presence of the fresher, intermediate Labrador Sea Water (dark blue) as well as the occurence of saline eddies near the surface (red) and gives an impression of the variability observed in the profiles.

The upper layer is one of many drawings made during CTD stations.

ISBN 978-90-393-5425-4

Table of content

Samenvatting

Het noordelijk deel van de Noordelijke Atlantische Oceaan krijgt van oudsher veel aandacht van oceanografen. Dit is deels te danken aan de centrale ligging tussen Europa en Noord-Amerika. Door de aanvoer van warm water vanuit het zuiden en de relatief koude lucht boven het zeeoppervlak staat de Noordelijke Atlantische Oceaan grote hoeveelheden warmte af aan de atmosfeer. Deze warmteoverdracht is deels verantwoordelijk voor het milde klimaat in West-Europa. Door de sterke afkoeling van het zeeoppervlak komt het in koude winters voor dat het oppervlaktewater zwaarder wordt dan het diepere water. Wanneer dit gebeurt zinkt het zwaardere water en komt het diepere, lichtere water naar boven. Dit proces, dat diepe convectie heet, kan tot op grote diepte de eigenschappen van de waterkolom aanpassen door menging. We noemen dit dan ook diep-waterformatie. Een ander proces van diep-waterformatie is de overstort van zeer dicht water, uit de zeeën ten noorden van IJsland, over de drempels in de rug tussen Groenland en Schotland in de Noordelijke Atlantische Oceaan. Deze drempels bevinden zich zowel west (in Straat Denemarken) als oost van IJsland (tussen IJsland en Schotland). Het diepe water in het westen wordt gekenmerkt door zijn zeer lage temperaturen terwijl het diepe water in het oosten vooral wordt gekenmerkt door zijn relatief hoge saliniteit. Vanaf het moment dat de diep-waterformatie door convectie of overstort stopt, begint de transformatie van het diepe water. Dit gebeurt door laterale menging met de naastgelegen watermassa's. Kleine intrusies van watermassa's zorgen voor menging op dichtheidsvlakken door een proces dat dubbele diffusie heet. Doordat de diffusie van temperatuur en zout niet gelijk op gaat wordt de water kolom plaatselijk onstabiel. Hierdoor mengen de twee watermassa's. Dit is een langzaam maar continue process. Samen bepalen deze drie processen voor een groot deel de hydrografie van de Irmingerzee. Deze zee is het gebied tussen het zuidoosten van Groenland en de Midden-Atlantische Rug. Vanaf het zuiden stromen grote hoeveelheden water, door diepe convectie in de Labradorzee gevormd, de Irmingerzee in. Het diepe water dat gevonden wordt langs de Groenlandse continentale helling en de Midden-Atlantische rug is afkomstig van de overstortplaatsen west en oost van IJsland. Laterale menging van watermassa's vindt bijna overal plaats waar laterale gradienten van zout en temperatuur aanwezig zijn, ook in de Irmingerzee.

Dit proefschrift onderzoekt de variaties die voorkomen in de hydrografie van de Irmingerzee en de oorzaken daarvan. Hiervoor wordt allereerst de basistoestand van de lokale hydrografie en de bovenliggende atmosfeer geschetst. Jaarlijkse waarnemingen vanaf schepen worden vervolgens gebruikt om de interjaarlijkse vari-

aties in de Irmingerzee en de naburige bekkens te beschrijven. Deze waarnemingen beslaan de periode tussen 1950 en 2008. Om de variabiliteit op korte tijdschalen (enkele minuten tot een paar jaar) te beschrijven worden waarnemingen vanaf verankeringen in de centrale Irmingerzee gebruikt. De instrumenten in deze verankeringen hebben dagelijks (of sneller) de stromingen en de eigenschappen van de waterkolom gemeten. Deze verzameling van snelle metingen beslaat de periode tussen oktober 2003 en september 2008. Er is dus ook in de winter gemeten, een periode waarin er over het algemeen zeer weinig scheepswaarnemingen zijn vanwege het slechte weer en het zeeijs in dit gebied. Hierdoor geven deze metingen veel inzicht in de variabiliteit die veroorzaakt wordt door diepe menging in koude winters. Omdat er slechts 5 winters met de verankeringen gemeten zijn onderzoeken we de gevoeligheid van de menglaagdiepte voor de verschillende lokale omstandigheden aan de hand van een simpel lineair model. Deze omstandigheden zijn de stabiliteit van de waterkolom in het najaar en de sterkte van de afkoeling in de winter. Ook onderzoeken we de resultaten van meer gecompliceerde modellen voor de Irmingerzee en de naburige Labradorzee. Hiervoor gebruiken we de klimaat modellen waarin de oceaan en atmosfeer gekoppeld zijn.

Uit de interjaarlijkse waarnemingen blijkt dat er in de bovenste 2 km een oscillatie in de temperatuur en het zout te zien is met een periode van ongeveer 50 jaar. Deze oscillatie loopt samen met een oscillatie met dezelfde periode in de rotatie van de windschuifspanning en de warmteflux van de atmosfeer. Hoge temperaturen en zoutgehaltes in de oceaan worden waargenomen tijdens een minimum in de rotatie van de windschuifspanning en de warmteflux. Waarschijnlijk zijn de variaties in de (afkoelende) warmteflux verantwoordelijk voor de veranderingen in de temperatuur, mogelijk in combinatie met een verschuiving van het Subpolaire Front. Diepe convectie, dat elke 10 jaar voor lijkt te komen in de Labradorzee, zorgt ervoor dat de afkoeling verspreidt wordt over de bovenste 2 km van de water kolom. Na een voorval van diep-waterformatie verspreidt het convectief gevormde Labradorzeewater zich naar de naburige bekkens. Het komt na ongeveer 2 jaar aan in de Irmingerzee en na plusminus 5 jaar in het IJslandbekken. Daar vormt het een lokaal minimum in de stabiliteit van de waterkolom en een maximum in het zuurstofgehalte. De laatste twee grote Labradorzeewater-klasses werden ook gekenmerkt door hun lage temperatuur en zoutgehalte. De karakteristieke mimima en maxima van het Labradorzeewater (Labrador Sea Water) nemen langzaam af in sterkte door laterale menging met de naburige watermassa's. De belangrijkste watermassa lijkt hierbij het IJslandse Hellingwater (Icelandic Slope Water) te zijn. Dit water, dat aan de rand van de Irmingerzee te vinden is, heeft dezelfde dichtheid als Labradorzeewater maar is zouter. Verder weg, in de Charlie-Gibbsbreukzone en het IJslandbekken mengt het Labradorzeewater

zich ook met andere watermassa's. Dit veroorzaakt een minimum in de temperatuur en het zoutgehalte van het Noordoost-Atlantische Diepe Water (North East Atlantic Deep Water) in de Irmingerzee, ongeveer 2 jaar na de aankomst van het minimum van het Labradorzeewater in de Irmingerzee.

Het water met de hoogste dichtheid in de Irmingerzee, het overstortwater uit Straat Denemarken (Denmark Strait Overflow Water) is zeer variabel. In de interjaarlijkse waarnemingen laat het grote schommelingen in de thermohaliene eigenschappen zien. Uit de snelle waarnemingen van de verankerde instrumenten blijkt echter dat de werkelijke schommelingen nog groter zijn. In de westelijke Irmingerzee lijkt dit diepe water te varieren tussen twee typen met dezelfde dichtheid. Het ene type is relatief zoet en iets kouder, het andere type is zouter en iets warmer. Een sterke piek van het zoete type werd waargenomen in 2004, de saliniteit nam toen in slechts 1 maand meer af dan de totale omvang van de gemeten interjaarlijkse variabiliteit. Niet alleen uit deze metingen blijkt dat de variabiliteit onderschat wordt door de jaarlijkse waarnemingen. Op alle dieptes blijken variaties in de tijdreeks van 5 jaar van de verankerde instrumenten groter dan de variaties in de tijdreeks van 20 jaar jaarlijkse waarnemingen. Een deel van de werkelijke variaties wordt gemist en een deel van de variaties wordt "ge-aliasd" op de langere tijdschalen. Ook het aliassen van ruimtelijke variaties, zoals wervels met een doorsnede van enkele tientallen kilometers, bemoeilijkt het interpreteren van de tijdseries.

Diepe convectie, wat in de winter plaats vindt en daarom meestal gemist wordt door metingen vanaf schepen, is ook waargenomen met de verankerde instrumenten in de Irmingerzee. Menging tot op zo'n 400 m diepte kwam in elk van de 5 gemeten winters voor. In de erg koude winter van 2007 op 2008 kwam zelfs menging tot op 1000 m voor. Deze diepe convectie vindt plaats in cellen van enkele kilometers doorsnee. Meestal werd de diepste convectie gevonden aan de westelijke kant van de Irmingerzee, waar de aanvangsstabiliteit van de waterkolom lager is. Tussen en na convectievoorvallen wordt de waterkolom opnieuw gestratificeerd door warm water uit de grenslaagstromingen aan de randen van de Irmingerzee. Door de resulterende sterke herstratificatie is er na de winter weinig bewijs terug te vinden van de convectie. Alleen na de winter van 2008 was er een uitdieping van het stabiliteitsminimum rond een diepte van 1000 m te zien in de metingen van de volgende zomer. Er lijkt dus geen diepe watermassa gevormd te worden door lokale diepe convectie in de Irmingerzee. Mogelijk draagt de convectie, door transport van het gemengde water naar de Labradorzee, wel bij aan het verlagen van de stabiliteit in de Labradorzee.

Uit een simpel mengingsmodel blijkt dat de aanvangsstabiliteit in de Irmingerzee zeer belangrijk is voor de uiteindelijke convectiediepte. Zonder relatief lage aanvangsstabiliteit kunnen ook koude winters niet voor convectie dieper dan 500 m zorgen. In de Labradorzee, waar de aanvangsstabiliteit over het algemeen veel lager is, is de sterkte van de afkoeling in de winter het belangrijkst voor de uiteindelijke menglaagdiepte. In de gecompliceerde gekoppelde klimaatmodellen blijkt het goed simuleren van de menglaagdiepte één van de problemen te zijn. Een aantal modellen laten geen diepe convectie zien en een paar andere modellen overschatten de menglaagdiepte sterk. Hierdoor onstaan er grote verschillen tussen de gesimuleerde hydrografie van de Irminger- en Labradorzee en de waargenomen hydrografie. Een ander probleem lijkt de opstartperiode van de modellen te zijn. Tijdens de opstartperiode past de gesimuleerde oceaan, die gebaseerd was op waarnemingen, zich aan de gesimuleerde atmosfeer aan. Hierbij blijkt de oceaan in de simulatie "weg te lopen" van de waargenomen situatie. Wanneer het enkele honderden modeljaren duurt voordat het model stabiel is kunnen de verschillen hierdoor erg groot worden.

De variabiliteit in de hydrografie van de Irmingerzee blijkt groter dan in het verleden aangenomen werd. Grote variaties kunnen op korte tijdschalen plaatsvinden. Er zullen meer snelle waarnemingen gedaan moeten worden om deze variabiliteit goed te vangen in tijdseries. Daarnaast moeten de jaarlijkse waarnemingen voortgezet worden. Naarmate deze tijdseries langer worden zal duidelijk worden of de decadale variaties inderdaad oscilaties zijn en wat hun oorzaak is.

Summary

The northern part of the North Atlantic Ocean has always received much attention from oceanographers. This is partly due to its central location between Europe and North America. The constant supply of warm water from the south, combined with the relatively cold air above the sea surface, causes the North Atlantic Ocean to relinquish large quantities of heat to the atmosphere. This transfer of heat contributes to the relatively mild climate of western Europe. The heat transfer, or cooling, increases the density of the sea surface. This causes the water column to become unstable in cold winters. When this occurs, the surface waters sink and are replaced by lighter, deeper waters. This process, called deep convection, adjusts the properties of the water column by mixing to great depths. The result is the formation of a deep water mass. Another process of deep water formation is the overflow of dense water from the Nordic Seas, across the Greenland-Scotland Ridge, into the North Atlantic Ocean. The overflows are located both west (in Denmark Strait) and east of Iceland (around the Faroe Islands). The western deep water is characterized by its low temperature, while the eastern deep water is relatively saline. The transformation of the deep waters begins as soon as the deep water formation, by convection or overflow, ceases. This is the result of lateral mixing with neighbouring water masses. Small intrusions of water masses cause mixing on density plains through double diffusion. The difference between the diffusion coefficients for temperature and for salinity causes the water column to become locally unstable. This results in mixing of the two water masses. This process is slow but continuous. Together, these three processes largely set the hydrography of the Irminger Sea, the area between southeast Greenland and the Mid Atlantic Ridge. Large quantities of convectively formed water flow out of the Labrador Sea and enter the Irminger Sea from the south. Deep waters, found along the continental slope of Greenland and the Mid Atlantic Ridge, originates from the overflows west and east of Iceland. Lateral mixing of water masses takes places nearly everywhere where lateral gradients are present, also in the Irminger Sea.

This thesis investigates the variability of the hydrography in the Irminger Sea and its causes. First, the reference state of the local hydrography and the overlying atmosphere is sketched. Annual surveys by ships are used to describe the inter-annual variability in the Irminger Sea and the neighbouring basins. These observations cover the period between 1950 and 2008. Observations from moorings in the central Irminger Sea are used in order to describe the faster variability. The instruments in these moorings make daily (or faster) observations of the currents and the properties of the water

column. This high temporal resolution data set covers the period between October 2003 and September 2008. These measurements also include the winters, in which there are rarely observations by ships because of bad weather and sea ice. Therefore these measurements give much insight into the variability caused by convective mixing in winter. Because only five winters have been observed with moorings, the sensitivity of the mixed layer depth to the local conditions is further investigated using a simple linear model. These conditions are the stability of the water column in fall and the strength of the winter cooling. Results of more complicated models, mainly coupled climate models, were also investigated.

In the annual observations we see an oscillation in temperature and salinity in the upper 2 km. This oscillation has an apparent period of about 50 year and nearly coincides with an oscillation with a similar period seen in the wind stress curl and the heat flux to the atmosphere. High temperatures and salinities are observed during a minimum in the wind stress curl and heat flux. Probably the variations in the cooling heat flux are responsible for the changes in temperature, possibly in combination with a shift of the Subpolar Front. Deep convection, which appears to occur every 10 year in the Labrador Sea, distributes the cooling over the upper 2 km of the water column. After a deep convection event, the convectively formed Labrador Sea Water spreads into the neighbouring basins. It arrives in the Irminger Sea after about 2 years and in the Iceland Basin after about 5 years. There it forms a local minimum in the stability of the water column and a maximum in the dissolved oxygen concentration. The two most recent classes of Labrador Sea Water were also characterized by their low temperature and salinity. These typical minima and maxima are reduced in strength over time due to lateral mixing with neighbouring water masses. The most important water mass for this process appears to be Icelandic Slope Water. This water, found along the boundaries of the Irminger Sea, has a similar density as Labrador Sea Water but is more saline. Further away, in the Charlie-Gibbs Fracture Zone, the Labrador Sea Water mixes with other water masses. This causes a temperature and salinity minimum in the North East Atlantic Deep Water, entering the Irminger Sea about 2 years after the arrival of the Labrador Sea Water minimum in the Irminger Sea.

The densest water in the Irminger Sea, the Denmark Strait Overflow Water, is highly variable. It shows large variations in its thermohaline properties in the annual observations. However, the fast observations from the moored instruments show that the actual variability is even larger. In the western Irminger Sea this deep water appears to vary between two types with similar density. One type is relatively fresh and slightly colder, while the other type is more saline and slightly warmer. A strong peak of the relatively fresh type was seen in 2004, when the salinity drop within one

month was larger than the total range of salinity in the inter-annual series. There are more observations that show that the variability is underestimated by the annual measurements. At all depths the variability in the 5-year series of the moored instruments is larger than the variability in the 20-year series of annual observations. Part of the actual variability is missed, another part is "aliased" onto longer time scales. The aliasing of spatial variability, such as eddies with a diameter of a few tens of km, also complicates the interpretation of these time series.

Deep convection, which occurs in winter and is therefore often missed by shipboard observations, has been observed in the Irminger Sea by the moored instruments. Mixing down to 400 m depth was observed in each of the 5 winters. Mixing down to 1000 m was observed in the cold winter of 2007-2008. This deep convection occurs in cells with a diameter of a few km. The deepest mixed layers are usually found on the western side of the Irminger Sea, where the initial stability of the water column is lower. Between and after convective events the water column is restratified by warmer waters from the boundary currents along the edges of the Irminger Sea. Due to the strong resulting restratification there is little evidence of convection left after winter. Only after the winter of 2008, a intensification of the stability minimum at 1000 m is seen in the following summer. It appears that there is no deep water formation by local convection in the Irminger Sea. Possibly the Irminger convection contributes to the reduction of the stability of the Labrador Sea, through advection of the mixed water to the Labrador Sea.

The results of a simple mixed layer model show that the initial stability of the water column is most important for the final mixed layer depth in the Irminger Sea. Without a relatively low initial stability even very cold winters do not induce convective mixing which exceeds 500 m. In the Labrador Sea, where the stability is generally lower, the strength of the winter cooling is most important for the eventual mixed layer depth. In the complicated coupled climate models the simulation of a realistic mixed layer seems to be one of the main problems. Some models have no deep convection while others strongly overestimate the mixed layer depth. This causes large differences between the simulated and observed hydrography of the Irminger and Labrador Seas. Another problem seems to be the spin up period of the models. During the spin up period the simulated ocean, which is initially based on observations, adjusts to the simulated atmosphere. This apparently causes the simulated ocean to "drift away" from the observed situation. This leads to large differences when it takes a spin up periods of several hundred model years in order to get the model to be stable.

The variability of the Irminger Sea appears to be much stronger than was previously

assumed. Large variations can occur on short time scales. In order to adequately catch this variability in time series, more rapid observations are necessary. Furthermore, the annual observations should be continued to study the decadal variations and their causes.

Chapter 1

Introduction

1.1 Ocean variability

In an article about the evolution of physical oceanography *Walter Munk* (2002) stated that "the oceans are the principle reservoir for the storage of CO_2, of heat and of ignorance". Much of the ignorance is due to the relatively small amount of available data. In attempts to reduce the number of unknowns in oceanography, large research programs, such as the World Ocean Circulation Experiment (WOCE), constructed atlases that describe the base state (the base being the early 1990s) of the ocean down to horizontal scales of about 20 km. During this, and earlier programs, it became apparent that the ocean is far more variable than previously thought. Original ideas assumed that the ocean currents were reasonably steady, with typical velocities of 10 ± 1 cm s^{-1}. With the increase in sampling accuracy and resolution it turned out that the current velocities are more like 1 ± 10 cm s^{-1}. One of the present challenges in oceanography is to describe and understand the ± 10 cm s^{-1}, which is the ocean variability. Much work and waiting remain until we will reach this goal. The time series that must be gathered need to be several decades long (hence the waiting) before we can see the decadal variability as a true variability signal, instead of successions of partial trends. And possibly more importantly, the resolution of the time series must be adequate to understand the fast and small-scale signals. With series of annual surveys of sections, such as those through the northern North Atlantic, and with long-term fast sampling moorings we have begun to form the time series we need. Now we need to describe and understand the variability we have observed until present. With this thesis I hope to do my part in reducing the storage of ignorance on the variability of the northwestern North Atlantic Ocean.

1.2 The northwestern north Atlantic Ocean

The study area of this thesis is the northwestern North Atlantic Ocean. It is the transition region between the warm (sub)tropics and the cold arctic region. The area is important both for the global ocean circulation and the atmospheric climate at the high latitudes of the northern hemisphere (Seager *et al.* (2002)). It is where the deep, cold waters of the Atlantic Meridional Overturning Circulation (the AMOC, sketched in Figure 1.1) are formed and where the warm surface waters surrender their heat to the atmosphere. It is crucial to know and understand the variability in the currents

and processes in the northwestern North Atlantic in order to understand their role in the global climate.

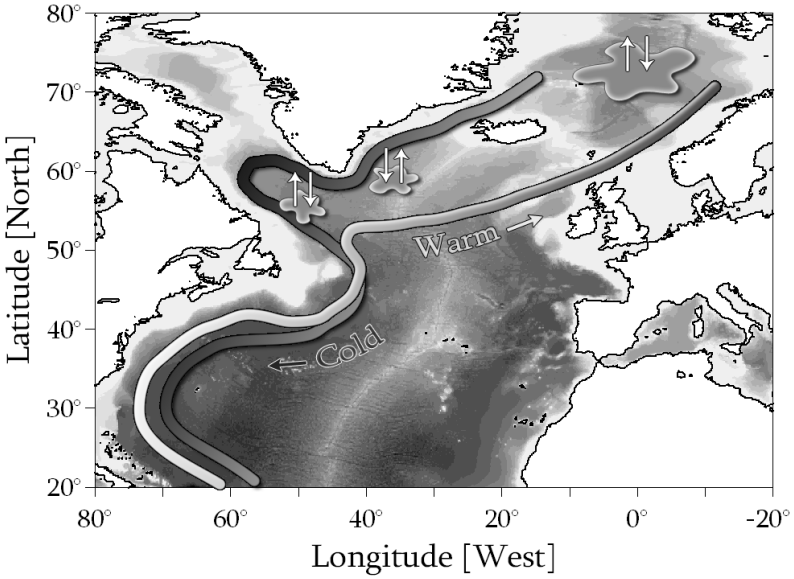

FIGURE 1.1: Crude schematic of the North Atlantic Meridional Overturning Circulation. Warm surface water flows northward in the North Atlantic Current system, compensated by a southward flow of cold deep water in the Deep Western Boundary Current. Sites of deep water formation are indicated by the grey patches.

Sites of deep water formation are rare in the oceans because of the special conditions that are required (van Aken (2007)). Two other areas of deep water formation exist outside the North Atlantic, in the Mediterranean and near Antarctica. The deep water formation site in the Greenland Sea is considered here as part of the North Atlantic deep water formation since these waters cannot take part in the AMOC unless they cross the shallow sills into the Atlantic.

The southward flow of deep water compensates the surface flow of warm subtropical water to the north. The amount of heat surrendered to the atmosphere only in part depends on the initial heat supplied by the southern source region. Also important is the residence time in the Subpolar Gyre (McCartney & Talley (1984)), which recirculates in the northern North Atlantic basins, and the strength of the local atmospheric cooling. Both are in part determined by the local topography which steers the currents and influences the atmospheric forcing. Part of the surface water continues north in the AMOC towards the Arctic Seas. The remainder of the water is steadily modified into a precursor of the deep waters. All the links in the AMOC, the advec-

tion of surface (deep) waters to the north (south), the heat transfer from the ocean to the atmosphere and deep water formation, are subject to change. To understand the causes and possible implications of these changes we must first briefly describe the processes themselves.

1.3 The role of deep water formation in the ocean

The research of the driving forces of the AMOC was (and still is) an important study area in physical oceanography. In the first half of the 20th century the focus of attention was on the buoyancy forcing. The forcing mainly considered was the heating in the tropics by the sun and cooling at high latitudes by convection. *Sandström* (1908) was one of the first to investigate the importance of convection to the overturning circulation. He experimented with buoyancy (heat and cold) sources at opposites sides of a water tank at various depths. He concluded that a thermally driven, steady circulation can only be established if the heating source is situated at a lower level than the cooling source. Since heating takes place at the surface while deep convection can reach down to over 2 kilometres, this would mean that a stable ocean circulation does not exist. Several years later, *Jeffreys* (1925) proposed that any horizontal density gradient induces a circulation, even if the heating takes place above the level of cooling, as long as turbulent vertical diffusion is included. As it turns out both *Sandström* and *Jeffreys* are right, but their arguments are not appropriate for the real ocean. If the ocean circulation was driven by the buoyancy forcing alone the circulation would be limited to a relatively shallow upper layer while the deep ocean was filled with dense homogeneous water from the high latitude convection area. We now know this is not true since observations show the deep ocean is stably stratified. Other energy sources must be available to the ocean in order for it to maintain its deep stratification.

This was investigated by *Munk* in 1966, and later again by *Munk & Wunsch* (1998). Their conclusion was that the ocean is a very inefficient heat engine, meaning that the ocean circulation cannot be driven by buoyancy forcing alone. In fact, the deep circulation is driven by energy supplied by winds and tides. The mechanical energy induces vertical mixing and a downward flux of heat, which is balanced by large-scale upwelling. This maintains the deep stratification in the ocean, and prevents the ocean from filling up with cold water. It is the combination of this mechanical energy with the buoyancy forcing that makes the ocean a very efficient heat transport engine. Thus, deep convection by itself is not an effective method to drive the ocean circulation, but it is an effective method to take out the heat supplied by the ocean circulation. As such it is important to study this process, its effect on the ocean stratification and its variability.

1.4 Topography of the northwestern North Atlantic

The topography of the northwestern North Atlantic Ocean plays a large role in the formation of water masses typical for the hydrography of the area. The topography of the land masses and sea floor around and in the northern North Atlantic Ocean is such that it divides the ocean into various smaller basins (Figure 1.2). This study focuses on the Irminger Sea, which is located southeast of Greenland. This basin has an open connection to the Labrador Sea, which is located west of Greenland, although the Eirik Ridge (just south of Greenland) does have some influence on the flow. The Irminger Sea is separated (at deeper levels) from the eastward located Iceland Basin by the Reykjanes Ridge (RR) and the Mid Atlantic Ridge (MAR). A connection exists between the two basins through the Charlie-Gibbs Fracture Zone (CGFZ), which consists of a series of deep, 3000 m, fractures in the Mid Atlantic Ridge (MAR). The Iceland Basin is bounded in the east by the shallow Rockall-Hatton Bank (RHB). Just west of this bank we find the deepest part of the Iceland Basin, Maury Channel (MC). Between the RHB and the European continent lies the Rockall Trough. All these deep basins are closed off from the north for all but the shallowest levels. The Irminger Sea, Iceland Basin and Rockall Trough are closed off to the north by the Greenland-Scotland Ridge, on which Iceland and the Faroe islands are also located. Some narrow and shallow channels and sills, Denmark Strait (DS, ~ 600 m depth), the Faroe bank Channel (FBC, ~ 800 m depth) and the Wyville Thomson Ridge (WTR, ~ 600 m depth), allow some dense, cold waters from the north to cross the ridge. The Labrador Sea has a shallow connection to the north through Davis Strait. The western boundary currents flow southwards (for the deep waters) and northwards (for the surface water) around the Grand Banks (GB) off the coast of Newfoundland and further along the American continent or towards the Norwegian Sea.

Not only the topography below sea level is of interest to the ocean circulation. There are some words to be said about the "dry" topography. The high topography of Greenland forces the westerly winds to go around the continent, which also causes them to focus and accelerate. Also, the ice cap on Greenland may someday add large amounts of fresh meltwater to the surface waters of this area. The central Canadian continent, which has a land climate due to its size, causes the westerly winds to be dry and cold in winter. This adds to the cooling capabilities of the atmosphere over the North Atlantic Ocean.

Since this thesis is mostly descriptive oceanography the topography has another important role in this story. Descriptive oceanography makes use of the concept of water masses to differentiate between volumes of water with different properties. As the properties of water masses are set in the region of origin they are usually named

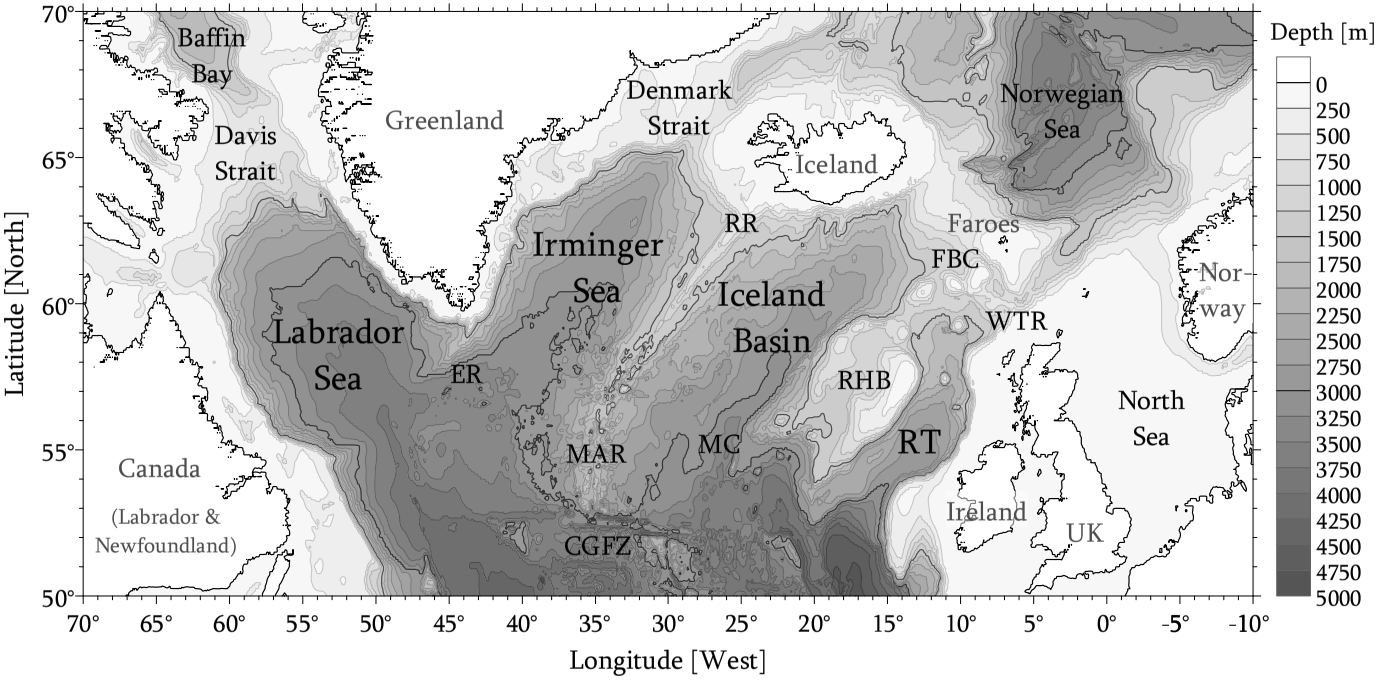

FIGURE 1.2: Topography of the northern North Atlantic Ocean. The acronyms of the topographic features indicated in the figure are (from west to east): GB; Grand Banks, ER: Eirik Ridge, MAR; Mid Atlantic Ridge, CGFZ; Charlie-Gibbs Fracture Zone, RR; Reykjanes Ridge, RHB; Rockall-Hatton Plateau and Rockall-Hatton Bank, RT; Rockall Trough, FBC; Faroe Bank Channel, WTH: Wyville Thomson Ridge.

after this region. A typical example is Labrador Sea Water, which is formed in the Labrador Sea. When several water types are formed in the same region it is common to add the depth level to the names, e.g. North Atlantic Deep Water. Water masses may also be named after their formation process, such as Iceland Scotland Overflow Water (formed over the sill of the Iceland-Scotland Ridge). All of these names are often abbreviated to their acronyms, *LSW*, *NADW* and *ISOW* for the examples given here. This may introduce some complications to the readers who are not used to the multitude of acronyms, of which many are nearly similar (e.g. *ISOW* and *DSOW*, Denmark Strait Overflow Water). Further complication may arise from the use of acronyms denoting the topography, institutes and data sets. For the reader's convenience these names and their acronyms are re-introduced regularly in the text. Also, in order to differentiate between the hydrographic acronyms and other acronyms, the hydrographic acronyms (for water masses and currents) are set in italic typeface. An appendix containing the complete list of acronyms and their explanation is provided at the back of this thesis.

1.5 Deep water formation in the North Atlantic Ocean

Deep water formation in the northwestern North Atlantic Ocean is threefold. There are the dense waters cascading over the sills of the Greenland-Scotland Ridge, the sinking of waters over the continental shelves and deep convection. Of these three, only the first two produce net sinking of water (Pickart & Spall (2001)) which is compensated by the large scale upwelling, and the latter is a buoyancy sink to the ocean. The sinking of water over the continental shelves is not covered in this thesis because this process is not captured by our deep water observations. Deep convection takes place both north and south of the Greenland-Scotland Ridge. In the north it sets the properties of the dense waters in the Greenland Sea. Part of these waters overflow into the North Atlantic and form the southward flowing Deep Northern Boundary Current. South of the Greenland-Scotland Ridge deep convection forms the intermediate waters of the North Atlantic, which are entrained into the deep flow. As such both the overflows and deep convection play a central part in setting the properties of the deep ocean (Marotzke & Scott (1999)).

1.5.1 The overflows

The overflows that allow Nordic waters to enter the North Atlantic are Denmark Strait and the Faroe Bank Channel. Some water also overflows over the Iceland-Faroe Ridge and the Wyville Thomson Ridge, but there are no main channels there that organize the flow. The Denmark Strait and Faroe Bank Channel overflows are outflows of dense waters through narrow channels, making them typical examples of density

driven currents. The outflow currents are in near-geostrophic balance, thus their current speed is mainly determined by their density, the Coriolis force and the slope of the topography (Price & Baringer (1994)). The bottom stress is also of importance, since it allows the currents to slowly descend down the slope to adapt to the overall density stratification of the ocean basin. The process of overflow water formation is sketched in Figure 1.3.

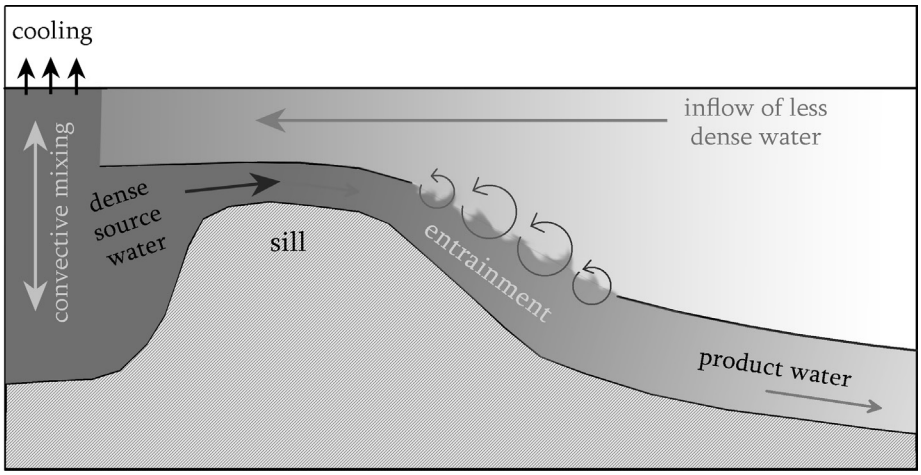

FIGURE 1.3: Schematic of overflowing density currents. Dense source waters formed by deep convection overflow the sill. As current speeds increase due to steeper topography the currents starts to entrain the ambient lighter waters, nearly doubling its volume. The properties of the product water depend on those of the source water and the entrained water.

The initial overflow current is strongly limited by the depth and width of the channel and the height of the interface between the dense water and the overlying water in the source region. The slope in the channel itself is usually small, keeping the current velocity in the non-turbulent regime (Froude number $F < 1$, where $F = U/\sqrt{H \cdot g'}$ with U the current speed, H the height of the current and g' the gravitational force due to the density difference with the environment, Price & Baringer (1994)). As the current leaves the channel the geostrophic balance forces it to follow the topography. When the current approaches the shelf-break the current speed increases due to the steeper topography. The higher velocities raise the Froude number above 1, which causes the current to entrain large volumes of (less dense) water from the environment. Due to this process the current can nearly double its volume in the first (few) 100 km downstream of the sill. Further downstream, the current velocity decreases due to the decreased density and slope angle. As the Froude number decreases, entrainment is strongly reduced and the potential density and volume of the overflow plume remain nearly constant.

Properties of the "product" water found downstream, depend on the properties of the source water upstream of the sill, the properties of the surrounding water in the entrainment area and their ratio in the final product. This ratio can vary through changes in initial transport over the sill, due to changing interface depth. Enhanced or lowered production of dense water or changes in wind stress and the resulting Ekman pumping can raise or lower the interface. Changes in convection can cause variation in the properties of the source waters and/or the entrained water.

1.5.2 DEEP CONVECTION

Deep convection is the deep turbulent mixing of water particles due to instability of the water column caused by severe cooling of the sea surface. It is a process that takes place only at a few locations in the world oceans, in the Greenland Sea, the Mediterranean, near Antarctica and in the northwestern North Atlantic Ocean, and even there only when several conditions are satisfied (Marshall & Schott (1999)). This is due to the fact that the ocean is inherently stable and a large forcing is needed to make it unstable. The convective area is made less stable in places where the atmosphere induces a (strong) cyclonic circulation. The cyclonic circulation is associated with upward doming isopycnals, which bring denser (less stratified) water closer to the surface. This stage is called preconditioning and is visualized in panel a of Figure 1.4. The preconditioning depends on the strength of the cyclonic gyre and on the stratification of the intermediate waters.

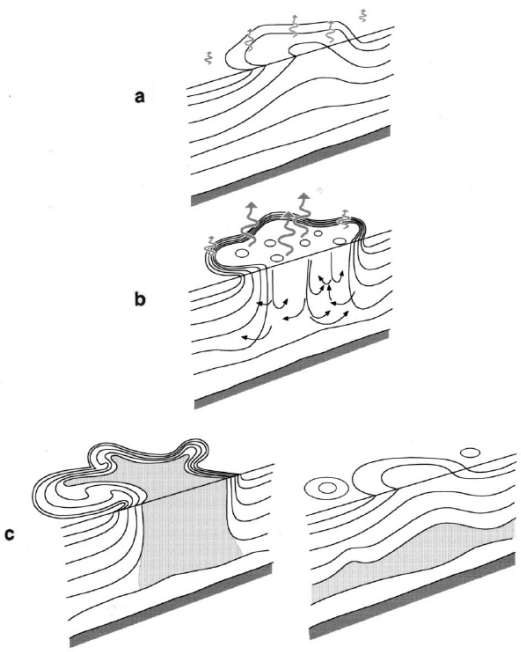

FIGURE 1.4: The stages of open ocean convection from Marshall & Schott (1999). (a) preconditioning, (b) deep convection, (c) lateral exchange and spreading. Buoyancy flux through the sea surface is represented by curly arrows, the underlying stratification/ outcrops is shown by continuous lines. The volume of fluid mixed by convection is shaded.

The second stage of the convection process is the convective mixing itself. It is brought about by large buoyancy loss (cooling) of the ocean surface to the atmosphere in winter, which erodes the remaining surface stratification. The surface density is increased to the point where the water column becomes unstable and the water overturns in convective plumes. The convective plumes, or cells, have a horizontal scale of about 1 km, close to the internal Rossby radius of deformation. The vertical scale varies between several 100 m to 2 km depth. The plume may be slightly slanted due to the horizontal component of the Coriolis parameter, which is non-zero outside the poles. Together the convective plumes mix an area ranging from 10 to some 100 km horizontally, called the mixed patch (sometimes also called chimney). By the mixing and cooling of these large volumes of water a great amount of heat is removed from the ocean in a short period of time. When the surface cooling is no longer enough to destabilize the water column the mixing stops and the third phase of the convection process (Figure 1.4c) sets in. This is called restratification. The mixed patch becomes subject to baroclinic instability and breaks up into smaller eddies. This allows the inflow of the surrounding, less dense waters over the convective area. The denser, convectively mixed waters sink down to their equilibrium depth and spread out laterally.

The strength and duration of a deep convection event depends on the initial preconditioning and the applied buoyancy flux (Marshall & Schott (1999)). A weakly stratified water column, due to a stronger cyclonic gyre or homogenization by convection in a previous year, requires less buoyancy forcing to initiate convection. Stronger buoyancy forcing creates longer lasting and deeper convective mixing events. Combinations of strong preconditioning and buoyancy forcing have been observed to cause convective mixing down to 2400 m in the Labrador Sea (Lazier *et al.* (2002)). During periods of weak preconditioning and forcing the mixing depths cannot reach below a few hundred meters. The properties of the resulting homogenized water mass also depend on the preconditioning and surface forcing. It is a mixture of the properties found in the overturned water column, strongly cooled and enriched in oxygen and other soluble gases due to its recent contact with the atmosphere.

Known and well documented convective areas in the North Atlantic Ocean are the Greenland Sea north of Iceland (Rudels *et al.* (1989), Watson *et al.* (1999) and Lherminier *et al.* (1999)), and the Labrador Sea (Talley & McCartney (1982), the Lab Sea Group (1998), Lazier *et al.* (2002), Yashayaev *et al.* (2008)). The Irminger Sea was mentioned as a convective area by *Nansen* in 1912, but observational evidence was scarce. The discussion about deep convection in the Irminger Sea and in a nearby area southeast of Greenland was rekindled by a paper of *Pickart et al.* (2003). Convective mixed layers have been observed in the central Irminger Sea (Bacon *et al.* (2003)), but

not yet down to the depths observed in the Labrador Sea. Also the effect and importance of convective mixing in the Irminger Sea remains unclear.

1.6 Variability on the small(est) scale: Intrusions

Water mass and tracer theory assumes that properties of slow moving water masses, both physical (e.g. salinity and temperature) and chemical (e.g. the oxygen and silicate concentrations), are more or less conserved as the water mass is advected along a certain path. For the parameters that partake in biological processes (like oxygen), the aging of the water mass must be taken into account. After the German Meteor Expedition, *Wüst* (1935) used the conservation principle to determine the paths of the Atlantic water masses. However, when we look closely we must admit that this simplified conservation principle is not entirely accurate. Given time, the properties of the water masses change due to lateral mixing or interleaving and vertical turbulent mixing with neighbouring water masses. The interleaving exists where ever there are lateral gradients of temperature and salinity. Interleaving intrusions can cause large lateral fluxes of heat and salt (Ruddick & Kerr (2003)), which cause water masses to gradually change their properties and decrease the gradients between these water masses.

The interleaving intrusions of the neighbouring water mass are seen in hydrographic profiles as density compensating inversions in the temperature and salinity profiles. They are sometimes attributed to a process generally called double diffusion, although differential diffusion is a more accurate name. Figure 1.5 shows an example of an early lab experiment of double diffusion by *Turner* (1978).

The process of double diffusion is based on the difference in the molecular diffusion of heat and salt. Heat diffuses more rapidly than salt, so a parcel of warm salty water will exchange (lose) its heat more rapidly with the environment than its salt content. This causes the density of the parcel to increase, while the density of the cooler, fresher environment (now heated by the parcel) decreases. Beginning with a small perturbation, the downward inclined moving parcel of warm, saline water, increases in density (downward buoyancy flux), which reinforces the initial motion of the parcel. Similarly, an upward inclined fresh and cool parcel gains heat from the environment, decreasing density, and continues to rise. This allows the initial perturbations, which may be caused by sheared lateral advection over a background temperature and salinity gradient, to grow.

The (nearly) horizontal interfaces between the intrusion and the environment are also subject to diffusive effects. The interfaces (density gradient) with cold-fresh water

above warm-salty water become sharper as the layer just above the interface warms and the layer below the interface cools. At the opposite side of the intrusion, where the warm-salty layer lies above the cold-fresh layer, the density gradient decreases until turbulent convective mixing, called salt fingering (Figure 1.5), removes the stratification. The net effect is a down-gradient (downwards) salt flux. A small part of the heat flux is also down-gradient, but most of it is horizontal to the adjacent waters. Thus, the mass flux is downwards, making the water column more stable over time. Most importantly, the double diffusion process is able to mix adjacent water masses with no other input of kinetic energy by tides or winds than the initial perturbation.

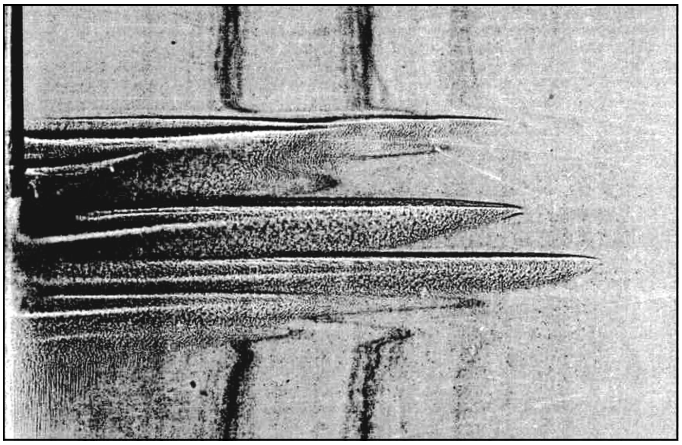

FIGURE 1.5: Intrusions with diffusive and salt fingering interfaces. (Figure 2 from Turner (1978), a lab experiment of a sugar solution intrusion into a linear salinity gradient. The sugar functioned as a replacement for temperature without the disadvantage of heat loss through the sides of the tank.).

1.7 HYDROGRAPHIC VARIABILITY VS. OBSERVATIONS

The variability in the processes described above has always been present in the ocean. But the ocean had to be observed, and observed accurately more than once, in order for the variability to become visible to researchers. The observations that have been used for this study are shipboard measurements of hydrographic profiles, mooring data, satellite data and ocean/atmosphere reanalyses. These observations span a range of sample intervals, from nearly annually (the hydrographic surveys by ships) to every 3 minutes (sensors in moorings), and a range of spatial resolutions, from a single location (moorings) to global 2° x 2° coverage (satellite/reanalysis). Each of these types of observations has its advantages and disadvantages with respect to its ability to capture variability signals. The satellite and reanalysis data seem to have the best coverage, but they do not reach (far) below the sea surface. The data obtained by sampling the deeper water masses have two main "problems".

The first problem is the aliasing of signals with short time scales unto larger time scales. An exaggerated example of this is shown in Figure 1.6. This figure shows an arbitrary ocean signal, composed of inter-annual variability, a seasonal cycle and random noise (e.g. caused by eddies). In the ocean it is not unusual to encounter seasonal or faster signals to be larger than the long term change (remember the 1 ± 10 cm s^{-1}). The original 4-year signal is sampled annually (twice), although with slightly varying intervals which is common for ship surveys. The two resulting annual series show quite different trends and would lead to diverging theories on their cause. The seasonal cycle is lacking completely, as could be expected, but it is severely aliased onto the observed signal.

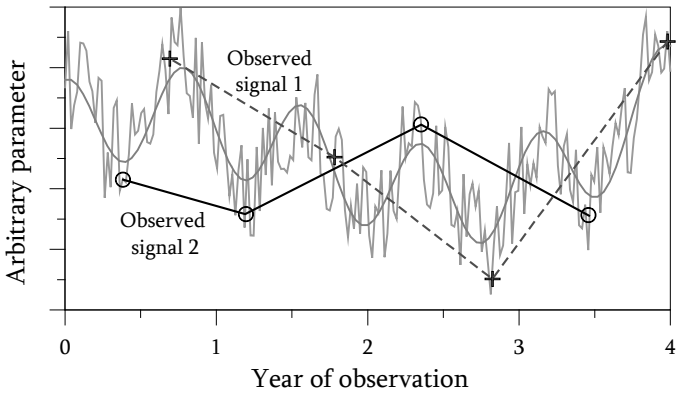

FIGURE 1.6: Aliasing of a signal composed of inter-annual variability, a seasonal cycle and random noise (grey lines). The signal is sampled annually twice (crosses and circles), which gives quite different results.

The second problem concerns the difference between the Lagrangian versus the Eulerian variability. For example, in order to see the evolution of a mixed layer in one particular convective cell, the convective cell needs to be followed and monitored while it travels through the ocean basin (the Lagrangian viewpoint). Through these observations the exact evolution of the mixed layer in this cell can be described, but it does not give information of the number of convective cells in the basin or the representativeness of the monitored cell. The fast sampling moored instrument, which are thus best equipped to monitor such an evolution, have the reverse problem since they are fixed in one location. These instruments measure the properties of the water which passes by (Eularian viewpoint). By the number of convective cells that pass by an estimation might be made on the total convective activity in the basin, but it is unclear how these cells evolve precisely. Again, one must estimate how representative the location of the mooring is for the larger study area. By combining the annual sections, which may include strong aliases but have the advantage of covering a horizontal cross section, with the observations of moorings, which resolve the fast signals at a single point in the section, a more complete picture of the variability can be sketched.

1.8 Observations vs. Models

One popular approach to fill up the holes in the observations is to design and run a numerical model. This has the advantage of high resolution, depending only on the limitations of the computing capacity, and of being able to create time series of several hundred years in a matter of days or weeks. Once the model is developed, the time series that are generated are relatively cheap compared to sea going expeditions.

The first climate models treated the ocean as a shallow layer with an infinite heat capacity, keeping the surface temperature constant at all times. One of the first models with a coupled ocean and atmosphere component had 5 ocean levels and grid points spaced 500 km apart (Manabe & Bryan (1969)). It did not have a realistic topography, there was one continent and one ocean, but the results were promising. Models have come a long way since then. Today's climate models (see Chapter 6 and the Appendix) have realistic topography, resolutions down to a few kilometres and are able to simulate observed features such as El Niño. However, the effects of sub-grid scale processes, such as turbulent and lateral mixing, still need to be parameterized. This is one of the major impediments in attempts to simulate an ocean which is full of fast, small scale variability. If the simulation by an ocean model strays off course, that is away from the observed state due to an inaccurate parameterization, numerical diffusion or too coarse resolution, errors built up through the model run. The ocean simulation then becomes something that no longer resembles the real ocean.

Ocean reanalyses (Köhl *et al.* (2003), Carton *et al.* (2005)) combine the advantages of the resolution of models, with the realism of observations. They use an ocean model to fill up the gaps in time and space that exist between observations. It forces the results to remain close to the observed state, but the time series are limited to the length of the observed series. Furthermore, where there are few observations, such as in the deep ocean, the ocean reanalyses still depend mostly on the programmed code. However, models are key in predicting changes in the future and as a method to gain insight into ocean processes by experimentation. It is exciting to see that the models simulations are increasingly realistic. However, comparing the results of the model simulations to the observations must remain one of the methods to validate these models and improve their results.

1.9 Research questions & ongoing discussions

Although much work has already been done on the topics discussed above, some issues of discussion still remain. With the combination of time series, such as the mooring data, the hydrographic surveys and the atmospheric reanalyses presented in this thesis, some form of answer may be given on the following questions.

- How large is the inter-annual variability in the northwestern North Atlantic?
- Which water masses and/or physical processes add to the variability?
- What does the variability look like on shorter time scales?
- What role does deep convective mixing play in the Irminger Sea?
- How well does the current generation of coupled climate models simulate the ocean state and variability of the northwestern North Atlantic?

1.10 This thesis

In answer to the questions phrased above this thesis covers the following topics.

- Chapter 2 introduces the reader to the general circulation, the hydrographic base state and the mean climatology of the Irminger Sea and Labrador Sea. We will refer to this base state and its characteristic water masses throughout the rest of the thesis.
- Chapter 3 describes the decadal and inter-annual variability as observed with the near-annual hydrographic surveys. Some of the processes that are thought to cause this variability are also discussed.
- In Chapter 4 the mooring data of two moorings in the Irminger Sea are presented and the variability on sub-annual time scales is described. Chapters 3 and 4 will show that deep mixing is one of the key processes responsible for both the inter- and intra-annual variability.
- Chapter 5 contains a sensitivity study of deep mixing. This is done by means of a simple (1D) encroachment model, which simulates the convective mixing in the Labrador and Irminger Sea with varying preconditioning and the atmospheric forcing.
- The performance of Coupled Climate Models with respect to the observations is investigated in Chapter 6.
- In the last chapter, Chapter 7, we will discuss to what extent the questions in Section 1.9 can be answered based on the results presented here.

Chapter 2

Circulation and Climatology

2.1 Introduction

The circulation and climatology of the northern North Atlantic Ocean play an important role in the thermohaline overturning circulation (the THC, van Aken (2007)). Heat stored in the surface waters is transferred to the atmosphere during winter, which contributes to the relatively mild climate of the North Atlantic region, particularly of western Europe (Seager *et al.* (2002)). During cold outbreaks in winter the buoyancy loss of the ocean is large enough to initiate deep convective mixing (Marshall & Schott (1999)). The northern North Atlantic Ocean is one of few areas where deep convection takes place, providing a link between the northward transport of warm surface waters and the southward transport of cold deep waters as was sketched in the previous chapter. Transport in the deep southward branch of the THC is facilitated mainly by the Deep Western Boundary Current. This current is fed with several dense waters of North Atlantic origin, which combine into North Atlantic Deep Water.

The characteristic surface circulation and the modification of subtropical waters to subpolar waters in the northwestern North Atlantic are sketched in this chapter. Also, the origin and advective pathways of the intermediate and deep waters, especially the constituents of North Atlantic Deep Water, are described. This description of the characteristic circulation in the northern North Atlantic Ocean will serve as a background for the discussion of the variability of the hydrography in Chapter 3. Although this thesis has a strong focus on the hydrography and variability of the Irminger Sea, this basin takes part in the greater circulation of the Subpolar Gyre. Therefore, we must also be familiar with the hydrography of the surrounding basins, primarily the Iceland Basin and the Labrador Sea, and their connecting advective pathways.

The surface circulation of the Subpolar Gyre depends strongly on the wind forcing. Also, many ocean processes that contribute to the characteristic hydrography and its variability, such as the modification of surface water and deep convection, are driven by the atmosphere. Therefore, the climatology of the atmospheric surface forcing of the Labrador Sea, the main convective region, and the Irminger Sea, our study area, are presented here. Since winter processes are important, both the long time mean and the annual cycle of the surface forcing, e.g. heat and freshwater fluxes and wind stress curl, are described.

The topography has been introduced in the previous chapter (Section 1.4). Here we will start with a description of the circulation and hydrography of the northern North Atlantic. The hydrographic data used to illustrate the circulation are presented in Section 2.2.1. The surface and deep circulation are described in Sections 2.2.2 and 2.2.3. The second part of this chapter, beginning in Section 2.3, discusses the climatology of the surface forcing. The climatological data are introduced in Section 2.3.1. The mean pressure fields and characteristic wind vectors are shown in Section 2.3.2. The surface heat and freshwater fluxes are described in Sections 2.3.3 and 2.3.4. Section 2.3.5 compares the relative importance of the heat and freshwater fluxes to the total buoyancy flux. Finally, Section 2.4 contains a summarizing discussion of this chapter.

2.2 CIRCULATION

2.2.1 HYDROGRAPHIC DATA

The hydrographic data used for this chapter originate from the World Ocean Circulation Experiment (WOCE) one-time surveys of the North Atlantic Ocean. The WOCE program was part of the World Climate Research Program, a research program of the World Meteorological Organization (WMO), the Scientific Committee of Oceanographic Research (SCOR, part of the International Council for Science (ICSU)) and the Intergovernmental Oceanographic Commission (IOC, part of the United Nations Educational, Scientific and Cultural Organization (UNESCO)). The goal of WOCE was to organize a comprehensive survey of the world's oceans in order to estimate its base state and determine its role in climate. The WOCE field campaigns lasted from 1990 to 1998, after which the data analysis period continued until 2002. From the WOCE hydrographic sections, the AR07 section, with a western part through the Labrador Sea (the AR7W section, Figure 2.1) and an eastern part from the southern tip of Greenland to Ireland (the AR7E section), is used to illustrate the hydrography of the northern North Atlantic Ocean.

The survey of the AR7E made in September 1991 by the research vessel Meteor from the Institut für Meereskunde, Hamburg, Germany, is the most complete survey from the beginning of the WOCE period and can serve as a base state for comparisons between surveys. Measurements were made at 58 stations between the Greenland slope and the slope of the European continent. The AR7W sector through the Labrador Sea is illustrated by data obtained on board the research vessel Dawson, from the Bedford Institute for Oceanography, Bedford, Canada, in July 1990. This shorter section, from the Labrador shelf to the Greenland slope, consists of 22 hydrographic stations. On both surveys temperature and salinity measurements were made with a CTD (Conductivity, Temperature and Depth) system and were collected in 2 dbar in-

terval CTD profiles. Tracer samples for oxygen, silicate, nitrate, nitrite, phosphate and chlorofluorocarbons (CFC-11 and CFC-12) were collected on most stations. Cruise documentation, CTD data and bottle data of the Meteor and Dawson cruises were obtained from the WOCE database at http://whpo.ucsd.edu/.

In order to visualize the hydrographic properties in a much larger area of the northern North Atlantic Ocean, more CTD data were obtained from the ICES (International Council for the Exploration of the Sea) data base. This second data set consist of CTD data in the area between 50° N and 70° N and between 70° W and 0° W. The CTD data set was downloaded from the ICES data base at http://www.ices.dk/ocean/aspx/HydChem/HydChem.aspx. These stations contain pressure (P), salinity (S) and temperature (T) profiles with varying vertical intervals, with recent stations having an 1 or 2 dbar interval. Potential temperature (θ), potential density (σ) and stratification (N^2 and PV) are calculated from the original profiles. Despite of its large size (the data set includes 32394 stations) the stations are spread inhomogeneous in both time and space. Station density is largest on the European continental slope, Denmark Strait and the Greenland and Labrador slopes (Figure 2.1). Most of the data is of the WOCE and post-WOCE period.

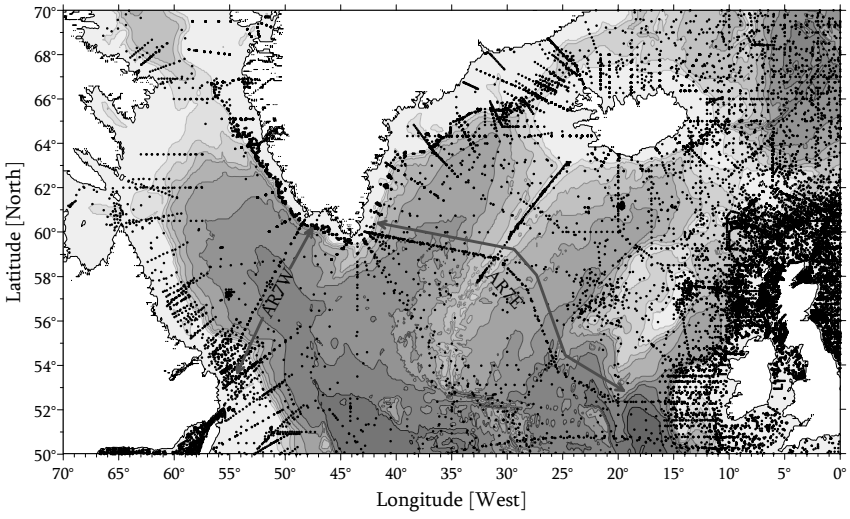

FIGURE 2.1: Overview of ICES stations in the northern North Atlantic Ocean. The ICES station positions are indicated by the black dots. The AR7W section, from southwest Greenand to Canada, and the AR7E section, from southeast Greenland to east of Ireland, are indicated by the grey lines.

ICES station data (on a pressure or density level) were mapped on a 1° longitude by 1° latitude grid. For each map the gridded station data are interpolated using a "inverse distance to a power" interpolation on a 0.5° x 0.5° grid. However, interpolated data over areas that are poorly sampled should be interpreted with some caution. To assure that values belonging to deep water masses in the Irminger and Iceland basins, which are physically separated by the Mid Atlantic Ridge, do not cross the ridge due to the interpolation, a break line is applied over the top of the Mid Atlantic Ridge during interpolation.

Sea surface temperature (*SST*) data were retrieved from the International Comprehensive Ocean-Atmosphere Data Set (ICOADS) 1° Enhanced. These were downloaded from http://www.cdc.noaa.gov/ (ICOADS data provided by the NOAA/OAR/ESRL PSD, Boulder, Colorado, USA). The downloaded data set contains monthly mean sea surface temperatures from January 1960 to July 2007. These data were averaged in time to get the mean surface temperature field. In contrast to the ICES data the mean ICOADS field contains nearly no data gaps. Thus the mean ICOADS sea surface temperature field offers a check for the gridding and interpolating of the ICES near surface (temperature) data.

2.2.2 Surface circulation

The mean sea surface temperature of the ICOADS data set (Figure 2.2) gives a reasonable indication of the temperature distribution created by the sea surface currents north of 50° N. Warm southerly waters flow north along the eastern side of the basin, while cold waters enter from the north and northwest. Figure 2.2 is very similar to the middle panel of Figure 2.3, which contains temperatures based on the ICES data. Therefore we assume that the other parameters based on ICES data, salinity and density, also give a reasonably reliable image of the northern North Atlantic hydrography. We shall discuss the surface currents and the most prominent surface water masses here. Various acronyms are used to denote these hydrographic features. In order to distinguish these acronyms from others (used for data sets and such) more easily, we have set the acronyms referring specifically to names of currents and water masses in an italic typeface. A list of all used acronyms can be found in the appendix.

The surface circulation of the North Atlantic Ocean consists of an anti-cyclonic, warm subtropical gyre and a cyclonic, cooler subpolar gyre. The western boundary current of the subtropical gyre, the Gulf Stream, continues partly into the Atlantic Subpolar Gyre as the North Atlantic Current (*NAC*, Fig. 2.4). After retroflecting in the Northwest Corner (Lazier (1994)) the *NAC* turns east crossing the Mid Atlantic Ridge

towards the Iceland Basin. Another warm current enters Rockall Trough following the European continental slope (van Aken (2002), therefore coined European Slope Current or *ESC*), which brings water from the Bay of Biscay and the west Iberian coastal regions to the north. The relatively warm, saline water in Rockall Trough is named North Atlantic Water (*NAW*, Meincke (1983)). The route of the warm water can be recognized in Figure 2.2 and in the middle panel of Figure 2.3, which show the ICOADS and ICES derived mean *SST* and near-surface temperature respectively.

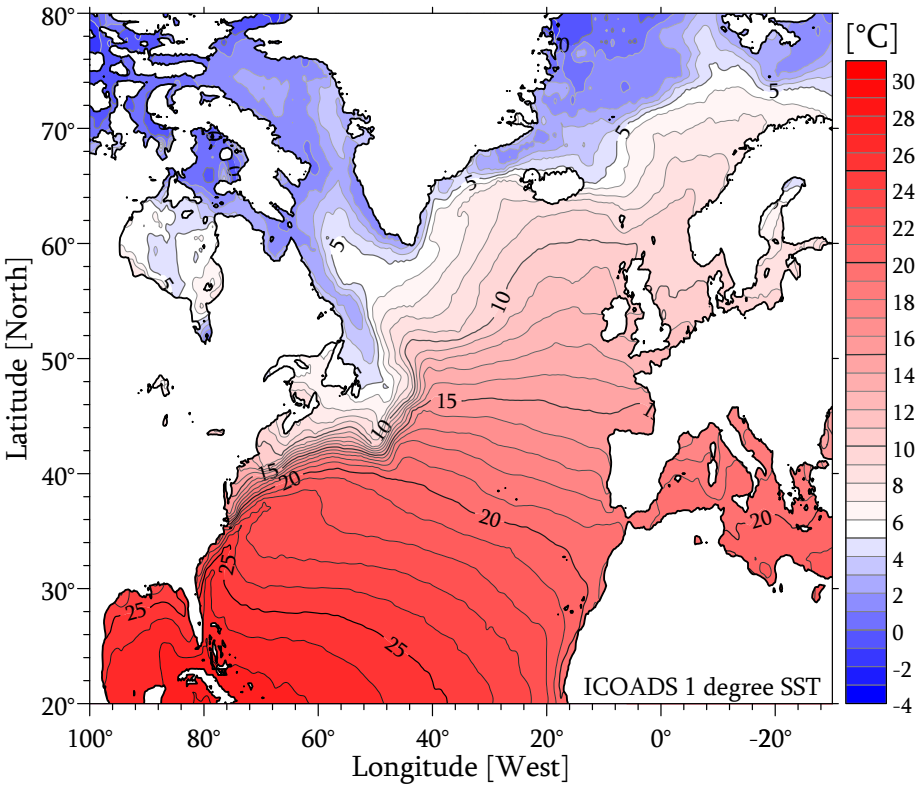

FIGURE 2.2: Mean sea surface temperature of the northern North Atlantic Ocean. Shown is the mean SST field over the 1960 to 2007 period derived from monthly mean ICOADS data. It shows relatively warm water from the south transported northward along the European coast and colder water from the north transported along the western boundary of the basin.

The sharp temperature and salinity front is clearly visible in the upper two panels of Figure 2.3, at about 45° W and 50° N off the Grand Banks. The most saline, warmest waters are found along the European shelf, with part of this water branching westward south of Iceland. The other fraction of these warm, saline waters turns northeast

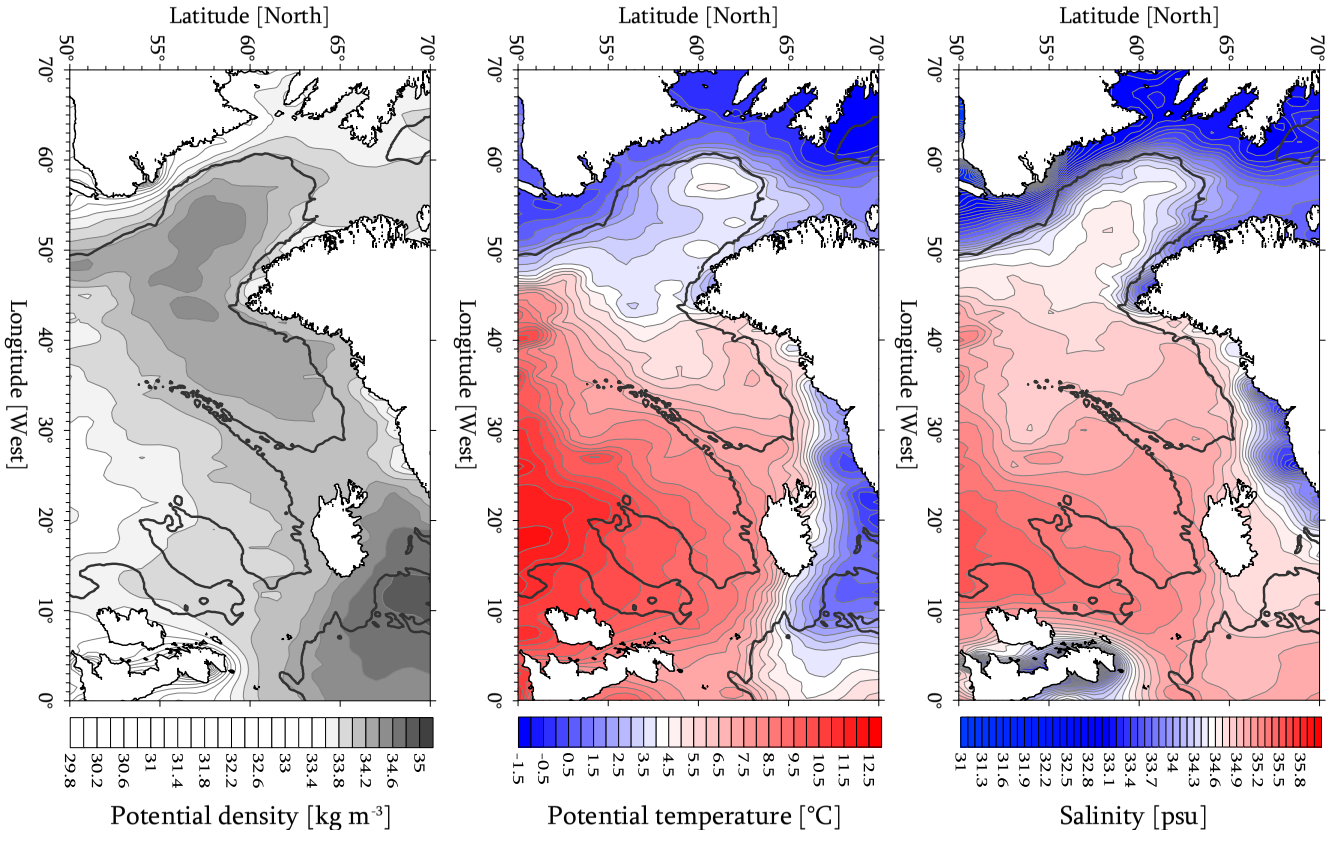

FIGURE 2.3: Mean salinity (top panel), potential temperature (middle panel) and potential density anomaly relative to 1500 dbar ($\sigma_{1.5}$, bottom panel) of the layer between the 0 and 200 dbar. The mean field are derived from the gridded ICES data. The 1500 m isobath (dashed grey line) is drawn to indicated the location of the Greenland-Scotland Ridge, the Mid Atlantic Ridge and the Rockall-Hatton bank.

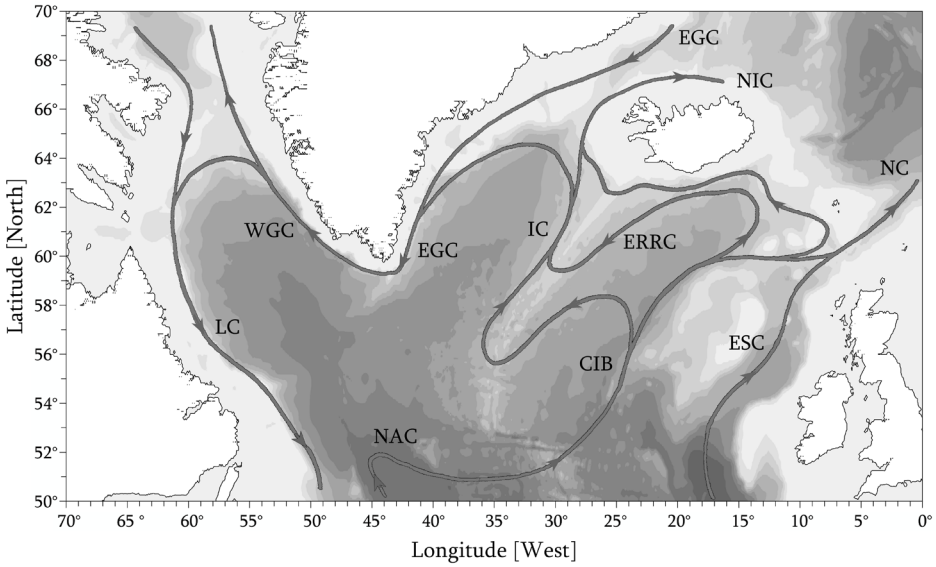

FIGURE 2.4: Schematic of surface currents in the North Atlantic, based on Figure 13 in McCartney & Talley (1982). The depth of the topography is illustrated by the grey shades, with the darker grey indicating the deeper parts of the basins. The acronyms denote the CIB: Central Iceland Branch, EGC: East Greenland Current, ERRC: East Reykjanes Ridge Current, ESC: European Slope Current, IC: Irminger Current, LC: Labrador Current, NAC: North Atlantic Current, NC: Norwegian Current, NIC: North Iceland Irminger Current, WGC: West Greenland Current.

north of Scotland, crossing the Iceland-Scotland Ridge into the Nordic Seas. Here it is known as the Norwegian Current (*NC*) or the Norwegian Atlantic Current. The Gulf Stream/*NAC*/*NC*/*ESC* system imports warm, saline waters into the Subpolar Gyre and arctic region, thus contributing an important part to the import of heat into the Subpolar Gyre and to the northward heat transport of the upper branch of the meridional overturning circulation (McCartney & Talley (1984), Østerhus *et al.* (2005)).

In the vertical cross section along the AR7E (the depth-longitude plot in Figure 2.5), the warm and saline North Atlantic Water (*NAW*) can be seen above the 34.50 kg m^{-3} isopycnal (the potential density relative to 1500 dbar, $\sigma_{1.5}$), more or less coinciding with the thermocline. The *NAW* originates from the waters in the North Atlantic Current branch, which retroflects in the Northwest Corner. It is further modified by heat loss to the atmosphere, causing the Central Iceland Branch to be somewhat cooler than the main *NAC* and *ESC* branches. This temperature (and salinity) difference creates the Subpolar front at ~22° W. Because of their current or recent exposure to the atmosphere, the surface and near-surface waters are high in CFC-11 content

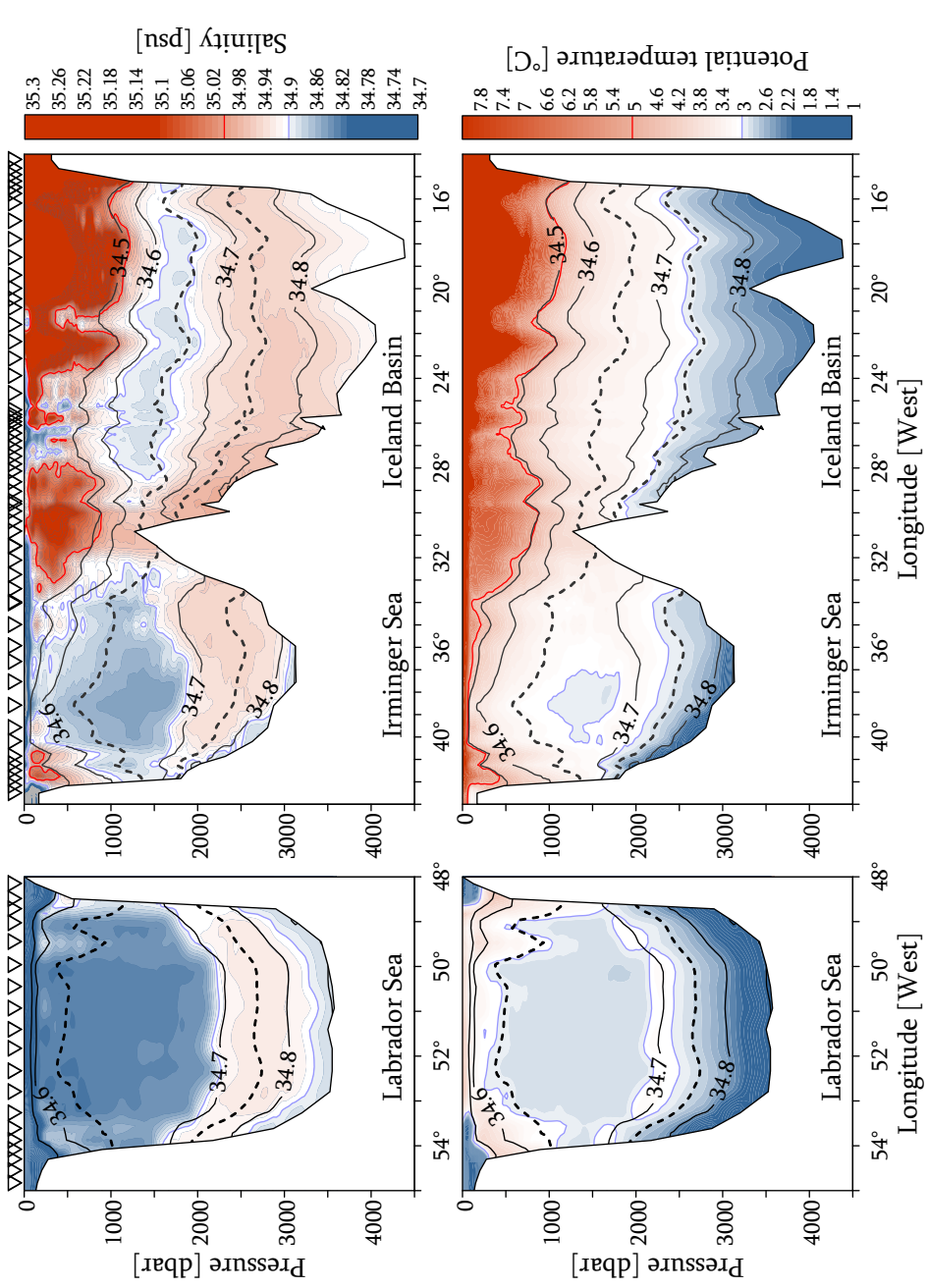

Figure 2.5: Depth-longitude distributions of salinity (top) and potential temperature (bottom) along the AR07 sections. The left panels illustrate the hydrography of the AR7W section through the Labrador Sea in 1990. The right panels illustrate the AR7E section through the Irminger Sea and Iceland Basin in 1991. Locations of CTD stations are marked by the triangles on the top panel. The black lines represent the $\sigma_{1.5}$ isopycnals between 34.50 and 34.80 kg m^{-3}.

(Fig. 2.6). However, due to biological primary production in the photic zone, the oxygen concentration in this layer is relatively low in the warmer, eastern upper layers. The biological processes also affect the nitrate and silicate concentrations, causing relatively low concentrations of these tracers in the warm upper layer (Fig. 2.7). In the west, particularly in the Labrador Sea, regular ventilation in winter by convective mixing raise the oxygen concentration and homogenizes the nutrient concentrations.

Sverdrup et al. (1942) estimated that about half the Modified North Atlantic Water (*MNAW*) does not cross the Iceland-Scotland Ridge, but turns west in the Iceland Basin instead. There it is further modified by cooling and convective mixing in the winter mixed layer forming the Subpolar Mode Water (*SPMW*). *McCartney & Talley* (1982) suggested that the *SPMW* continuously recirculates in the Subpolar Gyre, following the Irminger Current (*IC*) and the East Greenland Current (*EGC*). However, the *SPMW* found on the western side of the *NAC* branches and the density classes of *SPMW* of the Subpolar Front and the Central Iceland Branch do not appear to be interconnected (Brambilla & Talley (2008)). The *SPMW* at the Subpolar Front

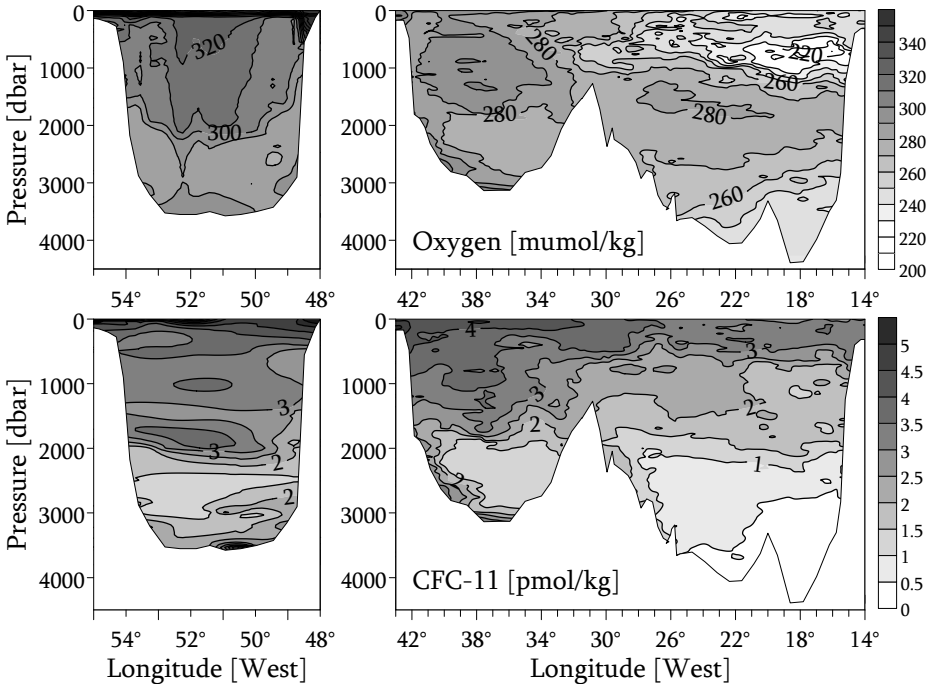

FIGURE 2.6: Concentrations of dissolved oxygen and CFC-11 along the AR07 section. The oxygen concentration is shown in the top panels and the CFC-11 concentration in the bottom panels. On the left is the AR7W section (on the left) surveyed by the Dawson in 1990 and on the right is the AR7E section surveyed by the Meteor in 1991.

continues northeastward, while only the *SPMW* of the Central Iceland Branch turn west towards the East Reykjanes Ridge Current (*ERRC*) and the Irminger Current. At the Greenland-Iceland Ridge the part of the Irminger Current continues northeast as the North Iceland Irminger Current (*NIC*), while the bulk of the Irminger Current circulates around the Irminger basin and joins the *EGC*, subducted below a relatively fresh shallow surface layer. During its passage through the Subpolar Gyre the *SPMW* is progressively cooled and freshened.

This progressive modification is discernible in Figure 2.3. It shows a warm, saline branch following the curve in the topography along the northern part of the Irminger basin. Also, a similar, but cooler, branch can be seen starting from the southern tip of Greenland and following the 1500 m isobath around the Labrador Sea. Due to the progressive cooling (and despite of the freshening), the *SPMW* density increases. It is most dense in the more-or-less closed cyclonic gyre in the centre of the Labrador Sea (Lavender *et al.* (2000)). There it becomes one of the more saline precursors of Labrador Sea Water.

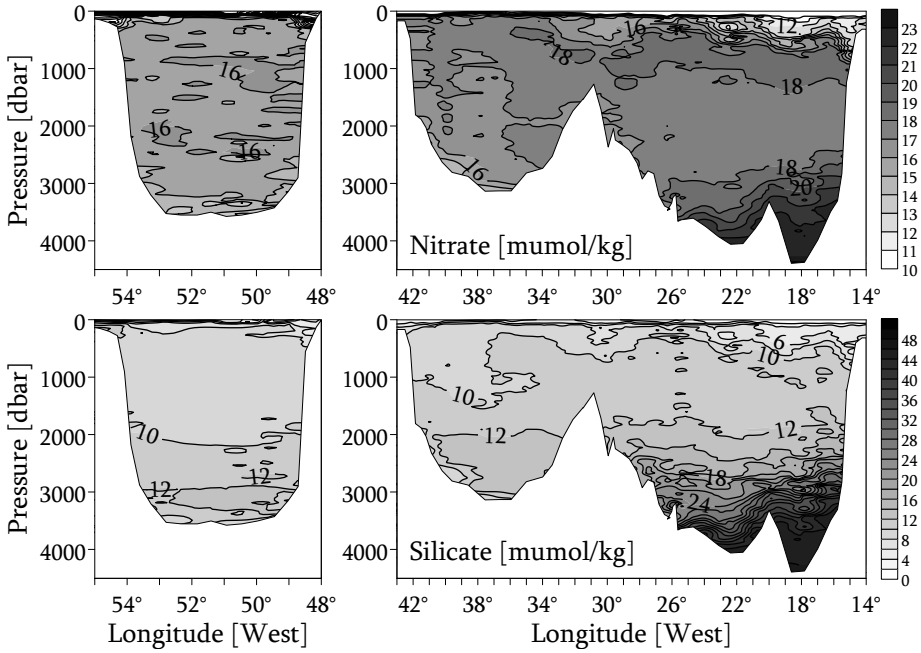

FIGURE 2.7: Concentrations of nitrate and silicate along the AR07 section. The nitrate concentration is shown in the top panels and the silicate concentration in the bottom panels. On the left is the AR7W section (on the left) surveyed by the Dawson in 1990 and on the right is the AR7E section surveyed by the Meteor in 1991.

The East Greenland Current and the inshore located, narrower East Greenland Coastal Current (*EGCC*) follow the continental slope of eastern Greenland (Bacon *et al.* (2002)). Both currents have a relatively cold and fresh surface signature as opposed to the warmer, more saline surface currents in the east (e.g. the *IC* and the *NAC*, Figure 2.4). The low salinity and temperature is derived from the transport of melting arctic sea-ice by the *EGC* and *EGCC*. Both currents merge south of Cape Farewell, the southern tip of Greenland, where the shelf edge widens. About one third of the relatively fresh current retroflects at Eirik Ridge and flows into the interior of the Subpolar Gyre, providing a source of freshwater for the central Irminger Sea (Holliday *et al.* (2007)). Two thirds continue around the Labrador Sea as the West Greenland Current (*WGC*). The relatively fresh water can be followed for most of its path along the western border in Figure 2.3, except for a section on the eastern Greenland coast where few observations were made on the shelf (Figure 2.1). Baroclinic instability on the steep Greenland slope causes the *WGC* to shed eddies into the central Labrador Sea (Hátún *et al.* (2007)). The upper 200 m of the anticyclonic meso-scale eddies is composed of fresh *WGC* water and provides a source of freshwater to the central Labrador Sea. Between 200 and 1000 m the eddies contain warmer, saline water from the Irminger Current and provide a source of heat and salt to the mid depths. By bringing stratified waters to the centre of the basin the eddies play an important part in the (re) stratification of the Labrador Sea (Katsman *et al.* (2004)).

2.2.3 Deep circulation

The deep (and intermediate) currents resemble the surface currents in the cyclonic nature of their circulation. The driving processes however, are different. While the surface currents of the Subpolar Gyre are mostly wind driven, the deep currents are density driven. This causes the deep currents to follow the topography even more closely (Figure 2.8). Velocities at these depths are slow, and one cannot speak of real currents for most of the deep circulation (Lavender *et al.* (2000)). However, the properties of the various water masses are conserved and can be used as tracers. The thus traced paths of the intermediate and deep waters are sketched in Figure 2.8. Due to its large volume the slow, deep circulation is able to balance the northward transport of water in the shallower, but faster surface branch of the meridional overturning circulation. The composite of dense northern water masses, the cold water mass called North Atlantic Deep Water (*NADW*), is transported southward in the Deep Western Boundary Current along the North American continent (van Aken (2007)).

The densest water mass is the Denmark Strait Overflow Water (*DSOW*), which originates from the relative fresh waters north of the Greenland-Iceland Ridge. It enters the Irminger Sea by the overflow across the shallow sill (680 m) in Denmark Strait

(Figure 2.8). The high density of *DSOW* ($\sigma_{1.5}$ > 34.80 kg m^{-3}) is primarily due to its low temperature (Figure 2.5). In Denmark Strait, Arctic water masses cross the shallow sill (Dickson *et al.* (2008)) and entrain waters from the overlying East Greenland Current (*EGC*) into the cold bottom layer. These surface waters contribute to the young high oxygen, high CFC signature of *DSOW* seen in Figure 2.6. Their high meltwater content also lowers the salinity of the *DSOW*. South of the sill, the *DSOW* gradually deepens and encounters the warmer, more saline water masses in the Irminger Sea, with which it mixes isopycnally. The *DSOW* is found in a thin layer near the bottom of the Greenland Slope at the AR7E section as a highly stratified cold and relatively fresh water mass. The transport of cold (< 2 °C) water through Denmark Strait was originally estimated to be 2.9 Sv (Ross (1984), with 1 Sv = 10^6 m^3 s^{-1}), but later current meter record showed the transport to be slightly higher (Macrander *et al.* (2005)). Denmark Strait Overflow Water contributes to the deeper, colder part of the North Atlantic Deep Water, which leaves the Labrador Sea in the Deep Western Boundary Current, and can be recognized there also by the thin layer of high CFC values above the bottom of the Labrador Sea.

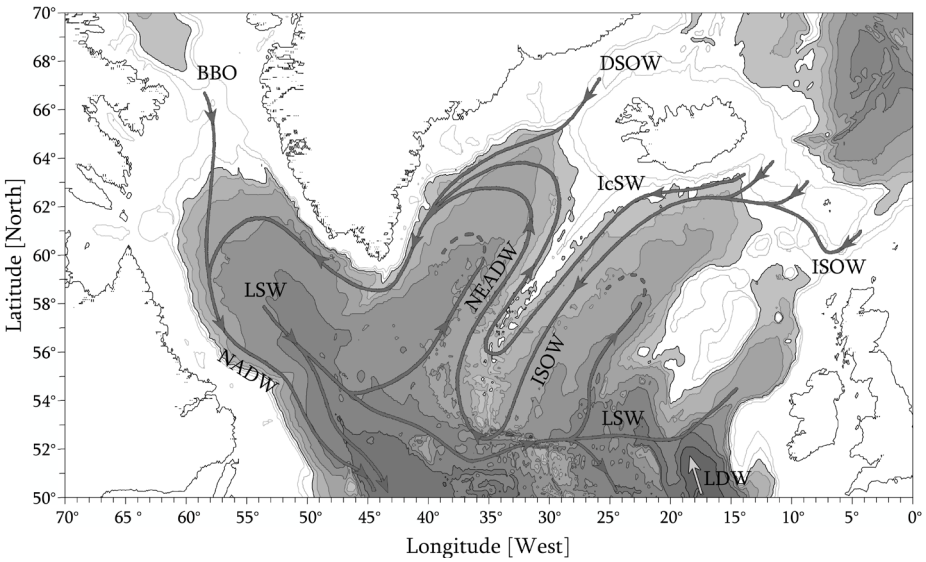

FIGURE 2.8: Schematic of the flow of the intermediate and deep waters in the northern North Atlantic Ocean. Topography contours below the 1500 m isobath are filled with grey scale colors, with darker grey indicating the deeper parts of the basin. The acronyms denote BBO: Baffin Bay Overflow, DSOW: Denmark Strait Overflow Water, IcSW: Icelandic Slope Water, ISOW: Iceland Scotland Overflow Water, LDW: Lower Deep Water, LSW: Labrador Sea Water, NADW: North Atlantic Deep Water, NEADW: North East Atlantic Deep Water.

Another dense overflow water, the Iceland Scotland Overflow Water (*ISOW*), originates from the Iceland-Scotland overflow, which is a combination of three pathways over the Iceland-Scotland Ridge. Dense waters, formed by cooling in the Nordic Seas, can enter the Iceland Basin over the Iceland-Faroe Ridge, through the Faroe Bank Channel or over the Wyville Thomson Ridge. Of these three, the Faroe Bank Channel has the deepest sill depth (840 m) and is the main outlet channel for the cold, dense Nordic waters (about 2.1 Sv, Hansen & Østerhus (2007)). At the sill, the warm and saline overlying North Atlantic Water is entrained, thus contributing to the characteristic high salinity signal of the *ISOW*. After passing the Iceland-Faroe Ridge, the Iceland Scotland Overflow Water follows the eastern slope of the Reykjanes Ridge in the Iceland Basin, while descending to the deeper parts of the basin. During this downwelling, ambient fresher and warmer *LSW* is entrained, thus diluting the low temperature, high salinity character of *ISOW*.

The deepest part of the Iceland Basin, the eastern part of the section through Maury Channel, is filled with dense ($\sigma_{1.5}$ > 34.80 kg m^{-3}) homogeneous bottom water. This is Lower Deep Water (*LDW*), which contains considerable amounts of Antarctic Bottom Water (*AABW*) the only water mass in the norther North Atlantic with its origin on the southern hemisphere. *AABW* is mainly formed in the Weddell Sea off the coast of Antarctica and is advected to the northern North Atlantic Ocean through Vema Channel and the Vema fracture zone (Morozov *et al.* (2008)). The *AABW* is substantially modified on its long way to the North Atlantic, entraining large amounts of the overlying deep water, and is therefore called Lower Deep Water here. The high silicate values and low oxygen and CFC values (below 3250 dbar, Figures 2.5, 2.6 and 2.7) reflect its old age and Antarctic origin relative to the overlying northern waters. The *AABW* mixes with the overlying waters, increasing silicate and lowering O_2 concentrations of *ISOW* as it turns into North East Atlantic Deep Water.

During its passage through the Charlie-Gibbs Fracture Zone the *ISOW* has entrained sufficient amounts of ambient water (mostly Lower Deep Water and Labrador Sea Water) to change its properties significantly from those seen in the Iceland Basin. It is fresher, warmer and has grown enough in volume to fill the lower (between 2000 and 3000 dbar, Fig. 2.5) eastern parts of the Irminger basin as a still relatively saline core. Because of the extensive modification of its properties the former ISOW is called North East Atlantic Deep Water (*NEADW*, as a deep water with eastern origin) on this side of the Mid Atlantic Ridge. The increase in age during transport is expressed in lower CFC-11 concentrations of *NEADW* in the Irminger basin with respect to the CFC-11 concentrations of *ISOW* in the Iceland Basin (Figure 2.6). The *NEADW* flows northward along the western slope of the Mid Atlantic Ridge and cyclonically

along the Greenland-Iceland Ridge and the eastern slope of Greenland (Figure 2.8). The *NEADW* encountered along the Greenland slope is further diluted but can still be recognized as a salinity maximum with respect to the low salinity, low oxygen intermediate water in the centre of the basin (at density levels of $34.60 < \sigma_{1.5} < 34.70$ kg m^{-3} in Figures 2.5 and 2.6). It continues to follow the Greenland slope towards the Labrador Sea where it becomes a saline, intermediate density constituent of North Atlantic Deep Water, found between the overlying Labrador Sea Water and the near bottom Denmark Strait Overflow Water.

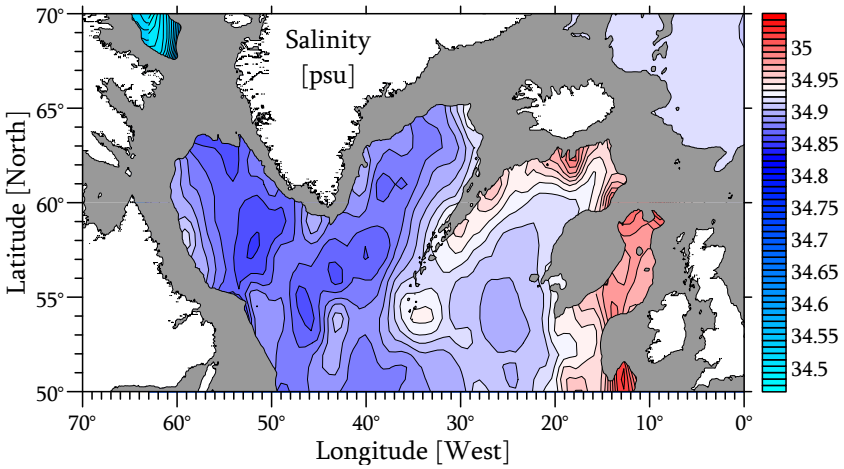

FIGURE 2.9: Salinity at intermediate depths of the northern North Atlantic. The salinity values are derived from the gridded ICES data, averaged over the layer between 1500 and 1700 dbar. The salinity contours are drawn every 0.01 psu. The topography above the 1500 m (0 m) is indicated by the grey (white) filled areas. The figure shows the relative saline Icelandic Slope Water and Iceland Scotland Overflow Water along the eastern slope of the Reykjanes Ridge and the slightly less saline North East Atlantic Deep Water on the western slope of the Reykjanes Ridge and flowing around the Irminger Sea. Relatively fresh Labrador Sea Water fills the center of the basins, while the mid levels of Rockall Trough are influenced by the saline North Atlantic Water flowing along the European coast.

Labrador Sea Water (*LSW*) is a homogeneous intermediate water mass (observed between 500 and 2000 dbar in Figure 2.5) formed in the Labrador Sea. It is the lightest component of North Atlantic Deep Water. Also, Labrador Sea Water is probably one of the best described water masses in the northwestern North Atlantic Ocean (Talley & McCartney (1982), the Lab Sea Group (1998), Yashayaev (2007) and Yashayaev *et al.* (2007) to name but a few). It can be recognized in Figure 2.9 as a low salinity water mass with its core near the Labrador coast and in Figures 2.3 and 2.5 as a large, relatively fresh, homogeneous water mass at intermediate density levels ($34.60 < \sigma_{1.5} < 34.70$ kg m^{-3}). The *LSW* is formed by surface cooling and deep convection. Deep con-

vection is an intermittent process, depending on the strength of the surface forcing in winter and the preconditioning of the water column (Marshall & Schott (1999)). The vigorous mixing typical of deep convection reduces the stratification within this layer to nearly zero. The recently ventilated, young *LSW* has a high oxygen and CFC content (Figure 2.6) and low nutrient concentrations (Figure 2.7). Its low salinity, typical for the *LSW* formed in the 1990s, is derived from fresh surface waters from the West Greenland Current and from the outflow of fresh water through the Canadian Archipelago (the Baffin Bay Overflow).

The volume of *LSW* in the Labrador Sea is drained into the Deep Western Boundary Current and into the nearby basins (Fig. 2.8), reaching the Irminger basin in 1 to 2 years, the Iceland basin in about 5 years (Yashayaev *et al.* (2007)) and Rockall Trough in 18 to 19 years (Read & Gould (1992)). In all basins it is recognizable as a large homogeneous water mass first emerging on the eastern side of the basin before spreading cyclonically and filling the centre of the basin. The salinity and temperature of the *LSW* increases with age (and distance) due to lateral mixing with the more saline water masses near the slopes of the basins (Fig. 2.5). Possibly the *LSW* in the Irminger Sea is also modified by convective mixing with the overlying *SPMW* in strong winters. Profiles recorded by floats (Bacon *et al.* (2003)) and the moored LOCO profilers (presented in Chapter 4) indicate mixed layers in winter in the centre of the Irminger Sea down to about 1000 m, into the *LSW* layer. Maps of CFC's and O_2 indicate a second maximum in the Irminger Sea, suggesting local ventilation of the LSW there (Pickart *et al.* (2003)). Convective mixing in the Irminger Sea is discussed more extensively in Chapters 4 and 5.

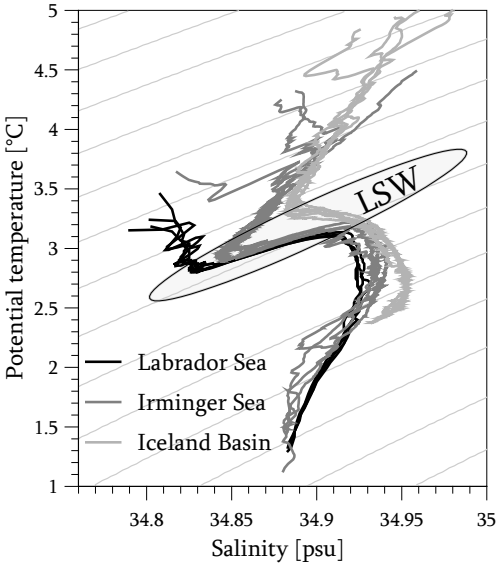

FIGURE 2.10: θ,S-profiles illustrating the transformation of the Labrador Sea Water formed in 1994 during advection to the nearby basins. Profiles are drawn for the center of the Labrador Sea (black lines) in 1994, the Irminger Sea (dark grey lines) in 1996 and Iceland Basin (light grey lines) in 1999. At these times the LSW salinity minimum occurred in each basin. The thin light grey lines are the isopycnals, which are drawn every 0.05 kg m^{-3}.

Figure 2.10 shows the transformation of the *LSW* (most clearly the salinity increase), which has taken place between the Labrador Sea, the Irminger Sea and the Iceland Basin, in θ,*S*-space. The Iceland Basin *LSW*, which is about 5 years old here, is most saline but still recognizable as a low salinity intermediate water. The increase in age of *LSW* in the Iceland Basin can also be seen in the lower oxygen and CFC values compared to those in the Irminger basin (Figure 2.6). A strong source of high salinity for the *LSW* residing in the Iceland and Irminger basins is Icelandic Slope Water (*IcSW*, van Aken & de Boer (1995), van Aken & Becker (1996) and Yashayaev *et al.* (2008)). *IcSW* is formed by direct mixing at shallow levels between *ISOW* and the overlying thermocline water in or near the Faroe Bank Channel. The *IcSW* temperature and salinity properties reflect its formation process, near the mixing line between cold overflow water and thermocline water at the Iceland-Faroe Ridge, making it more saline than the ambient *LSW* but with a nearly similar density. It is found above the *ISOW* on the slopes of the Faroe-Iceland Ridge, the south Icelandic slope and the shallower parts of the Reykjanes Ridge (Figures 2.9 and 2.11). At about 55° N the *IcSW* crosses the Reykjanes Ridge into the Irminger basin. The *IcSW* is a salt source which modifies the aging and spreading *LSW* by lateral mixing. As a result of the exchange with the relatively young and fresh *LSW*, the *IcSW* decreases in salinity and increases in oxygen and CFC content.

2.3 Climatology

2.3.1 Climatologic data

Atmospheric surface data, used to construct the climatology of the Labrador and Irminger Seas presented here, were obtained from the National Center for Environmental Prediction (NCEP) reanalysis project. These data are provided by the NOAA-CIRES Climate Diagnostics Center, Boulder, Colorado, from their web site at http://www.cdc.noaa.gov/. The parameter fields in the reanalysis project date back to January 1948 and are frequently updated with current data. For this study the daily mean values between January 1948 and July 2008 were downloaded. The reanalysis data are computed on a T62 Gaussian grid with 192 by 94 points, leading to a horizontal resolution of the parameter fields in the study area of approximately 1.9° by 1.9°. The parameter fields obtained from the NCEP reanalysis are: sea level pressure, eastward and northward wind components at 10 m height, cloudy sky shortwave and longwave radiation, net sensible and latent heat fluxes and the precipitation rate. The evaporation (E) was calculated from the latent heat flux through: $E = T_{latent}/L_E$, with T_{latent} the latent heat flux and the latent heat of evaporation $L_E = 2.49 \cdot 10^6$ J kg^{-1}.

The reanalysis fields have been processed to generate the time averaged climatology presented here. Monthly means were constructed from the daily mean air pressure fields to establish the seasonal cycle in the air pressure field. Wind field data were used to calculate wind stress and wind stress curl before compiling the monthly mean fields. The surface heat and freshwater flux data were spatially averaged over two boxes in the central Labrador and Irminger Sea in order to get time series for these areas. The Labrador Sea box runs from 50° to 55° W and from 56° to 60° N (enclosing 9 grid pints). The Irminger Sea box runs from 34° to 42° W and from 57° to 62° N (enclosing 12 grid points). These boxes are drawn in the left panel of Figure 2.12. For both boxes the area averages were determined separately for each day. Secondly, to determine the mean climatology of the two areas, monthly mean series were composed from the daily time series. Subsequently, the mean and standard deviation for each month (January to December) over the 60 years was determined resulting in a mean annual cycle of surface fluxes. The variability of the surface forcing will be discussed more extensively in later chapters.

To gain some insight into the climatology of the air-sea temperature difference, the sea surface data from the International Comprehensive Ocean-Atmosphere Data Set (ICOADS) 1° Enhanced, presented in Section 2.2.1, were used. The downloaded data set contains monthly mean surface temperatures from January 1960 to July 2007. These data were averaged for the same Labrador and Irminger Sea boxes, defined above, as were used for the NCEP fields

2.3.2 Air pressure, wind and temperature

The atmospheric pressure does not have a direct influence on the sea surface, other than the barometric effect, but the winds caused by the horizontal pressure gradients do effect the sea surface. The momentum transfer by the wind stress drives the surface Ekman circulation and both the sensible and latent heat fluxes depend on the wind speed. The dominant pattern in the mean sea level pressure field (Fig. 2.12) is such that the Irminger and Labrador Seas are both subject to the winds in the cyclonic circulation around the low pressure area near Iceland, with the lowest pressures on average found over the Irminger Sea. This dipole pattern, formed by this low area and the subtropical high pressure area, is variable in strength and is commonly referred to as the North Atlantic Oscillation pattern (NAO, Hurrell (1995)) and is found to be stronger in winter (Figure 2.12 and Table 2.1). Its strength is estimated by the NAO index, which is based on the normalized pressure difference between Iceland and a southern station, e.g. Portugal or the Azores. Positive indexes indicating a stronger meridional pressure gradient and negative indexes indicating a weaker gradient.

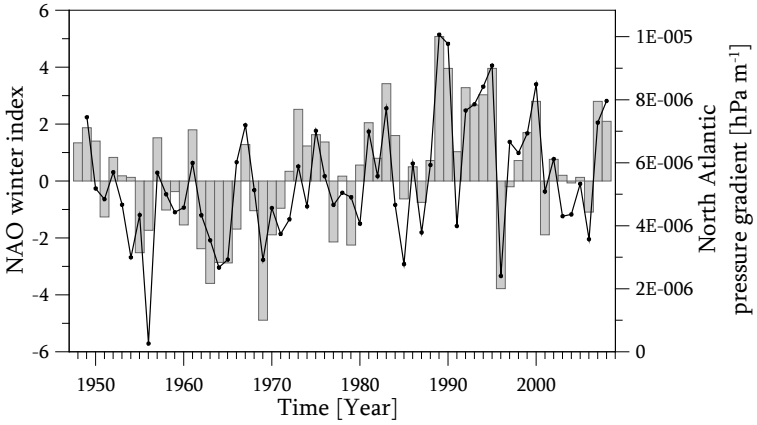

FIGURE 2.11: Time series of the winter NAO index and the large scale pressure gradient over the North Atlantic. The NAO index (bar graph) is the normalized sea level pressure difference between Lisbon, Portugal and Stykkisholmur, Iceland. The large scale pressure gradient (black line) is the actual gradient between the low pressure core south of 40° N and the high pressure core north of 50° N based on the NCEP reanalysis data. Both are the December to March winter mean. The mean value of the pressure gradient is centred on NAO index = 0.

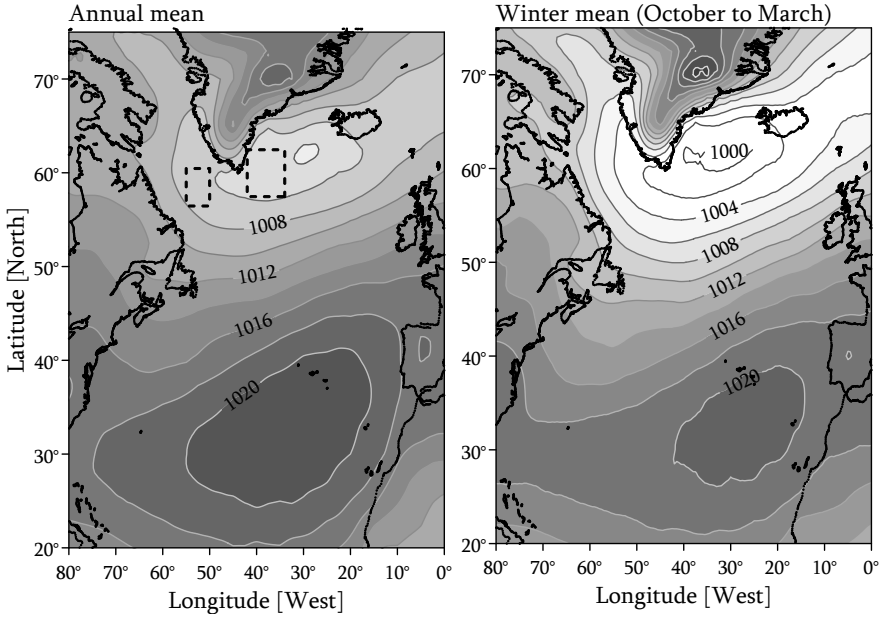

FIGURE 2.12: The annual (left) and winter (right) mean sea level pressure, averaged over the period from 1948 to 2008. Isobars are drawn every 4 mbar. The high pressure over Greenland is most likely due to the extrapolation of observed pressure over the high topography down to sea level. The analysis boxes over the Labrador and Irminger Seas are drawn in black.

To estimate the pressure gradient over the NAO dipole, the pressure values and locations of the centre of the high and low pressure areas were retrieved from the data. The low pressure core was defined as the grid point with lowest pressure between 50° N and 70° N and 50° W and the 0° meridian. The high pressure core was defined as the grid point with highest pressure between 20° N and 40° N and 50° W and the 0° meridian. The pressure difference was divided by the distance between the two grid points to obtain the pressure gradient. Overall, the December to March NAO index correlates well (R = 0.81) with the December to March pressure gradient series (Figure 2.11). However, this correlation is strongest after 1990 (R = 0.91 for 1990 to 2008), while the correlation is much weaker over the first part of the time series (R = 0.67 for 1949 to 1989). This may be due to a lack of pressure observations at sea during the first part of the record, but possibly the extreme pressure difference of the 1990s are better represented by the NAO index. For the study here, the 60-year time series was divided into an extended winter series, October to March, and a summer series containing the remaining half year. The values in Table 2.1 shows that the pressure gradient in winter is twice as strong as the summer gradient, mostly due to deepening of the Icelandic low pressure area.

TABLE 2.1: Maximum and minimum pressure over the northern North Atlantic and the associated horizontal pressure gradient. Values are displayed for the annual average, the extended winter (October to March) average and the extended summer average (April to September). The displayed standard deviations correspond to the standard deviation derived from 60 years of daily values to illustrate the synoptic variability.

	Annual	Winter	Summer
High pressure core [hPa]	1017.8 ± 3.3	1019.6 ± 3.6	1015.9 ± 1.6
Low pressure core [hPa]	1006.1 ± 6.5	1002.5 ± 6.7	1009.6 ± 3.8
Pressure gradient [10^{-6} hPa m^{-1}]	3.7 ± 2.7	5.2 ± 2.8	2.2 ± 1.6

Superimposed on the large scale mean sea level air pressure, shown in Figure 2.12, are the continuously passing synoptic pressure systems following the Atlantic storm tracks (Rogers (1997)). These relatively short lived systems cause the distribution of wind vectors over the Irminger Sea and over the Labrador Sea to exhibit a strong variability in direction and speed. There is however, an alignment of the strongest wind vectors with the mean pressure system and the Greenland topography, which gives the variance distribution an elliptic shape (Figure 2.13). The angles of the major axes are 41° for the Irminger Sea and 125° for Labrador Sea, with respect to north. These

orientations are slightly shifted to the north in winter (ONDJFM). The mean scalar wind speeds over the Irminger Sea are slightly smaller than over the Labrador Sea (Table 2.2), probably due to the proximity of the low pressure core to the Irminger Sea.

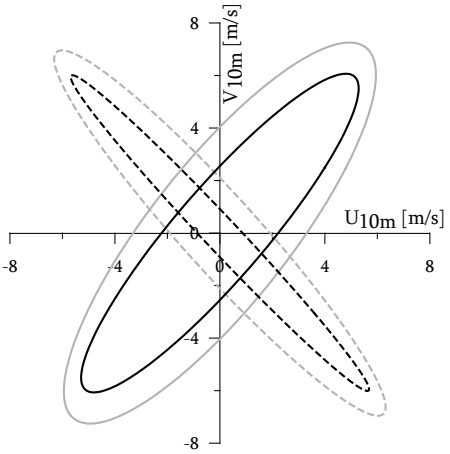

FIGURE 2.13: Variance ellipses for the 10 m wind vectors over the Irminger Sea (solid line) and the Labrador Sea (dashed line). The ellipses are drawn for annual (black lines) and winter (grey lines) data. The variance ellipses illustrate the alignment and spread of the wind vector distribution.

TABLE 2.2: The mean annual, summer (April to September) and winter (October to March) scalar wind speed at 10 m over the Irminger and Labrador Seas. The displayed standard deviation corresponds to the standard deviations derived from daily NCEP values between April 1948 and March 2008 to illustrate the synoptic variability.

	Labrador Sea			Irminger Sea		
	Annual	Summer	Winter	Annual	Summer	Winter
Wind speed [m s^{-1}]	7.7 ± 3.8	6.2 ± 3.1	9.1 ± 4.0	7.2 ± 3.8	6.0 ± 3.1	8.4 ± 4.0

In order to study the influence of the wind pattern on the circulation, the wind stress ($\vec{\tau}$) was calculated using equation 2.1.

$$\vec{\tau} = \rho_a C_D \vec{U} \left| \vec{U} \right| \qquad (2.1)$$

In which ρ_a is the density of air and C_D is the drag coefficient and the vector U is the wind at 10 m height. For the drag coefficients the empirical formulas proposed by *Yelland & Taylor* (1996) have been used. These drag coefficient formulas were determined for the open ocean and account for the difference in drag due to the difference in sea state in weak (Eq. 2.2) and strong (Eq. 2.3) winds conditions:

$$\text{for } U \leq 6 \text{ m s}^{-1}: \; C_D = (0.6 + 0.070U)/1000 \qquad (2.2)$$

$$\text{for } U > 6 \text{ m s}^{-1}: \; C_D = (0.29 + 3.1/U + 7.7/U^2)/1000 \qquad (2.3)$$

Figure 2.14 displays the curl of the wind stress over the northern North Atlantic Ocean averaged over the 60 years of the NCEP data set. It clearly shows two areas of positive wind stress curl, one over the Labrador Sea and a second over the Irminger Sea. Notably, the maximum values for both areas are nearly equal. Positive wind stress curl drives divergence of the surface flow and upward Ekman pumping. This causes the isopycnals to dome upwards in the centre of these basins, which was already shown in Figure 2.5. This doming reduces the heat content of the upper layers and is an important requirement for the preconditioning of open ocean convection, as described by *Marshall & Schott* (1999).

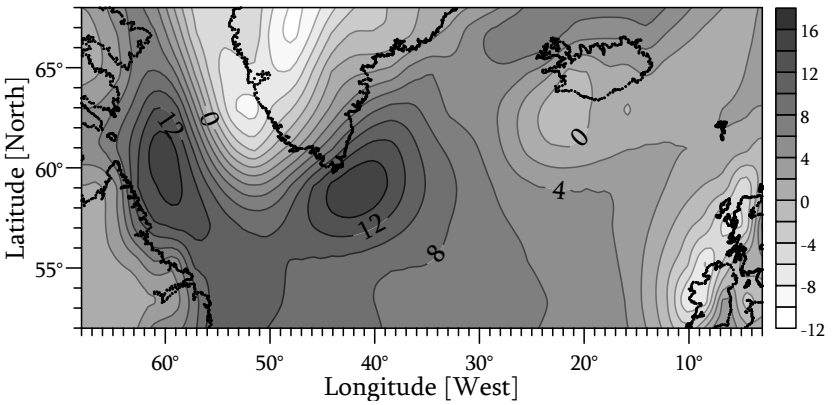

FIGURE 2.14: The long term mean wind stress curl pattern over the northern North Atlantic Ocean. The wind stress curl was derived from the 10 m height eastward and northward wind components of the NCEP data set. Wind stress curl values were averaged over the 1948 to 2008 period and are shown in 10^{-8} N m^{-3}.

Besides momentum transfer the wind also affects the heat and moisture transfer. The mean northwesterly winds bring air from the Canadian continent and Greenland to the northwestern North Atlantic. Especially during winter, cold, dry air is brought to the Labrador Sea. There, the air absorbs heat and moisture from the warmer sea surface (Table 2.3 and Figure 2.15). Subsequently, downstream over the Irminger Sea the air is warmer and moister than over the Labrador Sea (Table 2.3). This will become apparent in the comparison of the sensible and latent heat fluxes (in the next section). The air-sea temperature difference is illustrated by the graphs in Figure 2.15. The sea surface temperature (*SST*) follows the air temperature from April to December. During these (mostly summer) months the warming and cooling of the water is most likely restricted to a shallow upper layer and the heat from the atmosphere is absorbed quickly. The *SST* remains nearly constant from December to April, despite the lower air temperatures. In these winter months the surface water is cooled to a

density high enough to initiate mixing over a deeper layer. This deeper layer has a much larger effective heat capacity, thus dampening the decrease in temperature of the ocean surface layer.

TABLE 2.3: Air temperature and specific humidity at 2 m height over the Irminger and Labrador Seas. The values shown are the annual, summer (April to September) and winter (October to March) means and standard deviations of the daily NCEP values between April 1948 and March 2008.

	Labrador Sea			Irminger Sea		
	Annual	Summer	Winter	Annual	Summer	Winter
Air temperature [°C]	2.7 ± 4.1	5.1 ± 2.9	0.1 ± 3.6	4.6 ± 2.9	6.4 ± 2.2	2.8 ± 2.4
Specific hum. [10^{-4} kg kg^{-1}]	43 ± 13	50 ± 11	34 ± 9	49 ± 11	56 ± 10	42 ± 8

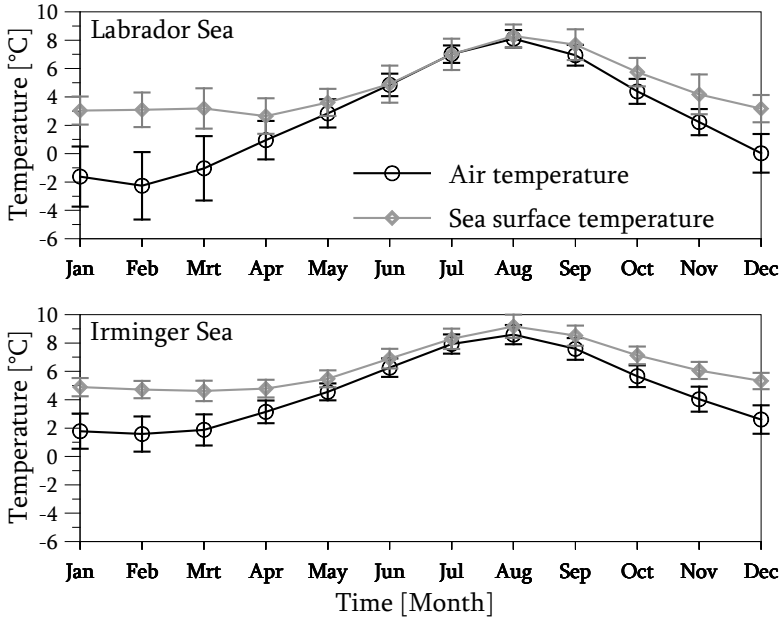

FIGURE 2.15: Mean annual cycle in air temperature at 2 m height and sea surface temperature in the centre of the Labrador Sea (top panel) and the Irminger Sea (bottom panel). Air temperatures are based on the time series of daily NCEP values between 1948 and 2008, and the sea surface temperatures are based on the ICOADS 1960 to 2007 time series of monthly means.

2.3.3 SURFACE HEAT FLUXES

The mean annual cycles of the heat fluxes over the central Labrador Sea and Irminger Sea are shown in Figure 2.16. The total heat flux (Q_{tot}) was calculated by adding the radiative fluxes, R_{short} for shortwave radiation and R_{long} for longwave radiation, taking in account the reflection of the shortwave radiation due to the albedo of the sea surface ($\alpha = 0.08$) and adding the turbulent fluxes $T_{sensible}$ and T_{latent}:

$$Q_{tot} = (1-\alpha)R_{short} + R_{long} + T_{sensible} + T_{latent} \qquad (2.4)$$

The Irminger Sea and Labrador Sea both have a positive net upward heat flux, e.g. the ocean loses heat to the atmosphere, averaged over the 1948 to 2008 period (Table 2.4). The Irminger Sea loses heat during 6 months of the year and gains heat during 4 (Fig. 2.16). In the months of April and September the net mean heat flux is about zero, thus the sea surface then experiences either heat loss or heat gain depending on the inter-annual variability. Heat loss over the Labrador Sea is stronger than over the Irminger Sea (by about 40%, Table 2.4) and lasts on average ½ month longer.

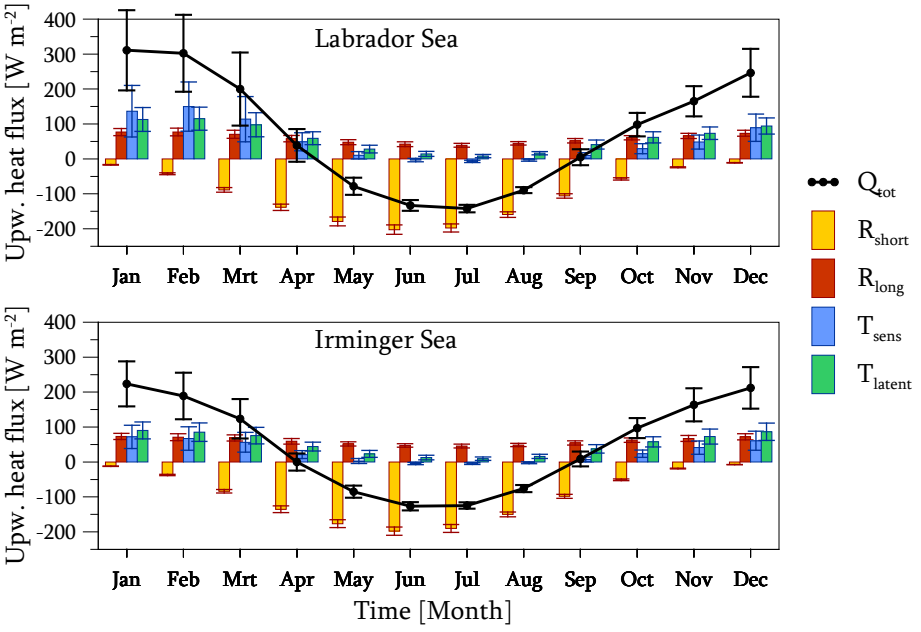

FIGURE 2.16: The seasonal cycle of the four term of the total heat flux and the total heat flux. Shown are the monthly mean upward heat fluxes (bars) and total mean heat flux (black line) for the Labrador Sea (top panel) and for the Irminger Sea (bottom panel). The error bars indicate the standard deviation over the 60 year time series of monthly means.

For both areas, the only atmospheric source of heat to the sea surface is solar shortwave radiation, which induces heating all year albeit very small in winter. The weak heating by the sun is the result of the high latitude and large cloud cover. Since the Labrador Sea and Irminger Sea are at a similar latitude and are subject to about the same type of synoptic atmospheric systems, the mean solar radiation over the two areas is quite similar. Averaged over 60 years the Labrador Sea receives an extra 5 W m^{-2} of shortwave radiation (Table 2.4). During winter, when the insolation is weak, the cooling fluxes dominate the total heat flux. Stronger winds and lower air temperatures over the Labrador Sea cause the stronger cooling fluxes with respect to those over the Irminger Sea. In January, on average the coldest month in both areas, the mean sensible heat loss is 150 ± 70 W m^{-2} over the Labrador Sea as compared to 72 ± 33 W m^{-2} over the Irminger Sea.

TABLE 2.4: Net shortwave, longwave, sensible, latent and total heat fluxes over the Irminger and Labrador Seas. Values are the annual, summer (April to September) and winter (October to March) means and standard deviations of the daily NCEP values between April 1948 and March 2008. The high standard deviations are due to large meso-scale atmospheric variability.

Upward heat flux [W m^{-2}]	Labrador Sea			Irminger Sea		
	Annual	Summer	Winter	Annual	Summer	Winter
Shortwave, $(1-\alpha)R_{short}$	-94 ± 70	-151 ± 51	-39 ± 33	-89 ± 69	-146 ± 49	-35 ± 32
Longwave, R_{long}	59 ± 26	47 ± 21	71 ± 26	60 ± 24	51 ± 20	69 ± 25
Sensible, T_{sens}	51 ± 94	9 ± 37	97 ± 112	28 ± 56	3 ± 22	54 ± 68
Latent, T_{latent}	60 ± 60	28 ± 34	92 ± 64	50 ± 55	23 ± 30	77 ± 61
Total heat flux, Q_{tot}	76 ± 209	-67 ± 95	220 ± 193	50 ± 166	-68 ± 76	165 ± 150

Net annual heat loss is partly caused by high sea surface temperatures relative to the air temperatures. This causes a loss by longwave radiation all year, which is slightly larger during winter because of reduced back radiation during periods of colder air temperatures. The turbulent fluxes of both sensible and latent heat contribute an important part to the total winter heat loss. They depend strongly on the wind speed as can be seen from their bulk formulas. The bulk formulas for the sensible (2.5) and latent (2.6) heat flux are:

$$T_{sensible} = \rho_{air}\, C_P\, U\, C_S\, (T_{sfc} - T_{atm}) \qquad (2.5)$$

$$T_{latent} = \rho_{air}\, L_E\, U\, C_L\, (q_{sfc} - q_{atm}) \qquad (2.6)$$

where ρ_{air} density of dry air, C_P the heat capacity of dry air, C_S and C_L are transfer coefficients, q_{sfc} - q_{atm} the specific humidity difference between the saturated air just above the sea surface (q_{sfc}) and the air at 10 m (q_{atm}), T_{sfc} - T_{atm} the temperature difference, and L_E latent heat of evaporation. This dependence on the wind speed introduces a large high-frequency variability (atmospheric meso-scale variability), which also enhances the inter-annual variability of the surface cooling (displayed as error bars in Figure 2.16) significantly. For example, the total air-sea heat flux anomalies in the winter of 2007-2008 exceeded 100 W m^{-2}, compared to the 2001-2006 base period, over parts of the Labrador and Irminger Seas (Våge *et al.* (2008)).

A comparison to values in literature shows that the NCEP sensible heat fluxes over the Labrador Sea appear to be quite accurate. Estimates of *Bumke et al.* (2002) for the sensible heat flux, based on observations on board the research vessel Knorr in February and March 1997, range between 200 and 209 W m^{-2}, while the mean NCEP sensible heat flux over February and March 1997 is 204 W m^{-2}. However, small scale synoptic features in the lee of Greenland over the Irminger Sea, are not well represented in the NCEP reanalysis (Pickart *et al.* (2003)) due to the relatively low resolution. The Greenland tip jet, a low level jet downstream (southeast) of Cape Farewell, is formed when a cyclone is positioned northeast of Greenland and the northwesterly flow is forced around the high topography of Greenland (Doyle & Shapiro (1999)). The tip jet can enhance surface fluxes up to 500 W m^{-2}, down to 800 km east of Cape Farewell, with a local maximum of up to 800 W m^{-2} (Doyle & Shapiro (1999)). A reversed Greenland tip jet also occasionally occurs, this is associated with cyclones south of Cape Farewell and barrier flows along the eastern coast of Greenland (Moore & Renfrew (2005)). The frequency of tip jet events is related to the phase of the NAO and to the position of the Iceland low pressure area. During years in which the Icelandic Low is located north of 63° N the annual average number of Greenland tip jet events is larger than 10, while the average number of tip jet events in years in which the Icelandic Low is located south of 57° N is smaller than 4 (Bakalian *et al.* (2007)). Reversed tip jets are more common during a negative NAO phase (Moore & Renfrew (2005)).

2.3.4 Surface freshwater fluxes

Both the Labrador Sea and the Irminger Sea have a net excess of precipitation (*P*) over evaporation (*E*) averaged over the year (Table 2.5). Although the annual cycles in evaporation and precipitation look very similar (Figure 2.17) over both the Labrador Sea and the Irminger Sea, their summed freshwater flux each shows a different behaviour throughout the year. While the Irminger Sea experiences a precipitation excess all year, the Labrador Sea apparently looses freshwater on average to the colder and dryer atmosphere in late winter.

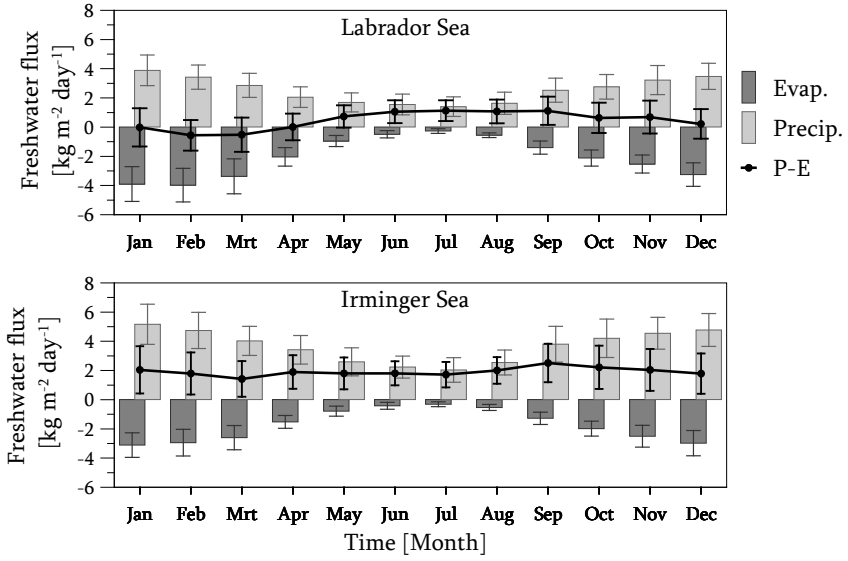

FIGURE 2.17: Monthly mean downward freshwater fluxes (bars) and total mean freshwater flux (lines) over the Labrador Sea (a, left) and the Irminger Sea (b, right). Error bars indicate the standard deviation over the 60 year time series of monthly means.

TABLE 2.5: Precipitation, evaporation and net freshwater flux over the Labrador and Irminger Seas. Values are the annual, summer (April to September) and winter (October to March) means and standard deviations of the daily NCEP values between April 1948 and March 2008.

Freshwater flux [10^{-6} kg m^{-2} s^{-1}]	Labrador Sea			Irminger Sea		
	Annual	Summer	Winter	Annual	Summer	Winter
Precipitation rate, *P*	29 ± 39	21 ± 35	37 ± 39	42 ± 53	32 ± 48	52 ± 55
Evaporation rate, *E*	24 ± 24	11 ± 14	37 ± 26	20 ± 22	9 ± 12	31 ± 24
Net freshwater flux, *P-E*	5 ± 43	10 ± 39	0 ± 46	22 ± 58	22 ± 51	21 ± 64

Freshwater fluxes from sea-ice, Greenland ice sheet meltwater, runoff from the Canadian Archipelago and other advective freshwater fluxes are not included in this figure but may also be important to the total local freshwater budget. Poor data coverage of precipitation measurements over the ocean also contributes to the uncertainty of the atmospheric freshwater fluxes discussed here. Therefore the heat fluxes related to precipitation (Sathiyamoorthy & Moore (2002)), from the melting of snow into water and raising or lowering the temperature of rain to the sea surface temperature, will also contain a large uncertainty and are not presented here.

2.3.5 IMPORTANCE OF HEAT AND FRESHWATER FLUXES

The density of seawater depends on temperature, salinity and pressure. Density differences, or differences in weight per unit volume $g\rho$, induce motion because of gravity forces exerted on the water parcels. Therefore $-g\rho$ is called buoyancy (Gill (1982)) and the buoyancy flux (B) is dependent on the heat and freshwater flux. A positive upward heat flux ($Q_{tot} > 0$) and net evaporation ($E\text{-}P > 0$) creates a positive upward buoyancy flux, e.g. the sea surface "loses" buoyancy to the atmosphere which means a gain in density. The buoyancy flux in J m^{-3} s^{-1} is given by Gill (1982) as:

$$B = (g\,\alpha\,Q_{tot})/C_P + g\,\beta\,(E\text{-}P)\,S_{ref} = B_{heat} + B_{salt} \qquad (2.7)$$

where g is the gravitational constant, C_p the heat capacity of water, S_{ref} a reference salinity and α and β the thermal expansion and saline contraction coefficients respectively.

Over the Irminger Sea, the surface experiences net cooling and freshening. These fluxes have an opposite effect on the surface buoyancy, that is the cooling leads to an increase in buoyancy and the freshening leads to a decrease in buoyancy. Since the net surface fluxes are known, their contribution to the annual mean buoyancy flux can be calculated. The annual mean heat flux is 49 W m^{-2} (Table 2.4) and the annual mean freshwater flux ($P\text{-}E$) is 22 10^{-6} kg m^{-2} s^{-1} (Table 2.5) over the Irminger Sea. The coefficients C_p, α and β are not constant, but depend on temperature, salinity and pressure. At a surface temperature of 6 °C and a salinity of 34.90 psu (typical for the central Irminger Sea) we can insert the following values into the equations for B_{heat} and B_{salt}: $g = 9.8\ m\ s^{-1}$, $\alpha = 1.2\ 10^{-4}\ K^{-1}$, $\beta = 7.7\ 10^{-4}\ psu^{-1}$ and $C_p = 4\ 10^{3}\ J\ kg^{-1}\ K^{-1}$. Which gives annual mean heat and salt contributions to the buoyancy flux of:

$$B_{heat} = (9.8 \cdot 1.2\ 10^{-4} \cdot 50) / 4\ 10^{3} = 1.5\ 10^{-5}\ [J\ m^{-3}\ s^{-1}]$$

$$B_{salt} = 9.8 \cdot 7.7\ 10^{-4} \cdot -22\ 10^{-6} \cdot 34.90 = -5.8\ 10^{-6}\ [J\ m^{-3}\ s^{-1}]$$

So, although both the heat flux and the freshwater flux play a role in the net buoyancy flux, the contribution of the heat flux is more than twice as large as that of the freshwater flux for the Irminger Sea. For the Labrador Sea, where the heat fluxes are larger and the freshwater flux is small, the annual average ratio of B_{heat} to B_{salt} is approximately 17:1. The winter heat flux over both areas is much stronger, which further increases the B_{heat}. Thus, the effect of atmospheric freshwater fluxes on the buoyancy flux over the Labrador Sea is relatively unimportant. Advective freshwater fluxes, in the East Greenland Current and through Davis Strait are expected to be of

much more importance. The effect of the atmospheric freshwater flux on convective mixing is investigated further in Chapter 5.

2.4 SUMMARIZING DISCUSSION

The ocean circulation in the basins of the northwestern North Atlantic Ocean is characterized by a cyclonic nature, both at the surface and in the deeper layers. At the surface, the warm, saline circulating water masses originating from the North Atlantic Current are continuously modified, e.g. mixed, cooled and freshened by air-sea interaction. Part of the modified waters finally enter the Labrador Sea as Subpolar Mode Water, the precursor of Labrador Sea Water (*LSW*). In the deep circulation two different overflow waters enter the North Atlantic basins from the north, the cold Denmark Strait Overflow Water and the saline Iceland Scotland Overflow Water. These dense waters contribute to the North Atlantic Deep Water. Labrador Sea Water is formed by convection in the Labrador Sea and enters the other basins from the west. In the Irminger Sea the *LSW* is possibly re-ventilated by convective mixing. A transformation of the relatively fresh *LSW* to more a saline, older type of *LSW* is seen in the basins downstream of the Labrador Sea. The *LSW* is the lightest, freshest constituent of the North Atlantic Deep Water. This water mass flows out of the Labrador Sea in the Deep Western Boundary Current along the American continental slope. The deep convection in the Labrador Sea and the overflow of dense Nordic waters into the Atlantic Ocean provide an important (downward) link in the thermohaline circulation.

The wind stress curl fields show two centres of positive curl, one over the Labrador Sea and one over the Irminger Sea. Through divergence of the Ekman transport the positive wind stress curl induces doming of the isopycnals, which is indeed observed in the hydrography. The doming of isopycnals is also part of the cyclonic circulation of the two subgyres that are seen in the Irminger and Labrador Seas (Lavender *et al.* (2000)). These basin scale gyres are the results of the wind forcing and topographic steering of the currents. Due to these cyclonic gyres both areas display the preconditioning necessary for convection. The climatologies of the Labrador and Irminger Sea further show that both areas experience net annual heat loss. Radiative, shortwave and longwave heat fluxes are of similar magnitude over both areas and provide heating during a short summer period and cooling during a longer winter period.

During winter, the turbulent (sensible and latent) heat fluxes are the largest contributor to the cooling of the surface waters. Turbulent heat fluxes over the Labrador Sea are larger than those over the Irminger Sea, especially in winter, due to higher winds

speeds and larger air-sea temperature differences. Possibly sensible heat fluxes over the Irminger Sea are enhanced significantly several times per winter by the Greenland tip jet, a synoptic feature not resolved in the NCEP data. Net freshwater fluxes are larger over the Irminger Sea than over the Labrador Sea. This is primarily caused by higher precipitation rates over the Irminger Sea. Also, stronger winds and larger air-sea temperature differences enhance evaporation rates over the Labrador Sea, thus further increasing the difference in the net freshwater flux. Freshwater contributions to the buoyancy flux are relatively small compared to the heat contributions, but cannot be neglected over the Irminger Sea. Their contribution for the Labrador Sea is relatively unimportant due to higher heat loss and lower freshwater fluxes there. Advective fluxes of freshwater (e.g. the East and West Greenland Current) are likely to be important to the total freshwater budget in both areas, but most important for the Labrador Sea which receives additional freshwater input from the Canadian Archipelago.

Advective fluxes of heat are also important to the northwestern North Atlantic, since the atmosphere does not provide input of heat on an annual basis. For the hydrography to remain stable, the net annual cooling of the sea surface by the atmosphere must be compensated by an import of warm (Modified) North Atlantic Water from the south. This advective import of heat implicitly means an import of salt, since this is also a property of North Atlantic Water.

CHAPTER 3

Inter-annual variability of the northwestern North Atlantic Ocean with focus on the Irminger Sea

3.1 Introduction

In order to describe the variability of any ocean, first a reference state needs to be established. This was done in the previous chapter, using the surveys of 1990 and 1991. Secondly, the variability needs to be observed for a period which is preferably much longer than the characteristic time scale of the variability which one would like to describe. To be able to understand and explain the observed variability in the ocean, its interaction with other components in the climate system, most importantly the atmosphere, must be investigated.

The World Ocean Circulation Experiment (WOCE), starting in 1990, was the first major attempt to study the oceans and their variability at large. Its goal was to establish the role of the oceans in the Earth's climate and to obtain a baseline data set against which future change could be assessed. The experiment contained a one-time survey of all the oceans to establish the reference state and a series of repeat sections to study the representativeness of the one-time survey. After an observational period of 8 years, the field phase of WOCE ended in 1997. This period appeared not long enough to adequately describe the ocean variability. Therefore, the repeat surveys were continued in the Climate Variability and Predictability Program (CLIVAR), part of the World Climate Research Programme. CLIVAR focuses on the role of the coupled ocean and atmosphere within the overall climate system, with emphasis on the ocean variability on seasonal to centennial time scales. The latter, centennial time scales, must be realized through ocean and climate models. Their prediction of multi-decadal and centennial variability will be validated with past and future observations. With the WOCE and CLIVAR data, researchers around the world have begun to describe the inter-annual and decadal variability and their understanding increases with each year added to the observational record.

To gain insight into the variability of the northwestern North Atlantic Ocean, and especially the Irminger Sea, the WOCE AR7E repeat section is of much importance.

This section runs from the south of Greenland to the Irish continental shelf (Figure 3.1). Hydrographic surveys of this section have been performed near-annually since the start of the WOCE Hydrographic Program in 1990. After the termination of the field phase of WOCE in 1997, the surveys continued until present (2008) as a contribution to the CLIVAR program. Institutes cooperating on the repeated survey of this section are the Institut für Meereskunde, Hamburg (IfMH), the Royal Netherlands Institute for Sea Research, Texel (NIOZ) and the Southampton Oceanography Centre, presently the National Oceanography Centre, Southampton (NOC). Survey cruises in the northern North Atlantic, like the AR7E section, are usually carried out in late summer or early autumn. In this period a minimum of sea-ice is encountered near Greenland and the storm season is not yet at its full strength. Thus, the intra-annual variability, such as the seasonal cycle, is not resolved and is aliased onto longer time scales. It does, however, resolve the inter-annual variability for the last 18 years. Historical data, from before 1990, originating from the Irminger and Labrador Sea, are also available in oceanographic data centres. These observations are more irregularly distributed in space and time. The resolution of time series based on these data are not high enough to resolve the variability on year-to-year time scales in much detail, but they offer interesting insights into the variability on decadal time scales.

The inter-annual and decadal variability in the hydrography of the Irminger Sea is presented in this chapter. The variability in the Iceland Basin is also described because of the advective pathways between both basins. Similarly the variability of the Labrador Sea is described, although this chapter relies heavily on the descriptions of the Labrador Sea Water provided by Yashayaev *et al.* (2008). In Section 3.2 the various data sets used in this chapter are introduced and a short description of the data processing is given. The observed variability is presented and described in Section 3.3. This is done by discussing the details of the variability in the various water masses typical for the Irminger Sea hydrography, which were introduced in Chapter 2. The last section, Section 3.4, investigates whether the observed changes can be explained using a simple model based on atmospheric forcing and concludes the description of the inter-annual variability with an overall summarizing discussion.

3.2 Data & data processing

One of the main data sets used for this study originates from the WOCE AR7E surveys through the North Atlantic Ocean. Two alternative AR7E tracks were used (Fig. 3.1). A northern route, mainly used by NIOZ and NOC, and a southern route mostly surveyed by IfMH. Both tracks coincide in the Irminger Sea west of 31° W, between Greenland and the Reykjanes Ridge. From the top of the Reykjanes Ridge the north-

ern track follows a short route through the Iceland Basin, over Rockall Bank and the Rockall Hatton Plateau and through Rockall Trough. The southern track follows a route around (south of) the shallower topography. The information of the AR7E surveys used in this study are summarized in Table 3.1. A similar section in the Labrador Sea, the AR7W, is regularly surveyed between the continental shelf of Newfoundland and Greenland.

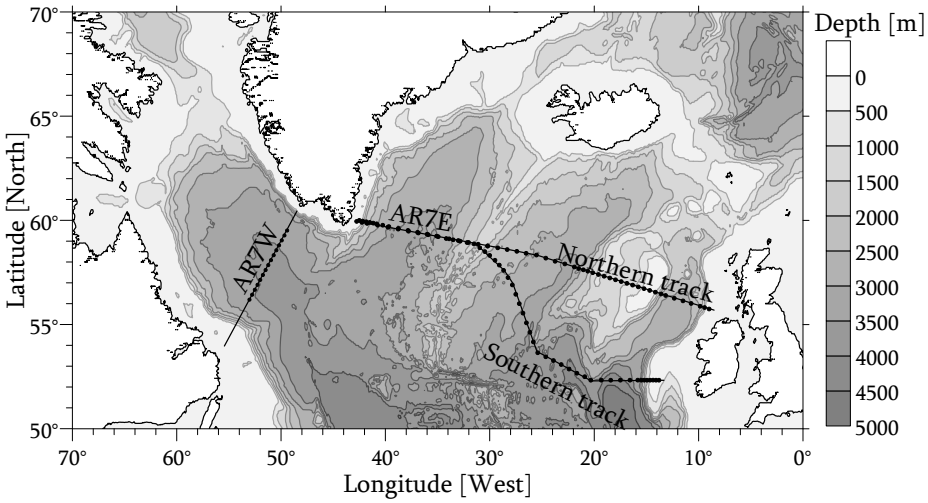

FIGURE 3.1: The AR7E and AR7W sections in the northern North Atlantic Ocean. Examples of station positions along the AR7W and AR7E section tracks are illustrated by the black dots. The topography of the northern North Atlantic Ocean is drawn with a 500 m isobath interval.

Stations on the AR7E and AR7W sections are typically spaced 30 miles apart. Over steep topography the station distances are usually reduced to 15 miles or less in order to sample the slope currents with higher resolution. During WOCE, hydrographic measurements were collected with a CTD system that includes a minimum setup of a Conductivity, Temperature and Depth (through pressure) sensors. In recent years additional oxygen, fluorescence and optical turbidity sensors are more commonly included in the CTD system. A typical CTD system such as used on the research vessels Pelagia and Discovery, is the Sea Bird Electronics-911. This system collects samples at 24 Hz, while the CTD frame is usually lowered and raised at a maximum speed of about 1 m s^{-1} at a hydrographic station. Measurements from the CTD sensors are filtered and averaged in 1 or 2 dbar intervals in order to suppress noise. These automatic measurements are calibrated against bottle salinity samples and temperature and pressure readings from reference instruments.

TABLE 3.1: The AR7E surveys (from Greenland to Ireland) used in this chapter. The survey track information (second column from the right) refers to the AR7E tracks east of the Reykjanes Ridge as drawn in Figure 3.1. No track information is given for cruises that did not survey east of the Reykjanes Ridge. If oxygen data are available it is indicated by a √.

Vessel	Year	Month	Track	O_2
RV Tyro	1990	July	South	√
RV Tyro	1991	April-May	North	√
RRS Charles Darwin	1991	August	North	√
FS Meteor	1991	September	South	√
FS Valdivia	1992	September	South	√
FS Meteor	1994	November	South	√
FS Valdivia	1995	June	South	
FS Valdivia	1996	August	South	
FS Meteor	1997	August-September	South	√
FS Valdivia	1999	May	South	
FS Poseidon	2000	August		
RV Pelagia	2000	September-October	North	√
FS Meteor & FS Komm. Jack	2001	June	South	
FS Alexander von Humboldt	2002	July		
FS Meteor	2003	July		
RV Pelagia	2003	August-September	North	
RV Alexander von Humboldt	2004	August		
RSS Charles Darwin	2004	September		√
RV Pelagia	2005	September	North	√
RSS Discovery	2006	August		√
RV Pelagia	2007	September	North	√
RSS Discovery	2008	August-September	North	√

The reference pressure and temperature sensors can only take one measurement, usually when the sample bottle is closed, but their accuracy is very high. Bottle samples can also be used to determine dissolved gasses (O_2, CO_2 and CFC's) and nutrient (Si, NO_3, NO_2 and PO_4) concentrations. The WOCE and CLIVAR sample and CTD data are subject to a prescribed series of quality checks, which guarantees high quality data. These quality checks are described in Chapter 4 of "WHP 90-1: Requirements for WHP Data Reporting Hydrographic Data Formats" which is available from the CLIVAR and Carbon Hydrographic Data Office at http://whpo.ucsd.edu/manuals/. Samples with questionable quality flags and outliers were removed from the data set. Because of the infrequent observations of most of the dissolved gases and nutrient, only the oxygen data (Table 3.1) are used in this chapter.

Several analysis method have been applied to the AR7E section data. In order to visualize the spatial structure of the temporal variability along the AR7E section, a series of time-longitude diagrams have been drawn (Figures 3.5, 3.6, 3.12 and 3.23). To ensure a good representation of the hydrographic structure on the standard longitude grid, stations located on the southern AR7E track between 30° W and 25° W are projected parallel to the topography on the northern track. The observation density distribution after the projection of the stations from the 22 surveys is shown in Figure 3.2. It shows the high density of observations near the slope of Greenland, where the between-station distances are decreased. It also shows the decrease in observations near the bottom. This is due to slight differences between the survey tracks, which result in differences in the height of the topography and thus in the depth of the hydrographic stations.

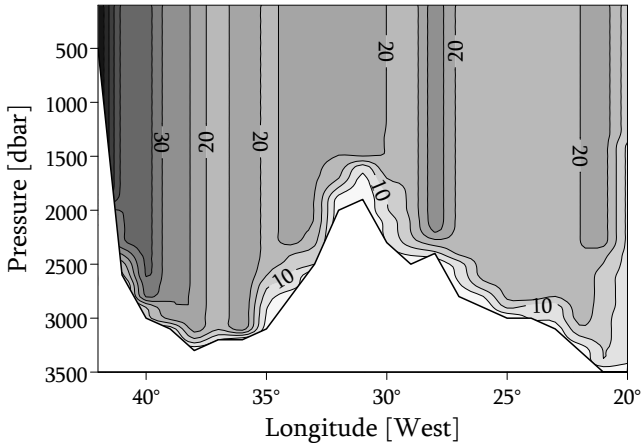

FIGURE 3.2: Longitude-depth observation density distribution of the AR7E surveys through the Irminger Sea and Iceland Basin after projection of the southern surveys on the northern track. The numbers refer to the number of sampled stations in a 1° longitude x 100 dbar interval, with lines drawn at intervals of 5 stations. The observation density decreases near the bottom due to differences in height of the topography between surveys. Plotted here is the median depth of the stations bottom samples, which is assumed to be the height of the topography.

Time-longitude diagrams were also composed of near-bottom data (Figure 3.23). For the se near-bottom diagrams, data from the lowest 100 m or 200 m of the CTD profile are used, which is assumed to end near the bottom. Anomalies in the bottom data fields due to shallower CTD profiles were avoided by using only data from profiles which ended within 100 dbar of the median of the depths of all CTD profiles at that longitude. This procedure removed nearly all of the bottom outliers.

Although values in time series resulting from the survey data are occasionally based on only 1 hydrographic station this does not necessarily imply that the uncertainties of these values (the within survey standard deviations) are large. The high vertical resolution of the hydrographic profiles combined with relatively small parameter gradients result in low uncertainties. For example, the mean distribution of the uncertainties (within survey standard deviation), calculated for 1° longitude × 100 dbar bins, is illustrated in the upper panels of Figure 3.3. Low values for the uncertainty in single surveys (≤ 0.05 °C and ≤ 0.004 psu) are found in the Labrador Sea Water (*LSW*), Iceland Scotland Overflow Water (*ISOW*), North East Atlantic Deep Water (*NEADW*) and Lower Deep Water (*LDW*). These water masses are denoted in the lower right panel of Figure 3.3, which contains the mean salinity distribution over all surveys (see Chapter 2 for a full description of the hydrography). The surface waters, as well as the Subpolar Mode Water (*SPMW*) and Denmark Strait Overflow Water (*DSOW*), all contain strong vertical gradients and show larger uncertainties (> 0.1 °C and > 0.005 psu). The time series shown in the following sections of this chapter are usually based on larger samples (with wider horizontal and vertical selection criteria). Thus, their uncertainties are expected to be of the same magnitude as the uncertainties shown in Figure 3.3 or better. Furthermore, the uncertainties are at least an order of magnitude smaller than the trends observed in the various water masses, except for the nearly stable *LDW* (shown at the end of Section 3.4). For this reason, and because of the different methods to extract time series from the data (with some based on other sub-sampled data sets), no error bars are drawn in time series graphs in this chapter.

Both the oxygen data and the historical hydrographic data from before 1990 rely strongly on bottle samples, also for temperature and salinity. For this sampling method a finite number of sample bottles are used. Water samples are distributed over the depth of the profile with a limited vertical resolution. Sample intervals are generally smaller, about 100 m, in the upper 1000 m (thermocline depth). In the more homogeneous deeper parts of the water column a vertical resolution of 250 m or more is common. The tracks of the measurement campaigns before 1990 were generally not organized along a common section. Despite this lower temporal and spatial resolution, the historical data still forms an important time series which offers insight into the multi-decadal and decadal variability of the northwestern North Atlantic Ocean.

Historical observations from before 1990 were obtained from the World Ocean Database of the National Oceanographic Data Center (NODC, http://www.nodc.noaa.gov/). Additional hydrographic data were obtained from the ICES (International Council for the Exploration of the Sea, http://www.ices.dk/) data base. With these data, backwards extended time series of salinity, potential temperature and oxygen

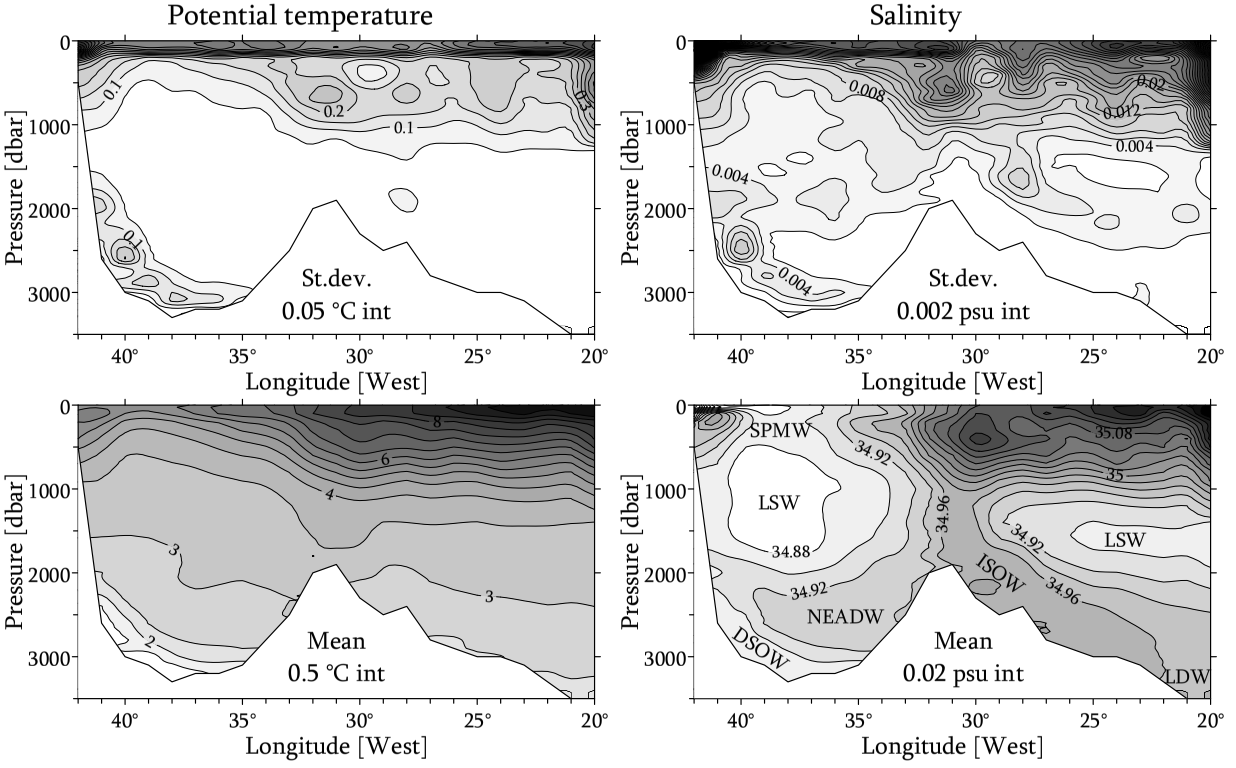

FIGURE 3.3: Distributions of the uncertainties (the within survey standard deviation) in potential temperature and salinity in bins of 1° longitude by 100 dbar averaged over all surveys.

The uncertainty distributions (top panels) exhibit large correlation with the main water masses seen in the mean distributions of potential temperature and salinity shown in the bottom panels. The uncertainties are relatively low for the LSW, ISOW, NEADW and LDW. The surface waters, SPMW and DSOW contain the largest uncertainties. The contour intervals are denoted in the panels

were composed for the centres of the Irminger and Labrador Seas from 1950 to the beginning of the 21th century. Within the available historical data, stations were selected between 56° N and 60° N in the Labrador Sea, and between 57° N and 62° N in the Irminger Sea. Data from the AR7E and AR7W sections are used for the years since 1990. Stations within the selected area that showed characteristics of the surface boundary currents were excluded from the data set. The method used to construct the resulting time series is similar to the method used by *Yashayaev* (2007), called robust averaging. First a median filter was used to remove outliers in salinity and temperature on density levels. Then the station data were isopycnally averaged and vertically gridded to create a profile representative of the centre of the basin.

Finally, the third data set consists of sea surface temperatures (*SST*) from the 1 Degree International Comprehensive Ocean-Atmosphere Data Set (1° ICOADS, introduced in the previous Chapter). The data set contains monthly mean surface temperatures from January 1960 to July 2007. However, also this set of observations is incomplete. Figure 3.4 illustrates the data coverage (in time) of the ICOADS data set over the northern North Atlantic. The northwestern part of the area has a lower data coverage due to the absence of shipping routes and because of ice and cloud coverage which block satellite observations of *SST*. There remains a reasonable amount of *SST* data for the central Irminger Sea (~85%). *SST* values for the Nordic Seas and the Labrador Sea should be regarded with some caution.

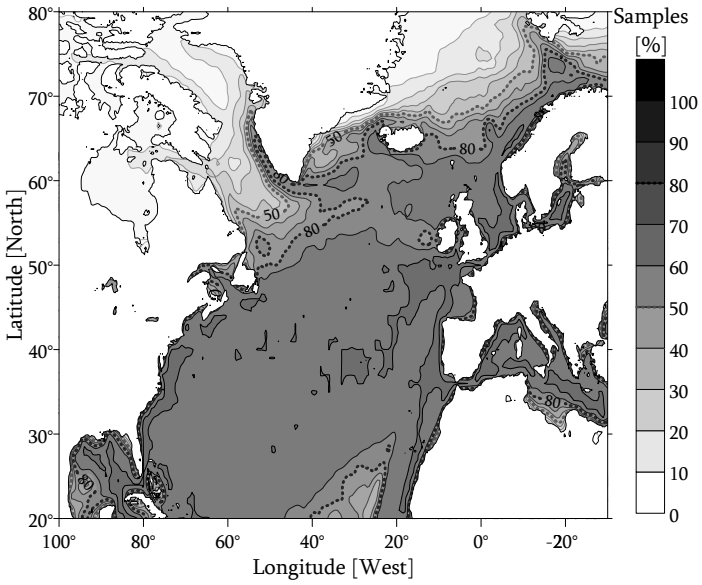

FIGURE 3.4: Data coverage of the 1°×1° grid boxes of the ICOADS sea surface temperature data set. The data coverage is indicated at each grid point as the fraction of the total record length filled with data. Most of the North Atlantic has good coverage, but the areas affected by sea-ice, in the northwest, have much poorer data coverage.

3.3 THE OBSERVED VARIABILITY

The data sets described in the previous section contain information about various types of variability. The backwards extended time series of stratification in the centre of the Labrador and the Irminger Seas reveal multi-decadal and decadal signals. We will show that these signals are related to the variability of the atmospheric forcing. The decadal to inter-annual variability of different water types along the AR7E section is described using the surveys since 1990. This description will start with the upper water masses, following with the intermediate waters and ending with the bottom waters (for the introduction of these water masses see Chapter 2). The processes likely to cause the inter-annual variability, such as the atmospheric forcing and lateral mixing of water masses, are also described.

3.3.1 A FIRST IMPRESSION OF THE LONG TERM VARIATIONS OF THE STRATIFICATION IN THE IRMINGER AND LABRADOR SEAS

The extended time series for the Labrador and Irminger Seas since 1950 offer insight into the variability in potential temperature, salinity and oxygen concentration. The averaging of the available profiles within one year removes part of the small scale variability, while the main multi-annual signals from the centre of the basins are expected to be preserved. However, we must keep in mind that the accuracy and resolution of the profiles before 1990 are less than that of the later WOCE cruises. Therefore the extended series are mainly used to analyse the variability in the centre of the Irminger and Labrador Seas on decadal time scales.

Figures 3.5 and 3.6 show the time-depth contours of the potential temperature, salinity and dissolved oxygen distributions in the centre of the Irminger and Labrador Seas. The general hydrographic stratification is easily recognized in these panels (see also Figure 2.6 in Chapter 2). Both basins show a similar vertical temperature structure, although the strongest subsurface stratification is found in the Irminger Sea. Overall, the Irminger Sea is more saline than its western neighbour, the Labrador Sea. This relatively high salinity is caused by the age difference between the water masses found in these basins. The Labrador Sea Water (*LSW*) starts out fresh in the Labrador Sea and becomes older and more saline on its way towards the Irminger Sea. On the other hand, the waters with eastern origins (Subpolar Mode Water, Iceland Scotland Overflow Water and Icelandic Slope Water), start out as saline water masses and become fresher as they are transported west towards the Labrador Sea. The dissolved oxygen concentrations near the surface are high in both basins, due to ventilation by the atmosphere, and generally decrease with depth. Oxygen values are higher in the near surface layer of the Labrador Sea, where ventilation is assumed to occur more

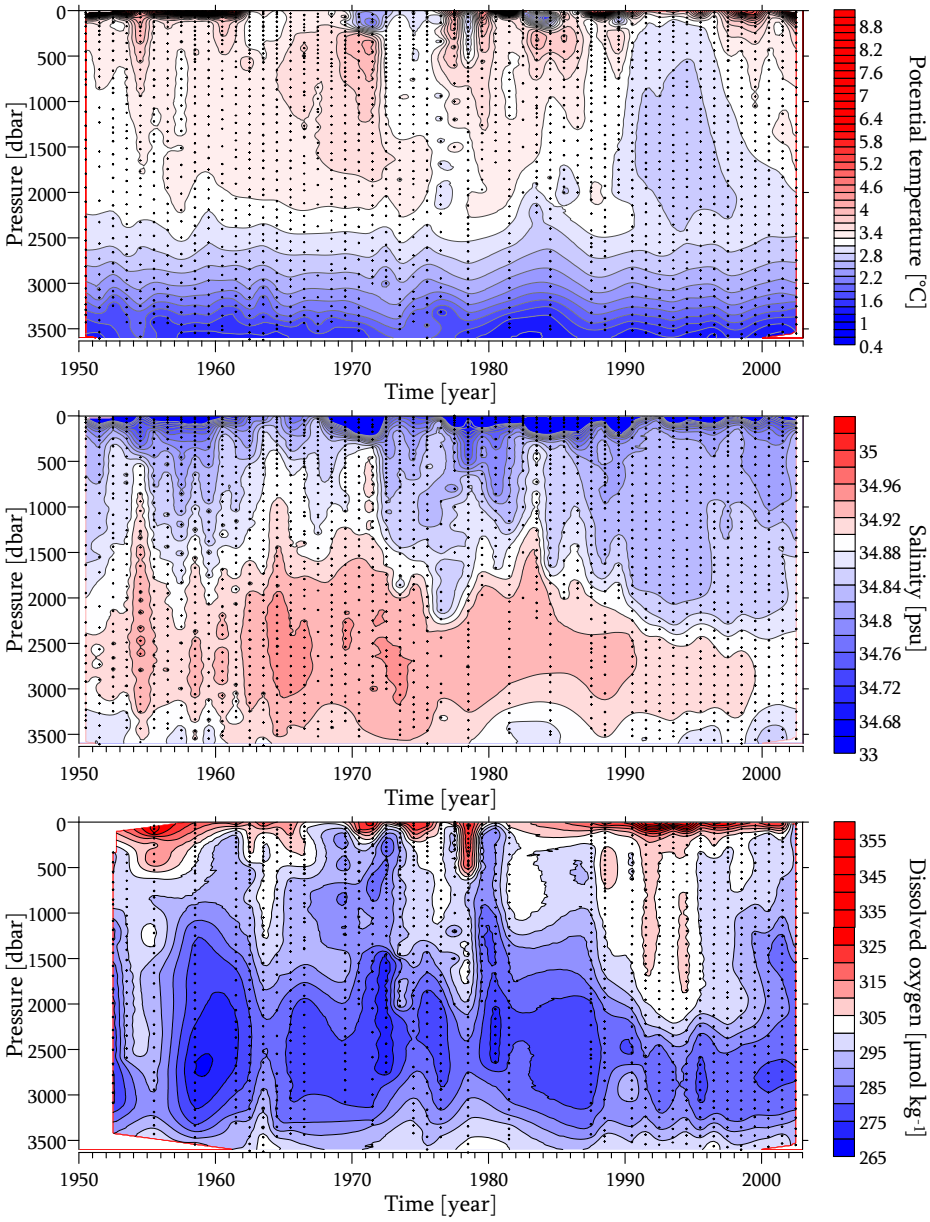

FIGURE 3.5: Time-pressure plots of potential temperature (top), salinity (middle) and oxygen concentration (bottom) in the Labrador Sea from 1950 to 2003. The contour intervals are 0.2 °C (temperature), 0.02 psu (salinity) and 5 µmol kg^{-1} (oxygen concentration). Timing and depths of bottle data are illustrated by the small dots. Note the scarcity of deep (>2000 dbar) observations between 1975 and 1990 and also of oxygen profiles from 1982 to 1987.

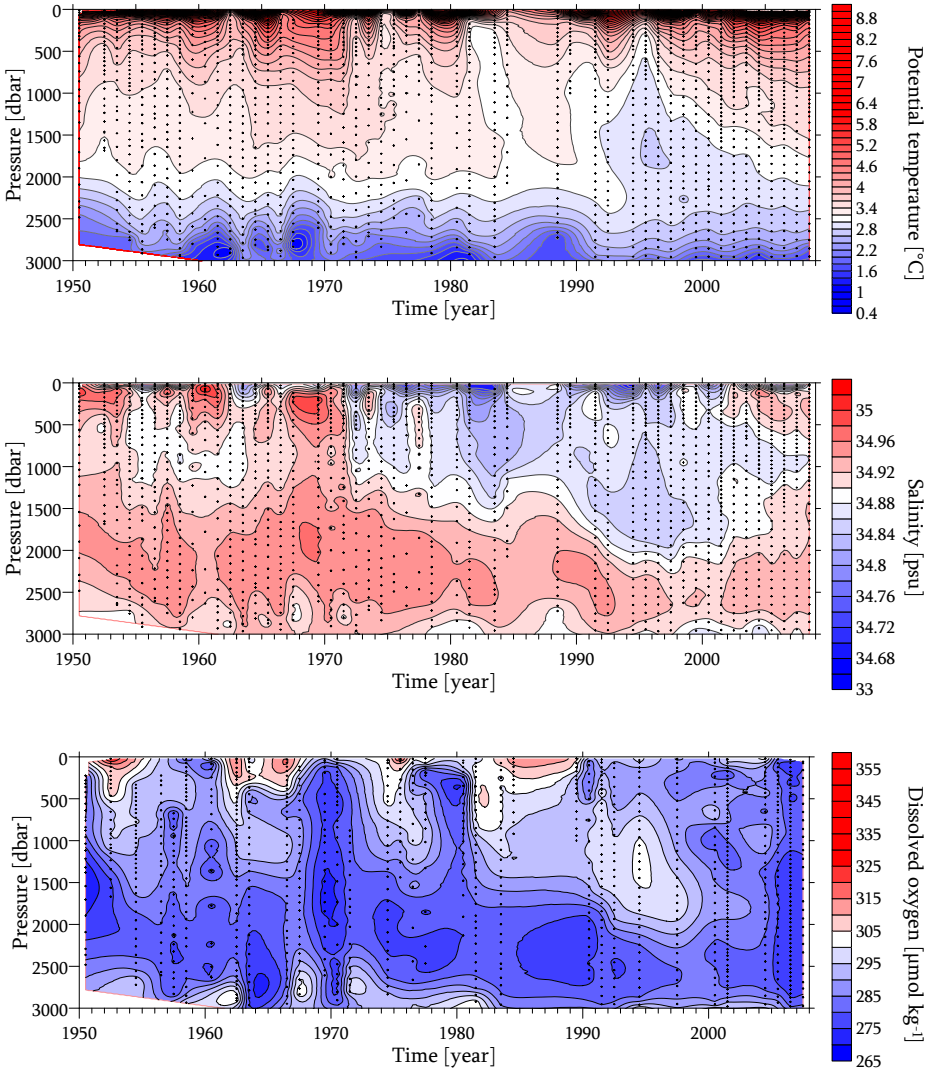

FIGURE 3.6: Time-pressure plots of potential temperature (top), salinity (middle) and oxygen concentration (bottom) in the Irminger Sea from 1950 to 2008. The contour intervals are 0.2 °C (temperature), 0.02 psu (salinity) and 5 µmol kg^{-1} (oxygen concentration). Timing and depths of bottle data are illustrated by the small dots. Note the lack of temperature and salinity observations between 1985 and 1988, and the scarcity in oxygen data compared to the Labrador Sea.

frequently and the sea surface temperature is lower. The oxygen concentration at the deep North East Atlantic Deep Water levels (*NEADW*, below 1500 dbar) is lower in the Labrador Sea due to the progressive aging of the *NEADW* during transport from the Irminger Sea towards the Labrador Sea.

There is quite some variability in this background stratification. At the longest available time scales we see a warming of the upper 2000 dbar in both basins from 1950 to 1970, followed by a cooling generating the coldest upper 2000 dbar in the middle 1990s. Since then, warming resumed until in the early 21th century the temperature structure was close to the 1950 situation. A similar multi-decadal signal can be recognized in the salinity in the upper 2000 dbar, with high (low) salinity coinciding with high (low) temperature.

Superimposed on this slowly varying stratification is a series of events at intermediate depth, which occur at decadal time scales in the upper 2000 dbar of both the Labrador and Irminger Seas. These events start with the appearance of large volumes of well oxygenated and occasionally relatively cold, fresh water at intermediate depths (*LSW*). These volumes of recently ventilated *LSW* are connected to the surface layer and seem to disappear again after some time. In between these events the water column loses oxygen, warms and salinifies, returning to the conditions of before the event. This pattern of alternations between an oxygen poor, warm and saline water column and an oxygen rich, cold and fresh water column is likely formed by intermittent periods of deep convection (cooling, freshening and ventilating large volumes of water) and of advection of older warm and saline water. These *LSW* events in the Labrador Sea are observed in the periods 1950-53, 1962-65, 1972-75, 1984-85 and 1990-1997, about once every 10 years (Figure 3.5). In the centre of the Irminger Sea near-coinciding *LSW* events are also observed (Figure 3.6). The large amplitude cold event in the middle of the 1990s forms the coldest part of the observational period. The formation of this large *LSW* volume was extensively described by *Lazier et al.* (2002) and *Yashayaev et al.* (2008). *Yashayaev* named the *LSW* vintage formed during this period LSW_{94}.

This pattern of the (multi-)decadal and inter-annual variability in the hydrography of the Irminger Sea is further investigated in the following sections. Particularly the inter-annual and longitudinal variability, which is smoothed in the annual mean profiles of Figures 3.5 and 3.6. The variability in the various water masses, introduced in Chapter 2, are presented and their causes and interactions are discussed. This description of the observed variability starts with the Subpolar Mode Water, before moving on to the deeper waters.

3.3.2 VARIABILITY OF THE SUBPOLAR MODE WATER

Subpolar Mode Water (*SPMW*) is found in the boundary currents of the Subpolar Gyre and, due to air-sea interaction, in a modified form in the centre of the Irminger gyre. Because of its relatively high temperature compared to the waters below, it is part of a strongly stratified layer (the thermocline). Thus, the *SPMW* is important to the preconditioning of the Irminger Sea to convection and the variability therein. However, the near-annual observations sub-sample the strong seasonal cycle of the surface waters and the *SPMW*, which will cause aliasing of this cycle onto the inter-annual variability. Due to the strong stratification the seasonal cycle, and thus the aliasing effect, decreases with increasing depth. To distinguish between the inter-annual and seasonal signals the sea surface temperatures (*SST*) from the ICOADS data set are first compared with temperature data from the extended time series. Then attention is given to the multi-decadal variability of the atmospheric forcing and the resulting *SPMW* properties. Finally the inter-annual and longitudinal variability along the AR7E section since 1990 is described.

A. Subpolar Mode Water and its relation to sea surface temperatures

From the ICOADS data set monthly and annual mean *SST* time series were derived for the centre of the Irminger Sea between 40° and 36° W, at about 59.5° N. The monthly mean *SST* of the Irminger Sea is immediately recognized in Figure 3.7 by its large seasonal cycle (with a range of ~5 °C). The annual mean *SST* follows the mean of the seasonal cycle and thereby shows the inter-annual variability of the Irminger *SST*, without aliasing problems. These two ICOADS *SST* time series are compared to time series of near-annual hydrographic observations to estimate the magnitude of the aliasing problem and to find a suitable hydrographic series representative of the *SPMW*. Two time series were constructed from the AR7E surveys through the Irminger Sea. These times series were constructed by taking the average values over the 40° to 36° W longitude interval, similar to the *SST* series, and start in 1991 (Figure 3.7). The first of these series represents the surface layer, composed of the mean temperature between 0 and 200 dbar. These temperatures are closest to the sea surface temperatures, but the aliasing is also expected to be stronger. The second series is a subsurface time series composed of the mean temperature between 200 and 500 dbar, a pressure interval coinciding with the subsurface salinity maximum characteristic for the *SPMW*. A third series (starting in 1950 but shown from 1960 onwards in Figure 3.7) is composed from the 200 to 500 dbar mean temperatures from the backwards extended hydrographic series. The resolution of this series is lower, but it shows the long term relation between the *SST* series and the subsurface series.

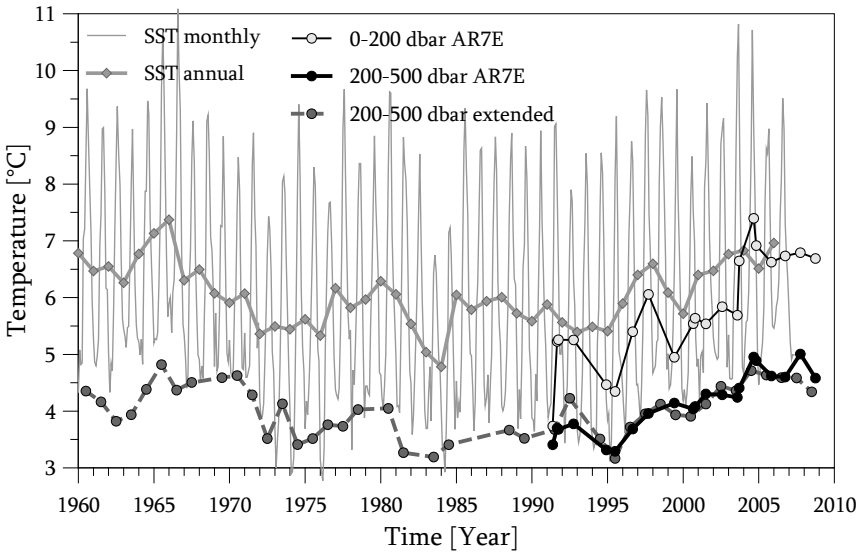

FIGURE 3.7: Time series of temperature in the centre of the Irminger Sea (40° to 36° W). The ICOADS monthly mean sea surface temperature (SST) and annual mean SST since 1960 are drawn in grey. The surface (0 to 200 dbar) time series from the AR7E surveys between 40° to 36° W is drawn with a thin black line and open circles. The subsurface (200 to 500 dbar) time series from the AR7E surveys between 40° to 36° W is drawn with a thick black line and filled circles. The subsurface series from extended hydrographic data from the centre of the Irminger Basin is drawn with the dashed line.

Figure 3.7 shows that the AR7E hydrographic series from the 200 to 500 dbar layer best follows the ICOADS annual mean *SST* series (R = 0.73). This correlation holds for the backwards extended 200 to 500 dbar series (R = 0.72). These subsurface temperatures series are on average 2.1 °C lower than the *SST* values and seem to reflect the *SST* conditions of the preceding winter. The surface, 0 to 200 dbar, AR7E time series exhibits a much larger variability than both the subsurface series and the *SST* series due to aliasing of the seasonal signal, with relatively low temperatures when surveys were conducted in late winter/early spring and higher temperatures during cruises made in late summer (Table 3.1). Due to this aliasing of the large seasonal cycle, the correlation of the surface layer temperature time series with the ICOADS annual mean series is reduced to R = 0.66. The ICOADS *SST* data and the subsurface (200 to 500 dbar) hydrographic data are used to further study the decadal variability of the temperature and salinity of the *SPMW*.

B. Multi-decadal variability of Subpolar Mode Water and atmospheric forcing

The ICOADS annual mean *SST* time series (Figure 3.7), and the subsurface (200 to 500 dbar) temperature and salinity series (Figure 3.8 top panel) all exhibit multi-decadal signals. They show what seems to be an oscillation with a period of about 50 years. The temperature and salinity where high in the late 1960s, low in the mid 1980s and again high at the end of the record. Because the changes in salinity follow the variability in temperature so closely (R = 0.84), it is likely that both properties are affected by the same process. Likely candidates for such a process are changes in the advection of heat and salt by the ocean circulation and changes in the atmospheric forcing of the northwestern North Atlantic Ocean. The NCEP data set (introduced in Chapter 2) supplies information about the major atmospheric forcing parameters. Three important atmospheric forcing parameters, the heat flux, the freshwater flux and the wind stress curl, are plotted in the bottom panel of Figure 3.8. The heat (freshwater) flux influences the oceans temperature (salinity) directly, while the wind stress curl influences the ocean circulation and thereby the advection of heat and salt in the ocean.

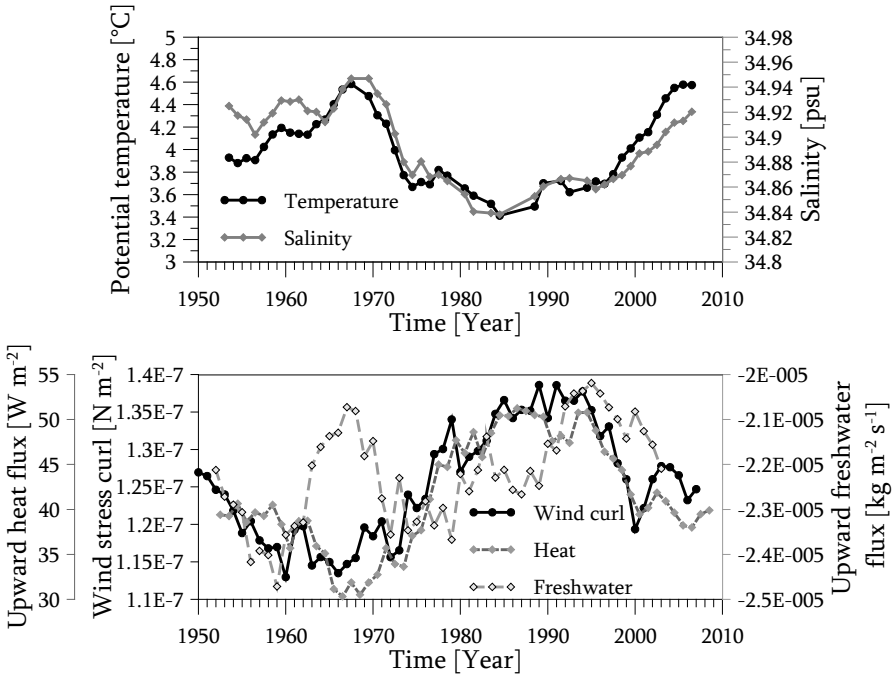

FIGURE 3.8: Time series of subsurface hydrographic properties and atmospheric forcing of the Irminger Sea. The 5-year running mean potential temperature (black line) and salinity (grey line) averaged between 200 and 500 dbar are plotted in the upper panel. The time series of the 5-year running means of the wind stress curl, the upward heat flux and the upward freshwater flux over the center of the Irminger Sea are shown in the lower panel.

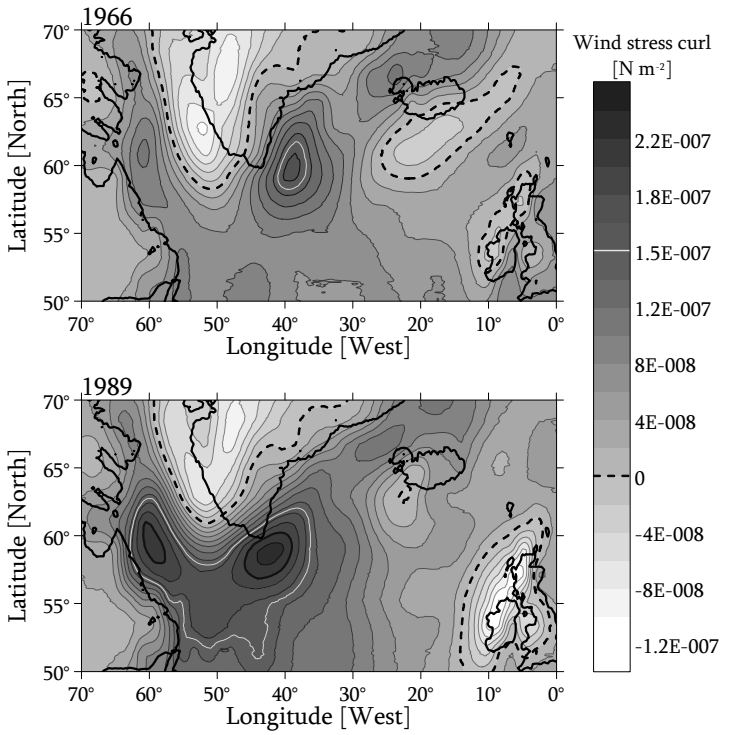

FIGURE 3.9: Wind stress curl over the northern North Atlantic during weak wind forcing conditions (top panel for 1966) and during strong wind forcing conditions (bottom panel for 1989). The white line indicates the $1.5 \cdot 10^{-7}$ N m^{-3} contour. The dashed grey line indicates the line of zero wind stress curl.

The freshwater flux does not correlate significantly (R = 0.14) with the observed changes in salinity in the layer between 200 and 500 dbar. Apparently, the salinity of the *SPMW* layer is mainly influenced by advective processes. The low-pass variations in the heat flux and the wind stress curl (5-year running mean) correlate strongly, and inversely, with the low-pass filtered time series of salinity (R = -0.68 for the heat flux and R = -0.64 for the wind stress curl). The correlation with temperature is lower (R = -0.41 and R = -0.31 respectively). When discussing which forcing factor is most important it must be kept in mind that the heat flux and the wind stress curl are not independent parameters, because both depend on the wind velocity. The heat flux is wind-dependant through the sensible and latent heat fluxes, which are both important over the Irminger Sea (Chapter 2). The wind velocity and direction over the Irminger Sea is partly determined by the large scale pressure dipole over the North Atlantic (Chapter 2). Therefore, the observed changes in temperature and salinity are expected to be part of larger scale changes. The spatial data in the NCEP and ICOADS data sets were used to investigate the large scale changes in the forcing and in the response of the sea surface respectively. Two typical situations for the wind stress curl are plotted in Figure 3.9. These panels illustrate the difference between a low wind stress curl year (1966) and a high wind stress curl year (1989). In 1989 the entire

western part of the northern North Atlantic, specially the Labrador and Irminger Seas, experienced strong wind stress curl forcing compared to 1966. Such large scale changes are expected to have an effect on the advection in the Subpolar Gyre and the resulting temperature and salinity fields.

High resolution time series of salinity fields are not available, but the *SST* fields can be investigated. The *SST* anomaly fields for the northern North Atlantic are drawn for the same two years, 1966 and 1989, in Figure 3.10. They show a warm anomaly in the northwest in 1966 and a cold anomaly in the northwest in 1989, in agreement with the temperature time series in Figure 3.8. In both situations the line of zero temperature anomaly runs from the southwest towards north of Ireland. Weaker changes (with opposing sign) are seen east of this line. The zero anomaly line approximately agrees with the front formed by the North Atlantic Current.

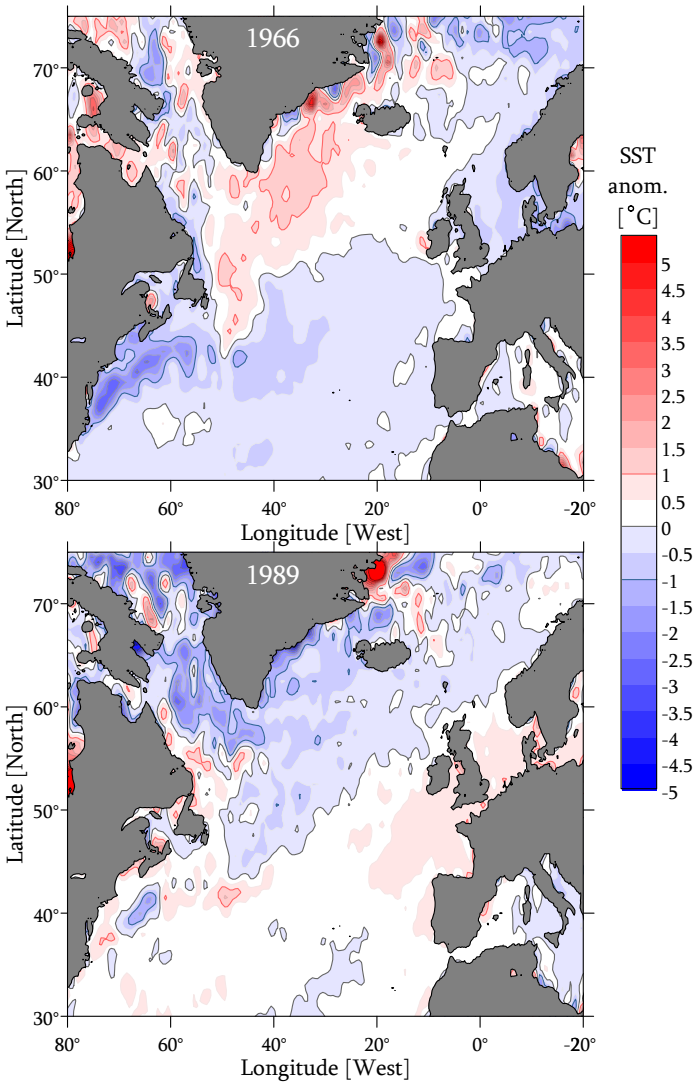

FIGURE 3.10: Annual mean SST anomaly with respect to the 1960 to 2007 mean SST field. In the top panel the anomaly field during low wind stress curl conditions (1966) is shown. In the bottom panel the anomaly field during high wind stress curl conditions (1989) is shown.

A similar pattern in *SST* changes was also found by *Flatau et al.* (2003), but for changes within a shorter period (the 1990s). They observed a spin up of the circulation and a shift of the axis of the North Atlantic Current to the east during a positive phase of the North Atlantic Oscillation (NAO, Hurrell (1995)). The eastward displacement of the Subpolar Front lowered the surface temperature on the western side of the subpolar basin. High wind stress conditions and consequential high sensible and latent heat fluxes may further reduce the sea surface temperatures according to *Flatau et al.* (2003). During negative NAO years this situation is reversed and the western basins experience warmer temperatures due to the westward shift of the Subpolar Front. *Hátún et al.* (2005) correlate the increase in temperature and salinity with a change in the shape of the Subpolar Gyre. During a weak gyre the inflow of warm, saline water from the North Atlantic Current into the Subpolar Gyre increases, while the transport of heat and salt towards the Nordic Sea decreases. The gyre index (Häkkinen & Rhines (2004)), which indicates gyre strength, was also shown to correlate with the salinity of the Irminger Current (Hátún *et al.* (2005)). Positive (negative) salinity anomalies in the Irminger Current corresponded with a weaker (stronger) gyre.

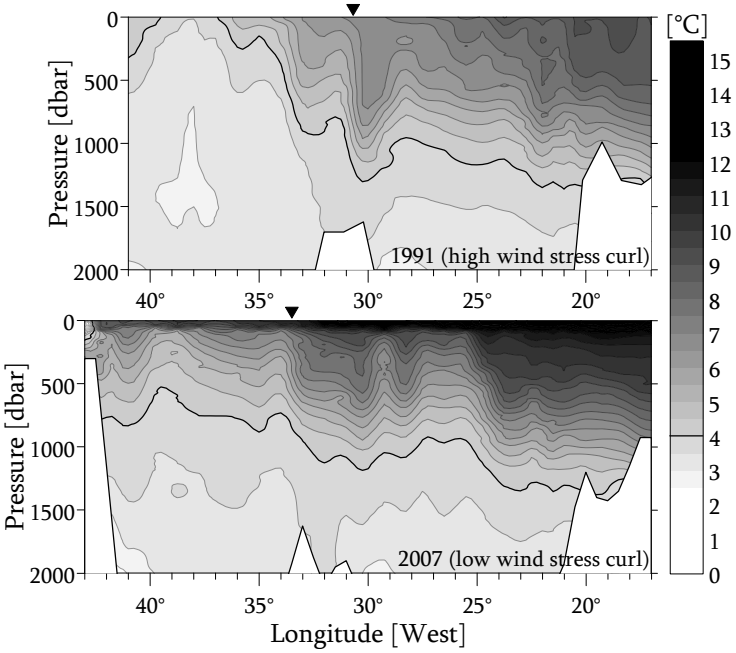

FIGURE 3.11: Contours of the potential temperature along the AR7E section in 1991 during high wind stress conditions (top panel) and 2007 during low wind stress conditions (bottom panel). The 4°C isotherm is drawn with the thick black line to indicate the doming of the isotherms in 1991 more clearly. The position of the front is indicated by the black triangle at the top of each panel. The shift to the west and the decrease in sharpness can be seen from these panels.

The eastward shift of the front and the related change in the baroclinic currents is also visible in the in the hydrographic sections. Although such surveys are not available for 1989 and 1966, the years 1991 and 2007 were subject to similar forcing conditions. In 1991 the NAO index was positive (Figure 2.11, in the previous chapter), the wind stress curl was high (Figure 3.8 lower panel) and the front was located at about 31° W (Figure 3.11). In 2007 the NAO and wind stress curl were low and the front shifted westwards to about 34° W, although it decreased in sharpness. The Irminger gyre had spun down and the isothermal dome (and thereby also the isopycnal dome) that was visible in 1991 had relaxed, allowing warmer waters into the upper layers of the centre of the Irminger Sea. The reduction of the horizontal density gradients due to the relaxation of the doming will also lead to a reduction in the baroclinic advection of warmer water in the Irminger and East Greenland Currents. *Häkkinen & Rhines* (2004) also reported this recent decline of the Subpolar Gyre. They noticed increasing sea surface heights and declining velocities measured by current meters. This decline started in 1994, after the maximum of the NAO index (Figure 2.11).

C. Inter-annual variability of the SPMW properties along the AR7E section

The inter-annual variability of the Subpolar Mode Water is better studied in the detailed AR7E surveys instead of the backwards extended hydrographic series, which only captures the variability in the centre of the basin. The longitude-time diagrams in Figure 3.12 illustrate the zonal structure of the inter-annual hydrographic variability of the *SPMW* along the AR7E section in the Irminger Sea and western Iceland Basin during the last 2 decades. It reveals the location of the warm, saline boundary currents and their inter-annual shift in more detail. Overall, the centre of the Irminger basin (38° to 39° W) is cooler and fresher than the boundary currents over the eastern (34° to 36° W) and western (40° to 42° W) slopes of the basin. This cold, fresh signal has its strongest expression at around 1995, coinciding with the temperature minimum in the extended record. The warming after 1995 also fits with the observed warming of the *SPMW* seen in Figure 3.8. The salinity structure and variability is very similar to that of the temperature. The cool, fresh phase around 1995 appears to be caused by at least two effects. First, the relatively cold and fresh intermediate water is brought upward by the doming of the Irminger gyre and influences the temperature and salinity of the 200 to 500 dbar layer shown here. Secondly, the more stagnant *SPMW* in the centre of the Irminger Sea is exposed to the strong cooling by the atmosphere seen in the early 1990s (Figure 3.8).

The differences in temperature and salinity in the centre of the Irminger Sea and the boundary currents (east and west) and their inter-annual variability are highlighted in the time series shown in Figure 3.13. Again, the centre is significantly cooler and

fresher, while the differences between the eastern and western boundary currents are nearly indistinct. The *SPMW* in the eastern boundary current is warmest during most of the record, leading to an average temperature difference with the western boundary current of 0.3 °C. It is less obvious which side of the basin, the west between 40° and 42° W or the east between 34° and 36° W, is more saline. The mean difference is small (0.002 psu) and not significant. Only further east, over the top of the Reykjanes Ridge, the higher salinities of the *SPMW* are clear (Figure 3.12). Overall, the salinity in the centre is about 0.05 psu lower compared to the eastern boundary current, mainly due to the stronger increase in salinity in the last part of the record. The temperature in the centre is about 0.9 °C lower than that of the eastern boundary current. The small difference in timing of the θ and S minima in the centre is not significant. The magnitude of the observed increase since 1995 (1996 for salinity) is about 1 °C and 0.05 psu, similar to the increase shown before in Figure 3.8. The correlation of the salinity in the centre with that of the boundaries is relatively high, R = 0.87 for the salinity in the east and centre of the basin and R = 0.74 for the salinity in the centre and western boundary current.

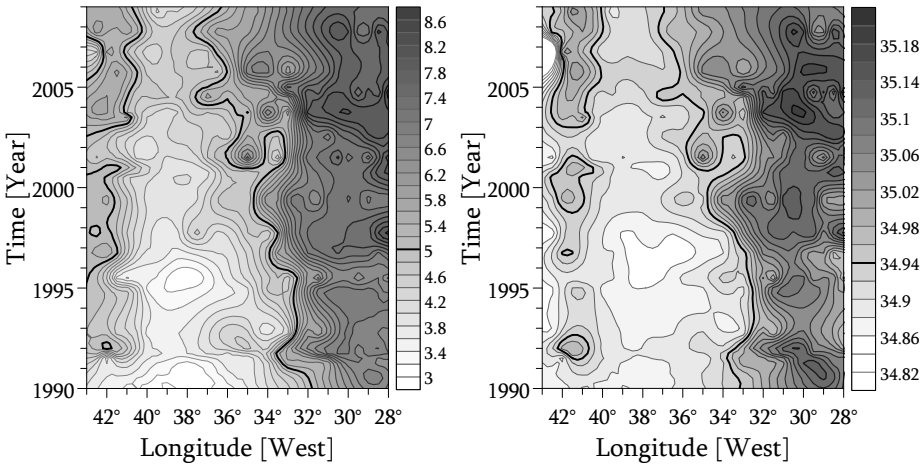

FIGURE 3.12: Time-longitude diagrams of the subsurface (200 to 500 dbar) properties in the Irminger Sea based on the surveys of the AR7E section. The subsurface temperature is shown on the left with isotherms at 0.2 °C intervals (the 5 °C isotherms is drawn with a thick black line). The subsurface salinity is shown on the right with isohalines at 0.02 psu intervals (the 34.94 psu isohaline is drawn with a thick black line). The warm, saline boundary currents are visible on the left and right sides of each panel. The top of the Reykjanes Ridges, which separates the Irminger and Iceland basins is located at about 31° W.

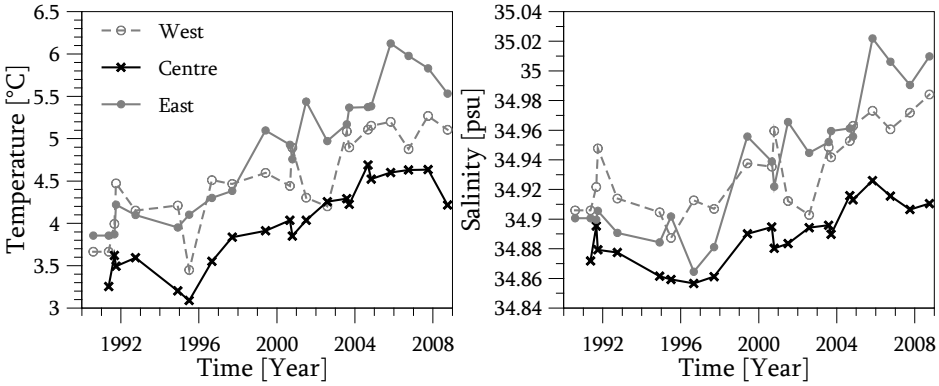

FIGURE 3.13: Time series of SPMW properties in different parts of the Irminger Sea (averaged between 200 and 500 dbar). The left panel shows the temperature and the right panel salinity on the eastern side (solid grey line), in the centre (black line) and on the western side (broken grey line).

D. Transport of boundary current SPMW anomalies around the Irminger Sea

Figure 3.13 illustrates that the multi-decadal trend of warming after 1995 is dominant over the small-scale inter-annual variability. This "noise" on top of the trend is caused by local processes, e.g. lateral exchange between the boundary currents and the centre by eddies and changes in local atmospheric forcing. The correlation between the inter-annual variability (noise) of the two boundary currents is not so good, despite of the cyclonic transport path of *SPMW* (and anomalies therein) around the Irminger basin. However, transport paths of surface drifters, reported by *Valdimarsson & Malmberg* (1999), indicate that drifters move around the Irminger Sea within one year. Also, four ARGO floats, with a parking depth of 1000 m, deployed in the centre of the Irminger Sea in 2007 left the basin at 43° W in 300 to 430 days. (Float ID numbers 6900383, 6900384, 6900385 and 6900386, at http://www.coriolis.eu.org/cdc/floats/cdcFloats.asp.) With such fast boundary currents in the upper 1000 m, *SPMW* anomalies are transported around and out of the basin well within a year. The sampling resolution of the AR7E surveys, with yearly intervals and at 30 nm (~55 km) station distance, is not sufficient to accurately determine an accurate time lag between (or follow the transformation of) *SPMW* anomalies on the eastern and western sides of the basin.

3.3.3 Changes in the intermediate layer: Labrador Sea Water

The intermediate levels in the Labrador and Irminger Seas are alternately occupied by oxygen rich, fresh and cold water and lower oxygen, warmer and more saline waters (Figures 3.5 and 3.6). The well ventilated oxygen rich water is the convectively formed

Labrador Sea Water (*LSW*). As extensively described in literature, the formation of the LSW_{94} vintage was the largest cooling and freshening event in the last 50 years (the Lab Sea Group (1998), Lazier *et al.* (2002), Yashayaev (2007) and Yashayaev *et al.* (2008)). The large volume of nearly homogeneous LSW_{94} is also seen as a substantial stability minimum in Figure 3.14. After its maximum extent in 1994, the LSW_{94} in the Labrador Sea declined by (lateral) mixing and by advection to neighbouring basins. The decline of the LSW_{94} stability minimum is succeeded by the formation of LSW_{2000} (Yashayaev *et al.* (2008)), formed in the winter of 2000. This is a lighter density class of *LSW*, filling a smaller and shallower volume but still visible as a stability minimum in the Labrador and Irminger Seas at about 1000 dbar. Also before the LSW_{94} formation, the intermediate layers in the northwestern North Atlantic Ocean have been ventilated regularly, as can be seen in the succession of stability minima (Figure 3.14) and coinciding oxygen maxima (lower panels of Figures 3.5 and 3.6).

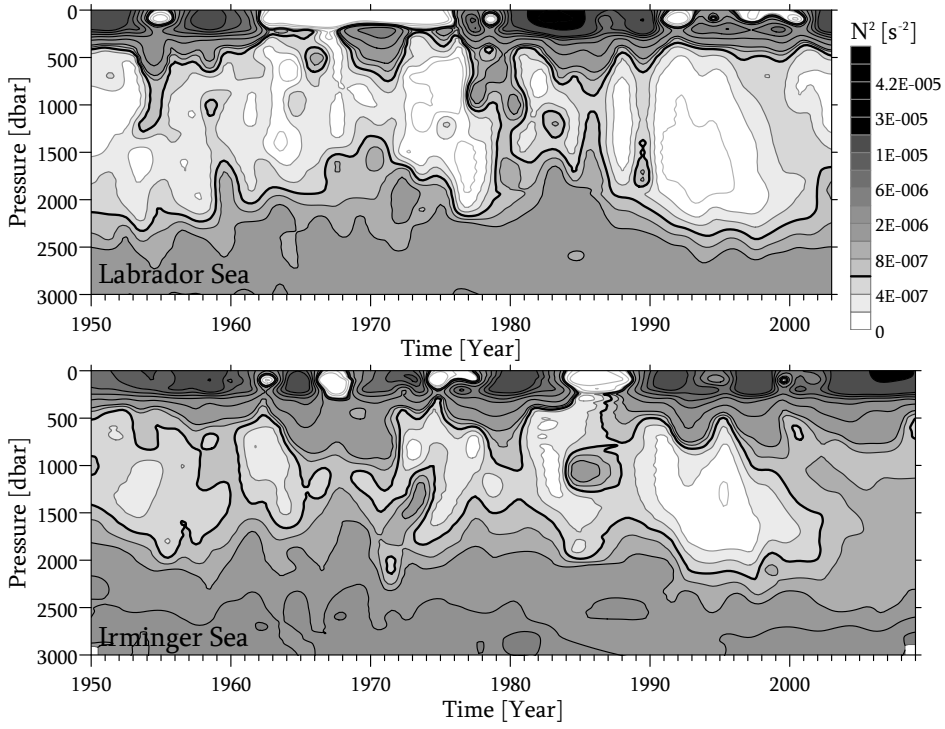

FIGURE 3.14: Time-depth diagram of the variability in the stability frequency squared (N^2). The values show are the 10log of N^2. The top panels shows the changes in N^2 in the Labrador Sea while the bottom panel shows the changes in N^2 in the Irminger Sea. The stability (N^2) was calculated over 100 dbar intervals.

A. Ventilation and water mass transformation events

Four earlier ventilation/homogenization events can be recognized by their high oxygen content and low stability (lower panels of Figure 3.5 and 3.6, and Figure 3.14). The first in the early 1950s, the second in the early 1960s, a large event between 1972 and 1977 and the fourth in the early 1980s. These ventilation events are seen both in the Labrador Sea and in the Irminger Sea, although arguably stronger in the Labrador Sea. The winter heat flux anomalies (Figure 3.15) illustrate the episodes of extensive surface cooling related to the strong convective mixing events after 1970, shown in Figure 3.14. All three major events, in the 1970s, 1980s and 1990s, coincide with periods of prolonged winter cooling. In the years before 1970 and after 1995 the heat flux anomaly was less pronounced, and the typical ventilation events reached less deep.

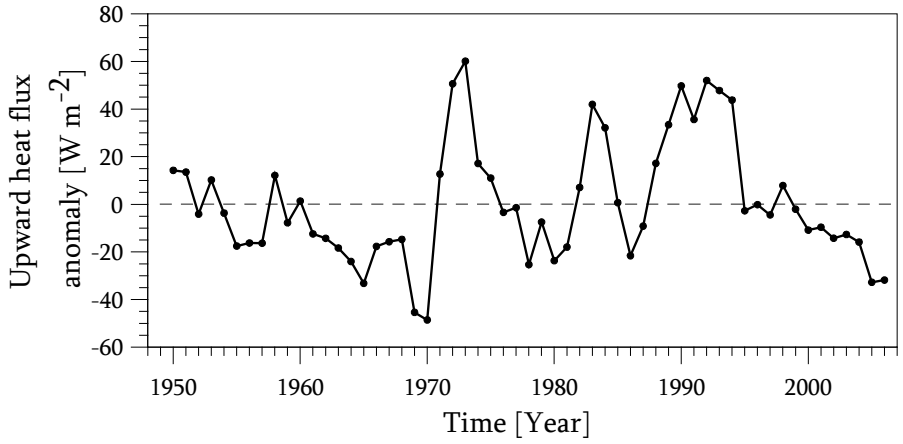

FIGURE 3.15: Time series of the Labrador Sea upward heat flux anomaly in the winter half year. Shown are the 3-year running means of the winter heat flux anomaly. Based on the data from the NCEP reanalysis.

The resolution of the time series, sampling annually at best, is not good enough to determine a general time lag directly between the events in both seas. (Yashayaev *et al.* (2007) determined a time lag of about 2 years for the LSW_{94} and the LSW_{2000} from survey data.) The succession of well ventilated Labrador Sea Water vintages is less well visible in the temperature and salinity plots (Figures 3.5 and 3.6). The large amplitude multi-decadal warming and cooling cycle of the upper 2000 dbar, mentioned in Section 3.3.1, dominates the variability in these properties.

B. The role of Icelandic Slope Water in the transformation and decay of LSW

In between the ventilation events, the Labrador and the Irminger Seas become increasingly warmer, more saline, and stable while the oxygen concentration declines. *Straneo* (2006) attributes this decay of Labrador Sea Water vintages to lateral mixing with the surrounding boundary currents near the continental slopes. A decrease in volume of the recently ventilated *LSW* is caused by advection of a large volume *LSW* out of the basins. The remaining *LSW* in the centre of the basins likely mixes isopycnally with Icelandic Slope Water (*IcSW*) advected in the saline boundary current. The *IcSW* is a saline water mass that coexist on the same density level as *LSW* (van Aken & de Boer (1995), Yashayaev *et al.* (2008) and Chapter 2 of this thesis). On the AR7E section, the *IcSW* is found in its strongest form along the eastern slope of the Reykjanes Ridge (RR) and the Mid Atlantic Ridge and in a more diluted form along the western slope of the RR (Figure 2.8 in Chapter 2). From the basin boundaries the *IcSW* spreads isopycnally towards the centres of the basins east and west of the Reykjanes Ridge. There it mixes laterally with the *LSW*, increasing the *LSW* temperature and salinity. *IcSW* occasionally even can be found in a thin saline layer between *LSW* cores at different densities. This is illustrated in Figure 3.16, which is partly similar to Figure 9 in *Yashayaev et al.* (2008). However, Figure 3.16 also contains θ,S-profiles of *IcSW* over the slopes of the RR.

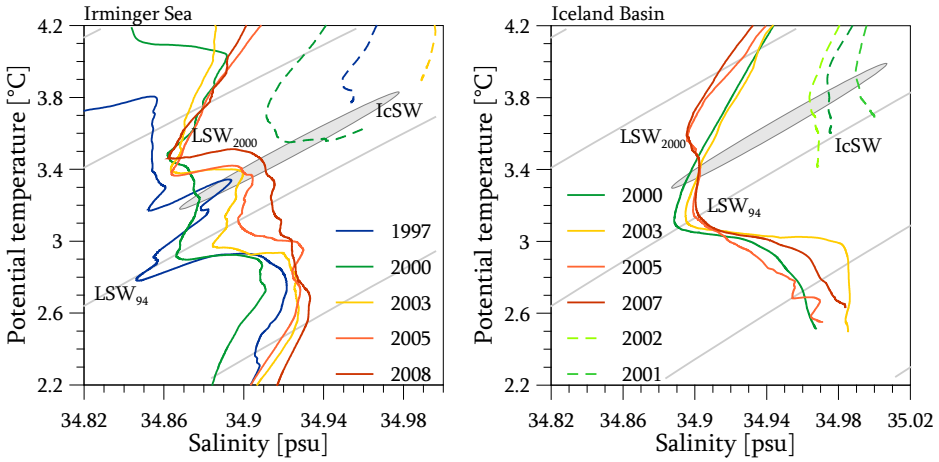

FIGURE 3.16: Transformation of LSW and intruding IcSW in the Irminger Sea (left panel) and Icelad Basin (right panel). The θ,S-diagrams illustrate the salinity minimum of the LSW_{94} at its most extreme in 1997 in the Irminger Sea and in 2000 in the Iceland Basin. Later profiles show the progressive transformation of the LSW_{94} to a more saline water mass, the arrival of the LSW_{2000} as a second salinity minimum and the saline IcSW, which coexists on the same density level (ellipse) and intrudes between the two salinity minima.

The θ,*S*-diagrams in Figure 3.16 illustrate the transformation and decay of the two recent Labrador Sea Water vintages, the LSW_{94} and the LSW_{2000} (Yashayaev *et al.* (2008)). Maximum extent of LSW_{94} is seen in the Irminger Sea in 1997 (left panel) and in the Iceland Basin (right panel) in 2000. After the formation of LSW_{2000} a shallower salinity minimum arrives in these basins, while a more saline water type intruded between the salinity minima of LSW_{94} and LSW_{2000}. Isopycnal mixing with Icelandic Slope Water, found in the saline boundary current, is a likely explanation for the phenomenon. In more recent years the salinity minimum at the LSW_{94} density level has nearly disappeared in the Irminger Sea and will probably disappear in the future from the Iceland Basin.

Although the temporal change in the Labrador Sea Water, with the decay of LSW_{94} and the emerging of LSW_{2000}, can be followed in Figure 3.16, the change in *IcSW* seems random. This is partly due to insufficient sampling, since the *IcSW* has a relatively small volume. An average of four stations are sampled in the Reykjanes Ridge (RR) area shallower than 2000 m (for an example see Figure 3.19 in the next section). This effectively means one station near or in the *IcSW*, which complicates the description of the variability of *IcSW* in much detail.

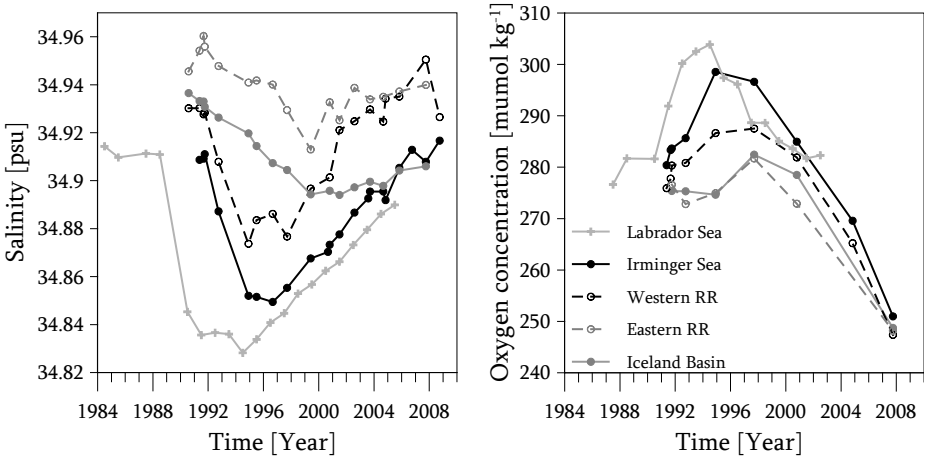

FIGURE 3.17: Properties of the LSW_{94} density layer (34.68 to 34.70 kg m^{-3} in the Irminger Sea and Iceland basin and 34.66 to 34.68 kg m^{-3} in the Labrador Sea). The left panel shows the salinity as observed in the northwestern Atlantic Basins and over the slopes of the Reykjanes Ridge. The right panels shows the oxygen concentration on the same density levels.

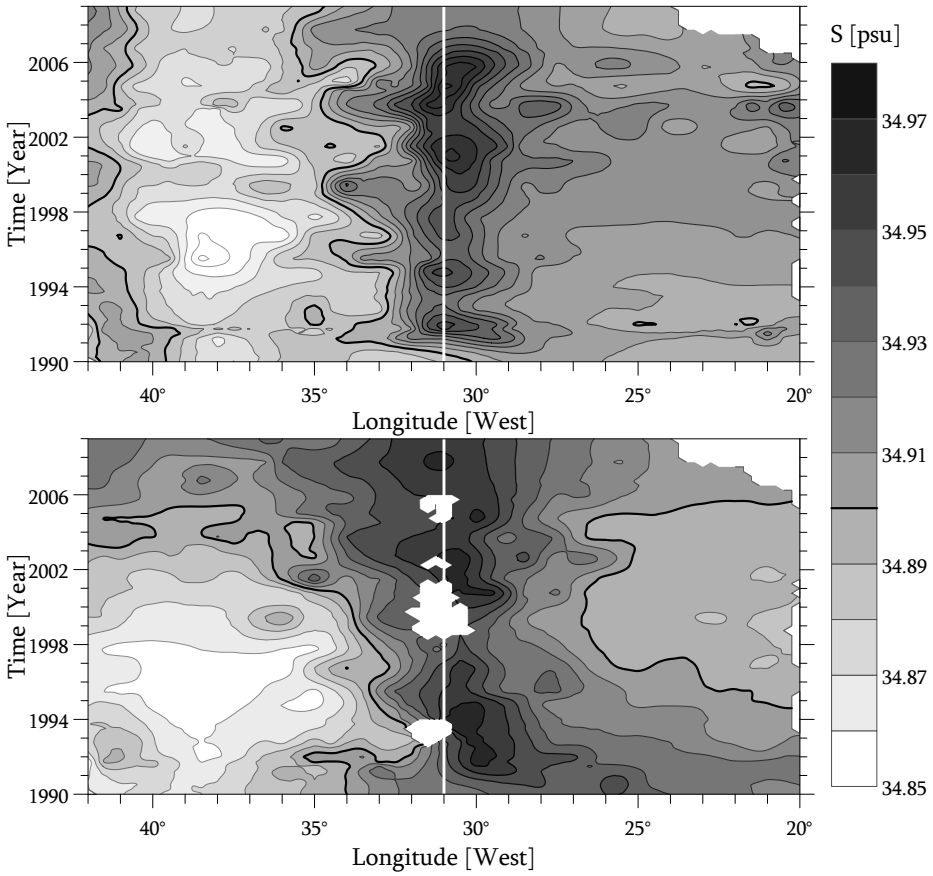

FIGURE 3.18: Hovmöller diagrams of the salinity distributions in the two LSW density layers. The left panels illustrates the layer between $\sigma_{1.5}$ is 34.58 and 34.62 kg m^{-3}, representative for the LSW_{2000}. The right panels illustrate the layer between $\sigma_{1.5}$ is 34.66 and 34.70 kg m^{-3}, representative for the denser LSW_{94}. The x-direction in both panels covers the Irminger Sea, the Reykjanes Ridge and the Iceland Basin. The blank spots are due to blocking by the topography, while the white vertical lines represent the top of the Reykjanes Ridge at 31° W.

Nevertheless, the time series of salinity and oxygen concentration at the density level of LSW_{94} and *IcSW* are plotted in Figure 3.17. Time series from 5 locations are shown, representing the centre of the Labrador Sea and of the Irminger Sea, the areas west and east of the Reykjanes Ridge and the centre of the Iceland Basin. The time series of temperature are not shown, since they covary with salinity on a density level. The cooling and freshening of the centre of the Irminger Sea leads to a minimum in θ and S in 1996. The oxygen concentration was not measured in the Irminger Sea in 1996, but does archive its maximum in the surrounding years. In the Iceland Basin the salinity minimum arrives somewhat later, around 1999. Again, oxygen values were not

measured in the Iceland Basin at that time, but reached the (observed) maximum in the preceding year. The temperature and salinity minima and the oxygen maximum in both basins are assumed to be caused by the arrival of the recently ventilated LSW_{94} (Yashayaev *et al.* (2008)). Thus, the transport time seems to be 2 years for the Irminger Sea and 5 years for the Iceland Basin. The arrival of LSW_{94} is followed by its transformation, warming and salinification, and decay. The minimum in S and maximum in O_2 caused by the LSW_{2000} is not visible since it did not reach down to this density level. The time series of the eastern and western side of the top of the Reykjanes Ridge indicate the presence of the more saline boundary current, consisting of older *IcSW*. Their variability covaries with the signals in the centres of their respective basins, probably due to lateral mixing or the displace of the *IcSW* by the more voluminous *LSW*.

More details are shown in a time-longitude diagram of the salinity at the densities of LSW_{94} and LSW_{2000} constructed from the station data along the AR7E section (Figure 3.18). The location of the saline *IcSW* is clearly visible at both density levels over the top of the Reykjanes Ridge (located at 31° W) and on its eastern side, with only a narrow band of saline water flowing along the western side. *IcSW* seems to appear on the western slope after 1998 with some reduction of high salinity values over the eastern slope shortly after this period. This seems to reflect the strong influence of the central *LSW* core in the Irminger basin on the surrounding *IcSW*. The patchiness of Figure 3.18 (especially of the lower density layer), which remains despite of some smoothing, is most likely due to under-sampling and to aliasing of occasional meso-scale eddies.

3.3.4 Variability in overflow waters of northeastern origin: Iceland Scotland Overflow Water & North East Atlantic Deep Water

Over the slopes of the Mid Atlantic Ridge, cold but saline water masses are found originating from the overflow across the Iceland-Scotland Ridge in the northeastern North Atlantic. The Iceland Scotland Overflow Water (*ISOW*) in the Iceland Basin is the densest of these waters and follows the continental rise near Iceland and the lower part of the eastern slope of the Reykjanes Ridge (van Aken & de Boer (1995)). The North East Atlantic Deep Water (*NEADW*) in the Irminger basin, over the western slope of the Reykjanes Ridge, has its origin in the *ISOW* (van Aken & Becker (1996)), but is substantially modified on its way through the Charlie-Gibbs Fracture Zone near 52° N (Figure 2.1 in Chapter 2). The *NEADW* also contains Lower Deep Water (*LDW*) and Labrador Sea Water. Figure 3.6 already revealed some of the variability in the *NEADW* in the central Irminger Sea, characterized by a salinity maximum

between 1500 and 2500 dbar. It shows high salinities in the late 1960s and a salinity minimum around 2000. However, since these waters follow the topography along the boundaries of the basins, the cores of the *NEADW* and the *ISOW* are not sampled in the centres of the basins. The variability is therefore analysed here by using data from the AR7E surveys for the two regions east and west of the top of the Reykjanes Ridge. The easternmost region is located between 27° and 30° W, in the Iceland Basin, and represents the *ISOW*. The western region is located between 30° and 33° W, in the Irminger Sea, and represents the *NEADW*. All data below the $\sigma_{1.5}$ = 34.70 kg m^{-3} isopycnal were vertically averaged over these longitude interval. Because the two regions are in the shallow parts of the Reykjanes Ridge (<2500 dbar), any variability signals from the densest waters (Denmark Strait Overflow Water and Lower Deep Water, which are found in the deepest parts of the basins) are likely to be excluded from the resulting time series. Station positions (triangles in Figure 3.19) and station density vary somewhat from year to year, while the flows of *ISOW* and *NEADW* may shift up and down the slopes. This will introduce some aliasing of the spatial variability into the time series, which has to be kept in mind when considering the results.

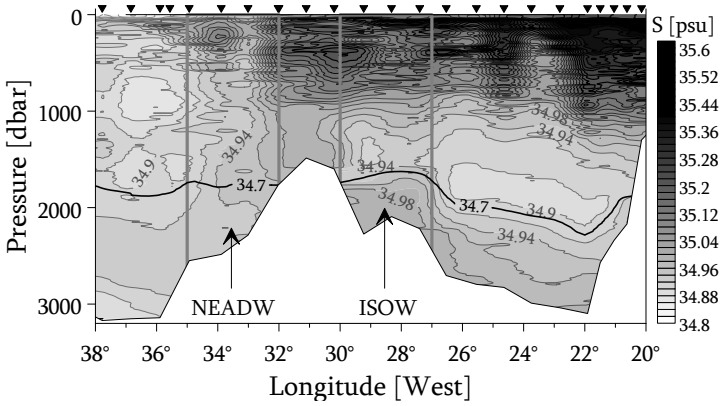

FIGURE 3.19: Contour plot of salinity observed over the Reykjanes Ridge in 2003. Salinity contours are drawn at 0.04 psu intervals. The $\sigma_{1.5}$= 34.6, 34.7 and 34.8 kg m^{-3} isopycnals are drawn in black. The rectangles encompass the two regions where data were selected. The triangles on top indicate the locations of the CTD stations surveyed in 2003.

A. From Iceland Scotland Overflow Water to North East Atlantic Deep Water

The resulting time series of potential temperature and salinity over the eastern and western slope of the Reykjanes Ridge (Figure 3.20) show that the *NEADW* is less saline than the *ISOW* (by 0.04 psu on average), because of mixing with the relatively fresh *LDW* and *LSW*. Both the *ISOW* and the *NEADW* show relatively lower salinity values around 1998, but this effect is strongest in the *NEADW*. The temperature difference between *NEADW* and *ISOW* is relatively small, ~0.03 °C on average. The

NEADW temperature also shows a considerable drop before 1998. The *ISOW* temperature has decreased during the first 6 years, after which it remained more or less constant.

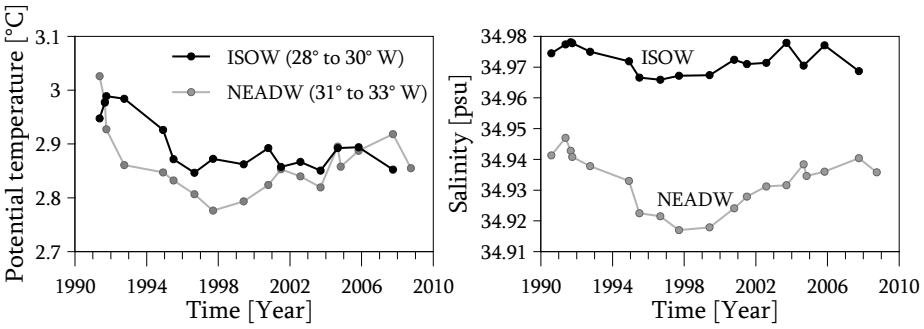

FIGURE 3.20: Time series of the mean potential temperature (left panel) and salinity (right panel) over the slopes of the Reykjanes Ridge below the $\sigma_{1.5}$= 34.70 kg m^{-3} isopycnal. The ISOW values (in black) are from the eastern region, 27° to 30° W. The NEADW values (in grey) are from the western region, 30° to 33° W.

The changes in salinity and temperature of the *ISOW* are not density compensating. The average density of *ISOW* increased over the total time series by about 0.01 kg m^{-3} (not shown). This density change is not due to a change in the depth of our selected upper isopycnal. The $\sigma_{1.5}$= 34.70 kg m^{-3} isopycnal remains at 1700 ± 50 dbar, thus the density change is due to an increasing density gradient between this isopycnal and the topography. The resulting density of *NEADW* over the western RR increases strongly (about 0.02 kg m^{-3}) during the first 3 years of the record, then levels off at about $\sigma_{1.5}$= 34.746 ± 0.003 kg m^{-3}. The initial increase in density is likely caused by the sharp drop in temperature from 1990 to 1993 after which the salinity and temperature variations compensate each other in density.

Notably, the decrease in salinity and temperature of the *ISOW* levels off before the *LSW* minimum arrives in the Iceland Basin, which suggest that this signal originates from upstream. Although the minima in temperature and salinity of the *NEADW* lag the *ISOW* minima with 1 to 2 year, it is probably not derived from the *ISOW*. Since NEADW is a diluted form of *ISOW*, any signal of the *ISOW* should be smaller in magnitude in the *NEADW*. Thus, the strong *NEADW* signal must be derived from elsewhere. The most likely source of the signal is the arrival of Labrador Sea Water (*LSW*) in the Charlie-Gibbs Fracture Zone (CGFZ), where the transition from *ISOW* to *NEADW* takes place. Since the *LSW* minimum reaches the Iceland Basin in about 5 years (Yashayaev *et al.* (2007)), it is likely that the *LSW* minimum arrives at the CGFZ

a short period after 1996 (the arrival of the salinity minimum in the central Irminger Sea). In the CGFZ, the *LSW* decreases the *ISOW* salinity due to mixing (cold entrainment) after which it is transported northward as *NEADW* along the western slope of the Reykjanes Ridge. The salinity minimum in the *NEADW* then reached the AR7E section in 1997, with a time lag of about 2 years with respect to the *LSW* minimum in the centre of the Irminger Sea. A second source of freshwater is the *LDW*. Variations in the contribution of dense *LDW* to the *NEADW* can also explain the large increase in density with respect to the *ISOW*. This density increase cannot be caused by the *LSW*, as it is lighter than *ISOW* and *NEADW*. The variability of *LDW* properties is discussed in the next section.

B. North East Atlantic Deep Water around the Irminger Sea

After leaving the CGFZ, the *NEADW* flows cyclonically around the Irminger basin and is seen again on the AR7E section over the Greenland continental slope. Figure 3.21 illustrates the variability of the *NEADW* on the west side of the Irminger Sea, between 40° and 43° W. These values were determined from the $\sigma_{1.5}$ = 34.70 to 34.80 kg m^{-3} density interval, above the denser Denmark Strait Overflow Water. Not surprisingly, the time series show that *NEADW* is cooled (by 0.2 °C) and freshened (by 0.03 psu) during its trip around the Irminger Sea, but the signals of the θ and S minima remain. Comparison of the curves in Figure 3.21 suggest that it takes about 2 years for the salinity minimum to travel around the Irminger basin. The temperature signal over the East Greenland slope is too noisy to draw a similar conclusion for the temperature field.

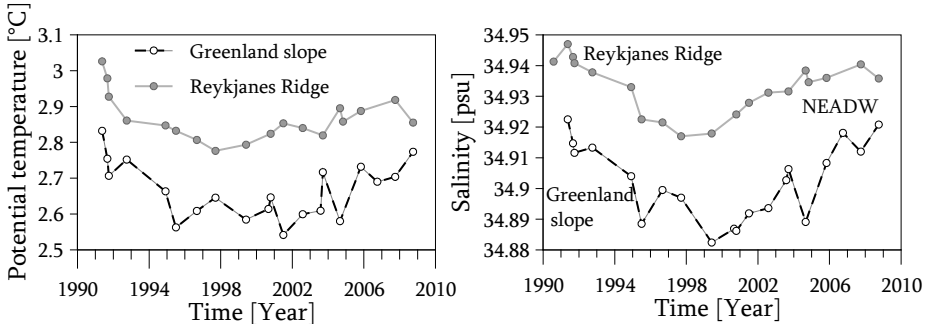

FIGURE 3.21: Time series of potential temperature (left panel) and salinity (right panel) of the NEADW over the slopes of the Irminger Basin. Values from the RR (in grey) are identical to the NEADW values in Figure 3.20. Values from the Greenland slope (40° to 43° W) are drawn in black. All values are from the $\sigma_{1.5}$ = 34.70 to 34.80 kg m^{-3} density interval.

3.3.5 THE DEEPEST BOTTOM WATERS: DENMARK STRAIT OVERFLOW WATER & LOWER DEEP WATER

The Denmark Strait Overflow Water (*DSOW*) is the coldest and densest deep water in the Irminger Sea, despite its relatively low salinity. Because of its high density it fills the bottom layer in the deepest parts of the Irminger basin, where its core can be found near the continental slope of eastern Greenland. Thus, by analysing the properties of the bottom layer, we find the properties of the *DSOW*. Similarly, the Lower Deep Water (*LDW*), with a southern origin, fills the deepest part of the Iceland Basin, overlain by the southward flowing Iceland Scotland Overflow Water. Its properties are visible in the bottom layer east of the Reykjanes and Mid Atlantic Ridge. In Figure 3.22 the salinity and temperature distribution versus longitude of all the AR7E surveys have been plotted. From this figure it is clear that the year-to-year variability in salinity and especially temperature in the *DSOW* in the Irminger Sea is much larger than that of the *LDW* in the Iceland Basin. Also, the lack of horizontal gradients in the *LDW*, despite of the large depth range, indicates that the *LDW* is indeed quite homogeneous.

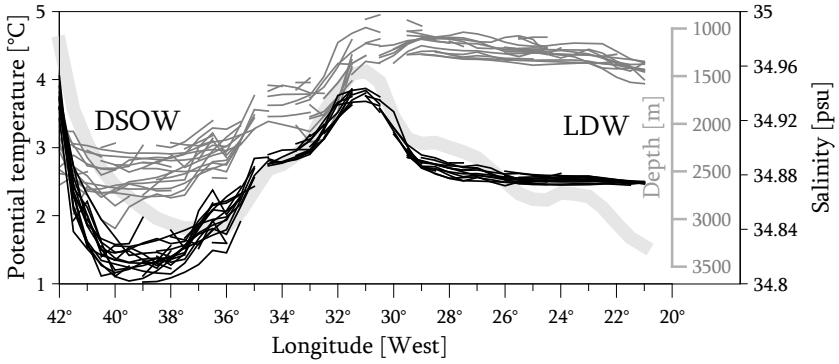

FIGURE 3.22: Properties of the bottom layer (100 m) versus longitude for all AR7E surveys. Potential temperature profiles are drawn in thin black line and salinity in thin grey lines. The thick grey line in the background displays the depth and shape of the bottom topography.

A. DSOW variability

The variability of the bottom properties (time versus longitude) is illustrated in Figure 3.23. The *DSOW* can be recognized by the lower temperature and salinity near the Greenland slope, at approximately 41° W. The *DSOW* shows 3 salinity minima between 1990 and 2008 (in 1995, 1999 and 2004), which coincide with lower *DSOW* temperatures. The time series of the salinity and the potential temperature between 38° and 40° W are plotted in Figure 3.24.

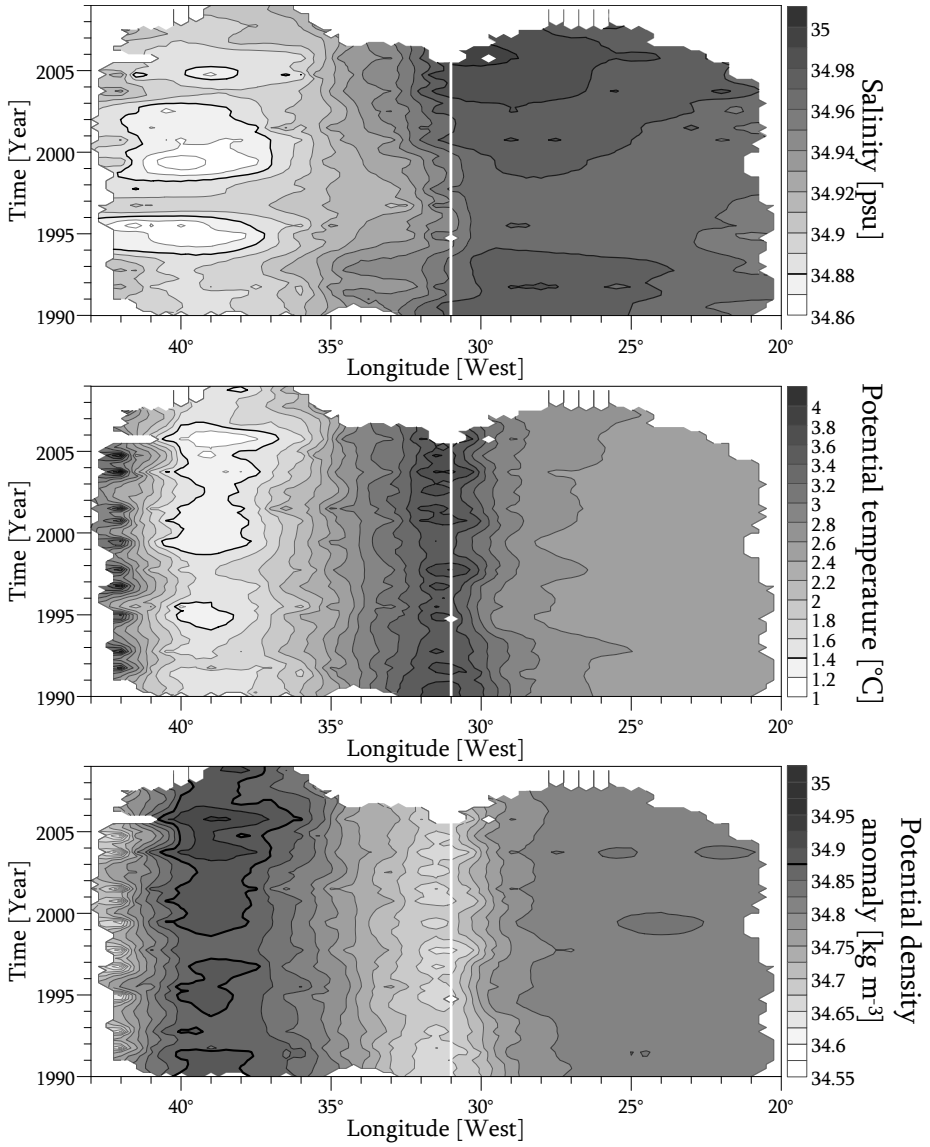

FIGURE 3.23: Longitude-time diagrams of the bottom 100 m of the water column in the Irminger and Iceland Basins. Shown is salinity (upper panel, contour interval 0.01 psu), potential temperature (middle panel, contour interval 0.2 °C), and potential density anomaly relative to 1500 dbar (lower panel, contour interval 0.025 kg m^{-3}). The top of the Mid Atlantic Ridge is indicated by the white lines.

In Figure 3.23 the two salinity minima in 1995 and 1999 are clearly visible, as well as a less pronounced minimum in the fall of 2004. The first two minima were already described by Dickson *et al.* in 2003, who reported a freshening and cooling trend of the *DSOW*, with a superimposed multi-annual to decadal variability. The pattern of change found in the western Irminger basin lagged behind the variability in upper Fram Strait (2500 km upstream) by 3 years (Dickson *et al.* (1999)). The freshening and cooling trends were suggested to mirror the multi-decadal freshening trend of the Nordic Seas described by Turrell *et al.* (1999). However, according to our more recent data, the freshening trend has changed since 1999 into a salinifying trend. The temperature of the *DSOW* also displays some variability, but no significant temperature trend can be recognized after 1990.

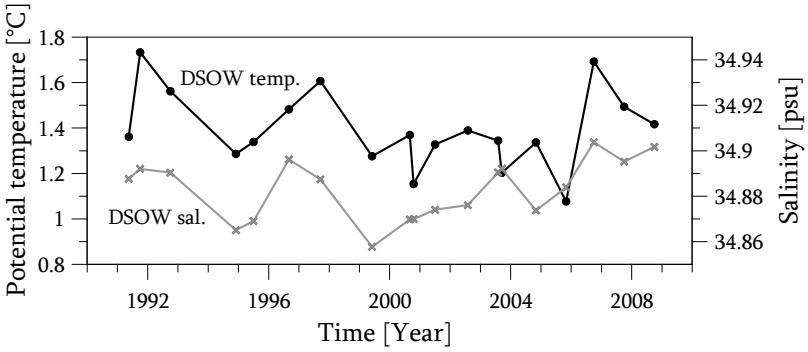

FIGURE 3.24: Time series of the mean potential temperature and salinity of the 100 m bottom layer between 38° and 40° W, representative for DSOW. The mean temperature in this longitude interval is drawn in black. The mean salinity is drawn in grey.

B. LDW variability

Changes in the Lower Deep Water in the Iceland Basin are an order of magnitude smaller than those of the *DSOW*, which is not unexpected due to its great distance from its source. The mean potential temperature and salinity of the *LDW* in the bottom 100 dbar between 22° and 26° W shows a minimum in salinity during the years 1994 to 1996, followed by a minimum in temperature in 1999 (Figure 3.25). This interval was chosen because of the limited number of observations further east. However, even for this wide longitude interval, enclosing the transition from *LDW* to *ISOW*, the changes are quite small (θ range ~0.15 °C and S range ~0.015 psu) and for salinity only about 5 times the accuracy of the sensor (given to be 0.0020 psu). At 21° W, in the *LDW* itself, the range for salinity is similar, but the range for temperature is much smaller (0.04 °C over 10 surveys). Thus, it can be assumed that the thermohaline properties of the *LDW* that contribute to the *NEADW* are relatively constant.

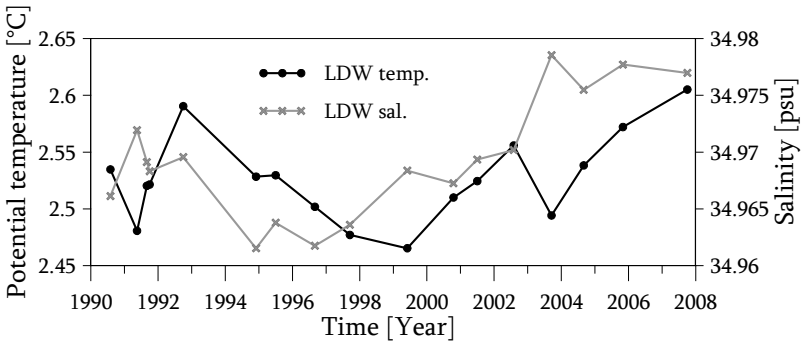

FIGURE 3.25: Time series of potential temperature (black) and salinity (grey) of the 100 m bottom layer between 22° and 26° W, representative for Lower Deep Water. Note the small scales on both axes relative to the previous figures.

3.4 SUMMARIZING DISCUSSION & CONCLUSION

A. The observed variability

Inter-annual to decadal changes in potential temperature, salinity and dissolved oxygen are observed throughout the water column in the northwestern North Atlantic basins. The strongest signal in the variability of the Irminger Sea is the cooling and freshening of the centre of this basin in the early 1990s and the successive warming. The vertically averaged temperature and salinity in the centre of the Irminger Sea decreased by about 0.2 °C and 0.02 psu from September 1991 (Figure 3.26, upper panel). After reaching a cold, fresh minimum in the fall of 1994 both the temperature and the salinity increased steadily until, at the end of the record in 2008; the temperature is 0.6 °C above the 1994 minimum and the salinity is raised by about 0.04 psu. The increases in temperature and salinity do not compensate completely in density leading to a significant decreasing trend in density since the start of the record in 1990 (Figure 3.26, lower panel). After 1995, the mean oxygen concentration in the centre of the Irminger Sea falls until 2007 with nearly 40 μmol kg^{-1} (Figure 3.26, lower panel). This indicates that the overall changes in the Irminger Sea are likely connected with the shut down of the deep ventilation after 1995.

The decline in temperature and salinity has been well described by *Dickson et al.* (2003), *Bersch et al.* (1999) and *Read & Gould* (1992). The reversal of this freshening trend in the early 2000s was also noticed (Holliday *et al.* (2008) and Safaranov *et al.* (2008)). Here we have extended the northwestern North Atlantic record to investigate the various interactions between the various water masses. The freshening phase of the North Atlantic has often been attributed to the development of a large volume

of fresh and cold Labrador Sea Water between 1987 and 1994 in the Labrador Sea (Lazier *et al.* (2002), Yashayaev *et al.* (2007)) which afterwards spread at intermediate depth to the nearby basins. However, some reservations must be made. Although the arrival of the *LSW* class is a striking event at this intermediate density level, it is not *LSW* formation alone that causes the variability. The decreasing and increasing salinity and temperature at intermediate levels is caused by an interplay of two main resident water masses. One fresh and cold, Labrador Sea Water, the other warmer and more saline, Icelandic Slope Water (*IcSW*, van Aken & Becker (1996)). Following episodes of consecutive cold winters, during which deep convection in the Labrador Sea produces large volumes of *LSW*, the mid-depth northwestern North Atlantic cools and freshens. These cooling and freshening events are interleaved with periods when the advection of *IcSW* regains dominance of these mid-depths, causing warming and salinification. This pattern of alternating cold/fresh and warm/saline periods is clearly seen in the extended time series of the Labrador and Irminger Seas since 1950 (Figures 3.5 and 3.6).

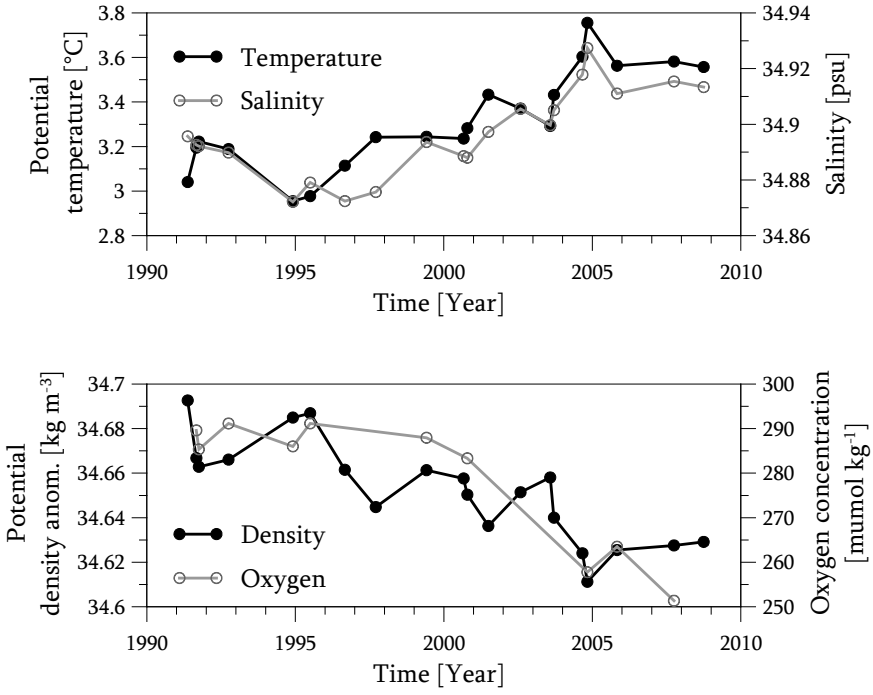

FIGURE 3.26: Average properties of the total water column in the center of the Irminger Basin (between 35 and 40°W). The top panel shows the time series of vertically averaged potential temperature and salinity. The bottom panels shows the time series of vertically averaged potential density anomaly ($\sigma_{1.5}$) and dissolved oxygen concentration.

How important is the variability of (and the interaction between) the *LSW* and *IcSW* to the variability observed in the centre of the Irminger Sea? The thickness of the layer affected by the *LSW* and *IcSW*, between $\sigma_{1.5}$ = 34.58 and 34.70 kg m^{-3}, is about 1200 to 1900 dbar. Since the temperature and salinity minima in 1995, the mean salinity increased in this layer by 0.046 psu and the corresponding potential temperature increased by 0.54 °C. The temperature and salinity increase in the intermediate layer, which fills about 40% of the water column, is responsible for roughly half the rise of 0.04 psu and 0.6 °C in the depth-average series.

The Subpolar Mode Water (*SPMW*) is another main contributor to the observed change in the Irminger basin. The subsurface *SPMW* temperature and salinity showed multi-decadal changes, with a steadily increasing trend since the mid 1980s. Assuming that the increase in the upper 200 m was similar in magnitude, as is suggested by Figure 3.7, the rise in temperature and salinity in the upper 500 m explains about one third of the rise in temperature and nearly half of the rise in salinity observed in the depth averaged series. The change in *SPMW* properties mainly reflect changes in atmospheric forcing, especially the wind conditions over the northern North Atlantic (Figure 3.8, lower panel).

The remaining part of the integrated variability in the central Irminger Sea (about 20%) is caused by changes in the deeper waters. Of these deeper waters, the North East Atlantic Deep Water (*NEADW*) also has a signal of an initial decrease in temperature and salinity (until 1998) followed by an increase and thereby add to the recent overall rise in temperature and salinity. Again, the *LSW* may be indirectly responsible for the temporary salinity and temperature minimum at deeper levels. The *NEADW* can pick up this signal from the *LSW* when Iceland Scotland Overflow Water moves west through the Charlie-Gibbs Fracture Zone. The densest water, Denmark Strait Overflow Water (*DSOW*), mainly adds to the inter-annual variability, since it does not show decadal trends since 1990. The inter-annual variability of the *DSOW* appears to be recognizable in Figure 3.26, with the three salinity and temperature minima (and density maxima) in 1995, 1999 and 2004 visible as smaller depressions (peaks) on top of the long-term trend. However, this inter-annual signal does not originate from the lower layers, rather it seems to be caused by the occasional presence of meso-scale variability (warm core eddies) in the upper 500 m of the Irminger Sea. The contribution of the *NEADW* and *DSOW* to the change in the vertically averaged properties are relatively small due to the relatively thin layer they inhabit, but that does not make their variability unimportant. The *NEADW* and *DSOW* are important for the properties of North Atlantic Deep Water. Together with the lower *LSW*, they determine the properties of the Deep Western Boundary Current, which moves southward from the Labrador Sea along the American continent.

B. Forcing processes behind the variability

The North Atlantic Oscillation or NAO (Hurrell (1995)) is often mentioned in relation to changes in the dynamic properties of the North Atlantic Subpolar Gyre (Bersch *et al.* (1999), Curry & McCartney (2001), Dickson *et al.* (2003), and Häkkinen & Rhines (2004)). The pressure dipole over the North Atlantic Ocean and its associated wind pattern is without doubt important to the ocean circulation and the Subpolar Gyre in particular. However, the North Atlantic Oscillation index is based on the pressure difference between two fixed locations. Therefore, shifts in the location of the core of the high and low pressure areas away from the NAO index stations, may lead to changes in the NAO index that are not necessarily correlated with changes in the strength of the wind stress curl. Furthermore, concerning large gyre changes, the ocean does not respond instantaneously and rather works as a integrator of the atmospheric forcing (Curry & McCartney (2001)). Low-pass filtered time series of atmospheric forcing and Subpolar Mode Water responses show considerable multi-decadal variability, which are well correlated (Figures 3.8). The winter NAO index appears, on the long term, to be well correlated with the wind stress curl over the Irminger Sea (Figure 3.27) and can give a first indication of the type of circumstances during a winter. However, the correlation between the annual wind stress curl and NAO index is not so good. In order to explain short term changes, one should also look at the forcing itself at the time and location of interest. That is why, parameters such as the wind stress curl and upward heat flux were used in this chapter to study the observed changes rather than the winter NAO index.

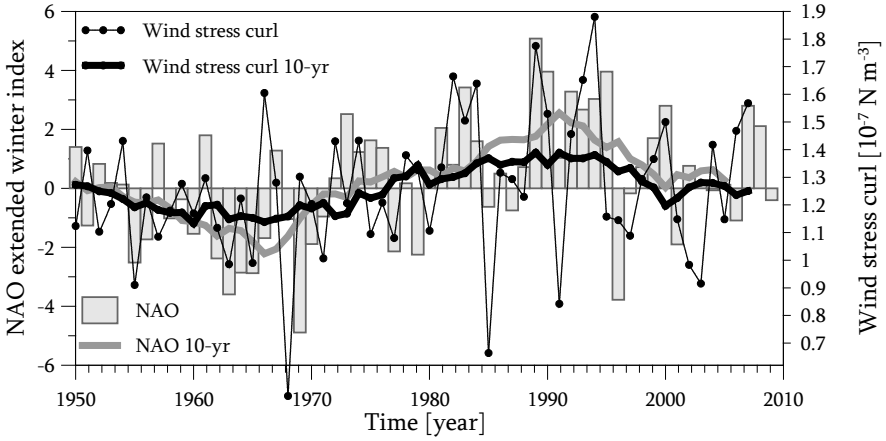

FIGURE 3.27: Relation between the NAO index and the annual mean wind stress curl over the Irminger Sea. The annual NAO extended winter indices are displayed in the bar graph and their 10-year running mean is drawn with the thick grey line. The annual mean wind stress curl over the Irminger Sea is drawn with the thin black line and black dots. The 10-year running mean of the wind stress curl is drawn with the thick black line

On average, the Labrador and Irminger Sea lose heat to the atmosphere by air-sea interaction (Chapter 2). Apparently, warming of the Subpolar Mode Water and Labrador Sea Water in these basins can only be driven by advection of warmer water. As has been described in this chapter, the likely candidates are the Icelandic Slope Water for the heating at intermediate levels and the shallower warm and saline cores in the Irminger and East Greenland Currents for the warming of the upper layers. It can be argued that long-term modulation of the wind stress curl, connected with NAO variations (Figure 3.27) will lead to a modulation of the location of the North Atlantic Current (Hátún *et al.* (2005)) and of the strength of the circulation in the Subpolar Gyre (Häkkinen & Rhines (2004)), including its warm and saline boundary currents. A multi-decadal variation of the advective heat input into the northwestern North Atlantic Ocean, which is cooled by the atmosphere, may lead to a multi-decadal variation in the mean temperature. *Hátún et al.* (2005) attribute the recent salinification and warming of the Irminger Sea to an increase in the North Atlantic Current, which feeds the Irminger Current. Such a multi-decadal temperature variability, nearly in phase with the wind stress curl and NAO index, is the dominant signal in the upper 2000 dbar of the Labrador and Irminger Seas (upper panels of Figure 3.5 and 3.6). The LSW_{94} happens to have been formed when the atmosphere-driven multi-decadal temperature oscillation was at its minimum (or was itself part of this cycle).

Another, simpler hypothesis tries to explain temperature changes in the Labrador Sea from changes in the heat flux only. This very simple model assumes that advection of heat into the Labrador Sea is constant (independent of the changes in the wind stress curl) and that the heat loss to the atmosphere is distributed over a layer of 2000 dbar depth by convective mixing. The change in temperature (ΔT_{atm}) in one year (Δt) due to the heat loss to the atmosphere (Q_{tot}) is determined by:

$$\Delta T_{atm} = (-Q_{tot} / H \cdot \rho \cdot C_p) \cdot \Delta t \qquad (3.1)$$

In which H is the depth over which mixing takes place (2000 m), ρ is the density and C_p is the specific heat of seawater. The total (yearly) change in temperature (ΔT) is the change due to the sea-to-air heat loss plus the constant advection term (ΔT_{adv}):

$$\Delta T = \Delta T_{atm} + \Delta T_{adv} \qquad (3.2)$$

The temperatures calculated in the model at any particular year *i*, is the temperature observed at the start of the record in 1950 ($T_{obs}(1950)$) plus the sum of the temperature changes between 1950 and year *i*. For the observed temperature record the mean temperature between 500 and 2000 dbar of the extended Labrador Sea series (Figure 3.5) is used. This depth interval was chosen in order to obtain the signal of the tem-

perature oscillation in the upper 2000 dbar without the seasonal signals of the upper layer. Temperatures in years without observations are interpolated. For the atmospheric heat flux the annual mean total heat fluxes derived from the NCEP reanalysis, as described in Chapter 2, were used. No smoothing is applied in either series.

Model temperatures were calculated for two different values of the advective heat flux. For the first value we assume that the advection balances the heat flux to the atmosphere. Since the change in temperature between 1951 and 2002 is negligible (0.01 °C), the mean heat flux over this period (68.2 W m^{-2}) is compensated by an advective heating of 0.263 °C $year^{-1}$. The second advection constant is tuned to fit the observed temperature record as much as possible. This led to a constant advective heating of 0.25 °C $year^{-1}$, which equals a mean heat flux of 64.8 W m^{-2}. Both resulting model temperature series are shown in Figure 3.28. As expected, the model temperatures based on compensating advection match the observed temperatures at the beginning and the end of the record. However, the rise in temperature between 1950 and 1970 is overestimated, leading to a positive temperature bias in most of the remaining record. The model temperatures based on the tuned advection follow the observed temperatures quite closely between 1950 and 1990. However, the model overestimates cooling between 1990 and 1994 and shows nearly no warming after 1994, contrary to the observations.

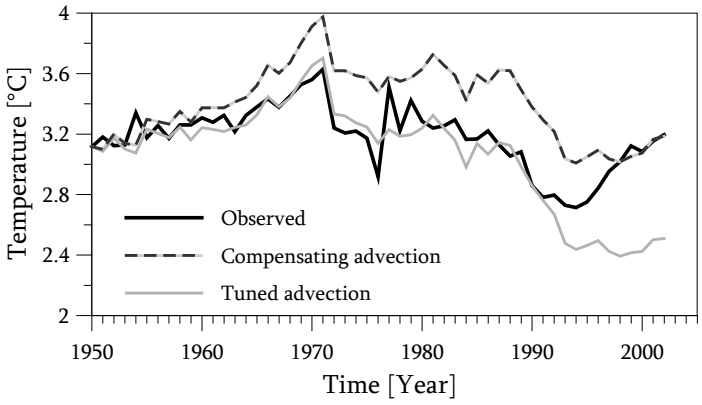

FIGURE 3.28: Time series of observed and modelled temperatures in the Labrador Sea. The observed temperatures are based on the mean temperature between 500 and 2000 dbar in the extended Labrador Sea series. The modelled temperatures assume that the annual heat loss to the atmosphere (from NCEP reanalysis) is distributed over the upper 2000 dbar and that the cooling by the atmosphere is compensated by advective heating. For the compensating advection it is assumes that the advection equals the mean heat over the record. For the tuned advection the advection constant is lowered until the modelled temperatures fit the observations for most of the record.

The difference between the advective heating in both models is quite small (less than 4 W m^{-2}) and both modelled series catch the observed temperature variability with quite some detail. Apparently, the heat flux is able to determine a large part of the temperature changes in the Labrador Sea and the successive formation events of Labrador Sea Water mainly work to distribute the heat loss over the water column. The mismatch between the tuned model and the observations after 1990 could be explained by the modulation of the inflow of North Atlantic Current water described by *Hátún et al.* (2005). The extra warming due to the inflow of warmer water is clearly missing after 1990. The relative importance of the heat flux and the wind stress curl is not a settled matter in our opinion and needs further investigation.

C. Temporal and spatial aliasing

Another problem that remains with the observed variability is the aliasing of small scale temporal and spatial variability onto the near annual hydrographic surveys. Some near-bottom water masses with a relatively small volume, such as the Icelandic Slope Water, remain under-sampled. Other, highly variable water masses, such as the Denmark Strait Overflow Water (Dickson *et al.* (2008)), bring forth seemingly multi-annual oscillations (Figure 3.24 and Dickson *et al.* (2003)) in the survey data that in fact may be taking place on much shorter time scales. To evaluate the significance of the observed annual variability one should also know the range of the meso-scale variability of these low-volume water masses. The survey data are more reliable for basin-wide changes, such as the variability of the Irminger Gyre (e.g. Figures 3.8 and 3.10), or for large volumes of water, such as the Labrador Sea Water class of 1994, since averaging filters out eddy variability. High frequency measurements of the moorings that were located in the Irminger Sea may reveal the nature and intensity of this short term variability. These will be discussed in the next chapter.

Chapter 4

Variability on sub-annual time scales as observed in the five year long records of two LOCO moorings in the Irminger Sea

4.1 Introduction

Although the WOCE AR7E repeat surveys give insight into the inter-annual and decadal variability of the northern North Atlantic, they only occasionally allow a glimpse into the variability on shorter time scales. Mostly these glimpses comprise of meso-scale features such as eddies and intrusions, which are recorded by one or more stations in a survey and are easily recognizable due to their typical "footprint" on the survey or hydrographic profile. Other, larger scale, changes are usually attributed to the inter-annual variability, since their evolution can not be monitored by the annual cruises. This means that the inter-annual time series contains aliases of intra-annual (seasonal and shorter) signals.

However, occasionally more than one survey traverses the Irminger Sea in one year. In 1991 there were three surveys, by the Tyro in April, by the Charles Darwin in August and by the Meteor in September. Together these surveys do give some insight into changes on seasonal time scales. They registered significant changes in the stratification in the centre of the Irminger basin (Figure 4.1). The density profiles observed through spring and summer of 1991 suggest that the upper 1000 m of the water column in the centre of the Irminger basin was subject to homogenization during winter (seen in the Tyro profiles in Figure 4.1) and restratification in late spring and summer (seen in the Darwin and Meteor profiles in Figure 4.1). The salinity profiles indicate that the restratification is not solely due to heating of the upper layers in summer, but also due to an increased salinity stratification. These warmer, saltier upper waters originate from the saline boundary currents of the basin (Figures 2.3 & 3.12). This seasonal variability in density and salinity in the Irminger Sea is very similar to the convection and restratification process described by *Marshall & Schott* (1999) and observed in the Labrador Sea (the Lab Sea Group (1998)). In the Labrador Sea this process description applies to the formation of Labrador Sea Water. In the Irminger Sea, however, there is still much discussion about the occurrence of deep convective mixing and its effect on the local hydrography (Pickart *et al.* (2003)).

Observations from the Irminger Sea, like those made by the Tyro in 1991, inspired several plans to observe the variability on sub-annual time scales in the Irminger Sea using moored instruments. Moorings were deployed in this area by the Woods Hole Oceanographic Institution (WHOI), the Institute für Meerskunde in Kiel (IfMk) and the Royal Netherlands Institute for Sea Research (NIOZ). The WHOI moorings were deployed between August 2001 and August 2003 at two locations, one over the continental slope (near 40° W) and the other on the 3000 m isobath (near 39° W). Both moorings were fitted with an autonomous CTD (Conductivity, Temperature, Depth) profiler, which recorded hydrographic profiles along the mooring cable. Two NIOZ moorings, fitted with a similar device, were deployed in September 2003 near the 3000 m isobath at 39° W and at 36° W. The eastern mooring has been observing until September 2008 and has collected a 5-year long record. The western mooring was recently (October 2009) recovered with its 6th year of data and is currently recording its 7th year. The IfMk mooring records hydrographic parameters with separate instruments placed at 12 depths between the surface and 1000 m depth. It has been deployed near 40° W from September 2003 until present. Unlike the WHOI and NIOZ moorings it has a satellite connection on the surface buoy which allows it to transmit data to shore in real-time. Unfortunately, this satellite connection failed on several occasions and data from the upper few hundred meters were lost. This makes the combined record of the NIOZ moorings the longest "high frequency" observation from the Irminger Sea so far. The observations recorded during the first 5 years from the LOCO 2 and LOCO 3 moorings are described in this chapter.

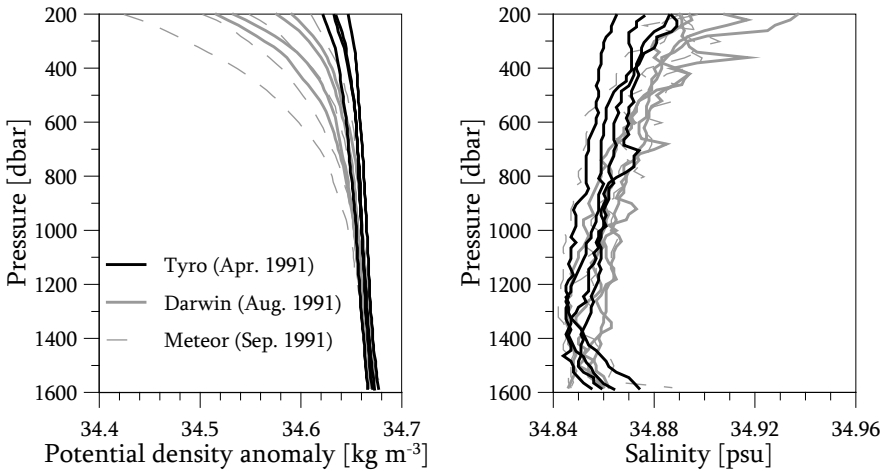

FIGURE 4.1: Potential density anomaly (relative to 1500 dbar) profiles between 36° W and 39° W in the Irminger Basin (left panel) and the corresponding salinity profiles (right panel). Profiles were observed by shipboard CTDs between April and September 1991.

The NIOZ moorings in the central Irminger Sea are part of the Long-term Ocean Climate Observations or LOCO program, which is an investment subsidy to facilitate Dutch contributions to the international CLIVAR (Climate Variability and Predictability) program. The moorings were placed on the 3000 m isobath in the Irminger Sea (Figure 4.2). The LOCO 2 location is near the centre of the cyclonic subpolar Irminger gyre, where the preconditioning is most favourable for convective mixing (it is where the weakest density stratification is found, for an example see Figure 2.5). The LOCO 3 location is further east, near the eastern rim of the Irminger Current. The continuous sampling by the moored instruments allows the process of convective mixing and restratification to be studied throughout the year. Thus, the continuous sampling by the mooring has an advantage over the annual hydrographic sections, which have nearly no winter coverage. A single mooring, however, offers little insight into the horizontal extent of the observed features. The two moorings together, combined with the annual section, give a more complete insight into the Irminger Sea variability than the individual observations taken separately.

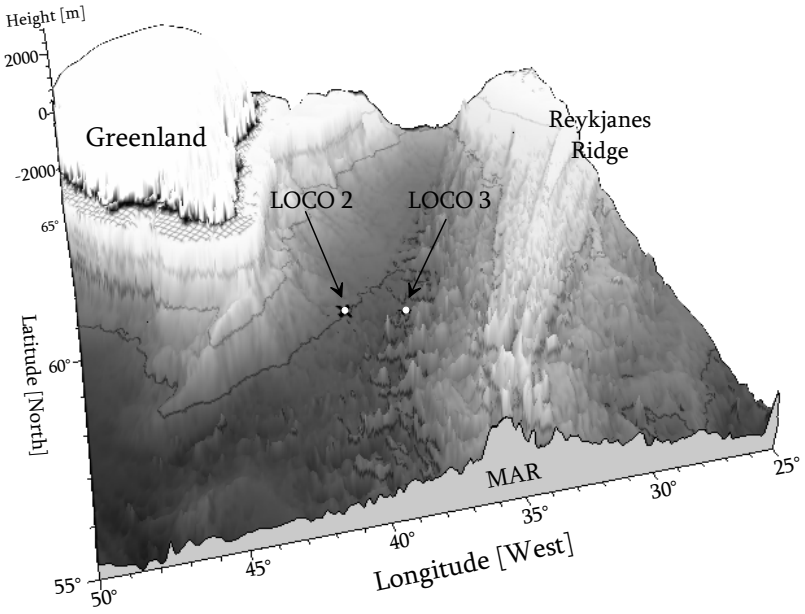

FIGURE 4.2: Topography of the Irminger Sea with the two NIOZ mooring locations. Darker colours indicate deeper depths and isobaths are drawn at 0, 200, 1000, 2000 and 3000 m. The shallow (< 200 m) continental shelf is hatched. Note the deep canyons near the Mid Atlantic Ridge (MAR) on the eastern side of the Irminger Sea. The topography data is derived from ETOPO1 (Amante & Eakins (2009)). The two mooring locations, near the 3000 m isobath, are indicated on the sea floor by the white dots.

In this chapter the fast variability in the Irminger Sea is described using the data collected by the LOCO moorings. The mooring design and the moored instruments are described in Section 4.2. Following, in Section 4.3, a report is given on the retrieved data, the data handling and calibration. In Sections 4.4 to 4.7 the variability is described by means of the mooring observations. The final part of this Chapter, Section 4.8, contains a summarizing discussion.

4.2 The LOCO moorings

4.2.1 Mooring deployments

The data set used in this thesis includes the five subsequent years recorded by two LOCO moorings between September 2003 and September 2008 in the Irminger Sea. The sixth year of the LOCO 2 deployment was recovered while this thesis was being finalised and this data is not included. All deployment information of the mooring is contained in Table 4.1. The western mooring, designated LOCO 2, is located at about 39° 31' W and 59° 12' N near the centre of the Subpolar Gyre. Originally the LOCO 2 mooring was placed slightly further to the northeast (at 39° 0' W and 59° 26' N), but its location was adjusted to be closer to the former WHOI mooring site as a way to extend the time series at this location. The mooring designated LOCO 3 was located on the eastern side of the Irminger Sea at 36° 23' W and 59° 15' N, near the warm Irminger Current (Figure 2.5). It is also closer to the rugged topography of the Mid Atlantic Ridge (Figure 4.2). The horizontal distance between the moorings is about 180 km. Both mooring locations have their pros and cons. The LOCO 2 site is closer to Greenland and the centre of the gyre, where the heat loss to the atmosphere is expected to be largest and the stratification in the near-surface layer is relatively weak. At the LOCO 3 site the water column is somewhat more homogeneous at mid-depth. However, the near-surface layer is much more strongly stratified. The eastern part of the basin is also subject to stronger restratification by eddies, due to the proximity to the Irminger Current and the Subpolar Front. The strong topography near the MAR is expected to influence (steer) the near bottom currents.

The two LOCO moorings were serviced annually. This occurred during the AR7E survey cruises of the Pelagia in 2003, 2005 and 2007, of the Charles Darwin in 2004 and of the Discovery in 2006 and 2008. All these cruises took place in late summer or early autumn (Table 3.1 and Table 4.1), but the exact timing varies between years. Therefore the moored instruments were programmed for a sample rate which would last for a minimum of 400 days before the batteries were depleted. This duration was exceeded only once, during LOCO 3-1 (Table 4.1), but without battery failure.

TABLE 4.1: Mooring deployment information. Date of deployment and recovery, duration of the deployment in days, latitude and longitude in degrees and decimal minutes and the uncorrected depth in meters.

Designation	Deployment	Recovery	Duration	Latitude N	Longitude W	Depth
LOCO 2-1	30 Sep 2003	01 Oct 2004	399	59° 25.78'	39° 00.09'	3000
LOCO 2-2	04 Oct 2004	15 Sep 2005	349	59° 12.21'	39° 30.48'	3041
LOCO 2-3	15 Sep 2005	24 Aug 2006	344	59° 12.20'	39° 30.48'	3054
LOCO 2-4	27 Aug 2006	11 Sep 2007	381	59° 11.76'	39° 30.61'	3037
LOCO 2-5	11 Sep 2007	10 Sep 2008	366	59° 11.91'	39° 31.87'	3045
LOCO 3-1	28 Sep 2003	05 Oct 2004	405	59° 14.21'	36° 23.84'	3021
LOCO 3-2	05 Oct 2004	14 Sep 2005	345	59° 14.00'	36° 25.61'	3035
LOCO 3-3	14 Sep 2005	28 Aug 2006	349	59° 14.90'	36° 24.08'	3073
LOCO 3-4	01 Sep 2006	09 Sep 2007	374	59° 14.21'	36° 23.98'	3034
LOCO 3-5	10 Sep 2007	14 Sep 2008	371	59° 14.76'	36° 22.20'	3036

4.2.2 Mooring design

Both moorings have a similar mooring design (Figure 4.3). The main mooring cable is a plastic coated steel cable with a diameter of 9 mm. The top buoyancy remains at a depth of about 100 m below the surface to avoid damage by strong wave action, passing fishing ships with trailing nets and icebergs. The buoyancy float is fitted with an ARGOS transmitter beacon and with a downward looking 75 kHz Acoustic Doppler Current Profiler (ADCP), which measures the currents in the 500 m below the ADCP. A second buoyancy float is fitted in the mooring some 30 m below the top float. Together the floats provide enough buoyancy to lift the mooring to the surface upon release and to keep it reasonably upright in strong currents. The stretch of cable between the second float (at a depth of about 130 m) and 2400 m is the domain of the McLane Moored Profiler (MMP). The MMP records vertical hydrographic profiles over this depth interval. Bumpers are fitted to the cable at each end of its domain as a safety, to stop the MMP if it does not stop at the pre-programmed pressure level. Below the lower bumper, at a depth of 2500 m, a downward looking ADCP is mounted to the cable. This ADCP monitors the currents in the bottom 500 m of the water column. The last observing instrument, a Sea Bird Electronics (SBE) Microcat type 37-SM, is fitted to the cable at about 10 m above the bottom. The Microcat records the hydrographic variables at this depth. The end of the mooring cable is attached to the bottom weights via two acoustic Ixsea Oceano releases.

4.2.3 RECORDING INSTRUMENTS

The ADCPs, obtained from Teledyne RD Instruments, are 75 kHz Workhorse Long Ranger ADCPs. The casing of the two lower ADCPs is thicker than that of the standard model in order to withstand the 3000 dbar pressure. Each ADCP has four acoustic transducers that are convexly oriented with a 20° angle with respect to the instrument's central axis. From the combinations of the four beams the horizontal and vertical velocity components are calculated. The beam width is 4°, which assures that the sample areas of the four beams do not overlap. The transducers send out a 75 kHz signal or ping. The signal reflects on scatterers present in the water and is received by the transducers. The Doppler frequency shift in the received signal is determined to obtain the velocity. Data from several pings are collected in an ensemble, with a larger number of pings increasing the accuracy of the measurement. A velocity profile is recorded by sampling the velocities at different distances from the transducers, equal to differentiating between different time lags between the ping and the received signals. The vertical layers in which the water is sampled are called bins. The number and size of the bins determines the vertical resolution of the velocity profile. Typical deployment settings for the LOCO ADCPs are a sample or ensemble interval of 15 or 20 minutes and 12 pings per ensemble. This setting ensures a standard deviation or uncertainty of the ensembles of 1.2 cm s^{-1}. The velocity profile contains 80 bins of 8 m depth or 64 bins of 10 m depth, covering roughly 600 m. However, the received intensity of the furthest bins is usually too low, making the actual obtained range about 500 m.

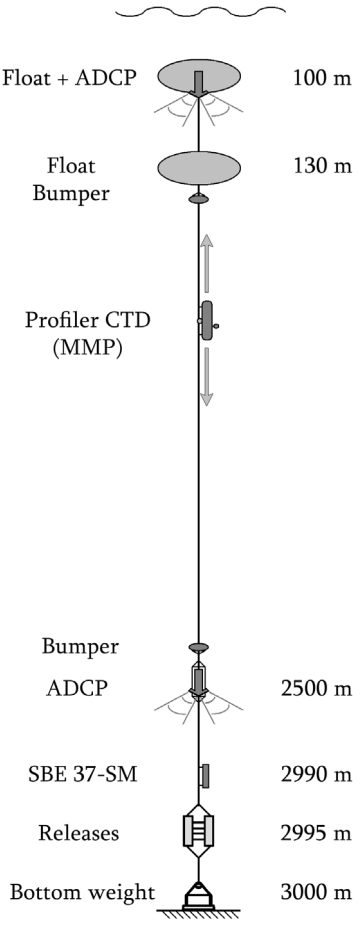

FIGURE 4.3: Schematic of the LOCO mooring design. The positions of the various instruments are indicated in the figure.

The McLane Moored Profiler (MMP) is an autonomous CTD profiler which records profiles of conductivity, temperature and pressure along the cable between pre-programmed depths (in this case about 140 dbar and 2400 dbar). The movement along the cable is provided by a small electric motor driving a wheel pressed to the cable with a spring. The MMP usually takes about 2.5 hours to cover the distance between the top and bottom. The profiler is allowed to stop when it gets within 60 dbar of the programmed pressure levels or, when it does not reach the programmed stop level, after a certain amount of time. If an obstacle is met along the way, often caused by bio fouling (e.g. a squid resting on the cable), the MMP backs up and goes forward again in order to try to ram through the obstacle (or scare it away). This is attempted a maximum of 6 times, after which the instrument is turned off if the last attempt was not successful. The LOCO MMPs are equipped with a EMCTD sensor from Falmouth Scientific Inc., which has a specified accuracy of 0.005 °C in temperature, 0.0005 S m^{-1} in conductivity and 0.05% of the full scale pressure, sampling at a frequency of 1.83 Hz. With the speeds achieved by the MMP this results in at least 8 samples per dbar. In order to allow the batteries to endure until recovery, the profiler was set to traverse the cable once per day. Thus, top-to-bottom and bottom-to-top profiles alternate in the resulting time series.

Finally, the SBE 37-SM Microcat is a small CTD sensor which can easily be fitted on the cable with clamps. It has a fast sampling and storage capability and records temperature, conductivity and pressure with high accuracy (0.002 °C, 0.0003 S m^{-1} and 0.1% of the full scale pressure respectively). The SBE 37-SM Microcats sample at a frequency of 2.6 Hz and were programmed to log ensemble measurements at 3 or 5 minute intervals. Through the rest of the thesis the SBE 37-SM Microcats will be simply referred to as the Microcats.

4.3 Data

4.3.1 Retrieved data

The ADCP data set consists of velocity profiles, which are build up of ensembles for 80 bins of 8 m depth, or 64 bins of 10 m depth at each time interval. Additionally, the instrument records pressure, temperature, reflectivity and the orientation of the instrument. Pressure sensors of the bottom ADCP in the LOCO 2 mooring failed on 2 occasions, during the first and second deployment. All other pressure recordings were without incident. The ADCPs themselves functioned without problems for nearly all deployments. There were only two exceptions. The bottom ADCP in the first LOCO 3 deployment only recorded velocities for the upper 7 bins (56 m) and the top ADCP in the fifth LOCO 3 deployment recorded for about 1 minute and then stopped.

NIOZ employed the McLane Moored Profilers (MMP) for the first time in the Irminger Sea LOCO moorings. The data retrieval is generally good (full top to bottom profiles) during the first few months of the deployments and gradually decreases as time expires due to lowered battery capacity and bio-fouling of the cable. Most deployments achieved a data recovery of over 80% (Table 4.2), but on three occasions the data recovery was significantly lower. Only one of these, during the fourth deployment of LOCO 2, was due to a technical failure of the device. An electrical cable was exposed to sea water due to chafing of the plastic cable cover, which caused a shortcut well before the end of the deployment. On the two other occasions the MMP was trapped on the cable by an unknown obstacle for long periods of time, and therefore could not complete its profiles.

The Microcats recorded temperature and conductivity during all deployments, but suffered several broken pressure sensors. During LOCO 2-2 the pressure sensor broke after 8 months. During the third deployment both the sensor in the LOCO 2 and in the LOCO 3 mooring malfunctioned, after 3 and 6 months respectively. For these instruments the nominal pressure was used to determine the salinity and potential temperature. The broken LOCO 2 Microcat was replaced by an intact Microcat for the next deployment, but due to lack of a second replacement instrument the LOCO 3-4 mooring was redeployed without a Microcat.

TABLE 4.2: Performance in data recovery of the LOCO MMPs. The data recovered is calculated by dividing the number of 1 dbar bin samples in the total record by the maximum possible number of samples (number of days in the deployment × the length of the longest profile in the deployment in dbar).

Designation	First profile	Last Profile	# of profiles	Data recovered	Remarks
LOCO 2-1	03 Sep 2003	01 Oct 2004	394	89%	
LOCO 2-2	05 Oct 2004	15 Sep 2005	345	88%	
LOCO 2-3	16 Sep 2005	24 Sep 2006	342	81%	
LOCO 2-4	28 Sep 2006	14 Apr 2007	299	53%	Electrical short cut
LOCO 2-5	12 Sep 2007	10 Sep 2008	364	83%	
LOCO 3-1	29 Sep 2003	05 Oct 2004	403	95%	
LOCO 3-2	06 Oct 2004	13 Sep 2005	343	44%	Bio fouling
LOCO 3-3	14 Sep 2005	29 Aug 2006	349	98%	
LOCO 3-4	02 Sep 2006	09 Sep 2007	372	21%	Trapped near top
LOCO 3-5	11 Sep 2007	14 Sep 2008	369	98%	

4.3.2 DATA HANDLING

The Acoustic Doppler Current Profiler data was processed as follows. The direction of the horizontal flow, as recorded by the internal compass of the ADCP, was corrected for the local magnetic deviation (about 25° West). After this correction, the magnitude and direction of the flow were decomposed into its east and north component. Due to friction the mooring line is occasionally dragged away from its vertical position in strong currents. This sideways drifting of the mooring line also results in a downwards displacement of the ADCPs (Figure 4.4). When available, the depth of the recorded bins was corrected for the depth of the instrument as recorded by the pressure sensor. The maximum encountered excursion of the ADCP was 420 m, a displacement of 52 bins. In order to remove sub-tidal noise, the velocity components were filtered using a running mean filter with a window of 3 hours. The tides were removed by applying 2 running mean filters, with windows of 24 and 25 hours, subsequently. With the two filtered time series, the tides were separated from the mesoscale and longer variability.

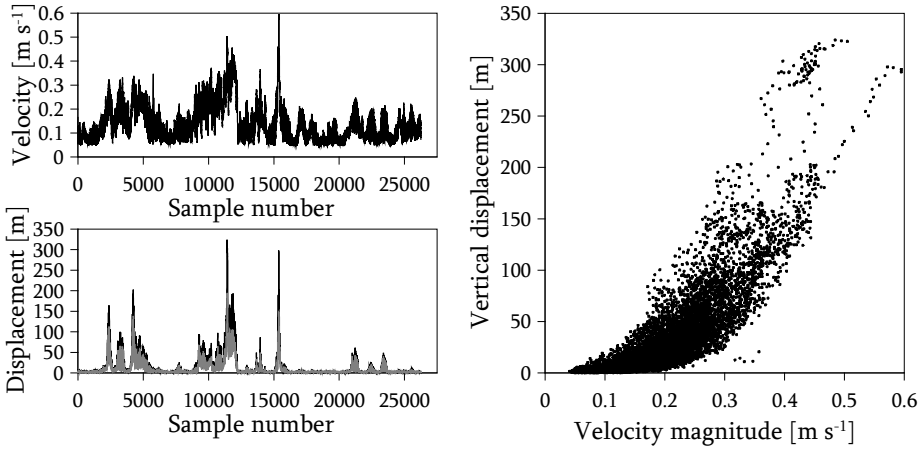

FIGURE 4.4: Example of the vertical displacement of a top ADCP during strong currents for one year of 15 minute data. The time series of the velocity of the horizontal currents at the top ADCP is shown in the upper left panel. The time series of vertical displacement of the top (black line) and bottom ADCP (grey line) are shown in the lower left panel. The right panel shows the displacement versus the current velocity.

The raw MMP data (temperature, conductivity and pressure at 1.83 Hz) were first despiked automatically and subsequently checked for remaining outliers by hand. Potential temperature, salinity, potential density and the Brunt Väisälä frequency were derived from the cleaned data. All data were collected in 1 dbar bins and averaged,

which strongly reduces small scale noise. The MMP data were calibrated using the CTD profiles, recorded at the time of deployment and recovery at the mooring location by the shipboard CTD. The biases between the MMP CTD and the ship's CTD were determined in the deeper parts of the water column, between 1750 and 2250 dbar, where the day-to-day variability is relatively small. For most biases it was assumed that the sensors drift was linear during the deployment of the MMP. These corrections were made for both temperature and salinity after which density was recalculated and checked for consistency with the CTD data and between subsequent deployments.

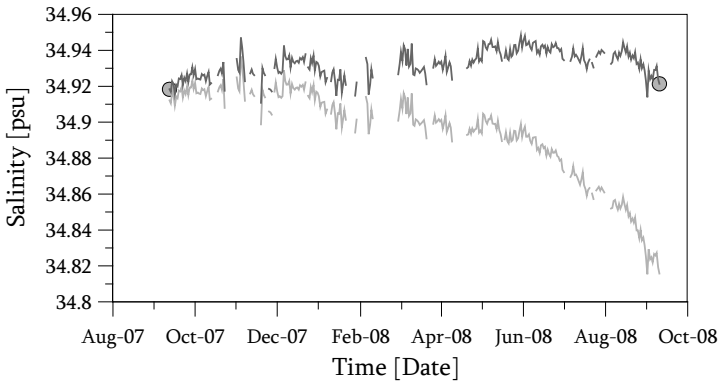

FIGURE 4.5: Salinity derived from the conductivity measurements by the MMP in the LOCO 2-5 deployment. Drawn are the mean salinity values between 1750 and 2250 dbar before (light grey line) and after calibration (dark grey line). The two circles represent the 1750-2250 dbar mean of the calibration CTD stations taken at deployment and recovery, which are assumed to be correct.

The maximum observed sensor drift over deployments LOCO 2-1 to 2-4 and LOCO 3-1 to 3-5 is 0.08 °C in temperature and 0.004 psu in salinity. However, during the fifth deployment of LOCO 2 the conductivity showed an exponentially increasing bias due to a damaged conductivity sensor. This bias has been corrected using a least squares exponential fit to the conductivity. After the correction of the conductivity with the fit the remaining small bias with the CTD profiles was removed assuming a linear trend. The original biased salinity series derived from the LOCO 2-5 conductivity, together with the corrected salinity and the ship's CTD data, are shown in Figure 4.5.

4.4 THE CURRENT STRUCTURE AT THE MOORING LOCATIONS: MEASUREMENTS BY ACOUSTIC DOPPLER CURRENT PROFILERS

The Acoustic Doppler Current Profilers observed the near-surface and near-bottom currents at the two mooring locations in de Irminger Sea. The total record length is 5 years for the top and bottom ADCP of LOCO 2. The bottom ADCPs in LOCO 3 recorded velocities in the upper 3 bins for all 5 years and filled the complete profile for 4 years. The top ADCP in LOCO 3 recorded 4 years. The sampling interval of 15 to 20 minutes allows for a separation of signals over a range of time scales, but not resolve turbulence. The fastest resolved signal is the tide, of which an example is shown in Figure 4.6.

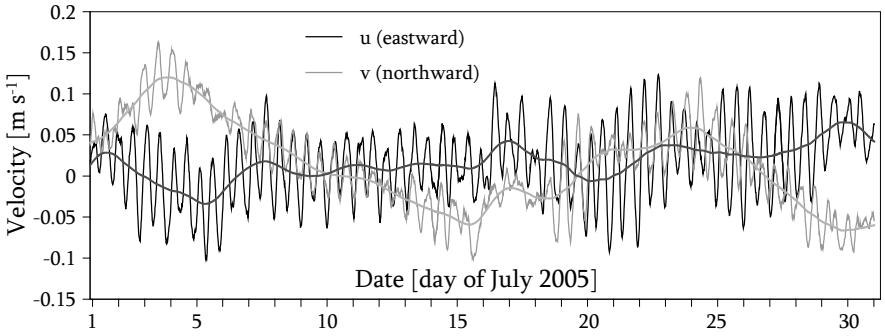

FIGURE 4.6: Eastward and northward velocity components at 200 m depth during one month recorded by the near-surface ADCP in the LOCO 2 mooring. Shown is the series including tides and daily variability (U & V), filtered only with a 3-hour running mean filter. Drawn over U & V are the series including only the daily variability (Udaily & Vdaily), filtered subsequently with a 24-hour and a 25-hour running mean filter.

The tides are not the main interest of this thesis. However, these back and forth moving currents are interesting from the perspective of aliasing. Therefore a short analysis of the tides is included here. This analysis of the tides was made using a harmonic analysis. For this analysis the velocities at about 2700 m depth were used, since they are least disturbed by the wind (near the surface) or friction (near the bottom). Three sets of time series are used in the analysis. The first set contains the 3-hour filtered series of eastward and northward velocities, *U* & *V* (Figure 4.6). The 3-hour window filter reduces sub-tidal noise, but leaves the signals of both the tides and the meso-scale variability intact. The second set of time series, *Udaily* & *Vdaily*, are the *U* & *V* series filtered with subsequent running-mean filters of 24 hours and 25 hours. This nearly completely removes the (semi-diurnal and diurnal) tidal cycles from the series, leaving only the meso-scale signals in the series (Fig. 4.6). The last set contains *Utide* & *Vtide*, which are assumed to include the daily tidal cycle only. They are the original series (*U* & *V*) minus the daily series (*Udaily* & *Vdaily*).

A least square harmonic analysis (Dronkers (1964)), using 144 tidal constituents representative for the Atlantic tides, was then performed on each one year *Utide* and *Vtide* series. Figure 4.7 shows the amplitudes of the low frequency constituents for the LOCO 2 and 3 one year series with the best tidal fit to highlight the major tidal constituents. For LOCO 2 the fourth year is shown, with a correlation *R* between the input signal *Utide* and the *Uharm* (composed by the tidal analysis) of 0.83 and between *Vtide and Vharm* of 0.60. For LOCO 3 the third year is shown, with a correlation between *Utide and Uharm* of 0.71 and between *Vtide and Vharm* of 0.34. These correlations are not strong enough to synthesize the tidal signal for the entire five year record, but the results of the tidal analysis do give some information about the nature of the tidal signal.

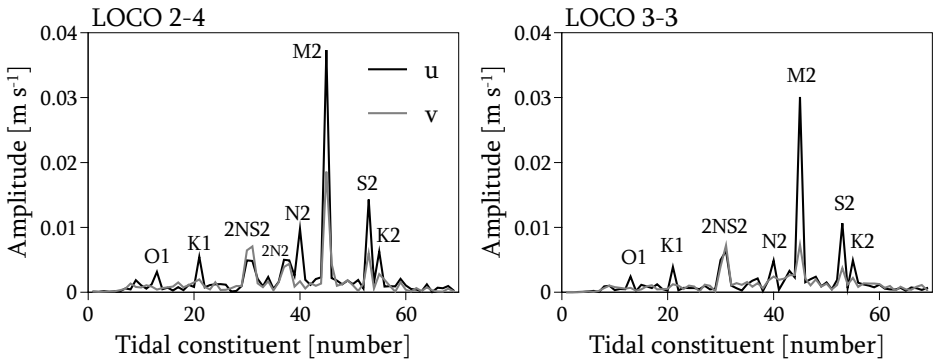

FIGURE 4.7: The amplitudes of the first 70 tidal constituents found in the LOCO 2-4 series (left panel) and the LOCO 3-3 series (right panel). The amplitudes found for Utide are drawn in black and the amplitudes found in Vtide are drawn in grey. The names of the tidal constituents with the largest amplitudes are denoted in the figure. The higher frequency constituents (71 to 144) have amplitudes < 0.001 m s^{-1} and are not shown for this reason.

TABLE 4.3: Root mean square (rms) velocities of the time series containing the tidal signal (Utide & Vtide) and of the times series containing the day-to-day variability (Udaily & Vdaily). The root mean square velocity of the magnitude ($M = \sqrt{(U^2 + V^2)}$) of the original series is also included.

ADCP	rms Utide [m s^{-1}]	rms Udaily [m s^{-1}]	rms Vtide [m s^{-1}]	rms Vdaily [m s^{-1}]	rms M [m s^{-1}]
LOCO 2 top	0.04	0.09	0.02	0.08	0.13
LOCO 2 bottom	0.04	0.08	0.03	0.07	0.12
LOCO 3 top	0.03	0.10	0.03	0.09	0.14
LOCO 3 bottom	0.04	0.06	0.03	0.04	0.09

It also tells us that the time series used for the harmonic analysis includes additional signals besides the tides, even after removing the daily to meso-scale variation. However, the diurnal lunar (M2) and solar (S2) tide are both clearly visible as the main contributors to the tidal signal at both mooring locations. At the LOCO 2 location, closer to the Greenland slope, more higher harmonics seem to add to the tidal signal. This is possibly due to generation of internal tides near the continental slope.

The root mean square velocities (Table 4.3) of the tidal and daily series indicate that the variability in the *Udaily* & *Vdaily* series (meso-scale without tides) is larger than the variability in *Utide* & *Vtide*, and probably has a larger effect on the variability of the hydrography. Root mean square velocities are about 0.09 m s^{-1} in the daily series and 0.03 m s^{-1} in the tidal series. Only the bottom ADCP in LOCO 3 has lower values for the daily variability. The meso-scale signals can be visualized by plotting the cumulative vector diagrams (Figure 4.8) derived from the daily mean velocities.

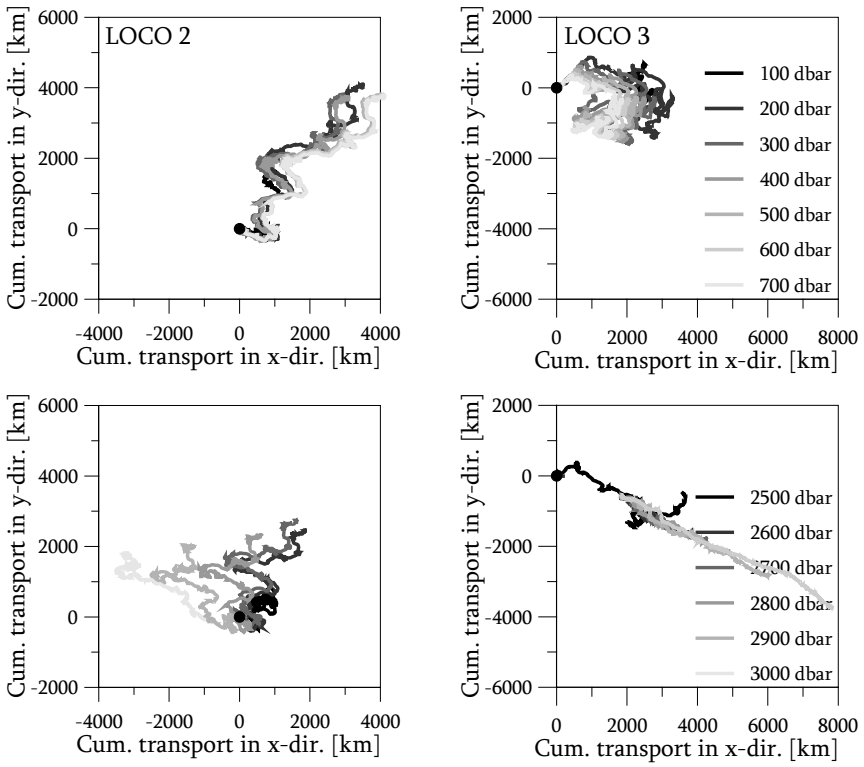

FIGURE 4.8: Cumulative transport by the daily mean velocity for the four ADCP locations. The upper panels contains near-surface transports and the lower panels contains near-bottom transports at the LOCO 2 (left panels) and LOCO 3 (right panels) mooring. The initial position is indicated by the black dot.

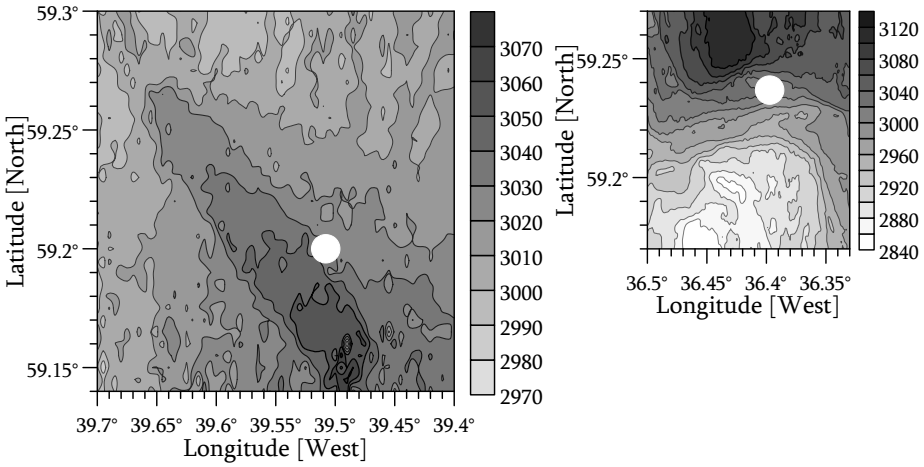

FIGURE 4.9: Local topography at the mooring positions as measured by the multibeam of the Pelagia. The topography at the approximate locations of the LOCO 2 mooring (for deployments 2 to 5) is shown in the left panel. Similarly the topography at the approximate LOCO 3 location (for all five deployments) is shown in the right panel. The mooring positions are indicated with a white dot in each panel.

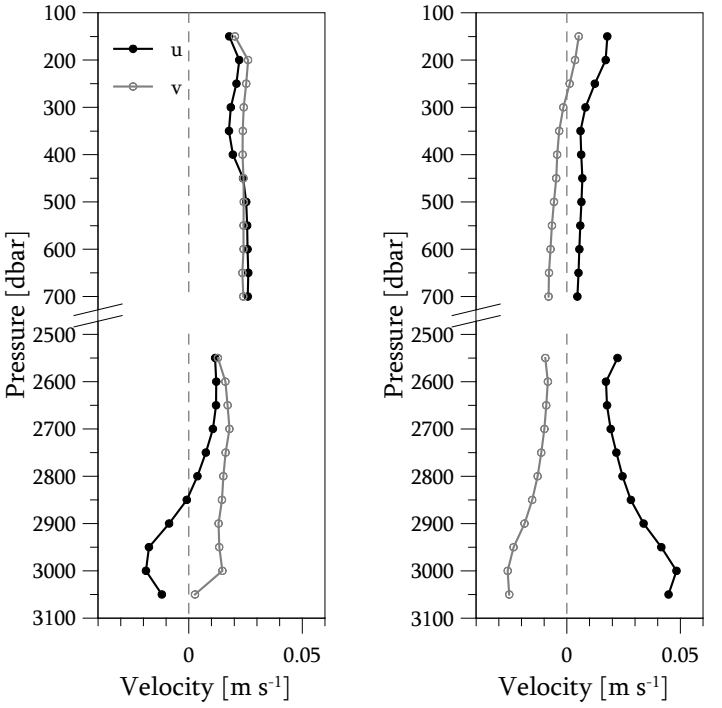

FIGURE 4.10: The mean vertical profiles from the four ADCP locations. The left graph contains the near-surface and the near-bottom mean profiles for the western mooring, LOCO 2. The right graph contains the mean profiles for the eastern mooring, LOCO 3. Northward currents (V) are drawn in grey and eastward currents (U) are drawn in black.

The large correlations between the vertical layers observed at each ADCP location are clearly visible in this Figure. The current variability at eddy time scales, observed by the near-surface and the near-bottom ADCP in the LOCO 2 mooring, also show a very coherent behaviour although there does seem to be some directional shear near the bottom. This shear is likely due to the topographic steering (convergence/funnelling) by the small canyon close to the mooring location (Figure 4.9).

The coherence between the near-surface and near-bottom currents at the LOCO 3 location is much weaker. The currents near the surface at the mooring are strongly influenced by meso-scale eddies (Figure 4.8), which typically do not extend beneath 1000 m. These eddies are likely to originate from the front of the Irminger Current east of the LOCO 3 mooring. There seems to be little net transport near the surface, which indicates that the mooring is placed well outside the Irminger Current itself. In contrast to the near-surface layers, the near-bottom currents at the LOCO 3 site show relatively large net transports and very little directional (meso-scale) variability. Also, there appears to be a shear in the magnitude of the velocity, with the deepest currents going fastest. There is only some meso-scale variability in the shallowest level observed by this ADCP (~2500 dbar). This lack of directional variability is suspected to be caused by the steeply sloping topography near LOCO 3 or by funneling (convergence) of the currents by the local canyon.

Overall, the long-term mean velocities at the LOCO mooring locations in the Irminger Sea are quite small for ocean currents (Figure 4.10), and much smaller than the observed local tidal velocities. This indicates that the moorings were indeed deployed at their intended positions, which were near the centre of the Subpolar Gyre (LOCO 2) and west of the Irminger Current (LOCO 3). The northeastward currents at the LOCO 2 location seem to indicate that the mooring is positioned east of the centre of the cyclonic gyre. Also, the LOCO 2 moorings seems to be outside the (southward directed) flow of Denmark Strait Overflow Water (*DSOW*) although the near-bottom profile does indicate that there is an enhanced bottom current shear.

4.5 Temperature and salinity of the bottom waters: Microcat measurement

Near-bottom temperatures and salinities at the two mooring locations were monitored by the SBE 37-SM Microcats (at ~10 m height above the bottom). During the first deployments of the moorings it was intended that the Microcat of the western mooring, LOCO 2, would observe the properties of the *DSOW*. However, as indicated by the observed current direction (previous section), the LOCO 2 mooring was not placed in the core of the southwestward moving bottom flow of *DSOW*. Nevertheless,

the density observed at the LOCO 2 site (Figure 4.11) is sufficiently high to assume that the sampled water mass is mainly composed of *DSOW*. The LOCO 3 Microcat was located further to the east and thereby closer to the deeper parts of the North East Atlantic Deep Water (*NEADW*). However, the density observed at LOCO 3 (Fig. 4.11) shows a variability far exceeding the expected ranges of *NEADW* density changes. In fact, Figure 4.11 suggests that the density at LOCO 3 switches between a density close to the *DSOW* density observed at LOCO 2 and the lighter density class associated with *NEADW*. Various mixing products are observed between the dense and light states.

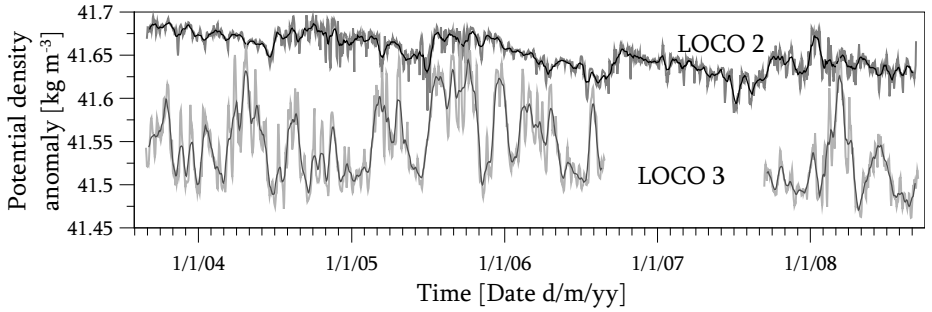

FIGURE 4.11: Potential density anomaly σ_3 as measured by the LOCO 2 and LOCO 3 Microcats. Shown are the daily mean σ_3 (grey lines) and the smoothed σ_3 (darker overlying lines), which are the daily means filtered with a 15-day running mean filter.

The nature of this "switching" is more clearly seen in a *θ,S*-diagram, as shown in the top panel of Figure 4.12. This panels shows two things. First, the variability in the LOCO 2 measurements, which we assume to be representative for the *DSOW*. These measurements show a large variability from year-to-year, mainly in salinity. Secondly, the LOCO 3 measurements illustrate the even larger variability in the east, which seems to be the result of mixing between the *DSOW* properties (observed by LOCO 2) and the properties in the *NEADW* core (as observed further east by the AR7E surveys). The fresher and saline branches seen in the LOCO 3 measurements reflect the *DSOW* salinity variations at LOCO 2, but mixed with different rates of *NEADW*. During the deployments 2-3 (in yellow, Fig. 4.12), 2-5 (in red) and part of 2-1 (in blue) the *DSOW* was predominantly saline and warm with respect to the bulk of *DSOW* samples. During this time the LOCO 3 samples formed the more saline branch between *NEADW* and *DSOW*. During the 2-2 (in green) and part of 2-1 deployment the *DSOW* was considerably less saline, forming the less saline branch in LOCO 3 samples. During the fourth deployment the Microcat on LOCO 3 was absent. An intermediate branch might have been formed during this deployment, since the LOCO 2-4 *DSOW* samples (in orange) are of intermediate salinity.

FIGURE 4.12: Variability of the bottom waters in θ,S-space.

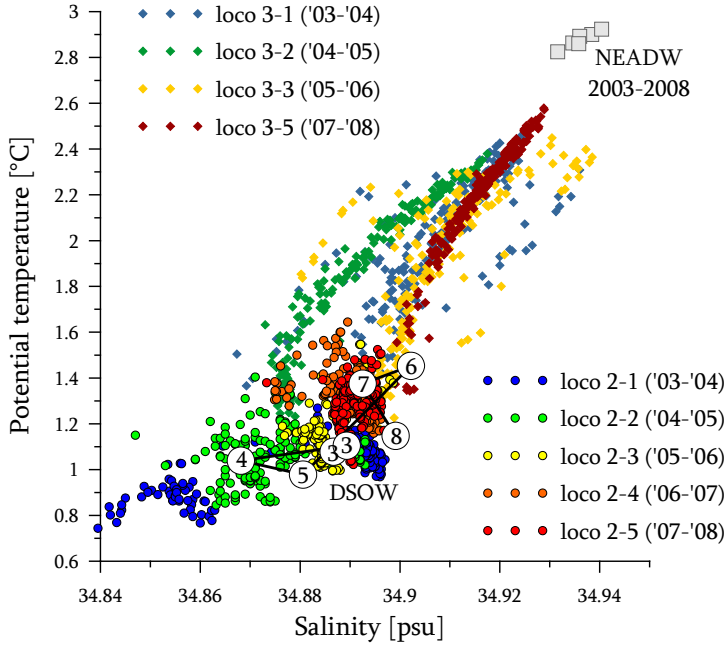

Top panel: The colored symbols illustrate the range of the Microcat observations. Each deployment is plotted in a different colour, with the LOCO 2 observations encircled by a black line. Also shown are the AR7E observations of the DSOW (NEADW) during the LOCO deployments with circles (squares). The numbers in the circles denote the year of observation (e.g. 3 = 2003).

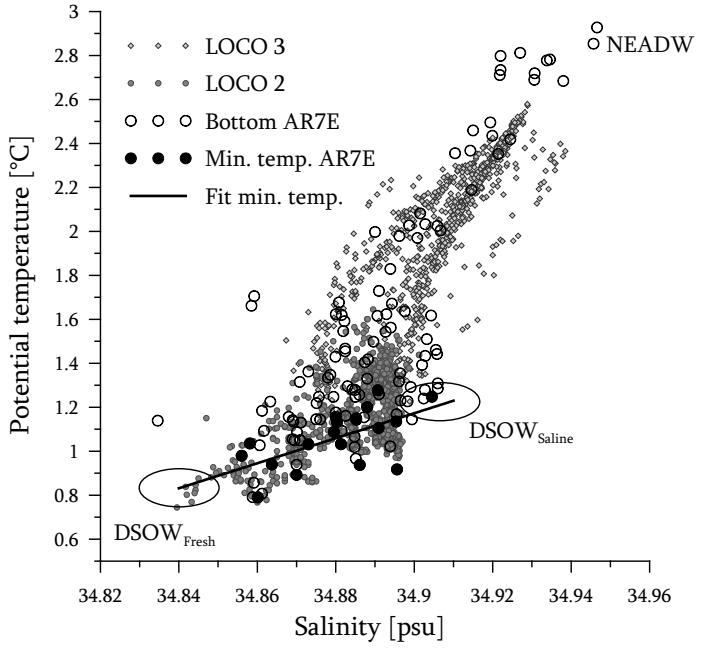

Bottom panel: The range of Microcat observations (grey symbols) versus the range of AR7E bottom observations since 1991 (open circles). The AR7E observation are from the area between 42 and 34 °W. The AR7E observations where the minimum temperature (DSOW) was encountered are plotted with black circles. The strait line is the fit of the minimum temperature observations.

The bottom panel of Figure 4.12 shows that the five years of θ and S observations from the LOCO moorings form an envelope around the AR7E bottom observations since 1991. Thus the *observed* short term (5 minutes to 5 years) variability is larger than the *observed* inter-annual variability in the 22 year long AR7E record. The similarity between the LOCO 2 observations and the series of minimum temperature (and the corresponding salinity) from the AR7E sections indicates that the LOCO 2 Microcat indeed samples the *DSOW*, despite of the fact that locally the currents are not directed southward. Together, the AR7E and the LOCO observations reinforce the impression of a mixing triangle between three water types, which was given by the top panel of Figure 4.12. Two types of *DSOW* seem to span the range in *DSOW* salinity and form the bottom of the triangle, while NEADW forms the top. We identify the *DSOW* types here as $DSOW_{fresh}$ at ~34.84 psu and $DSOW_{saline}$ at ~34.90 psu. The linear fit to the θ-minimum values corresponds to the 41.67 kg m^{-3} isopycnal (relative to 3000 dbar), thus both *DSOW* types are of similar density. The variability in *DSOW* from $DSOW_{fresh}$ to $DSOW_{saline}$ is assumed to originate from changes in the supply of source waters north of the sill. A large fraction of saline Atlantic Return Water creates $DSOW_{saline}$ and a larger fraction of fresher Polar Intermediate Water creates $DSOW_{fresh}$.

The salinity time series in Figure 4.13 indicates that the bulk of the *DSOW* measurements are of the more saline type. A short but strong pulse of fresh *DSOW* reached the LOCO 2 mooring in the summer of 2004. This fresher *DSOW* was somewhat cooler, as expected from Figure 4.12. The bottom water slowly returned to its former saline state over a period of nearly 2 years. During the same period the LOCO 3 measurements occupy the fresh branch in θ,S-space (Figure 4.12), which exhibits itself in the salinity time series as intermittent observations of the lower salinities (S < 34.89 psu in Figure 4.14) and cooler water. Although the potential temperature and salinity covary at LOCO 3, they do not compensate in density (Figure 4.11). The cause of the fast switching between warm-saline and cold-fresh water remains unclear. A significant correlation with the current direction or the velocity in the profiles from the LOCO 3 near-bottom ADCP was not found. Most likely, these θ-S changes are related to "sloshing" of the high density *DSOW* against the irregular topography of the MAR. Similarly, the annual cycle that is present in θ (Fig. 4.13), and through θ also in density (Fig. 4.11), at the LOCO 2 site remains unexplained. The timing of the large steps in θ and σ do not correspond to the timing of the yearly mooring/instrument replacements. Probably the signal is caused by a seasonal cycle upstream, most likely in Denmark Strait.

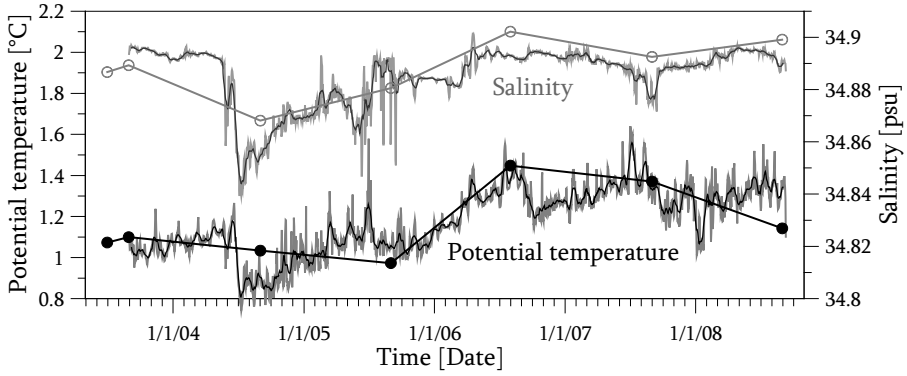

FIGURE 4.13: Salinity and potential temperature as measured by the LOCO 2 Microcat. Shown are the daily means (grey lines) and the smoothed properties (black lines), which is the daily mean filtered with a 15-day running mean filter. Plotted with dots over the Microcat measurements are the properties of the 100 m bottom layer at 39° W as observed in the CTD taken at the mooring location for calibration purposing during the AR7E surveys.

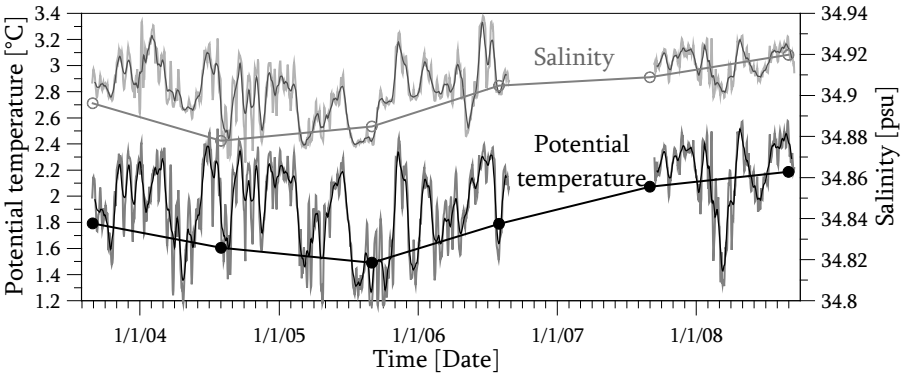

FIGURE 4.14: Salinity and potential temperature as measured by the LOCO 3 Microcat. Shown are the daily means (grey lines) and the smoothed properties (black lines), which is the daily mean filtered with a 15-day runningmean filter. Plotted with dots over the Microcat measurements are the properties of the 100 m bottom layer at 36° W as observed in the CTD taken at the mooring location for calibration purposing during the AR7E surveys.

Naturally, the Microcat measurements with a sampling interval of 3 to 5 minutes catches the variability of the bottom layer with a much larger detail than the near-annual AR7E surveys. This is illustrated by the thick lines plotted through the dots in Figures 4.13 and 4.14. They show the measurements of θ and S from the bottom layer (100 m) of the AR7E sections at the mooring locations (the calibration CTDs). Both figures show that, although the values observed in the AR7E sections are representative for the bottom layer, the highly variable signal is notably aliased to larger time

scales in the annual samples. From the AR7E time series alone one would estimate that the variability at both mooring locations is similar in magnitude and behaviour. However, we have already shown that the Microcat signals of these two moorings show very different behaviour. The inter-annual observations give no indication of the switching between the *DSOW* and *NEADW* like waters at LOCO 3 and the fresh-water pulse in 2004 at LOCO 2 is underestimated.

4.6. VARIABILITY IN THE HYDROGRAPHIC STRATIFICATION: PROFILING CTD MEASUREMENTS

The profiles recorded by the MMP (the profiling CTD) sample most of the main water masses in the centre of the Irminger basin. Only the *DSOW*, which resides in the near-bottom layer, is out of reach of the MMP and is therefore sampled with the Microcats. Figure 4.15 shows the mean θ,*S*-profile observed by the MMPs at the two mooring sites. The two Labrador Sea Water (*LSW*)classes as well as the upper *SPMW* and the deeper *NEADW* are indicated in the figure. The generally strong temperature stratification in the surface layer is not observed, as the MMP stops at 130 dbar.

Both LOCO moorings sample the Labrador Sea Water density classes, LSW_{94} and LSW_{2000}. The LOCO 3 moorings seems to be located closer to the remaining cores of the *LSW*. Assuming that the *LSW* flows round the Irminger Sea in a cyclonic fashion as shown by *Lavender et al.* (2000), the LOCO 2 mooring is indeed further downstream. Thus the *LSW* there has had more time to become progressively saline due to lateral mixing. The proximity to the warm and saline Subpolar Front is noticeable in the Subpolar Mode Water (*SPMW*) in the top of the profile of LOCO 3, while *SPMW* at the LOCO 2 location has clearly experienced significantly more cooling and freshening. The MMP profiles end at about 2400 m depth. Therefore the bottom waters are not represented in the (mean) profiles.

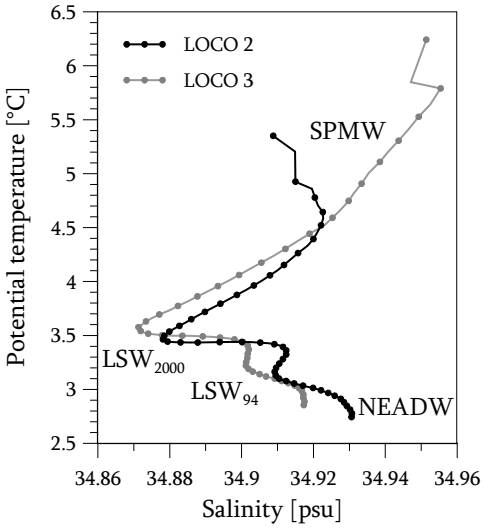

FIGURE 4.15: The time averaged θ,S-profiles from the CTD profiler (MMP) in the five deployments of LOCO 2 and LOCO 3. The two LSW cores are indicated in the figure. The dots are plotted at 50 dbar intervals.

4.6.1 Decay of the Labrador Sea Water

The gradual deepening and decay of the two LSW cores, as described in the previous Chapter, can be seen in the potential temperature and salinity time series of the MMPs (Figure 4.16, the two *LSW* cores are indicated in the lower left panel). At the start of the record the LSW_{2000} is recognizable in temperature as a colder and more homogeneous layer at around 1000 dbar depth, just above the 3.4 °C isotherm. During the first four years of the record the temperature slowly increases in this layer. At the same time, the salinity at this depth gradually increases, thus removing the low salinity signature of the *LSW*. The older, deeper LSW_{94} is mainly visible in salinity, as a second salinity minimum in the vertical profile at about 1600 dbar. The temperature stratification is also slightly reduced at this level. The LSW_{94} signature is strongly reduced compared to the late 1990's (see previous Chapter) and continues to decline. This salinity minimum has nearly disappeared at the end of the record. Also, the isotherms at the depth of LSW_{94} are more closely spaced (indicating a less homogeneous water column) towards the end of the record. Figure 4.16 and 4.17 show that this trend of deepening isothermals and isohalines, observed during the first four years, is halted during the last year. New layers, homogeneous in temperature, seem to have been formed at about 1000 dbar depth in this last year of the record. We will focus on this change later in this section.

As stated, the trends seen from the start of the record in 2003 to 2007 resembles the trends already observed in the AR7E observations. However, the local variability recorded by the LOCO MMP is much larger than one would estimate from the annual CTD surveys. Figure 4.17 shows both the time series observed by the profiler and the values obtained from the calibration CTDs, which are part of the annual surveys. The values shown are the mean salinity and potential temperature in the density layer of the LSW_{2000} ($34.58 \leq \sigma_{1.5} \leq 34.62$ kg m^{-3}) and the LSW_{94} ($34.66 \leq \sigma_{1.5} \leq 34.70$ kg m^{-3}). Despite the vertical averaging over the density interval, there is a large amount of fast variability in these time series. At the western mooring, LOCO 2, the variability is mostly daily variability and the meso-scale variability is small. Further east, at LOCO 3, the variability is composed of both daily variability and strong meso-scale variability, probably the eddies that were visible in the ADCP data. Again, much of this variability is missed by the annual sections.

4.6.2 Convective mixing and restratification

We now focus on the variability in the stratification of the water column and on the winter convective mixing. The daily vertical hydrographic profiles of the MMP are uniquely suitable to observe fast changes in the stratification.

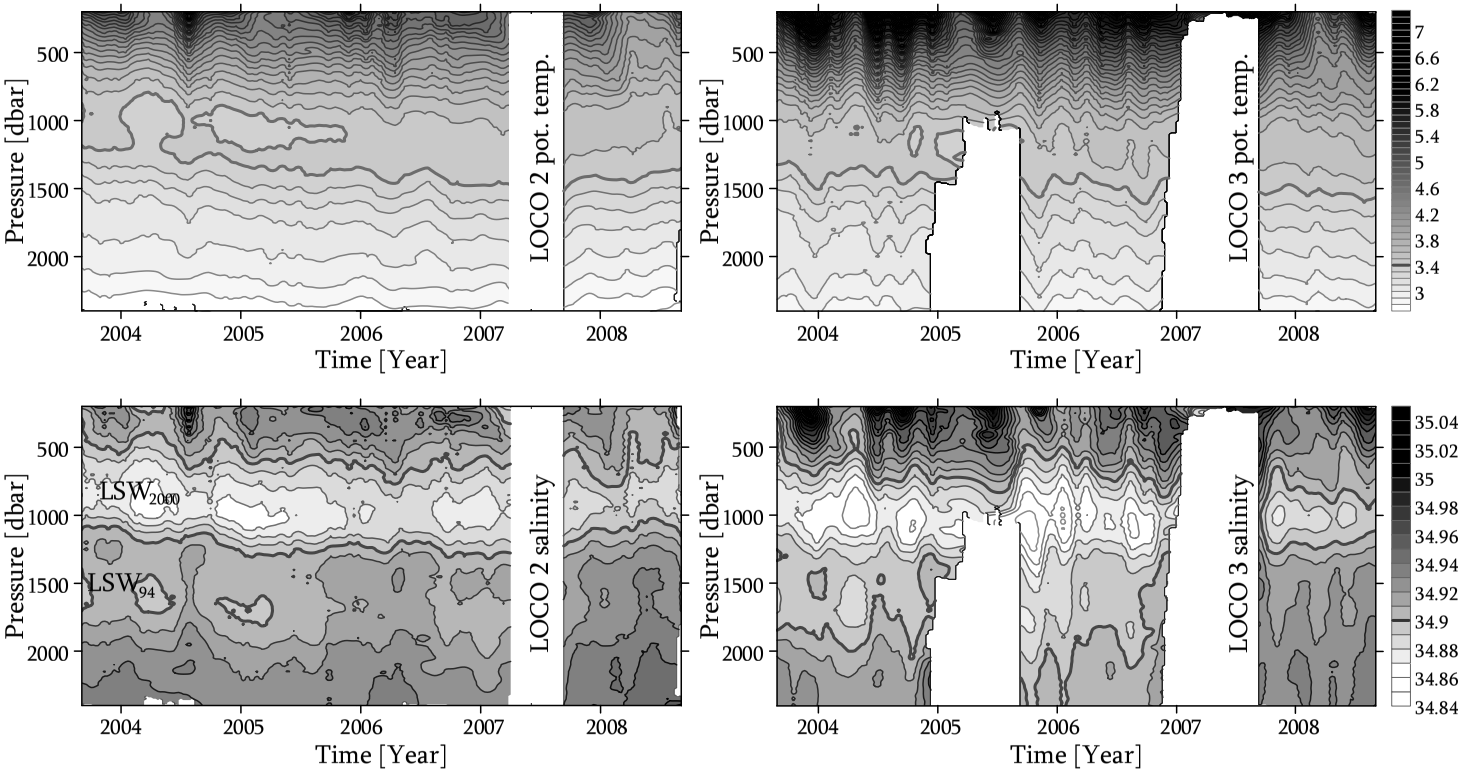

FIGURE 4.16: Time-depth diagrams of the weekly mean potential temperature (top panels) and salinity (bottom panels) as observed by the MMPs. Observations of the LOCO 2 mooring are shown on the left, observations from LOCO 3 are shown on the right. Contours are drawn every 0.1 °C and 0.01 psu. The 3.4 °C isotherm and the 34.90 psu isohaline are indicated by the thick lines to illustrate the deepening and loss of volume of the LSW more clearly. The depths of the LSW cores are indicated in the lower left panel.

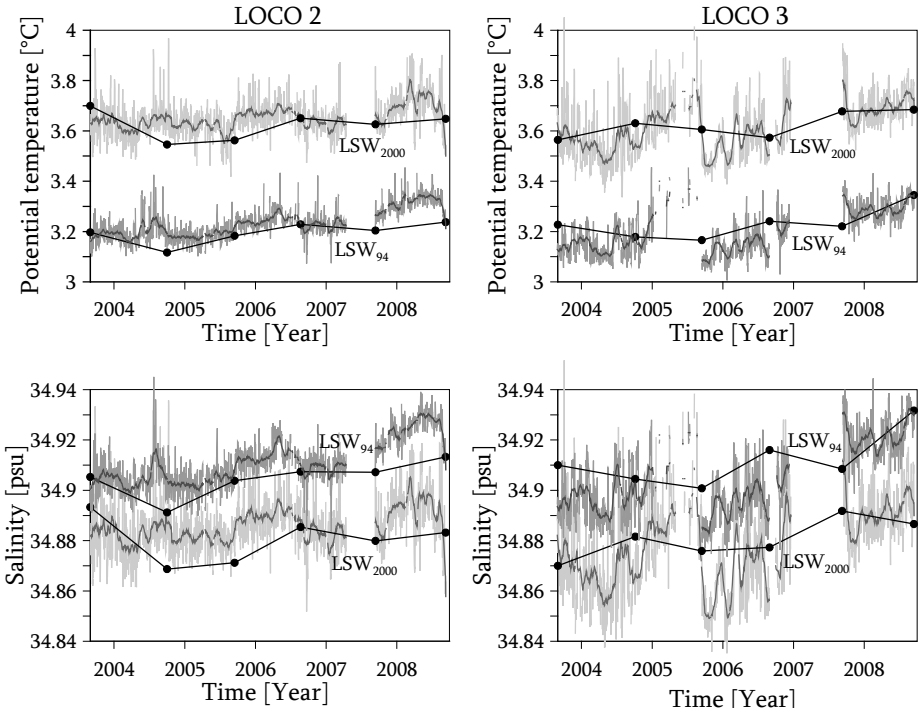

FIGURE 4.17: Potential temperature (upper panels) and salinity (lower panels) for the two LSW layers at LOCO 2 (on the left) and LOCO 3 (on the right). as observed by the MMPs The daily values for LSW_{2000} in the density interval of $34.58 \leq \sigma_{1.5} \leq 34.62$ kg m^{-3} (LSW_{94}, $34.66 \leq \sigma 1.5 \leq 34.70$ kg m^{-3}) are drawn in light (dark) grey . Drawn on top are the 30-day running-mean of the daily series (dark lines) and the values from the shipboard CTDs (dots and black lines).

Although the MMP takes about 2.5 hours to complete the profile, we assume here that the changes within this time frame are small and that the profile is made instantaneous. The upper 150 m, which is affected by the waves and wind mixed layer, are not observed by the MMP. Since wind induced mixed layers rarely reach below 100 m (the typical local Ekman depth is 40 m, see next chapter) we assume that mixed layers reaching below 150 m are caused by convective mixing, rather than by turbulence due to kinetic input by the waves and wind.

The seasonal cycle in the stratification is shown in Figure 4.18, which illustrates the change in stability of the upper 1200 dbar of the water column. During each winter the upper ocean stratification is removed. This process usually begins with shallow mixed layers in January and ends more suddenly in April after the deepest mixing layers have been reached (for an example see Figure 4.19). The most homogenous

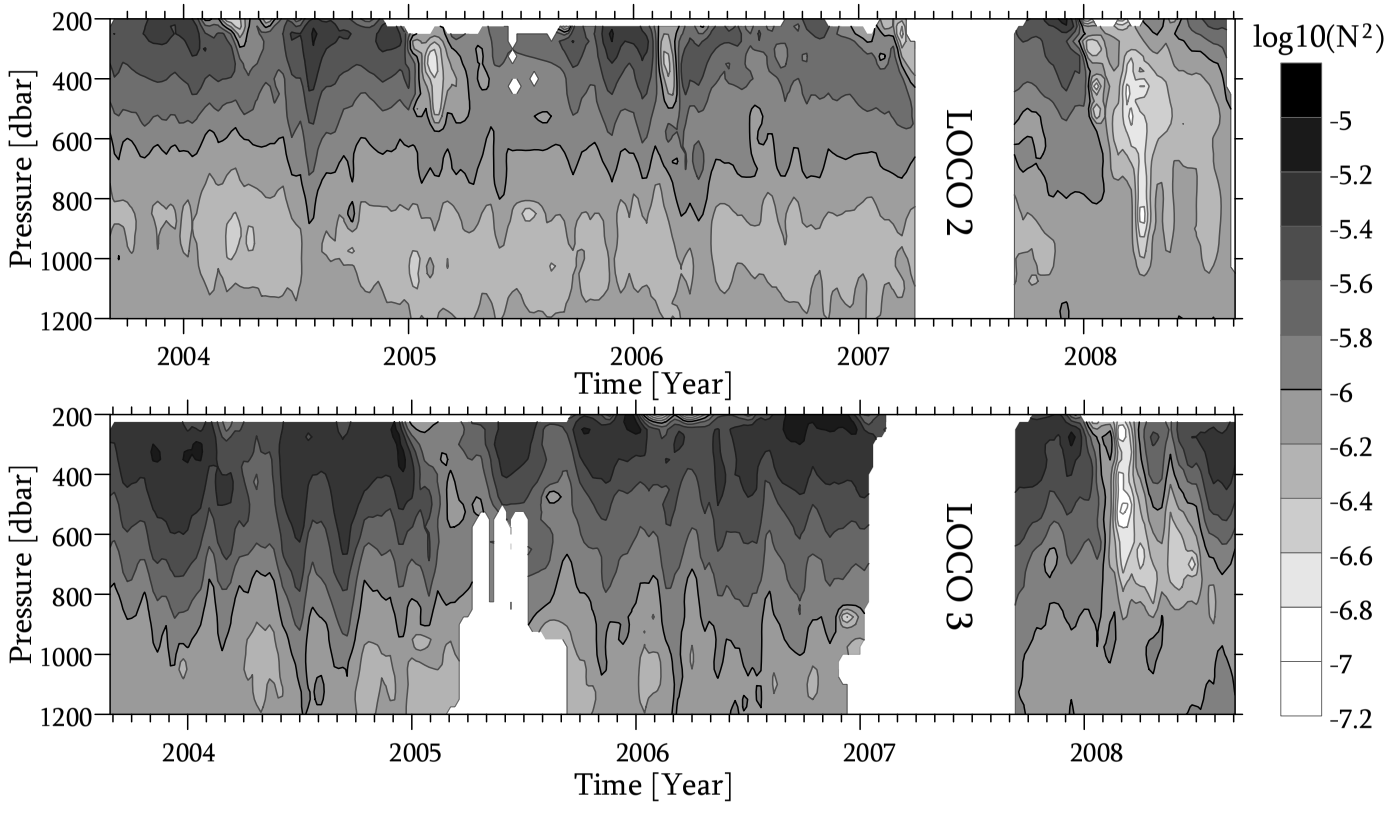

FIGURE 4.18: Contour plot of the stability at LOCO 2 and LOCO 3. The plotted values are the 10log of the Brunt Väisälä frequency squared (N^2). The values shown are weekly means of N^2 calculated over 25 dbar vertical intervals of the MMP profiles. White areas indicate missing data.

and deepest mixed layers are formed at the LOCO 2 site, where the initial (summer) stratification is weaker. After winter the water column restratifies quickly, accelerated by eddies shed from the warmer boundary currents (Katsman *et al.* (2004)). During the last winter of this record, the winter of 2007-2008, the mixing was significantly stronger and deeper than during the previous four winters. The initial formation of homogeneous water near the surface started in January 2008 at LOCO 3 and slightly later in winter at LOCO 2. The stratification was affected down to about 1000 dbar, a situation which lasted for several months (Figure 4.18). Contrary to the first four winters, the mixing during this last winter was more intense at LOCO 3 despite the stronger summer stratification. At both locations, the upper part of the water column quickly restratified in March/April and the new homogeneous water mass subducted to the level of the upper Labrador Sea Water (LSW_{2000}).

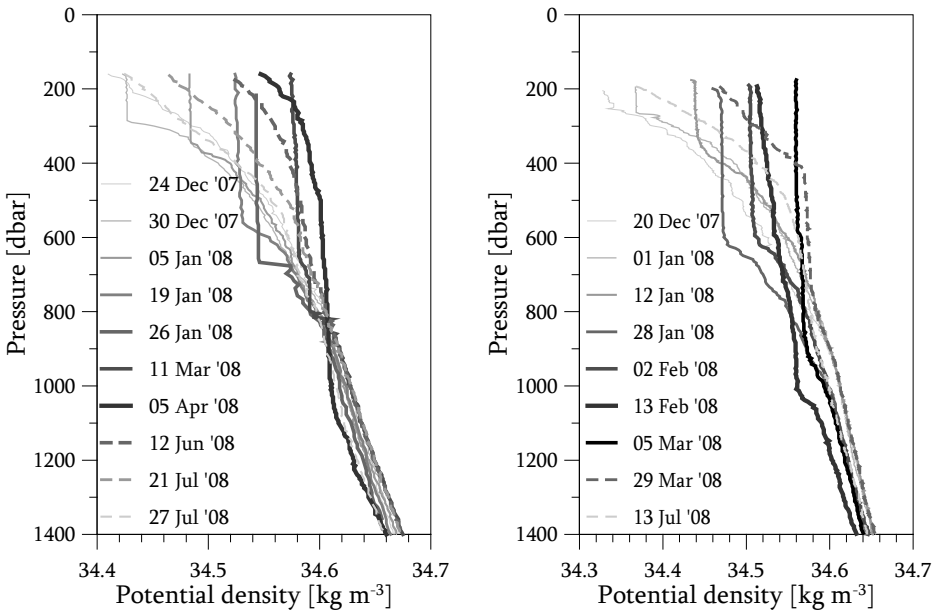

FIGURE 4.19: Examples of vertical density profiles recorded by the CTD profiler in the winter of 2007-2008. Profiles from the western mooring, LOCO 2, are shown in the left panel. Profiles from the eastern mooring, LOCO 3, are shown in the right panel.

Examples of individual vertical profiles during mixing and restratification in the winter of 2007-2008 are plotted in Figure 4.19. These profiles illustrate the gradual increase in mixed layer density and depth in winter. The mixed layers observed at LOCO 2 reached down to 800 dbar in March. In April a homogeneous layer was observed between 500 and 1000 dbar. This is interpreted as the remnant of homogene-

ous water (capped by a restratified layer) formed down to 1000 dbar as is seen further east, at LOCO 3, where mixed layer depths reached down to 1000 dbar in February. After these deep February mixed layers the density of the upper 1000 dbar continued to increase although the subsequent mixed layers seem to be shallower. After the main mixing period, the restratification at LOCO 3 initially created a sharp transition between the stratified 400 dbar of the upper water column and the homogeneous water below (as is illustrated by the profile of 29 March). Restratification started later at LOCO 2. There, the April profile showed the first signs of restratification in the upper 500 dbar while the layer below (between 500 and 1000 dbar) remained relatively homogeneous. At both mooring locations, the stratification was restored to its former (summer) strength in July.

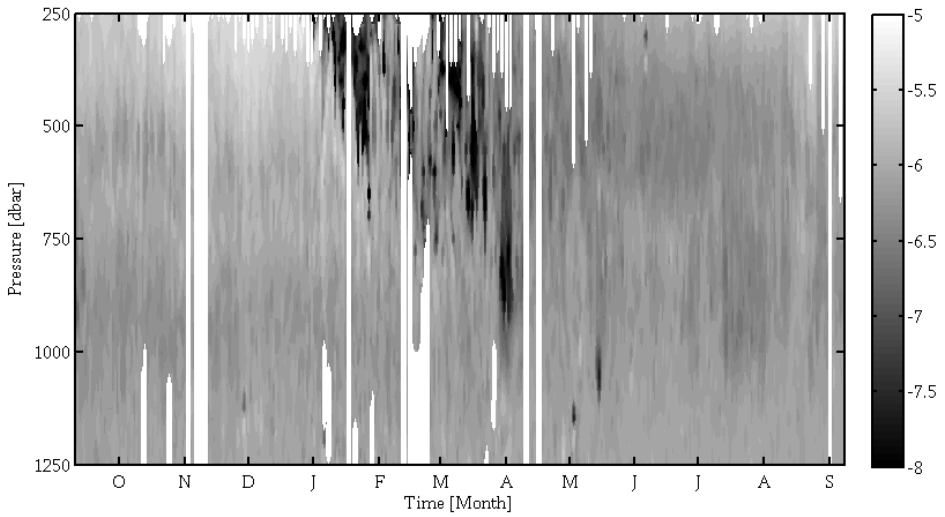

FIGURE 4.20: Contour plot of stability during LOCO 2-5. The plotted variable is the daily value of the 10log of N^2 (the Brunt Väisälä frequency squared in s^{-2}) derived over 25 dbar intervals. White areas indicate missing data. The time axis runs from September 2007 to September 2008.

Figures 4.20 and 4.21 show that the homogenizing process is locally much more intermittent than the schematic impression given by Fig. 4.19. The details of the last year of stability data (used here is the Brunt Väisälä frequency squared, N^2) reveal the short time scales on which the water column is homogenized and restratified. Several mixing events take place during this winter. These mixing events can be related to the peaking of heat fluxes over the Irminger Sea, derived from the NCEP reanalysis.

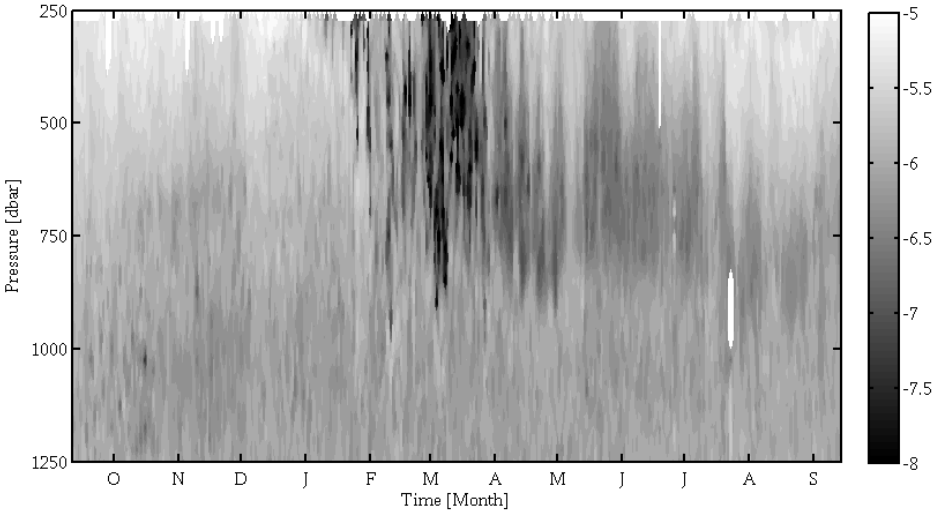

FIGURE 4.21: Contour plot of stability during LOCO 3-5. The plotted variable is the daily value of the 10log of N^2 (the Brunt Väisälä frequency squared in s^{-2}) derived over 25 dbar intervals. White areas indicate missing data. The time axis runs from September 2007 to September 2008.

In the winter of 2007-2008

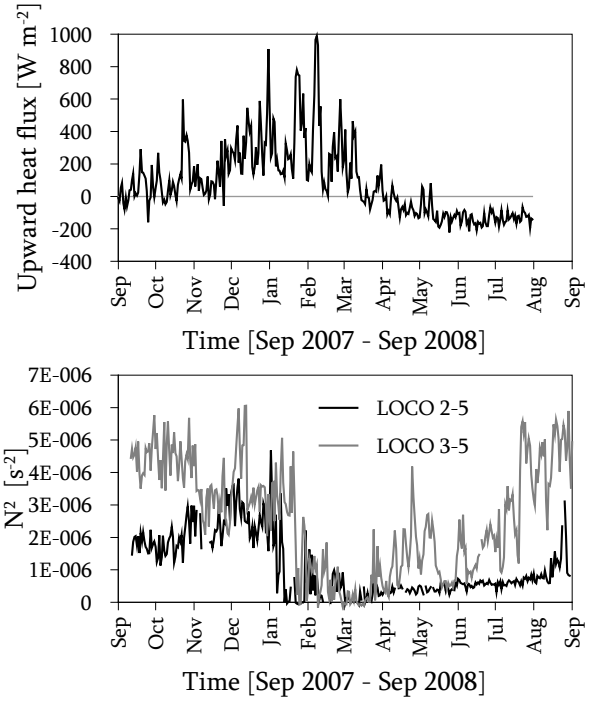

FIGURE 4.22:
Heat fluxes and mixing.

Top panel: Daily values of the total heat loss over the central Irminger Sea from the NCEP reanalysis (introduced in Chapter 2).

Bottom panel:
Time series of the stratification at 400 dbar depth at LOCO 2 (black line) and LOCO 3 (grey line) locations. Shown are the daily values of N^2.

substantial heat loss of the sea surface to the atmosphere started in late October (Fig. 4.22 upper panel). Although this initial cooling most likely removed some of the upper stratification, no mixing layer depths are as yet observed below 200 m (the approximate upper limit of the MMP) at this time. A second, longer period of strong cooling commenced in December 2007. During this cooling period the mixing depths increased rapidly as was shown in Figure 4.19. The two peaks in heat loss in late January and early February strongly decreased the stratification at both moorings. Deep mixed layers are seen in Figure 4.19 and the lower panel of Figure 4.22 shows a quick drop in stratification (to near zero) at 400 dbar depth in these months. Cooling and warming occurred intermittently in March. At this time the mixed layer had already reached into the weakly stratified LSW_{2000}. Thus these winter cooling events are enough to increase the mixed layer depth down to the 1000 dbar observed at LOCO 3, while the short intermittent warming had little effect. Only at the onset of spring, the increased warming stopped the mixing and rebuilds the stratification (most likely assisted by eddies). This happened most quickly at the eastern LOCO 3 location, where the initial stratification was also stronger due to the nearby Irminger Current. The stratification at LOCO 2 took much longer to recover.

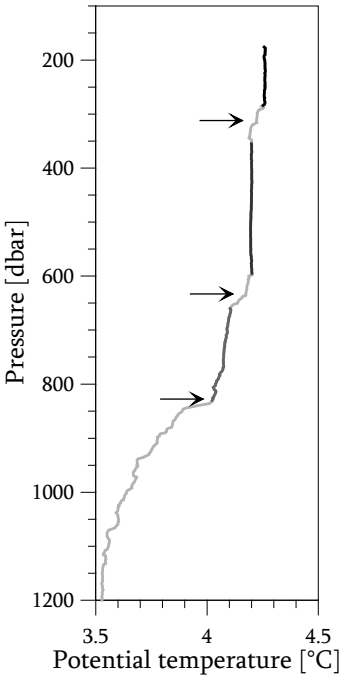

FIGURE 4.23: A potential temperature profile from the LOCO 3-5 deployment showing stacked mixed layers. The temperature gradients at the bottom of the mixed layers are indicated by the arrows.

Evidence of the continuation of (shallower) mixing events after the peak heat fluxes is found in profiles with stacked mixed layers (Figure 4.23). The three temperature gradients in this profile (marked by the arrows) indicate the bottom depths of successive mixed layers. The coldest, densest water was formed in a mixed layer that reached down to 800 dbar. The other mixed layer remnants contain successively lighter and warmer water, indicating an input of heat between the three mixing events. This profile was taken in the first week of March, thus warming by the atmosphere had not yet taken place according to the NCEP fluxes (Figure 4.22 upper panel). Therefore the input of warm water must have been through advective restratification. Apparently, later cooling events were less strong and initiated shallower, warmer mixed layers.

An example of alternating mixing and restratification is shown in Figure 4.24. The period covered by this Figure, 23 January to 29 February 2008, consisted of reasonably strong surface cooling only (see Figure 4.22, top panel). Nevertheless, the profiles show that mixed layers are regularly replaced by stably stratified water columns or shallower mixed layers. This suggests that convective mixing occurs in relatively small cells, which are transported past the moorings by the local currents or tides. The size of the mixing cells can be estimated from the ADCP velocities. If we assume that the tides transport the convective cells past the mooring in half a tidal period, with a root mean square of the velocity of 0.15 m s^{-1}, the horizontal scale of the convective cell will be about 3200 m or less. The local Rossby radius of deformation L_R as explained by *Marshall & Schott* (1999) is $L_R = NH/f$, in which H is the depth of the ocean and f is the Coriolis parameter. In areas where the ambient stratification, and thus N, is reduced by recurring convection the Rossby radius of deformation can be as small as a few km. During convection in the central Irminger Sea (H = 3000 m), N reaches values of $1 \cdot 10^{-7}$ s^{-1} and the associated Rossby radius of deformation is 2400 m.

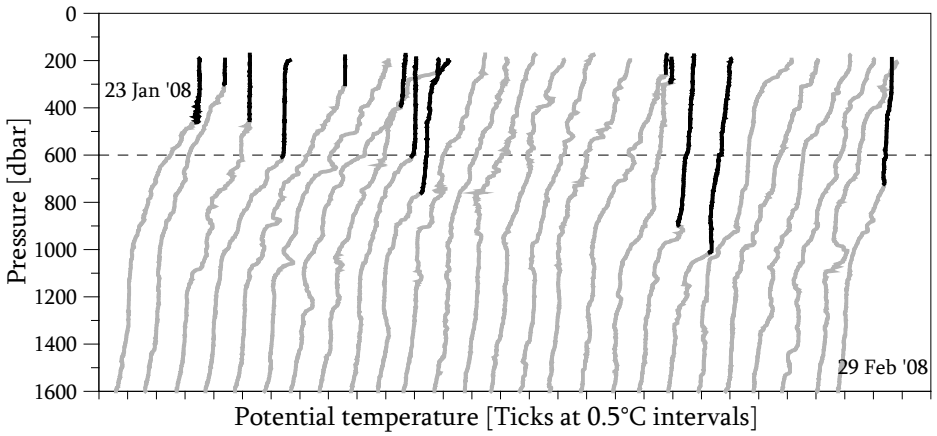

FIGURE 4.24: A series of consecutive potential temperature profiles during winter 2007-2008. These profiles were recorded by the profiling CTD in LOCO 3. The first profile was taken on January 23 after which profiles are shown for each day until February 29. Each profile is displaced by 0.5 °C with respect to the previous profile. The vertical profiles are drawn in grey with the intermittent mixed layers drawn in black.

The suspected input of heat by advective restratification is supported here by a short calculation. This calculation will show that the amount of heat stored in the upper layers of the ocean during restratification in spring (relative to a mixed winter profile) cannot originate from surface heating by the atmosphere alone. Figure 4.25 shows three potential temperature profiles from the winter and spring of 2008. The first profile is a stratified profile from the start of winter, the second profile has a deep

mixed layer and the third profile is the first profile from the next summer in which the stratification is fully restored. The temperature profile above 200 dbar is assumed to be linear (grey lines), which is a conservative estimate for the warm season since the temperature stratification generally increases (exponentially) towards the surface. The estimated temperature difference (ΔT) at the surface between the mixed and stratified profiles is about 2.2 °C, which makes the amount of seasonal heat stored in the stratified profiles above 640 dbar (Δz) about $2.8 \cdot 10^9$ J m^{-2} ($\Delta T \Delta z c_p/2$, with c_p the heat capacity of seawater). In order to add this heat in the 3 months between the profiles would require a mean upward heat flux of -360 W m^{-2}. However, the mean heat fluxes observed over the Irminger Sea between 1 April and 1 July 2008 are -100 W m^{-2} (-50 W m^{-2} for 1 March to 1 July due to a period of cooling in March 2008). These observed -100 W m^{-2} are clearly not enough to explain the -360 W m^{-2} warming of the upper 640 dbar of the water column. This discrepancy shows that advection of warmer water must supply most of the heat during restratification. Similarly, the upward heat flux needed to remove the December stratification in the 2½ months can be calculated. This would require about 400 W m^{-2}. Since the mean heat flux over the central Irminger Sea between 1 December 2007 and 1 March 2008 was 330 W m^{-2} it can be assumed that most of the observed cooling takes place locally by air-sea interaction.

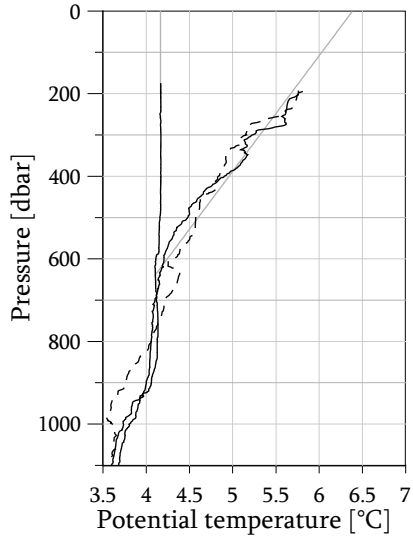

FIGURE 4.25:
Estimated heat loss and input between three profiles of potential temperature at LOCO 3. The broken line corresponds to a profile from late December 2007. The two solid line are a mixed (March 2008) and a restratified profile (July 2008). The grey lines are the estimated temperature profiles between the top of the observed profile and the sea surface.

The heat removed by mixing and the heat input during restratification are nearly equal and are estimated to be $2.8 \cdot 10^9$ J m^{-2}. This leads to an average cooling of 400 W m^{-2} (for 2½ months) and an average warming of 360 W m^{-2} (for 3 months).

So far, we have mainly focussed at the strong winter of 2007-2008, which led to the deepest observed mixed layers. We now look into the effects of winter cooling in all five observed winters in the LOCO 2 and 3 records. Figure 4.26 illustrates the daily and weekly mean heat fluxes derived from the NCEP reanalysis (top panel) and the

stratification (N^2) at 400 dbar depth (bottom panel) at the two mooring locations between September 2003 and September 2008. The statistics of the NCEP heat fluxes in each of the five observed winters are contained in Table 4.3.

TABLE 4.3: Characteristics of the October to April heat flux over the central Irminger Sea based on the upward heat fluxes from the NCEP data set. The summed daily heat flux is calculated over the entire period from the start of cooling (first positive upward heat flux) to the end of cooling (last positive upward heat flux) and thereby accounts for differences in the length of winter as well as for intermitted warming periods.

Winter period	Mean heat flux [W m^{-2}]	Standard dev. [W m^{-2}]	Max heat flux [W m^{-2}]	Summed daily heat flux [W m^{-2}]
2003 - 2004	124	119	627	22735
2004 - 2005	160	203	1201	29351
2005 - 2006	127	117	507	23309
2006 - 2007	172	128	794	31538
2007 - 2008	221	212	989	40377

The removal of the stratification in the upper layer in all five winters is shown by the sharp drops in N^2 in the bottom panel of Figure 4.26. These sharp drops indicate the arrival of mixed layers at this depth, which is also seen in the hydrographic profiles (not shown). The duration and depths of the winter stratification minimum apparently depends both on the total heat loss and on the shape of the heat loss curve (top panel Figure 4.26). The strongest winters (high mean heat flux and high maximum heat flux, Table 4.3) were the second (2004-2005) and the last winter (2007-2008) of the record. These winters show deep, long minima in the stratification. During weaker, shorter winters (low mean heat flux and low summed daily heat flux, Table 4.3) the stratification minimum is less deep and the stratification is restored quickly. The changes in stratification at the two mooring locations occur nearly simultaneously, with higher values for the (summer) stratification at the eastern LOCO 3 site. Why the stratification at 400 dbar depth continues to decrease at LOCO 2 during the summer of 2006 is unclear, possibly advective changes or increased doming of the Subpolar Gyre are the cause of this. Overall, the MMP observations from the Irminger Sea, with a rapid drop in stability in (most) winter(s) and the gradual restratification in spring and summer is very similar to the observations of convection in the Labrador Sea (Lilly *et al.* (1999)). The main differences between deep convective mixing in the Labrador and Irminger Seas are the depth of the mixed layers and the strength of the modification (cooling and freshening) of the hydrographic properties on a basin scale.

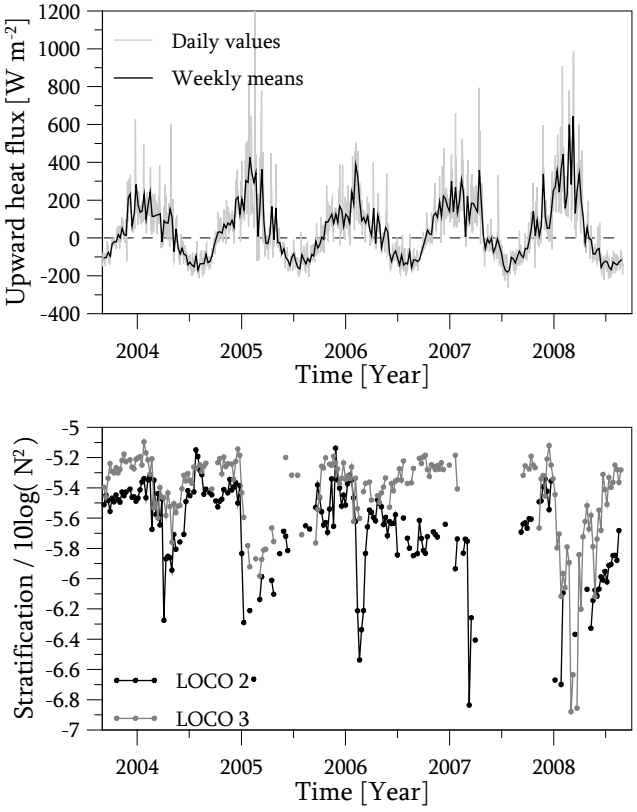

FIGURE 4.26: Heat loss and related decrease in stability.

The upper panel shows the daily (light grey) and weekly (black) mean upward NCEP heat fluxes over the central Irminger Sea during the 5-year LOCO deployment.

The lower panels shows the stratification (10log of N^2) at 400 m depth at LOCO 2 (black line) and LOCO 3 (grey line).

4.7 SMALL SCALE VARIABILITY

Although the convective cells are relatively small, a few km wide and several hundred meters deep, there are even smaller scale processes visible in the daily hydrographic profiles. Here we focus on this small scale, day-to-day variability, which was not visible in the smoothed contour figures shown before (such as Figure 4.16 & 4.18). Figure 4.27 contains a colour time-pressure plot of the unsmoothed salinity, which shows variability at all time scales (inter-annual to daily) with various vertical extent. More detail and small scale variability can be seen in a cutout defined by the box in Figure 4.27. This series of 100 profiles (= 100 days) between 1100 and 1500 dbar is enlarged in Figure 4.28. It shows that the salinity gradient beneath the fresh LSW_{2000} (found at ~1000 dbar) is neither smooth nor constant. Instead, Figure 4.28 shows a background gradient, with relative fresh water above more saline water, interleaved with many intrusions of small vertical extent. The horizontal dimension (time) shows us that the smallest intrusions, which are a few tens of dbar vertically, do not often last longer than 1 day. Larger fresh or saline anomalies (extending over this entire 500 dbar section) can last for a period of several days.

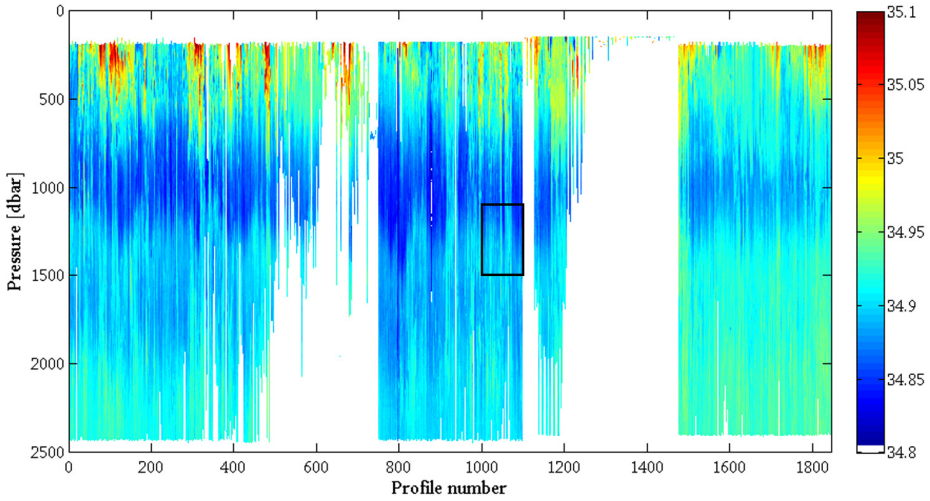

FIGURE 4.27: Colour time-depth plot of 5 years of salinity data recorded by the LOCO 3 profiler. In this plot each 1 dbar bin in each profile is plotted separately, thus no smoothing in the vertical or time occurs. Areas without data are left white. The black box defines the cutout of a 100 days shown in Figure 4.28.

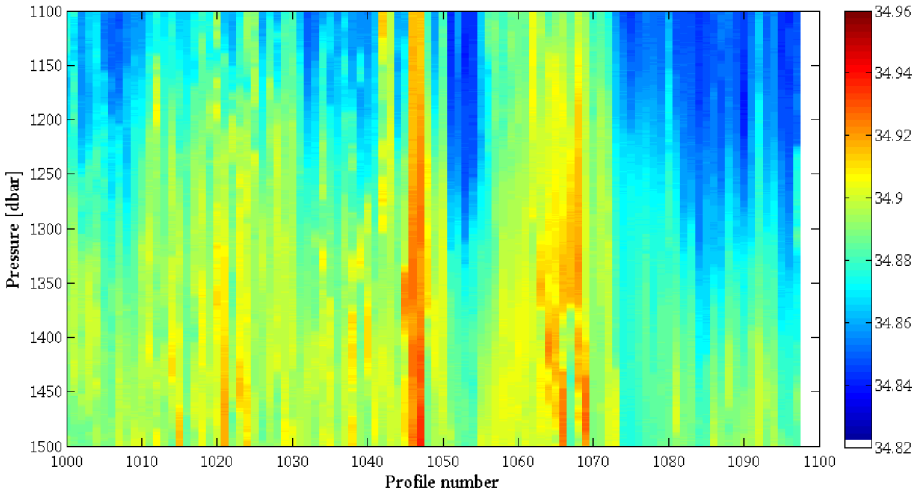

FIGURE 4.28: As Figure 4.27, but for the cutout of profiles 1000 to 1100 (100 days) between 1100 and 1500 dbar of the salinity record of LOCO 3 shown in Figure 4.27. This figure shows a background gradient, with relative fresh water above more saline water, interleaved with many intrusions of small vertical extent. Large intrusions can last for several days.

The nature of these anomalies cannot be estimated from Figures 4.27 and 4.28. They only show the salinity variability and do not give information about density changes. To investigate the nature of the θ and S variability and its density structure on monthly to daily time scales both the 5-year temperature and the 5-year salinity records of LOCO 2 and LOCO 3 were used. On each pressure level two time series were created. The first time series contains the monthly variability. To remove the daily variability from this series it is first smoothed with a 31-day running mean filter. Secondly, to remove the inter-annual variability, a 5-year series smoothed with a 1-year running mean filter is subtracted. A second series containing the daily to weekly variability is created by subtracting the series smoothed with the 31-day filter from the original unfiltered series.

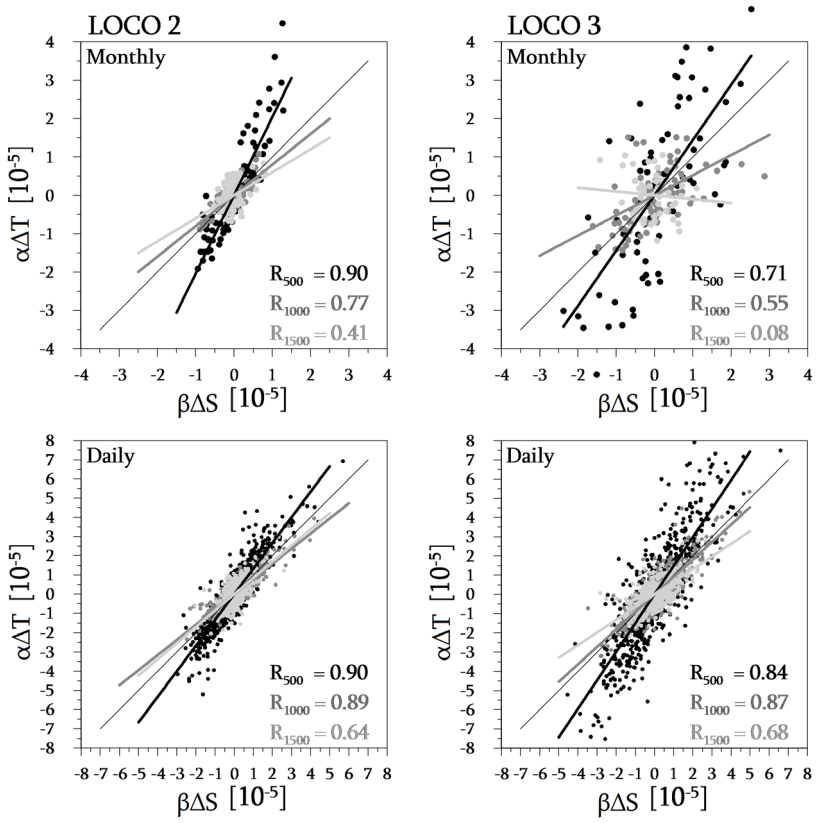

*FIGURE 4.29: Anomaly plot (βΔS versus αΔT) for the monthly and daily variability. The left (*right*)column shows the monthly (upper panels, plotted every 2 weeks) and daily (lower panels, plotted every 2 days) anomalies for LOCO 2 (LOCO 3). Shown are the temperature and salinity anomalies at three depths, 500 dbar (black), 1000 dbar (dark grey) and 1500 dbar (light grey). The fit and the corresponding correlations are shown in matching colours. The thin black line of slope 1 indicates purely isopycnal changes.*

The two resulting series contain the monthly temperature and salinity anomalies (ΔT and ΔS) and the daily temperature and salinity anomalies. By plotting these anomalies in a diagram (Figure 4.29) in which the temperature anomalies are multiplied by the thermal expansion coefficient ($\alpha\Delta T$) and the salinity anomalies multiplied by the haline contraction coefficient ($\beta\Delta S$) it is easily visible whether the changes are isopycnal or not. For isopycnal changes the slope of the fit should be exactly 1.

The first two things that stand out in Figure 4.29 is that the variability is largest in the shallow layers (500 dbar) and that overall the variability is largest at LOCO 3. The first is caused by the strong (near) surface variability which can support larger anomalies, the second is likely to be caused by the close proximity of the Subpolar Front to the location of LOCO 3 and to the frequent occurrence of meso-scale eddies there. More surprisingly, the range of the variability is a factor 2 larger in the daily series than in the monthly series, indicating that the daily variability is stronger than the meso-scale variability. This range difference was already visible in Figure 4.17, which showed large fast variability around the smaller meso-scale variability at intermediate levels.

To each $\beta\Delta S,\alpha\Delta dT$-distribution on a pressure level (10 dbar intervals) a linear least squares fit through the origin was determined. These lines are plotted for all three depth levels in Figure 4.29. The slope of these lines indicates whether the variability is isopycnal (slope = 1), or either temperature or salinity variations are dominant for the density variations. For temperature dominant signals the slope is > 1, for salinity dominant signals the slope is < 1. All four panels in Figure 4.29 seem to indicate that the temperature changes are dominant in the uppermost layer (500 dbar) and salinity changes are more important in the deeper layers at both daily and monthly time scales. However, in the upper right panel the changes in the deepest layer (1500 dbar) are more or less random and the correlation of the fit is not significant. A comparison of the slope of the $\beta\Delta S,\alpha\Delta T$-distributions over the whole profile with the vertical temperature and salinity gradients (Figure 4.30) reveals more information about the type of signals. Large slopes (> 1) appear in the upper 800 dbar where the temperature gradient is largest. Slopes approaching 1, indicating isopycnal changes, appear where the vertical salinity gradient is close to zero and temperature gradients are small (around 800 dbar and 1600 dbar). Small slopes (< 1) appear where salinity gradients are relatively large and temperature gradients are small. Thus relatively large temperature changes are mostly found in the strong near-surface temperature stratification and large salinity changes are found in the salinity gradients between the fresher Labrador Sea Water and the more saline layers (Icelandic Slope Water and North East Atlantic Deep Water). Also, on shorter (daily) time scale the variability has a more isopycnal nature, which points towards intrusions and interleaving, while the monthly vari-

ability is much less density compensating and is likely to be caused by passing mesoscale eddies (at both mooring locations) or displacements of the Subpolar Front (near LOCO 3). In the deepest parts of the profiles (for all but the daily variability of LOCO 3) correlations of the temperature and salinity anomalies are not significant.

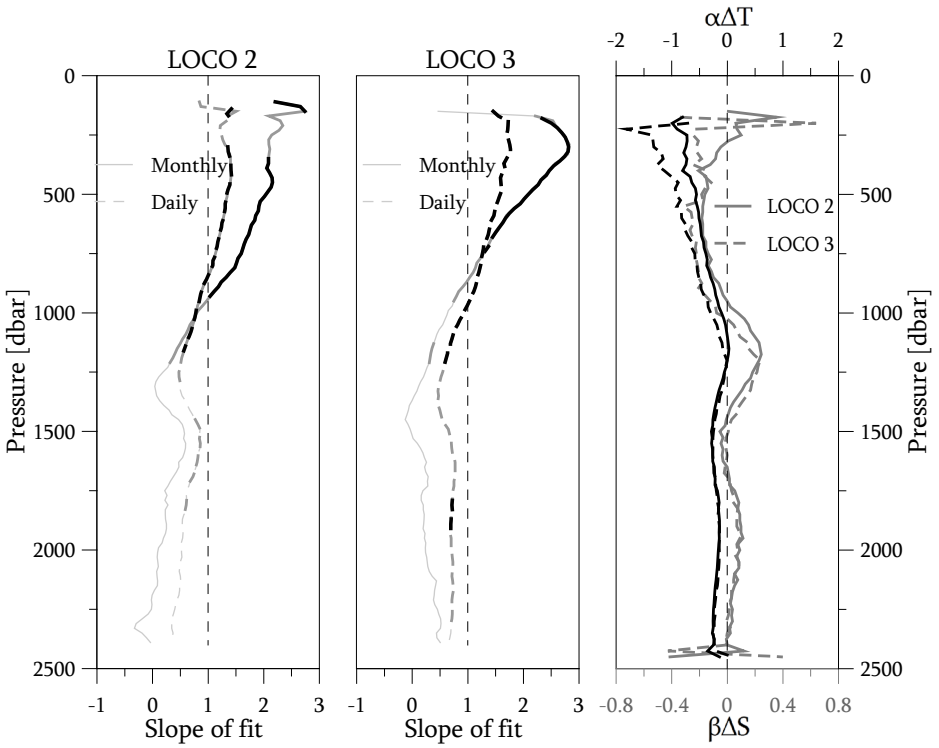

FIGURE 4.30: Vertical profiles of the slope of the βΔS, αΔT - distributions and profiles of the vertical temperature and salinity gradient. The left (middle) panels shows the profiles for the slope of the monthly (solid line) and daily (dashed line) variability distributions at 25 dbar intervals for LOCO 2 (LOCO 3). The profiles are drawn in black when the fit has a R ≥ 0.8, in dark grey for R ≥ 0.6 and with a thin light grey line for R < 0.6. The right panels shows the 5-year mean vertical gradient of temperature (black) and salinity (grey) over 25 dbar intervals. The temperature (salinity) gradient has been multiplied by the thermal expansion (saline contraction) coefficient to better show their relative importance.

Krauss (1995) found that both the horizontal and the vertical stratification in the Irminger Sea supports interleaving of water masses. He found a horizontal salinity gradient across the Irminger Current front of 0.10 psu / 300 km and a horizontal temperature gradient of 2 °C / 300 km. This implies that also in the horizontal direction the temperature stratification is dominant. Density ratios ($R_\rho = \alpha T_z / \beta S_z$, as defined by *Krauss* (1995)) were not computed because the vertical gradients observed here, especially the salinity gradient, are too small.

Through diffential (or double) diffusion intrusions can lead to density overturns (small density instabilities) in the vertical density profile. An example of density overturns are shown in Figure 4.30. Density instabilities lead to vertical mixing and thereby have an effect on the vertical eddy diffusivity (*Kz*). The value of the resulting *Kz* can be estimated from the vertical displacements of density (the overturns), which are visible in the density profile when the temperature and salinity anomalies are not density compensating. Since these overturns are quite small vertically the raw hydrographic data (pressure, conductivity and temperature as a function of time, without bin-averaging) are used. Firstly, all outliers in the conductivity and temperature are removed and interpolated. Secondly, all samples belonging to a monotonously increasing pressure are removed. Thirdly, the neutral density is calculated from the profile using the algorithm described by *Eden & Willebrand* (1999). Fourthly, the neutral density is passed through a moving average filter of 25 measurements, equaling a window of 2.5 to 3 dbar. This filter preserves the density disturbances that exceed the instrument noise, but removes the noise itself and remaining spikes. In order to obtain the vertical displacements the neutral density profile is sorted to a profile that increases monotonously with pressure, while keeping an account of the old and new vertical positions of the neutral density values. The used vertical displacements are the difference between the old and new vertical positions. From the new monotonous neutral density profile the background stratification (the buoyancy frequency, N_b) is calculated. The profiles of displacements and stratification are sub-sampled by taking the root mean square (rms) of 1 dbar segments. The rms values of the displacement are the Thorpe length scales (L_{Th}, Dillon (1982)). Finally, for the computation of K_z we consider L_{Th} and N_b over scales longer than the largest overturns in the profile. Therefore, both parameters are passed through a moving rms filter with a window size of 100 dbar.

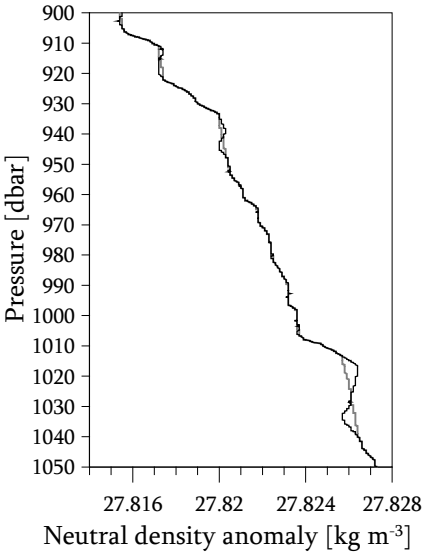

FIGURE 4.31: Example of density overturns observed in the MMP profile. Shows is the neutral density profile from the observed hydrographic profile (black line) at LOCO 2 on 3 February 2003 and the sorted, monotonously increasing profile (grey line). Density overturns are visible at pressures of 915, 940 and 1030 dbar.

From the large scale parameters, L_{Th} and N_b, the following are calculated:

The Ozmidov length scale: $L_{Oz} \approx L_{Th}/1.1$ *(4.1)*

The dissipation rate estimate: $\varepsilon = N_b^3 \cdot L_{Oz}^2$ *(4.2)*

The vertical eddy diffusivity: $K_z = 0.25 \cdot \varepsilon / N_b^2$ *(4.3)*

The background values of K_z found in the profiles vary between 10^{-7} and 10^{-5} m^2 s^{-1} (see Figure 4.32). The largest values of K_z (up to 10^{-2} m^2 s^{-1}) are found in the upper layer in winter. For the example shown here, the first deployment of LOCO 2, these values are found down to about 300 dbar between day 150 (end of January) and day 230 (mid April). These high values of K_z (and of L_{Th}) in the upper layer coincide with the observed convective mixing. A second high K_z layer is found in the weakly stratified layer of Labrador Sea Water between 700 and 1200 dbar. The weak background stratification amplified the vertical displacements of density anomalies with respect to anomalies of a similar magnitude elsewhere in the water column. The high vertical eddy diffusivity is thought to be one of the dominant processes in the transformation and decay of the *LSW*.

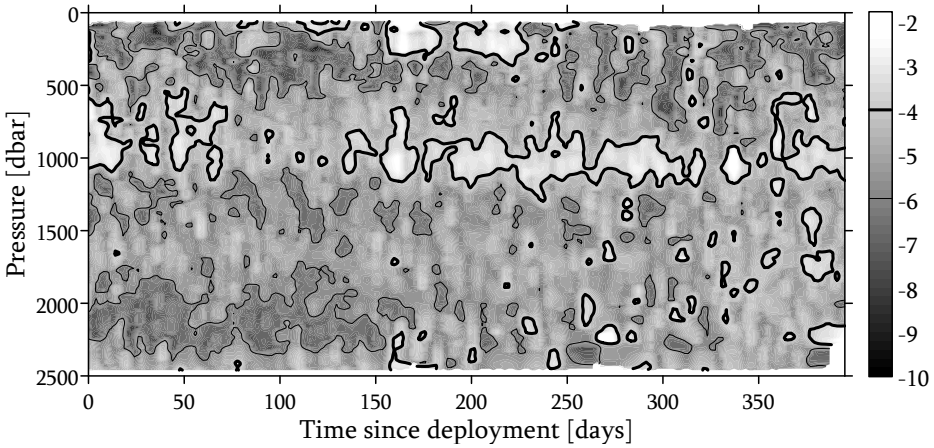

FIGURE 4.32: Values of K_z (plotted as the 10log) calculated from density displacements. Shown as an example are the values from the first year of the LOCO 2 deployment between 30 September 2003 (day 0) and 1 October 2004 (day 395). The thick black contour indicates $K_z = 10^{-4}$ m^2 s^{-1}, thin contours indicated subsequent lower values of K_z (10^{-6} m^2 s^{-1}).

4.8 SUMMARIZING DISCUSSION

Fast variability in the Irminger Sea

The hydrography in the Irminger Sea is characterized by large day-to-day variability, which exceeds the range of the meso-scale and inter-annual variability. Accoustic Doppler Current Profiler (ADCP) measurements show day-to-day changes in both current direction and velocity superimposed on the tides (predominantly M2 and S2). The mean current variability is largely barotropic with strong topographic steering only in the lowest 250 m (Figure 4.8) due to the presence of canyons near the mooring locations. Meso-scale eddies occur at both mooring locations, but are strongest near the Subpolar Front (LOCO 3). Despite of its location near the bottom of the Greenland slope the LOCO 2 mooring did not observe the expected southward flow of Denmark Strait Overflow Water (*DSOW*). Only a weak, mainly westward, mean velocity was present, most likely due to local topographic steering.

Near bottom measurements by Microcats (small CTD recorders) show that the hydrographic properties at LOCO 2 closely reflect the *DSOW* core, although it is not located near the southward core of the *DSOW* velocity maximum. The bottom water varies between two types of *DSOW*, one fresh and cold the other warmer and more saline (Figure 4.12). The two types of *DSOW* are likely caused by changes at or northwest of the overflow in Denmark Strait. Further east, at LOCO 3, the near bottom waters vary between the two *DSOW* types and the North East Atlantic Deep Water (*NEADW*). These variations occur in a form of switching between the dense *DSOW* and lighter *NEADW* rather than slow transitions (Figure 4.14). The switching could not be related to the currents observed by the near-bottom ADCP and are therefore probably not locally generated. The properties of the *DSOW* like water at LOCO 3 are near synchronous in time with the fresh or saline type of *DSOW* found at LOCO 2. A time lag correlation showed a best fit with a delay of ~1 month for LOCO 3.

Moored CTD profiler (MMP) hydrographic profiles show large day-to-day thermohaline variability over the full depth of the profile (200 to 2400 dbar). The daily variability has a near isopycnal nature at depth levels where the vertical gradients in temperature and salinity are small. In the upper part of the water column (0 to ~800 dbar) the density variability is dominated by anomalies in temperature, which can be large because of the strong temperature stratification. In the lower parts of the water column the variability is either strongest in salinity or nearly random in both salinity and temperature. The daily temperature and salinity anomalies, which are often of small vertical extent, are typical for intrusions or interleaving between neighbouring water masses. A calculation of Thorpe lengths and vertical eddy diffusivity (K_z) and from density displacements showed large values of K_z (order 10^{-2} m^2 s^{-1}) in the weakly

stratified Labrador Sea Water. We suspect that this type of variability (and mixing) causes the gradual change / aging of water masses, such as the warming and salinifying of the originally fresh and cold Labrador Sea Water (*LSW*) cores. The meso-scale variability, on monthly time scales, is smaller than the daily variability but also less isopycnal in nature. These changes are most likely caused by eddies shed by the boundary currents. Meso-scale eddies are abundant in the Irminger Sea as was shown by *Volkov* (2004) using altimetry data. The eddy-related θ and S variability is strongest near the Irminger Current (LOCO 3). *Knutsen et al.* (2005) also found large values for the eddy kinetic energy from shipboard ADCPs, with a minimum in the central Irminger Sea and maxima near the East Greenland Current and Irminger Current. A model study showed that boundary current eddies are important to the restratification process in the Labrador Sea (Katsman *et al.* (2004)). The eddies transport warm boundary current water into the central Labrador Sea. It is very likely that the eddies in the Irminger Sea play a similar role in the restratification of the central Irminger Sea.

Overall, the hydrography of the Irminger Sea is highly variable down to the shortest observed time scales presented here. The range of the day-to-day variability, observed at all depth levels, is often larger than the inter-annual changes seen in the annual sections (Figures 4.13, 4.14 & 4.17). These high frequency signals are strongly aliased in the annual sub-samples of the AR7E surveys and therefore can create seeming trends were there are none or underestimate short lasting trends. An example is the sharp drop in salinity of the *DSOW* in 2004 (Figure 4.13).

Deep convective mixing

The profiles recorded by the moored CTD profiler indicate the removal or reduction of the stratification in the upper 500 m in each winter. Mixed layers are observed during the later part of winter, February to April, occasionally down to 1000 m depth in strong winters. The mixing appears to occur in small convective cells, only a few km in diameters, which are subject to the local advection patterns. These cells occur both at LOCO 2 and LOCO 3, thus covering an area of at least 200 km wide. Also, the AR7E surveys from 2007 and 2008 show a expansion of the stability minimum after the winter of 2007-2008 over the entire central Irminger Sea (Figure 4.33). This decrease in stability is mostly caused by the homogenization of the temperature stratification (not shown) between 500 and about 1200 dbar, down to the level of the LSW_{2000} salinity minimum. Thus the Irminger *LSW* stability minimum, that has been weakening during the last years, seems to be "rejuvenated" by the 2007-2008 winter deep convection in the Irminger Sea.

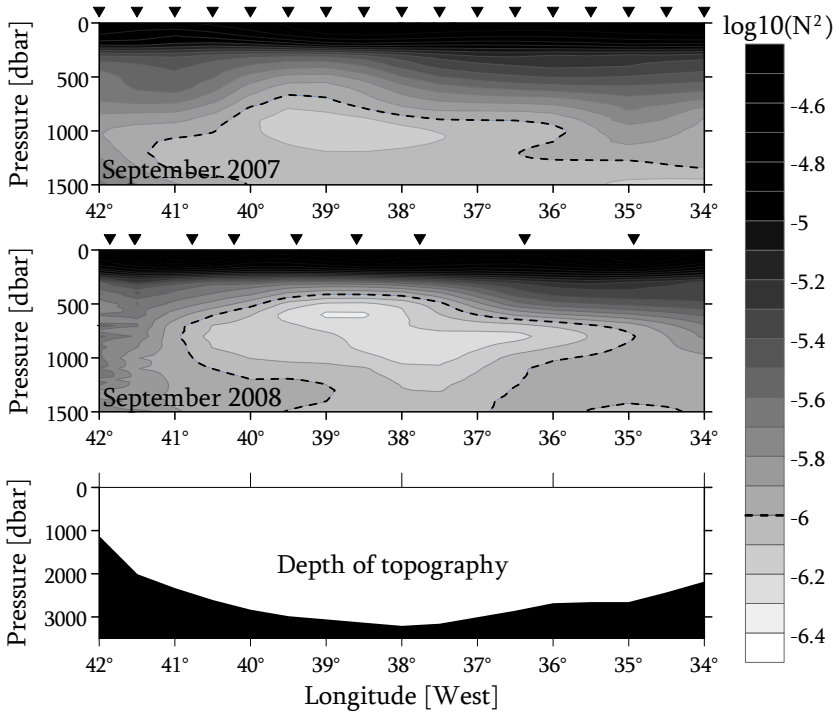

FIGURE 4.33: Contour plots of stability (shown as the 10log of N^2) in the Irminger Sea as observed during the 2007 Pelagia survey (upper panel) and the 2008 Discovery survey (lower panel). The dashed lines indicates $N^2 = 10^{-6}$ s^{-2}. The diamonds at the top of each panels indicates the position of the surveyed CTD stations.

The idea of deep convective mixing in the Irminger Sea is not new. *Sverdrup* (1942) already suggested that deep water formation takes place in the Irminger Sea. He based this on hydrographic stations from 1935 and 1933 showing nearly uniform temperature and salinity profiles as well as a high oxygen content. More recently, mixed layers have been observed down to 600 m by profiling floats in the winter of 1996-1997 (Bacon *et al.* (2003)). Also, the occurrence of mixed layers reached down to about 1000 m in the winter of 2007-2008 is not surprising, given the fact that mixed layers down to 1800 m were observed in the same cold winter in the Labrador Sea (Våge *et al.* (2008)). Both basins are affected by the same type of cold winters/weather and are similarly preconditioned.

We do not propose that *LSW* is formed in the Irminger basin as was forwarded by Pickart *et al.* in 2003. Convective mixing in the Irminger Sea might precondition the Subpolar Mode Water before it enters the Labrador Sea for its final conversion to *LSW* (McCartney & Talley (1984)). The more or less closed circulation through the Labra-

dor and Irminger Sea (Lavender *et al.* (2000)) then brings the *LSW* from the Labrador Sea to the Irminger Sea, but it also brings the products of Irminger convective mixing from the Irminger Sea to the Labrador Sea. By doing so, both convective products precondition their neighbouring basin to further convective mixing. Undoubtedly, the adjustment of θ,*S*-properties of the affected water mass is largest in the Labrador Sea, where cooling is strongest and freshwater is supplied from the Canadian Archipelago, thus making the *LSW* an easily recognizable water mass. Adjustments of the hydrographic properties in the Irminger Sea are expected to be smaller, due to the warmer and more saline *SPMW* between the surface and the *LSW*. However, this does not exclude the finding of deep convection in the Irminger Sea. Possibly the estimations of the volume of *LSW* towards the Irminger Sea are too large and part of the *LSW* in the Irminger basin is formed, or at least temporarily prevented from disappearing, by local deep mixing.

Chapter 5

Variability in mixed layer depths investigated by means of a linear mixed layer model

5.1 Introduction

The observations of mixed layer deepening by the two LOCO moorings (Chapter 4) give some indication of the mixed layer depths that can be reached in the Irminger Sea, but the available records cover only five winters and two locations. Also, despite of the fact that the winter of 2007-2008 was a cold winter compared to the four preceding winters, all five winters started with quite similar hydrographic conditions. To gain more insight into the processes responsible for the variability in mixed layer depth a simple encroachment model was developed. This model calculates the maximum mixed layer depth based on a given initial stratification and atmospheric forcing. By varying the initial stratification, the influence of preconditioning can be studied. Preconditioning is the predisposition of a cyclonic gyre to overturn locally (Marshall & Schott (1999)). A strongly preconditioned water column is characterized by a weak intermediate stratification underneath a shallow thermocline. The strength of the preconditioning in the Labrador and Irminger Seas varies from year to year. Next to preconditioning, the mixed layer depth also depends on the surface buoyancy forcing. Therefore, the influence of the surface buoyancy forcing is investigated by using the observed inter-annual variability in the heat and freshwater fluxes in the time series since 1948 (from the NCEP reanalysis, introduced in Chapter 2).

The results of four experiments are presented in this chapter. The first experiment is a model simulation of the mixed layer depth as a result of the mean hydrographic preconditioning and forcing (introduced in Chapter 2). The results illustrate the general functioning of the model. Furthermore, this mean situation simulation is used to estimate the error in mixed layer depth as a result of a possible bias in the freshwater fluxes. Secondly, an experiment is run in which the mean surface forcing is applied on the hydrographic profiles observed in the AR7E and AR7W section since 1938 (described in Chapter 3). This experiment clarifies the importance of preconditioning to deep mixing as well as the differences in the hydrographic situation of the Irminger and Labrador Seas. Thirdly, an experiment is run in which the NCEP surface heat and

freshwater fluxes from 1948 to 2007 are applied on the mean hydrographic profiles of the Irminger and Labrador Seas. The results of this experiment illustrate the relation between the variable surface forcing and the maximum winter mixed layer depth. Both experiments 2 and 3 are run with and without the freshwater flux in order to determine the influence of the freshwater flux on the maximum mixed layer depth. The last experiment combines the variability of the two previous experiments. On each observed hydrographic profile the surface forcing of the following winter is applied. This experiment is most straightforward to compare to the observation, but lacks the possibility of the sensitivity analysis.

The choice to use observed hydrographic profiles and atmospheric fluxes as input data, as opposed to artificial input data, is made consciously. While artificial data may be made to cover more fully the spectrum of possible profiles and fluxes, it does make it harder to compare the results to the observations. Since the record of observations covers both periods of very strong convection and periods of weak convection, the spectrum created by the observed hydrographic profiles should be wide enough to study the effect of preconditioning. Similarly, the fluxes observed between 1948 and 2007 cover a range of weak and strong winters. Thus, using the observations as model input will give a reasonable assessment of the importance of preconditioning and forcing, while yielding a more realistic range for the inter-annual variability of the maximum winter mixed layer depth than would have been obtained using artificially constructed input data.

The linear one dimensional model used for this study is introduced in Section 5.2. The input data for the model, both the hydrographic profiles and the heat and freshwater fluxes, are described in Section 5.3. The results of the first three experiments, which investigate the sensitivity of the mixed layer depth to the various parameters separately, are presented in Sections 5.4.1 to 5.4.3. In Section 5.4.4 the results of the fourth experiment, which combines the variability in the preconditioning and the forcing, are presented. This chapter concludes with the comparison of the results of experiment 4 with the observations, a discussion of the general results and their implications in Section 5.5.

5.2 Model set up

The encroachment model used for this study is a one-dimensional column model programmed in Matlab. The model assumes the existence of a shallow surface mixed layer, conservation of heat and freshwater (or salt) and as dynamics only the “no instability” condition. The model does not include entrainment and assumes a wind

mixed layer of constant depth. The model grid, between the sea surface and the sea floor, has a resolution of 1 dbar. The time steps, Δt, in the model are 2 hours. The model is stable with these time steps, the application of smaller time steps does not change the results. The model is initialized with an observed hydrographic profile of temperature (T) and salinity (S). NCEP reanalysis heat (Q) and freshwater fluxes (F) are applied on this profile using conservation of heat and freshwater. The application of Q and F on the temperature and salinity profile, as opposed to the direct application of the resulting buoyancy flux of the density profiles allows to see the seasonal changes in T and S at the mid-levels affected by mixing.

The surface fluxes routine assumes that a homogeneous wind mixed layer of 70 dbar depth exists throughout the year. Although this is strongly simplified, it is not unrealistic for the study area. The typical Ekman depth ($D_E = 4.3 \cdot W/(\sin \Phi)^{1/2}$ assuming that the surface currents (V_0) and wind speeds (W) are related as $V_0/W = 0.0127/(\sin \Phi)^{1/2}$, from *Pond & Pickart* (1983)) is about 40 m, using the mean winter wind speed of 8.4 m s^{-1} (Chapter 2). *Våge et al.* (2008) arrived at a similar mixed layer depth with the application of a wind driven mixed layer based on the bulk Richardson number and the gradient Richardson number.

All applied fluxes are first distributed over the shallow wind mixed layer, which causes it to act as a buffer to large density changes. The temperature of the surface layer is changed by the heat flux through Equation 5.1:

$$T(t_1) = T(t_0) + \frac{1}{\rho C_p} \frac{Q \Delta t}{D_w} \qquad (5.1)$$

In which T, the temperature of the wind mixed layer at time t_1, is determined by the temperature at the previous time step, t_0, and the heat flux Q distributed over the depth of the wind mixed layer D_w. C_p is the heat capacity of seawater and ρ is the density of the wind mixed layer at t_0. Similarly, the salinity of the wind mixed layer is changed by the freshwater flux through Equation 5.2:

$$S(t_1) = S(t_0) - \frac{S_{ref}}{\rho} \frac{(P - E)\Delta t}{D_w} \qquad (5.2)$$

In which the salinity at time t_1 is determined by the salinity at t_0, and the freshwater flux *(*here *P-E)* distributed over the wind mixed layer D_w. The reference salinity, S_{ref}, is assumed to be the mean salinity of the upper 100 dbar of the initial salinity profile.

After application of the surface fluxes on the wind mixed layer, the stability of the water column is evaluated. As long as the density of the wind mixed layer is lower than the density at deeper levels, the water column is stable and the model continues to the next time step. However, when the density of the surface mixed layer surpasses that of the lower layers, the model proceeds with the mixing routine. In this routine the mixed layer depth initially increased with increments of 2 dbar, which was changed to 5 dbar later to reduce the number of iterations. The density of this new deeper mixed layer is calculated by homogenizing (averaging) the temperature and salinity profile over the new mixed layer depth. The density is then recalculated and the profile is reevaluated for stability. If the profile is found to be stable the model continues to the next time step, otherwise the mixed layer depth is increased again until the water column is stable. At each new time step the model starts again with an initial mixed layer depth of 70 dbar. This allows heat to be stored in the wind mixed layer during intermittent warming events, which must be removed by the following cooling fluxes before mixing can resume.

The model runs from the beginning of the cooling season, usually October, until the end of the cooling season some 190 to 280 days later. During the first part of the cooling season the summer stratification is removed and the mixing depth increases. Nearing spring the cooling is no longer sufficient to increase the mixed layer depth, a situation which may also occur intermittently during winter. Finally, the warming season starts and the model stops. The "mean" model run and the resulting mixed layer depths (MLDs) and hydrographic profiles are shown in Section 5.4.1. The mixing depths calculated by this encroachment model are considered maximum mixed layer depths. There is no advection in the model, making restratification by advection of warmer waters from the boundary currents impossible. Therefore the actual mixing depths in the Labrador and Irminger Sea are expected to be shallower. However, the model does give a qualitative indication of the response of the maximum possible mixing depth to changes in the initial profile and the applied surface flux.

5.3 Input data

5.3.1 Initial hydrographic profiles

The initial temperature and salinity profiles that are used as model input originate from the AR7E section (for the Irminger Sea) and from the AR7W section (for the Labrador Sea). These profiles and their variability were introduced and described in Chapter 3. The Labrador Sea time series consists of 62 temperature and salinity profiles observed between 1938 and 2005. The Irminger Sea time series consists of 50 temperature and salinity profiles observed between 1950 and 2008. Here the density

stratification of these profiles is briefly described. The observed density gradients in various parts of the water column of the central Irminger and Labrador Seas are contained in Table 5.1.

TABLE 5.1: Mean density gradients for different parts of the water column of the Irminger Sea and Labrador See. Also shown is the standard deviation, which is a measure for the inter-annual variability of the density stratification.

Depth interval [dbar]	Labrador Sea		Irminger Sea	
	mean [10^{-5} kg m^{-3} dbar^{-1}]	std [10^{-5} kg m^{-3} dbar^{-1}]	mean [10^{-5} kg m^{-3} dbar^{-1}]	std [10^{-5} kg m^{-3} dbar^{-1}]
1 to 200	13.30	12.19	248.15	138.70
200 to 500	16.58	9.06	20.55	10.90
500 to 1000	4.88	1.62	6.62	2.90
1000 to 1500	4.04	1.53	5.79	2.43
1500 to 2000	5.68	2.10	6.69	1.84

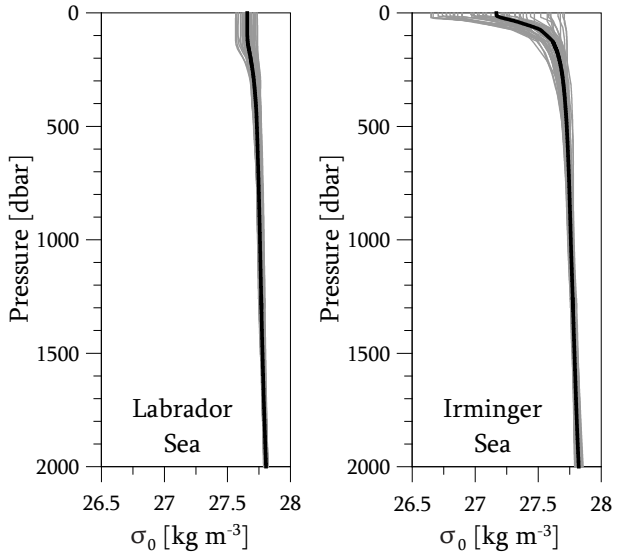

FIGURE 5.1: Potential density anomaly (σ_0) profiles from the Labrador Sea (on the left) and from the Irminger Sea (on the right). All observed profiles are drawn in grey, the mean profile is drawn in black.

The upper two layers, above 500 dbar, contain the strongest stratification. Many profiles are made at the end of summer, thus the profiles can be considered to be fully (re-)stratified. Notably, the stratification in the Irminger Sea is an order of magnitude larger than in the Labrador Sea. This can also be seen from Figure 5.1, which illustrates the vertical density profiles. The Subpolar Mode Water in the Irminger Sea,

originating from the warm boundary currents, creates a strong temperature stratification near the surface and thereby a strong density gradient. The boundary currents in the Labrador Sea are colder and denser, leaving the centre of the basin less stratified than that of the Irminger Sea (Figure 5.1). The intermediate and lower layers in the Irminger and Labrador Sea are quite similar in stratification (Table 5.1 & Fig. 5.1). These are the layers where Labrador Sea Water is found in both basins. Its interannual variability in stratification is relatively low.

It is expected that the stratification in the upper 500 dbar is an important parameter determining the maximum mixed layer depth in winter, especially in the Irminger Sea. There the surface stratification is both strong and highly variable, which makes it likely that it will produce a high variability in maximum mixed layer depths. In the Labrador Sea the surface stratification is both lower and less variable, and the variability in surface forcing is expected to contribute most strongly to the variability in the maximum mixing depths.

5.3.2 Surface forcing

The input fluxes used for the model are the heat (Q) and freshwater (F) fluxes from the NCEP reanalysis. These data are provided by the NOAA-CIRES Climate Diagnostics Center, Boulder, Colorado, from their web site at http://www.cdc.noaa.gov/. Daily mean values for the total heat flux and freshwater flux between January 1948 and July 2008 were used for this study (Chapter 2). Here the average daily mean heat and freshwater fluxes were used as input for the model. The average daily means were composed by averaging the daily means for each day of the year (with the exception of February 29th) in the 1948 to 2007 NCEP time series. The resulting mean time series for cooling period over the Labrador Sea and the Irminger Sea are shown in Figure 5.2. The cooling period is defined here to be the period from the first day with cooling fluxes in autumn to the last day with cooling fluxes in spring. This definition was chosen over the standard extended winter, October to March, because it allows intermittent warming events to be included in the winter period and does not "cut off" winter cooling that continues after March.

The mean cooling season over the Labrador Sea lasts 221 days, has an average downward heat flux of -184 W m^{-2} and a minimum (max. cooling) of -379 W m^{-2}. The freshwater flux over the Labrador Sea is positive at the beginning of winter and negative towards the end of winter, leading to an average freshwater gain of $1.4 \cdot 10^{-5}$ kg m^{-2} day^{-1}. Over the Irminger Sea the cooling period lasts 210 days, has an average heat flux of -146 W m^{-2} and a minimum of -269 W m^{-2}. The atmospheric freshwater flux over the

Irminger Sea remains positive throughout winter, giving an average freshwater flux of $2.2 \cdot 10^{-4}$ kg m^{-2} day^{-1}, an order of magnitude larger than the freshwater flux over the Labrador Sea. Most of the meso-scale variability is suppressed in these averaged time series, but some daily variability remains (Fig. 5.2).

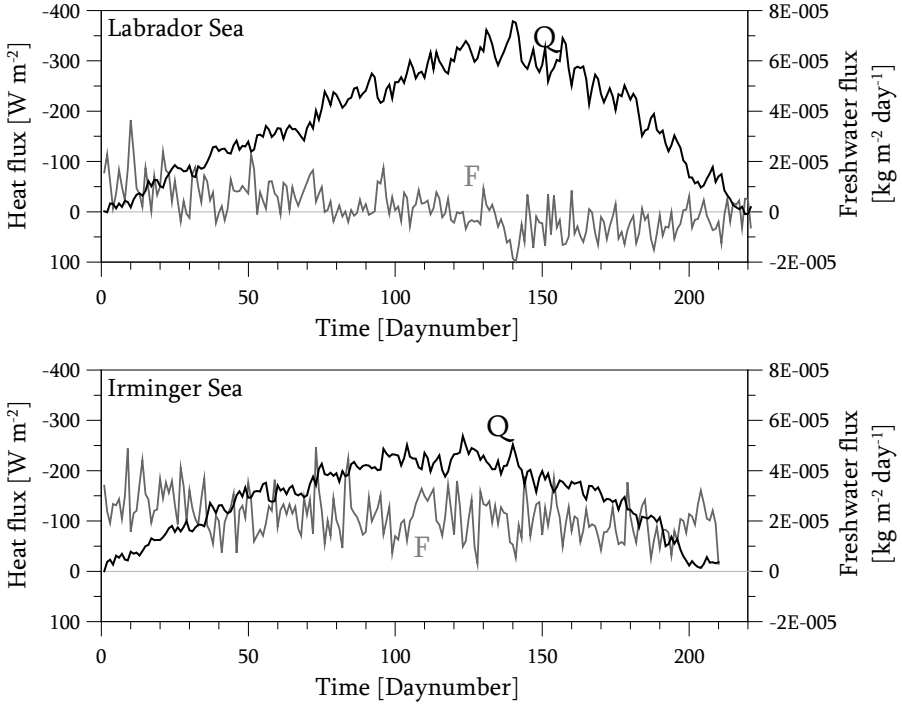

FIGURE 5.2: Mean forcing over the Irminger and Labrador Seas based on the time series of the net heat flux (with negative fluxes indicating heat loss for the ocean) and the net freshwater flux (positive fluxes indicate freshwater gain) derived from the 1948-2008 NCEP reanalysis data. The upper panel illustrates the 1948-2007 average daily mean forcing for the Labrador Sea, with the heat flux drawn in black and the freshwater flux in grey. The lower panel shows the time series of the heat (black line) and freshwater forcing (grey line) over the Irminger Sea.

The inter-annual variability in the heat and freshwater forcing over the Irminger and Labrador Sea is much larger than the seasonal variability. The time series of the mean heat and freshwater flux for each winter cooling period are shown in Figure 5.3. In this figure the summed daily heat and freshwater fluxes are also shown. The cumulative winter fluxes (*Qsum* and *Fsum*), or summed daily heat flux, are the sum of all the daily fluxes during the cooling period. This formulation takes both the variability in strength of the fluxes and in the length of the cooling season into account. Nevertheless, the correlation between the mean heat flux (*Qmean*) and *Qsum* is high, R^2 =

0.87 for the Irminger Sea and $R^2 = 0.92$ for the Labrador Sea. The range of variability is larger over the Labrador Sea, with values of *Qmean* between -99 and -269 W m^{-2}, compared to the range over the Irminger Sea (between -70 and -166 W m^{-2}). Although the cooling fluxes over the Irminger Sea are smaller than those of the Labrador Sea, they are still considered high for the open ocean and may initiate similar, although shallower, mixing as observed in the Labrador Sea. However, the variability in mixed layer depth is expected to be larger for the Labrador Sea, due to the large range of the cooling fluxes.

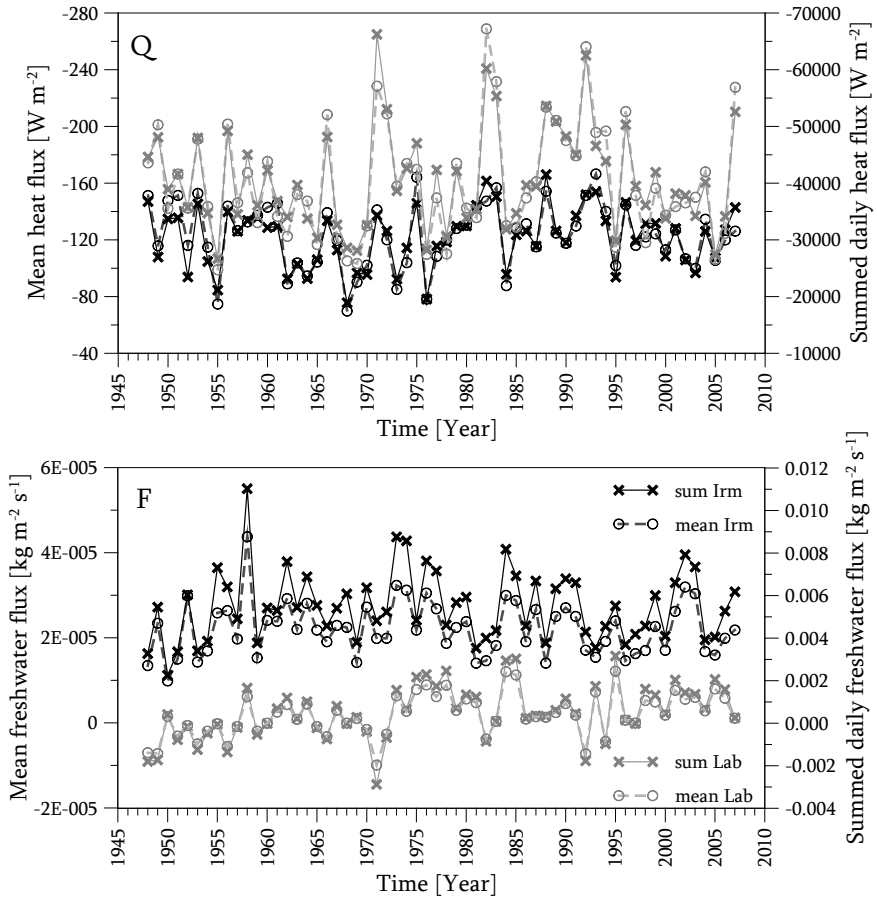

FIGURE 5.3: Year-to-year variability in the winter (cooling period) heat and freshwater flux illustrated by the time series from the NCEP reanalysis. Time series are shown for the Labrador Sea (in grey) and for the Irminger Sea (in black). The upper panel shows the mean winter heat fluxes (dotted line with open circles) and the total winter summed daily heat flux (solid line with crosses). The lower panel shows the mean winter freshwater flux (dotted line with open circles) and the total winter summed daily freshwater flux (solid line with crosses).

The situation is reversed for the freshwater fluxes, with larger mean fluxes and variability over the Irminger Sea. The freshwater fluxes are between $1.0 \cdot 10^{-5}$ and $4.4 \cdot 10^{-5}$ kg m^{-2} day^{-1} there. Labrador Sea freshwater fluxes are alternating between net negative winter fluxes and net positive fluxes, with a range between $-1.0 \cdot 10^{-5}$ and $1.2 \cdot 10^{-5}$ kg m^{-2} day^{-1}. The inhibiting effect of atmospheric freshwater fluxes, which lower the density of the surface, is therefore expected to be largest over the Irminger Sea. The parameter *Fsum* is the summed daily freshwater flux over the cooling period. The correlation between *Fsum* and *Fmean* is also reasonably high, $R^2 = 0.95$ for the Irminger Sea and $R^2 = 0.99$ for the Labrador Sea.

The temporal variation of the atmospheric fluxes, both heat and freshwater, over the Irminger Sea seem to follow those over the Labrador Sea. This may be expected, since both areas are exposed to similar large scale weather systems. However, the actual correlation between the Labrador and Irminger fluxes is not so high. For *Qsum* $R^2 = 0.53$, which may still be considered to be significant. For *Fsum* the correlation is lower, with $R^2 = 0.16$. Thus different processes seem to be at work here.

5.4 Results

5.4.1 Mixing in the mean situation

The first experiment examines the mean behaviour of the mixed layer depth in the model. The long term (1948 to 2007) mean NCEP heat and freshwater fluxes over the central Irminger Sea (Fig. 5.2) are applied on the mean temperature and salinity profiles of the 1950 to 2008 time series of the Irminger Sea (Fig. 5.1). Similarly, the long term NCEP mean fluxes over the central Labrador Sea are applied to the mean hydrographic profiles of the 1938 to 2005 time series of the Labrador Sea. The evolution of the simulated mixed layer depth and of the temperature and salinity profiles is illustrated in Figure 5.4.

The Labrador Sea is more strongly predisposed to deep mixing due to stronger cooling, a lower freshwater flux and a weaker initial stratification. This results in a maximum mixed depth of 2005 dbar for the mean Labrador Sea situation. The maximum mixed layer depth in the Irminger Sea is 905 dbar for the mean situation. This shallower depth is due to the combination of weaker cooling, stronger initial stratification and a freshwater flux that is an order of magnitude larger than that of the Labrador Sea. This experiment does not show which of these factors is most important for the mixed layer depth, this is investigated in the following experiments.

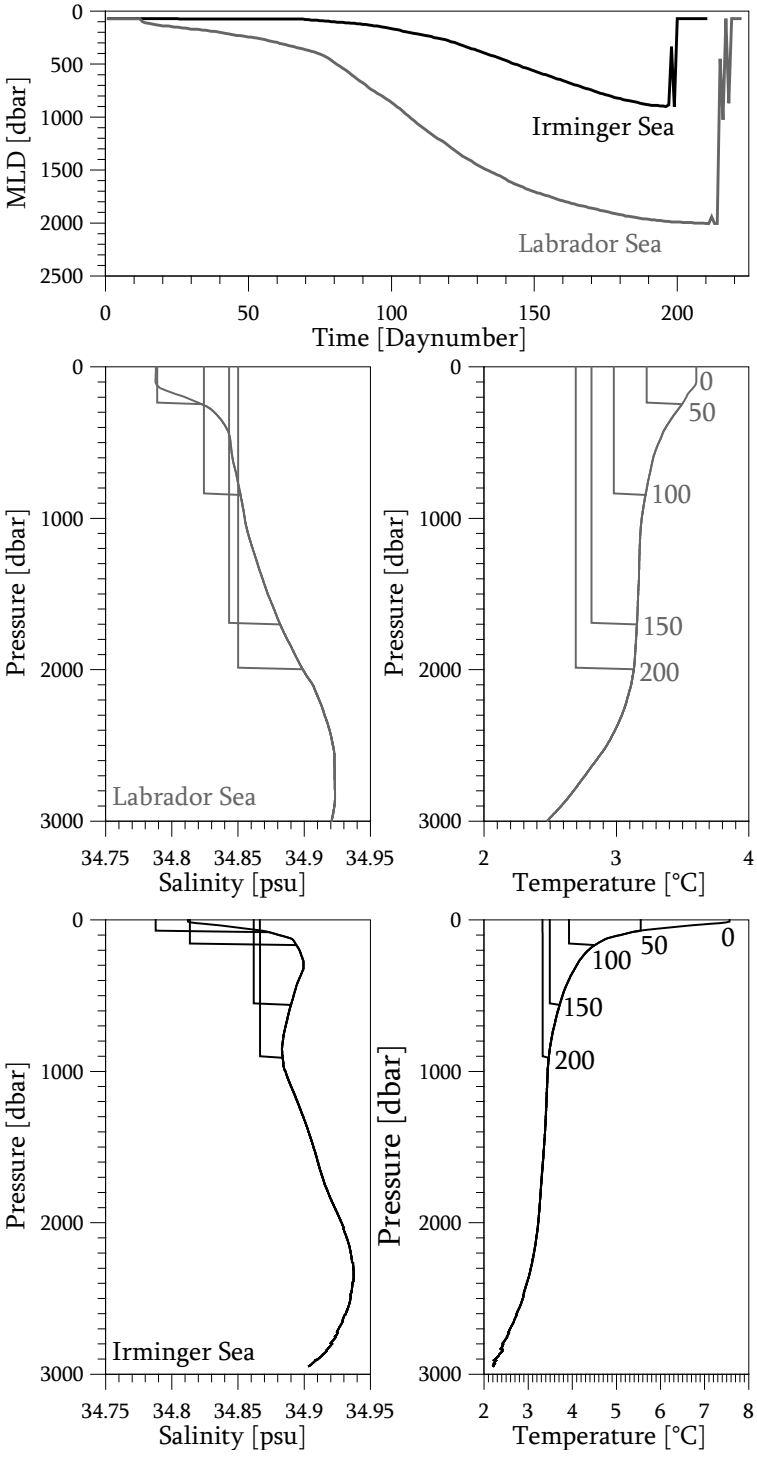

FIGURE 5.4: Evolution of the mixed layer depth in mean conditions.

The top panel shows the time series of the mixed layer depth for the Irminger Sea (in black) and for the Labrador Sea (in grey).

The lower four panels shows the hydrographic profiles at day 0, 50, 100, 150 and 200. Shown are the profiles for salinity (left) and temperature (right). The sequence of profiles from the Labrador Sea is shown in the middle panels. The sequence of profiles from the Irminger Sea is shown at the bottom.

The evolution of the vertical profiles is illustrated in Figure 5.4, which contains the initial vertical salinity and temperature profiles as well as the profiles at day 50, 100, 150 and 200, for the Labrador and the Irminger Seas. One of the main differences between mixing in the Labrador Sea and the Irminger Sea which becomes apparent here, is the time needed to remove the stratification in the near-surface layer. In the Labrador Sea the salinity stratification over the upper 200 dbar is removed in the first 40 days and the mixed layer depth reaches 500 dbar in 81 days. The initial temperature stratification is relatively small and is also strongly reduced during these 80 days. After this period the mixed layer depth increases rapidly. This is both due to the weak remaining stratification and the continued increase in cooling fluxes after day 80 (Fig. 5.2). The increase of the mixed layer depth slows down around day 160, after maximum cooling has taken place. The mixed layer depth continues to increase slowly until a few days before the end of the cooling period. The variation in mixed layer depth at the end of the cooling period is due to some intermittent warming. The temperature profile at day 200, near the end of the mixing period, shows a strongly cooled mixed layer. A quick examination of the salinity profiles shows that the surfaces between the initial profile and the profile at day 200, above and below their intersection at ~900 dbar, are nearly equal. Thus the resulting salinity of the mixed layer is set by homogenization of the salinity profile, rather than freshwater input from the atmosphere.

In the Irminger Sea the mixed layer is limited to the wind mixed layer until the strong temperature stratification in this near-surface layer is removed (Figure 5.4, note the difference between the temperature scales for the Labrador and Irminger Seas). The salinity profiles show initial freshening of the mixed layer due to the collection of precipitation. This increases the salinity stratification and delays the increase in mixed layer depth compared to the Labrador Sea. The stratification over the upper 200 dbar is removed in 106 days and after 143 days the mixing depth reaches beneath 500 dbar. At this time the heat flux has already passed its maximum cooling flux. Decreasing cooling fluxes and stronger stratification in the layer between 500 and 1000 dbar (Table 5.1) slows down the increase in mixed layer depth compared to the Labrador Sea. At day 210, the cooling period over the Irminger Sea ends. At this time the mixed layer depth has reached 905 dbar, the approximate level of the mean salinity minimum. By mixing down to this depth, the salinity minimum receives additional fresh water(from the overlying waters and the precipitation excess). However, this mixed layer depth is not deep enough to reach into the most weakly stratified layer of the Irminger Sea (1000 to 1500 dbar, Table 5.1).

Errors due to the uncertainty in freshwater fluxes

The results of the mean simulation for the Irminger Sea suggests that the freshwater flux may be an important inhibitor for mixed layer deepening. However, the uncertainty in the freshwater fluxes is large (Chapter 2) and may result in errors in the simulated mixed layer depth. In order to get an estimate for these errors the model is run again with the mean heat flux, but once with the freshwater flux (F) set to zero and once with a double freshwater flux. For the Irminger Sea, the change in the maximum mixed layer depth is -330 dbar for the double F case and +275 dbar for the zero F case. If we assume that the error in the freshwater fluxes does not surpass 50% of the mean freshwater flux, then the expected resulting error in the maximum mixed layer depth will be ~200 dbar in the Irminger Sea.

For the Labrador Sea the change in mixed layer depth is only -5 dbar for the double F case and +10 dbar for the zero F case. This is due to the small value of F over the Labrador Sea. When combining the Irminger Sea mean freshwater flux, which is an order of magnitude larger, with the Labrador Sea profile and heat flux the original mixed layer depth of 2005 dbar is reduced by 130 dbar. This shows that not only the (influence of the) atmospheric freshwater flux is smaller over the Labrador Sea, but also that the Labrador Sea is more stable to changes in the freshwater flux, making the expected error in the maximum mixed layer depth for the Labrador Sea only 10 dbar.

5.4.2 Sensitivity to preconditioning

In this experiment the mean heat and freshwater flux from the Irminger and Labrador Seas are applied on the time series of hydrographic profiles from the respective basins. These profiles were observed during times of strong convection (early 1990s) as well as during periods of weak or nearly no convection. This allows us to investigate the influence of the stratification (preconditioning) on the maximum mixed layer depth that may be reached in winter.

Four model runs were performed for this experiment, two for each basin. In the first set, the mean winter heat and freshwater fluxes of the Irminger (Labrador) Sea were applied on the series of hydrographic profiles from the Irminger (Labrador) Sea. In the second set the mean heat flux was applied as before and the freshwater flux was set to zero. The resulting maximum mixed layer depths are plotted against the initial stratification in Figure 5.5. Shown on the x-axis is the initial density stratification in the layer that correlated best with the calculated mixed layer depths. The results for the Irminger Sea give a range of mixed layer depths of 275 to 1950 dbar, with an average of 800 dbar. Here, the maximum mixed layer depth correlates best with the

stratification in the layer between 200 and 500 dbar, with an R^2 of 0.53. Out of the 50 hydrographic profiles from the Irminger Sea only 15 allow a MLD surpassing 1000 dbar. These 15 deeper mixed layers also correlate similarly ($R^2 = 0.53$) with the stratification between 1000 and 1500 dbar. The difference between the resulting mixed layer depth with and without freshwater fluxes is 192 dbar on average, which is within a likely error. Model runs without applied freshwater flux correlate slightly better with the stratification between 200 and 500 dbar ($R^2 = 0.56$) in the Irminger Sea.

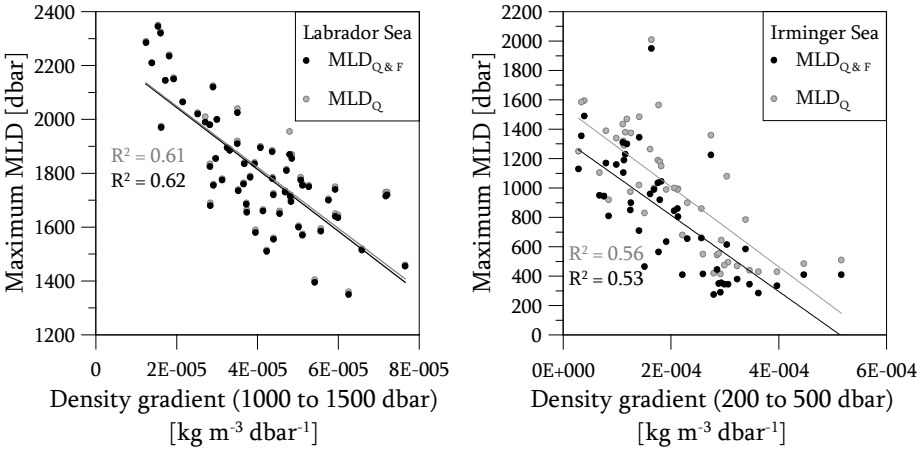

FIGURE 5.5: Maximum mixed layer depths (MLD) versus stratification. The MLDs are plotted against the stratification of the layer that correlates best with the MLD. This is the layer between 1000 and 1500 dbar for the Labrador Sea (on the left) and between 200 to 500 dbar for the Irminger Sea (on the right). Note the difference in scale on the bottom axes, this is due to the different reference layers for the density gradient in both basins.

For the Labrador Sea, the range of mixed layer depths is 130 dbar to 2345 dbar, with an average MLD of 1812 dbar. The difference in MLD with and without freshwater flux is barely visible in Figure 5.5. The average difference is only 7 dbar, within the estimated error. Because of the weaker surface stratification, the maximum mixed layer depth in the Labrador Sea correlated best to the density gradient in the layer between 1000 and 1500 dbar. The correlations are given in Figure 5.5.

5.4.3 Sensitivity to atmospheric forcing

This forcing experiment subjects the mean hydrographic profiles of the Irminger and Labrador Seas to their annual winter fluxes from the NCEP reanalysis. These fluxes, which cover the winters from 1948-1949 to the winter of 2007-2008, exhibit a large range in variability, especially in the heat fluxes (Fig. 5.3). The resulting range in

mixed layer depths is 1420 to 2255 dbar for the Labrador Sea and 205 to 1325 dbar for the Irminger Sea. Without freshwater forcing the range is slightly smaller for both seas, between 1495 and 2210 for the Labrador Sea and between 455 and 1430 for the Irminger Sea. Surprisingly, the larger range in heat fluxes over the Labrador Sea does not lead to a larger range in mixed layer depth. Due to the weaker surface stratification and generally high cooling in the Labrador Sea the mixed layer always reaches below 1000 dbar in this experiment, thus mixed layers are deep but the variability is low compared to the Irminger Sea.

Also for these experiments the model runs were performed with and without freshwater fluxes. The resulting maximum mixed layer depths are $MLD_{Q\&F}$ (with the heat and freshwater flux) and MLD_{Q} (only the heat flux, without freshwater flux). The range in the change in mixed layer depth (MLD_{Q} - $MLD_{Q\&F}$) in the Labrador Sea is small, between -45 and 85 dbar (Figure 5.6), due to the small range in freshwater fluxes. Negative freshwater fluxes also cause a deepening of the MLD here due to their added density contribution. The range in MLD changes in the Irminger Sea is an order of magnitude larger, 90 to 540 dbar (Figure 5.6). Thus, as expected, the larger freshwater fluxes over the Irminger Sea can cause a significant reduction in the mixed layer depth, up to several hundred dbar.

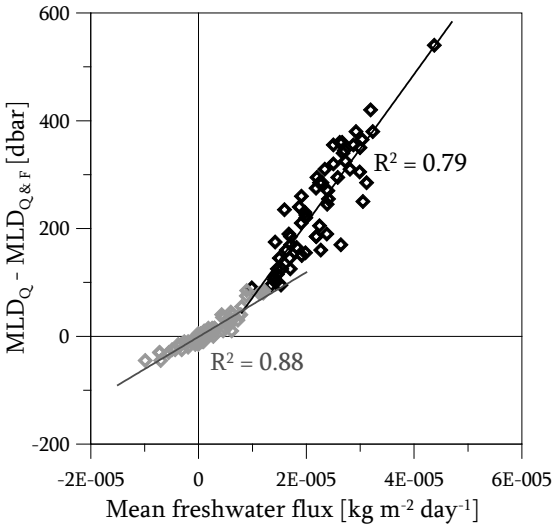

FIGURE 5.6: Change in mixed layer depth due to the freshwater forcing versus the mean winter freshwater forcing. Values for the Irminger (Labrador) Sea are plotted in black (grey).

The mixed layer depths (both with and without the freshwater forcing) correlate well with the mean and cumulative winter heat flux (Figure 5.7). The correlation is better for the Labrador Sea, but still strong for the Irminger Sea. The correlation of the mixed layer depth with the various parameters related to the heat and freshwater flux are summarized in Table 5.2 for the Labrador Sea and in Table 5.3 for the Irminger Sea.

Overall, the mixed layer depth correlates best with the parameter that accounts for both the strength and the duration of the winter period, the summed daily heat flux. This parameter explains almost all of the variability. Notably, the correlation with the maximum heat flux is much lower, while it is often assumed that very short but strong cooling events cause deep mixed layers (Marshall & Schott (1999)). Apparently, these strong cooling events or cold bursts are only sufficient for deep mixing when they add to an already high mean (and summed) heat flux or when the cold bursts are numerous enough to raise the mean heat flux. Some examples of this are shown in Figure 5.8.

In this figure the daily heat fluxes and daily mixed layer depths are shown for three winters. The first winter, that of 1982-1983, has the highest summed heat flux in the NCEP time series, both due to its long duration (274 days) and its high maximum fluxes. The mixed layer reached deepest during this winter. The second winter, 1993-1994, is known for its high heat fluxes and the formation of LSW_{94} in the Labrador Sea. This winter has the highest mean heat flux, but maxima were lower than those seen in 1982-1983. The cooling period lasted only for 231 days, making the cumulative heat flux much lower. Nevertheless, maximum mixed layer depths are not much shallower than in the previous

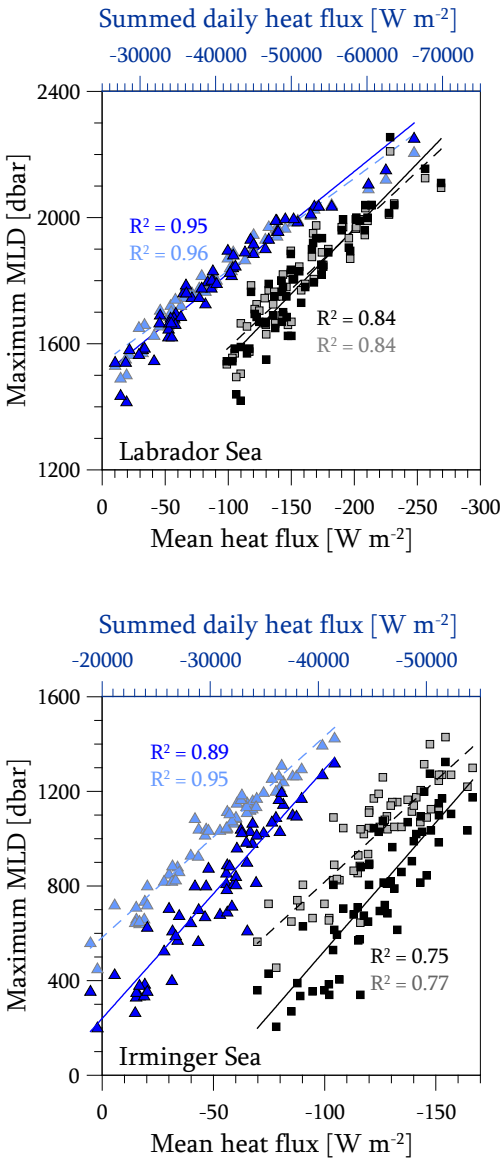

FIGURE 5.7: Mixed layer depths versus mean applied heat fluxes (black and grey squares, bottom axis) and summed heat flux (dark and light blue triangles, top axis). Values for the Labrador (Irminger) Sea are in the upper (bottom) panel. Results from model runs with (without) freshwater fluxes are plotted in darker (lighter) colours.

case. The third winter, 2004-2005, was similar to the first winter in the maximum heat fluxes that were reached, but both *Qmean* and *Qsum* are much lower. Due to the short and strong cooling events the MLD reached down to 860 dbar, but the mixing was frequently interrupted by warming periods. Possibly short cooling events are more important in the real ocean, where the mixing must outpace the restratification by eddies from the encircling boundary current. However, even in the real ocean a large amount of heat needs to be removed to reduce the initial summer stratification. The total heat lost in winter must therefore also be one of the important factors that determine the maximum mixed layer depth in winter.

TABLE 5.2: Coefficients of determination (R^2) for the correlation between mixed layer depths and forcing for the Labrador Sea. $MLD_{Q\&F}$ is the simulated maximum mixed layer depth using both the heat and freshwater fluxes, MLD_Q is the maximum mixed layer depth using only the heat flux.

	$MLD_{Q\&F}$	MLD_Q	MLD_Q - $MLD_{Q\&F}$
Mean *Q*	0.84	0.84	-
Max *Q*	0.46	0.50	-
Sum *Q*	0.95	0.96	-
Mean *F*	0.35	-	0.88
Max *F*	0.00	-	0.05
Sum *F*	0.34	-	0.88

TABLE 5.3: Coefficients of determination (R^2) for the correlation between mixed layer depths and forcing for the Irminger Sea. $MLD_{Q\&F}$ is the simulated maximum mixed layer depth using both the heat and freshwater fluxes, MLD_Q is the maximum mixed layer depth using only the heat flux.

	$MLD_{Q\&F}$	MLD_Q	MLD_Q - $MLD_{Q\&F}$
Mean *Q*	0.75	0.77	-
Max *Q*	0.28	0.30	-
Sum *Q*	0.89	0.95	-
Mean *F*	0.46	-	0.79
Max *F*	-0.05	-	0.07
Sum *F*	0.42	-	0.75

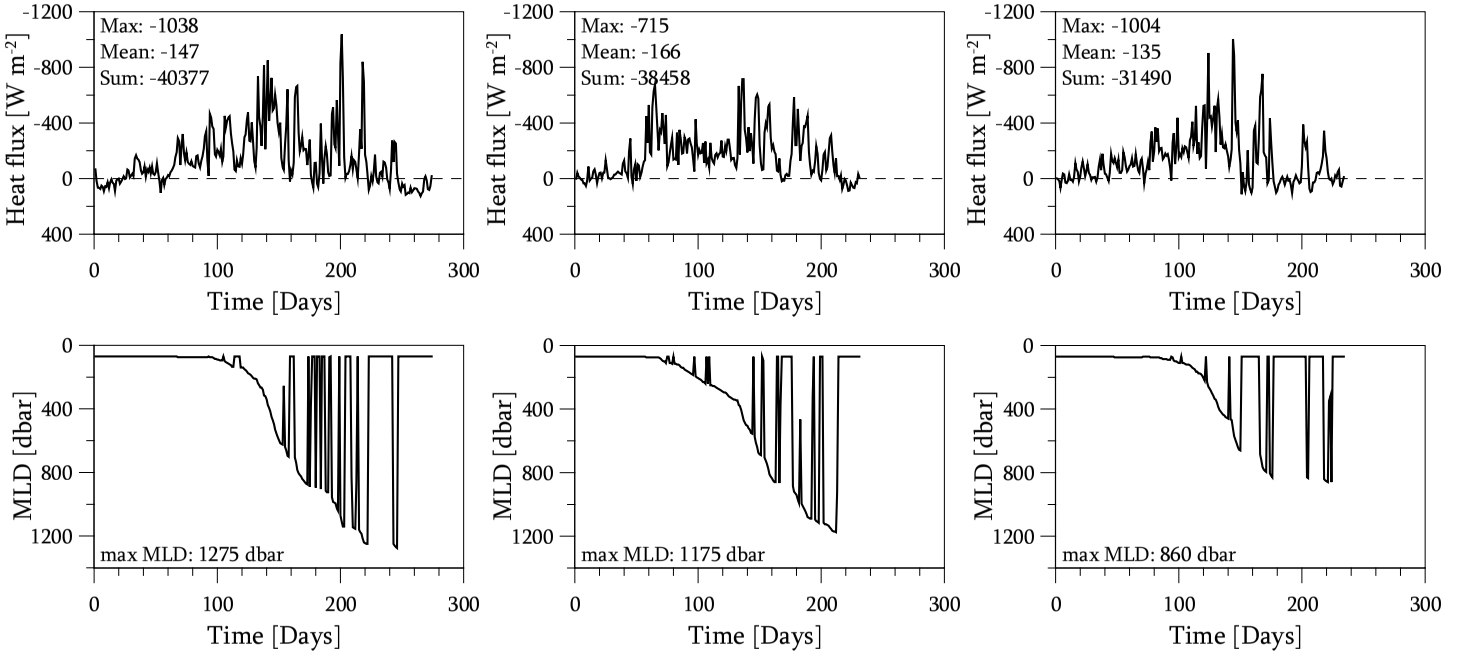

FIGURE 5.8: Three examples of applied heat fluxes and resulting mixed layer depths in the Irminger Sea. The three panels show the winter of 1982-1983 (on the left), 1993-1994 (in the middle) and 2004-2005 (on the right). The heat fluxes during the cooling period are drawn in the top panels. The values for the mean, summed (cumulative) and maximum heat flux are indicated in the graph. Daily mixed layer depths are drawn in the bottom panels, with the maximum mixed layer depth indicated in the graph.

5.4.4 TOTAL INTER-ANNUAL VARIABILITY IN MIXED LAYER DEPTH: ANNUAL FLUXES APPLIED ON ANNUAL HYDROGRAPHIC PROFILES

Finally, in this last experiment, the hydrographic profiles from 1948 to 2007 were exposed to the respective heat and freshwater fluxes from their year of observation. The hydrographic profiles from before 1948 were not used because reliable estimates of the atmospheric forcing from these years are not available in the NCEP reanalysis. The combination of the inter-annual variability in the hydrographic profiles with the inter-annual variability in surface fluxes is expected to give the largest range in maximum mixed layer depths. Also, the mixed layer depths, simulated in this experiment, should resemble the observed mixed layer depths best. Therefore the resulting time series of maximum mixed layer depths in the Labrador Sea, together with the time series of stratification and cumulative heat flux for the Labrador Sea are presented in Figure 5.9.

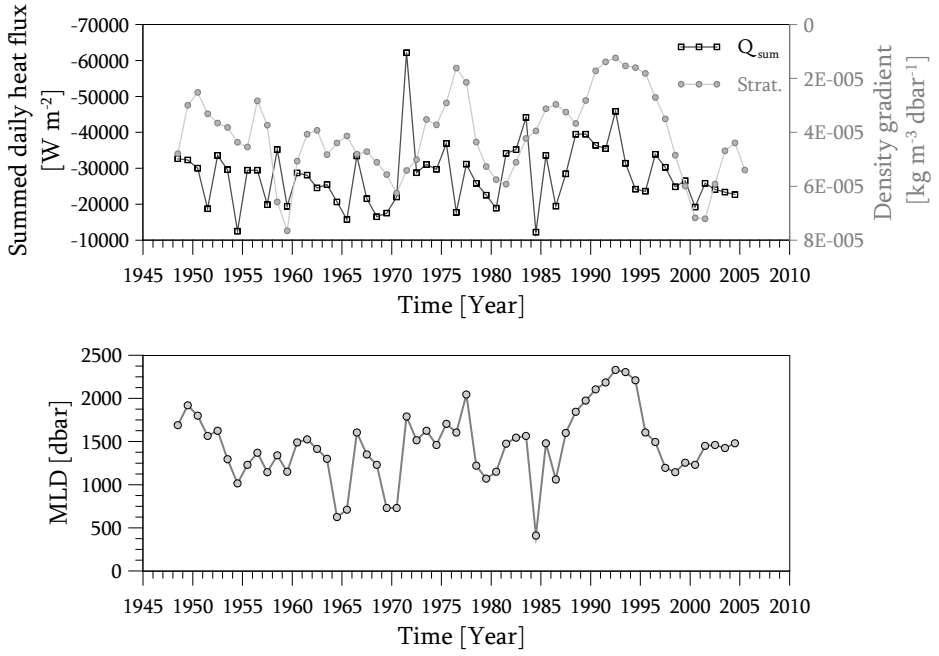

FIGURE 5.9: Labrador Sea stratification, daily summed heat flux and simulated maximum mixed layer depth (MLD) as a function of time. The top panel contains the observed density gradient over the layer between 1000 and 1500 dbar (grey line and filled circles) and the summed daily heat flux (black line and open squares). The bottom panel contains the time series of annual maximum mixed layer depths calculated by the model.

The range of resulting maximum mixed layer depths in the Labrador Sea is 410 to 2330 dbar, with an average depth of 1453 dbar. The mixed layer depth follows both (or rather alternatingly) the heat flux and the stratification. For example, between 1960 and 1970 the MLDs mainly follow the heat flux. During this period the heat fluxes were too low to initiate mixing into the weakly stratified layer. In the 1980s the MLD first follows the heat flux, with the sharp drops in 1984 and 1986. During the late 1980s and the late 1990s the preconditioning density gradient seems to determine the MLD again. However, the deep mixed layers during this period are a combination of the weak stratification and the high heat fluxes that were also observed during this time.

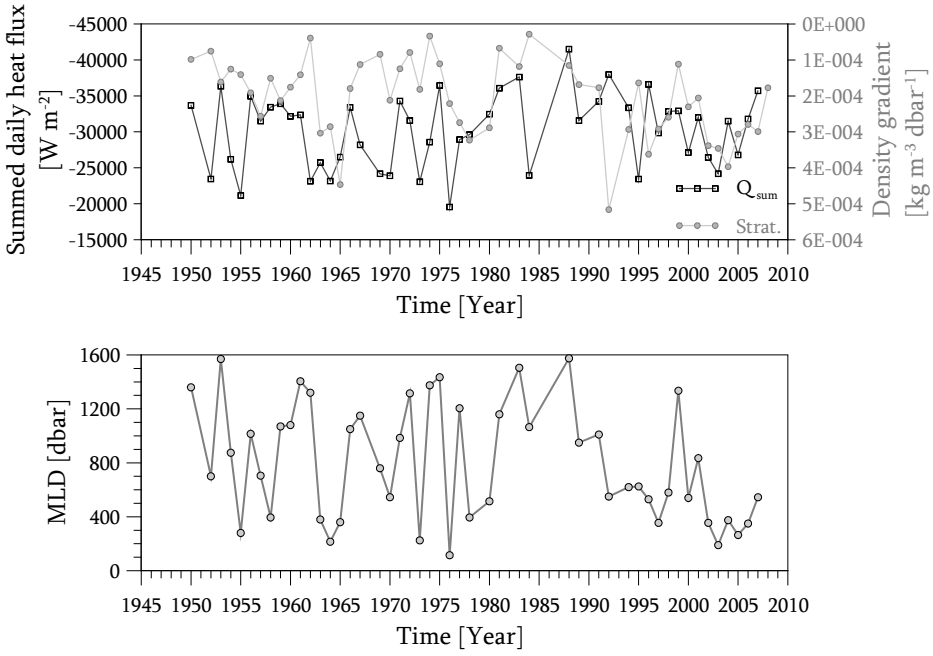

FIGURE 5.10: Irminger Sea stratification, annual cumulative heat and simulated mixed layer depth. The top panel contains the observed stratification over the layer between 1000 and 1500 dbar (grey line and filled circles) and the annual cumulative heat flux (black lien and open squares). The bottom panel contains the time series of annual maximum mixed layer depths calculated by the model.

In the Irminger Sea (Figure 5.10) the range of mixed layer depths is 115 to 1575 dbar, with an average of 798 dbar. Although the overall range is smaller than that of the MLDs simulated in the Labrador Sea the year-to-year persistence is clearly less. This could be due to the dependance of the Irminger Sea mixed layer depth on the stratification of a relatively shallow layer (200 to 500 dbar), in which the inter-annual

variability is large. For the Labrador Sea this is less so, since it seems to depend on the stratification of the layer between 1000 and 1500 dbar, where changes are slower and smaller (Figure 5.9). Further comparison between the mixed layer depths simulated in the Labrador and Irminger Seas shows that nearly all simulated mixed layers for the Irminger Sea are shallower than those simulated in the Labrador Sea in the same year. In the Irminger Sea the mixing is not able to reach below 500 dbar in about 30% of the simulations (14 years). Only 2% of the simulations (1 year) do not reach below this depth in the Labrador Sea. These shallow mixed layers are mostly related with relatively low heat fluxes in winter, but some combinations of high fluxes and very strong stratification also occur.

The simulated time series of mixed layer depths can be compared with the observed mixed layer depths in the Labrador and Irminger Seas. *Lazier et al.* (2002) and *Yashayaev et al.* (2008) describe the depth of the mixed layers in the Labrador Sea between 1990 and 2000. They mention mixed layer depths exceeding 2000 dbar and increasing to 2300 dbar in the early 1990s, decreasing to about 1000 dbar between 1995 and 1999, followed by a convective event reaching down to 1600 dbar in the winter of 2000 (Figure 5.11). *Lilly et al.* (1999) describe observations of a mixed layer depth of about 1700 dbar for the winter of 1994-1995 in the Labrador Sea and *Rhein et al.* (2007) describe depths between 1200 and 1300 m from 2003 to 2005. These observed values are plotted together with the simulated values from the last experiment in the left panel of Figure 5.11. The strong convective event in the early nineties is captured reasonably well by the simulations of this experiment. However, the simulated mixed layer depths in the late nineties seem to overestimate the observed mixed layer depth.

Observations of mixed layers are less abundant in the Irminger Sea, but there are some. In Chapter 4, Figure 4.1 illustrated the restratification after mixing in the winter of 1990-91. From this figure the estimated mixed layer depth for 1991 is at least 1000 dbar. In 1997 mixed layers down to 600 dbar were observed by floats in the Irminger Sea (Bacon *et al.* (2003)). The LOCO moorings, also described in the previous chapter, observed mixed layers down to 400 dbar in the winters of 2003-4 and 2006-7 and somewhat deeper mixed layers, down to 600 dbar, for the winters of 2004-5 and 2005-6. The fifth winter of the LOCO record, 2007-8, showed the deepest mixed layers, down to 900 dbar. These observed depths have also been plotted in Figure 5.11 (right panel).

For the Labrador Sea the model does well to simulate the deep mixed layers observed in the early nineties as well as the reduction of MLDs after 1994. However, the model tends to overestimate the maximum mixed layer depth in later years. The latter is

most likely caused by the lack of advection in the model. Advection of warm (or fresh) water from the boundary currents to the convective area restratifies the water column, thus counteracting the removal of stratification by cooling and mixing. The close match between the observed and simulated mixed layer depths in 1991 to 1994 is likely due to the strong stratification in the deeper layers. This strongly stratified layer acts as a restricting factor to the increasing mixed layer depths, rather than advective restratification. As stated above the low stratification at intermediate depths in the Labrador Sea hardly restricts deep convection. The deep stratified layer below 2100 dbar acts as a natural threshold for deep mixed layers, making it increasingly difficult to deepen the mixing layer below this level and thus making it also increasingly difficult to overestimate the deep mixing layers of the early nineties.

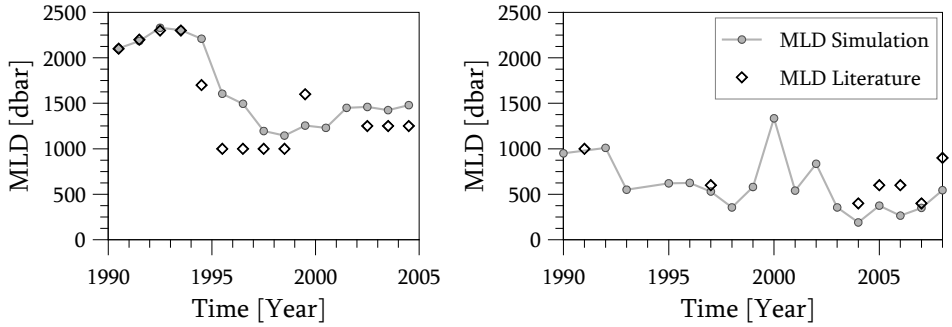

FIGURE 5.11: Simulated mixed layer depths from the last experiment, including all variability, and the observed mixed layer depths. On the left the values for the Labrador Sea, with the simulated MLDs drawn in small grey circles and the observed values in the black diamonds. On the right the values for the Irminger Sea, with the simulated MLDs drawn in small grey circles and the observed values in the black diamonds.

For the Irminger Sea the simulated time series of mixed layer depths predicts relatively low values, below 1000 dbar (Figure 5.11). There are a few exceptions, at the beginning of the series (in 1990 and 1992) and two peaks in 2000 and 2002. The difference between the deep mixing depths simulated in 1990 and 1992 and those of 2000 and 2002 is that homogeneous intermediate layers were present during the first period, but they were not observed during 2000 and 2002. The intermediate stratification was relatively strong during these years. These last two peaks are probably caused by a combination of low near-surface stratification and slightly higher than average cooling fluxes. The observed mixed layer depth in the winter of 1990-91 could not be simulated, since a 1990 hydrographic profile was not available in our time series. If we assume that the 1990 profile is similar to the 1989 profile, the resulting mixed layer depth for the 1990-1991 winter is 1000 dbar. This is similar to the simulated mixed

layer depth in the adjoining years. The mixing depth for 1997 is close to its observed value. The simulated MLDs near the end of the record are less than observed. Probably the locally observed deep mixed layers are not representative for the whole of the Irminger Gyre.

However, this model is too simple to accurately simulate the observed mixed layers and was only designed to test the sensitivity of the mixed layer depth to the various forcings. In order to estimate the relative importance of the stratification, the heat flux and the freshwater flux, in this sensitivity experiments, the MLDs from this experiment were plotted against the parameters that correlated best in the previous experiments (Fig. 5.12). These are the stratification between 200 and 500 dbar (1000 and 1500) for the Irminger Sea (Labrador Sea), the cumulative (summed daily) heat flux, and the mean freshwater flux. Their correlations with the MLD are indicated in Figure 5.12 and summarized here in Table 5.4.

TABLE 5.4: Coefficients of determination (R^2) for the correlations between the maximum mixed layer depths (MLD) in the Labrador and Irminger Seas with the stratification between 200 and 500 (1000 and 1500) dbar in the Irminger (Labrador) Sea, the cumulative heat flux (Q_{sum}) and the mean freshwater flux (F_{mean}).

	MLD Labrador Sea	MLD Irminger Sea
Stratification	0.32	0.43
Q_{sum}	0.41	0.26
F_{mean}	0.00	0.06

Due to the use of more than one variable parameter, the stratification and the atmospheric (heat and freshwater) forcing, the correlations in Table 5.4 are reduced with respect to the results of the previous experiments (Tables 5.2 and 5.3). However, the general conclusions remain the same. The variability in the freshwater flux is not of influence to the variability in the maximum mixed layer depth. The stratification (preconditioning) is most important in the Irminger Sea. Naturally, a weak stratification alone cannot cause deep mixing, surface heat fluxes are very important, but it is the strongest inhibiting factor for deep mixing in the Irminger Sea. In the Labrador Sea the situation is reversed. The stratification is weak enough to allow deep mixing in nearly all years. Here it is the strength of the winter cooling that strongly determines the maximum mixing depth. The variability of the stratification is also important, but less so.

5.5 Discussion & conclusion

The model results show that under mean conditions, applying the 1948-2007 mean freshwater and heat flux on the mean hydrographic profile (based on profiles collected between 1938 and 2005 for the Labrador Sea and between 1950 and 2008 for the Irminger Sea), gives a maximum mixed layer depth of 905 dbar in the Irminger Sea and 2005 dbar for the Labrador Sea. The deeper mixed layers in the Labrador Sea are caused by a combination of weaker stratification (stronger preconditioning) and larger winter heat loss. Uncertainties in the freshwater flux result in uncertainties in the simulated maximum mixed layer depth. Simulating the mean situation for the heat flux and the hydrographic profile with a freshwater flux set to zero and with a double freshwater flux gives an estimated maximum uncertainty. For the Labrador Sea this maximum uncertainty was estimated to be 10 dbar, while the estimated maximum uncertainty for the mixed layer depth of the Irminger Sea is 200 dbar. The larger estimated uncertainty for the Irminger Sea is caused by the magnitude of the Irminger freshwater flux, which is an order of magnitude larger than that of the Labrador Sea. Due to the relatively strong temperature stratification in summer these large freshwater fluxes are collected in the wind mixed layer where they enhance the stability of the salinity stratification and slow the convective mixing. In the Labrador Sea the deepening of the mixed layer in winter increases more quickly. This shortens the period in which the freshwater fluxes are collected in the upper layer and allows them to be distributed over the water column, which reduces their stabilizing effect on the salinity profile.

Further sensitivity studies show a strong dependance of the maximum mixed layer depth on the stratification between 200 and 500 dbar in the Irminger Sea. This is not unexpected since the stratification is quite strong and highly variable in this layer. The cooling fluxes are such that the convective mixing depth almost always reached beneath 200 dbar, even in relatively weak winters, making the stratification in the uppermost layer (0 to 200 dbar) less important. Since this layer is also affected by wind and wave mixing in the real ocean, which strongly reduces the stratification without cooling, this layer is not expected to be important for convective mixing in the Irminger Sea. Secondly the Irminger mixed layer depth depends on the surface heat flux. A large part of the winter cooling is needed to remove the temperature stratification in the upper 500 dbar before convection can reach deeper. This requires 75% of the mean winter flux for the mean hydrographic profile. The remaining 25% of the winter cooling is used to further increase the mixed layer depth below 500 dbar.

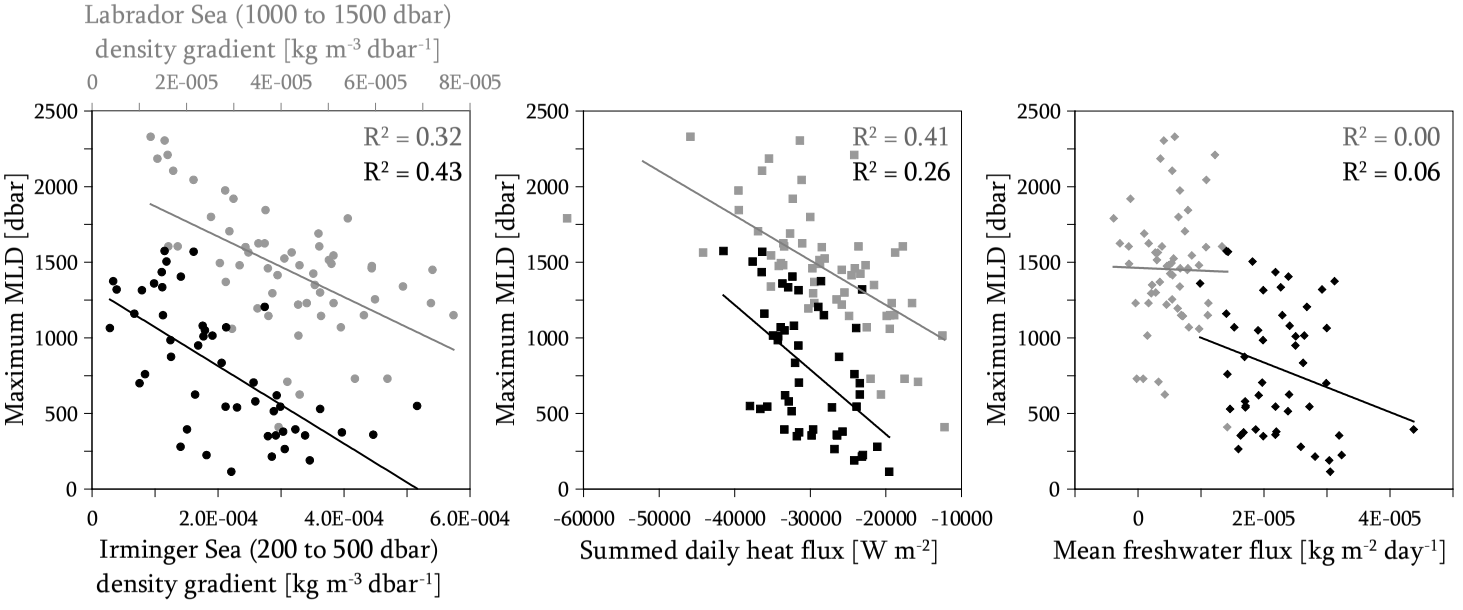

FIGURE 5.12: Mixed layer depths versus stratification (top panel), summed heat flux (middle panel) and the mean freshwater flux (bottom panel). Values for the Labrador Sea are drawn in grey. Values for the Irminger Sea are drawn in Black.

For the Labrador Sea the situation is reversed. The strength of the surface heat flux is most important and the stratification is of secondary importance. Due to the relatively weak stratification only 22% of the mean winter cooling is needed to remove the stratification over the upper 500 dbar of the mean hydrographic profile (in magnitude equivalent to 30% of the Irminger mean cooling flux). This means that a much larger portion of the total winter cooling is available to remove the stratification in the deeper layers. Based on observations from the Labrador and Irminger Seas where deep convection resumed in the cold winter of 2007-2008 without previous preconditioning, Våge *et al.* (2008) concluded that preconditioning is of secondary importance for both the Labrador and Irminger Seas. The model results agree with this conclusion for the Labrador Sea. In the Irminger Sea the stratification in the upper 500 dbar is most important in the experiments performed here. However, since this is a relatively shallow layer it would not need mixing down to 1000 dbar to be preconditioned (as is necessary in the Labrador Sea). Mixing down to depths of 400 dbar is regularly observed in the Irminger Sea (Chapter 4 and Bacon *et al.* (2003)). The preconditioning in the Irminger Sea may therefore depend more strongly on the build-up of stratification in summer, rather than the break-down of stratification in the previous winter.

Using both the variability in the atmospheric forcing and the hydrographic profiles, the model estimates a range for the inter-annual variability of the maximum mixed layer depth in the Labrador Sea of 410 to 2330 dbar (average 1453 dbar) and for the Irminger Sea a range of 115 to 1575 dbar (average 798 dbar). A comparison with the observations shows that mixed layers observed to be about 1 km deep in the Labrador Sea are overestimated by the model, while deeper mixed layers are modelled satisfactory (Figure 5.11). The overestimation of the shallower mixed layers is probably caused by the absence of an advective restratification process in the model, which would reduce mixed layers through the constant supply of lighter boundary current water to the convective area. It may also be due to an overestimation of the cooling fluxes by the NCEP reanalysis (Renfrew *et al.* (2002)). For the deep (>2000 dbar) mixed layers in the early nineties restratification is apparently less important for the maximum mixed layer depth, which is determined by the strong stratification beneath 2100 dbar. In the Irminger Sea the model does not overestimate the maximum mixed layer depths observed by the LOCO moorings (Chapter 4) between 2003 and 2008. Apparently the maximum mixed layer depth obtained at a single moment by the mooring overestimates the maximum mixed layer depth typical for the whole centre of the Irminger Gyre.

Overall the model results show that occasional convective mixing down to intermediate depths (>1000 dbar) is possible in the Irminger Sea. However, the conditions needed for convective mixing to reach below 1000 dbar in the Irminger Sea are stronger, or more strict, than in the Labrador Sea. The preconditioning must be such that the stratification in the upper 500 dbar is relatively weak. Furthermore the sea-to-air heat flux must be high, possibly enhanced by the Greenland tip jet (Pickart *et al.* (2003)), and last for a long time. During more moderate winters the convective mixing is unlikely to be able to reach below 500 dbar, independent of preconditioning. Thus, modification of the Subpolar Mode Water, which is found in the upper 500 dbar, and not formation of a type of "Irminger" Labrador Sea Water seems to be the prevailing mode of mixing in the Irminger Sea.

Chapter 6

A comparison of hydrographic observations and simulations by Coupled Climate Models and ocean reanalyses

Based on the paper:
M.F. de Jong, S.S. Drijfhout, W. Hazeleger, H.M. van Aken & C.A. Severijns (2009). Simulations of hydrographic properties in the northwestern North Atlantic Ocean in Coupled Climate Models, Journal of Climate, 22, 1767-1786, doi:10.1175/2008JCLI2448.1

6.1 Introduction

The performance of coupled ocean-atmosphere climate models (CCMs) in simulating the present climate has improved greatly during recent years. This is partly due to increased model resolution and a better understanding of physical processes. However, the resolution of the ocean component of global models is often still limited to about 1° x 1° (Table 6.1 in data section) which is about 90 x 90 km at 60° N. At this resolution many small scale ocean processes and boundary currents, which play an important role in the northwestern North Atlantic Ocean, cannot be resolved. Surface fluxes, which have a poor observational coverage over the ocean, have a major role in local adjustment of water masses and the formation of mode waters (Brambilla & Talley (2008)). The surface waters are furthermore dependent on a combination of sea-ice melt and advection. Convection plumes (~1 km) and convection areas (~100 km) are crucial in intermediate water mass formation (Marshall & Schott (1999)). Meso-scale eddies (~10-50 km), which are a large source of variability (Volkov (2005)), bring boundary current water to the centres of the basins and facilitate restratification after convection. The deep currents are gravity flows originating from the overflows, which are shallow (650 to 850 m depth) and narrow enough to fall between model grid points. All of these processes are difficult to include correctly into models and have a relatively large influence on the (local) ocean state and variability.

The northwestern North Atlantic Ocean is an important area in constituting the Meridional Overturning Circulation (MOC) and the climate of the North Atlantic region

(Marshall *et al.* (2001)). This makes it a particularly interesting area to assess model performance in simulating the local ocean state and its variability. This study aims to assess the ability of the present generation of CCMs used for the IPCC 4AR (Meehl *et al.* (2007), IPCC (2007)) to simulate the hydrography of the central Labrador and Irminger Seas, similar to the study of *Sloyan & Kamenkovich* (2007) of water masses in the Southern Ocean. A model-observation and model-model intercomparison will highlight model biases and indicate points on which models might be improved. For this purpose we use the pre-industrial simulations of the CCMs, which are closest to the initial (observed) ocean state. A comparison with the 20th Century simulations (which are usually initialized on the pre-industrial runs) has also been made, but we will show that these results do not significantly deviate from those of the pre-industrial simulation. Furthermore, two ocean reanalyses (ECCO, SODA, Table 6.2B in data section) and an ocean model driven by observed fluxes (NEMO-OPA) are compared to the observations and the coupled models to gain insight into the possible causes of simulation biases.

The mean state as well as the variability of the potential temperature, salinity, potential density and stratification is investigated in 3 layers, the surface layer (0 to 200 dbar), the intermediate Labrador Sea Water layer (750 to 1250 dbar) and the deep North East Atlantic Deep Water layer (2000 to 2500 dbar). Details of the analyzed observational and model time series are given in Section 6.2. A short description of the observed hydrography and causes of its variability are contained in Section 6.3. Section 6.4 deals with the analysis of the observed and simulated data and the use of error scores based on the analysis by *Schmittner et al.* (2005). Section 6.5 will begin with a general overview of the model results and continues with the differences between the pre-industrial and 20th century simulation and the influence of the seasonal cycle on the assessment of model performance. This section continues with the results of the pre-industrial simulation-observation comparison. Subsequently, the results of the model-model intercomparison are discussed in Section 6.6. The final two sections, 6.7 and 6.8, comprise of the discussion of possible causes of model biases and the conclusions.

6.2 Data

6.2.1 Observational time series

The observational data used for this study originate from the hydrographic sections (the AR7 line) through the Labrador and Irminger Seas. During the World Ocean Circulation Experiment (WOCE) Hydrographic Program, from 1990 to 1997, these were surveyed annually in order to study whether the WOCE one-time survey was repre-

sentative for the overall ocean hydrographic structure in the 1990s. The (near) annual survey of this line was continued after the termination of WOCE as a contribution to the Climate Variability and Predictability Program (part of the World Climate Research Programme). The western part of the AR7 section, the AR7W line between Labrador and Greenland, has been surveyed by the Bedford Institute of Oceanography, Nova Scotia (BIO). The resulting data set along the AR7W line was extended backward to 1938 by I. Yashayaev of the BIO, using available historical hydrographic data. Near annual observations are available from 1949 onwards.

The eastern part of the AR7 section, the AR7E line from Greenland through the Irminger Sea and ultimately ending on the Irish continental shelf, has been surveyed near-annually since 1990 until present by the Institute for Sea Research, Hamburg (IfMH) and the Royal Netherlands Institute for Sea Research, Texel (NIOZ) with one survey in 1991 by the Southampton Oceanography Centre, presently the National Oceanography Centre, Southampton (NOC).

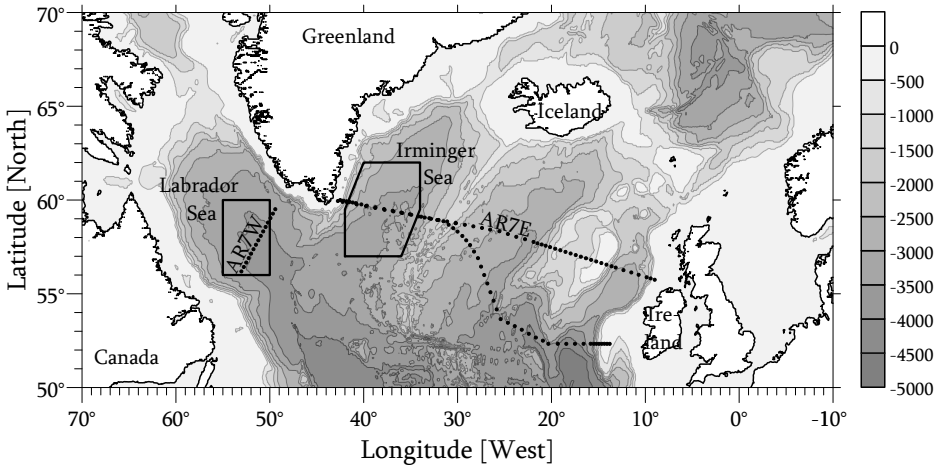

FIGURE 6.1: Topography of the northern North Atlantic Ocean with contour lines at 500 m intervals. The black dots represent examples of locations of hydrographic stations along the WOCE AR7W and AR7E sections. The areas in the Labrador and Irminger Seas in which the data are compared are enclosed by the thick black lines.

For this study, hydrographic observations were selected from the boxes in the central Labrador and Irminger Seas, shown in Figure 6.1. These boxes do not include the slope regions, only the deepest parts of the basin where dense overflow waters are found as well as the areas where deep convection has been observed or is expected (Marshall & Schott (1999), Pickart *et al.* (2003)). The profiles within these boxes were isopycnally averaged per survey in order to generate a single profile per survey, rep-

resenting the characteristic properties in the centre of that basin. This is done by robust (isopycnal) averaging as described by *Yashayaev* (2007) using density intervals of 0.005 kg m^{-3}. From these mean survey profiles of temperature and salinity (S), potential temperature (θ), potential density relative to the surface (ρ_0), the potential density anomaly (σ_0) and Brunt-Väisälä frequency (N) were calculated. The resulting series of hydrographic property profiles were regridded at equal time intervals, using a Kriging technique. This prevented disproportional contributions of years with multiple hydrographic surveys. The resulting final equidistant time series contained 75 time steps for the Labrador Sea (from 58 surveys) and 25 time steps for the Irminger Sea (from 16 surveys). We have to note here that, since very few research cruises in the Irminger Sea and Labrador Sea were carried out in winter because of the adverse weather and sea-ice conditions, these time series have a bias towards the summer half year. The hydrographies of the Labrador and Irminger Seas and their temporal variability have been analyzed in detail by *Yashayaev* (2007), *Hendry et al.* (2007) and *Yashayaev et al.* (2007). A description of the observed hydrography follows in Section 6.3.

6.2.2 Simulated time series

In order to compare the hydrographic observations with CCM model simulations, twenty years of monthly temperature and salinity data were obtained from the pre-industrial simulations (Picntrl runs) from each of the eight models (Table 6.1). These data are available from the World Climate Research Program (WCRP) Climate Model Intercomparison Project 3 multi-model dataset (CMIP3, Meehl *et al.* (2007)). These model simulations are part of the extensive model data set used for the IPCC AR4 report (IPCC (2007)) and represent the state-of-the-art in climate modeling. The selection of the models is based on the availability of ocean volume data and the absence of flux adjustment in the models. The models that exhibited either a too strong (>30 Sv, where 1 Sv = 10^6 m^3 s^{-1}) or too weak (<10 Sv) Atlantic MOC in the analysis of *Schmittner et al.* (2005) were not included in the selection. For the pre-industrial simulations these models use modern day topography and ice sheet coverage, a constant solar constant of 1365 W m^{-2} and greenhouse gas concentrations at the low levels from before the industrial revolution. Most of the models are initialized from an ocean at rest, with the temperature and salinity distribution set at values from one of the Levitus data sets (Levitus & Boyer (1994) and Levitus *et al.* (1998)). Three of the models (Table 6.1) are initialized with the final ocean state of a previous version of the model. The models are spun up for 70 to 330 years to ensure that remaining trends are small. The results from these pre-industrial control runs are assumed to give a good assessment of internal model differences in the ocean mean hydrographic state and variability, without trends caused by anthropogenic climate forcing.

In order to guarantee that the model biases found in the pre-industrial simulations are not the result of the difference between pre-industrial CO_2 forcing and current climate, a comparison with the 20th century control simulations (20C3M runs) has also been made. Most of these 20C3M runs are initialized with the results of the pre-industrial control simulation, thus possible biases in the pre-industrial simulations have an effect on the 20C3M results. The applied solar forcing in the 20C3M control runs is based on a reconstructed time series or a constant value, both within the range 1365 - 1370 W m^{-2}. CO_2 and aerosol concentrations based on annual observations and no volcanic variability. The 20C3M simulations generally run from 1850 to 2000. For this study the last 20 years (1980-2000), which coincide with the observations, were analyzed.

TABLE 6.1: Information of the coupled climate models used in this study. Here the acronyms that are referred to in the text are displayed, the full names can be found in Appendix B. The resolution is denoted in degrees longitude by degrees latitude by the number of vertical levels. The spin up time is denoted in years.

Coupled climate model	Resolution	Spin up	Initial condition
BCCR-BCM2.0	1.5° × 1.5° × 35L	80	Levitus (1982)
CNRM-CM3	2° × 2° × 31L	70	Previous model
GFDL-CM2.0	1° × 1° × 50L	300	Levitus (1992)
IPSL-CM4	2° × 2° × 31L	330	Levitus (1992)
MIROC3.2 (hires)	0.28° × 0.19° × 47L	109	Previous model
MIROC3.2 (medres)	1.4° × 1.4° × 43L	109	Previous model
UKMO-HadCM3	1.25° × 1.25° × 20L	300	Levitus (1995)
UKMO-HadGEM1	1° × 1° × 40L	85	Levitus *et al.* (1998)

A simulation originating from an ocean and sea-ice only model driven by realistic surface forcing was added to the data set to determine whether the coupling to other models (most important the atmospheric and sea-ice components of the CCM) has a significant effect on the performance of the ocean model. The ocean model that was chosen is the NEMO-OPA (Table 6.2A) model version 2.0 (Madec (2008), http://www.locean-ipsl.upmc.fr/NEMO/) from the ORCA group of ocean models. This model is very similar to the ocean component included in some of the CCMs (ORCA in IPSL-CM4 and OPA 8.1 in CNRM-CM3). The NEMO-OPA simulation uses the downward short wave and long wave radiation forcing from the Coordinated Ocean and sea-ice Reference Experiment (CORE), also used in the experiments of the

DRAKKAR group (DRAKKAR, 2007). For the precipitation a modified CORE field is used in which precipitation is reduced by 15-20% northward of 30° N. The turbulent fluxes are calculated from temperature, humidity and wind fields from the European Centre for Medium-range Weather Forecasts ERA-40 combined with sea surface temperature generated by the ocean model. No restoring surface conditions are used. The NEMO-OPA ocean model includes the LIM sea-ice model (also LIM in IPSL-CM4 and GELATO 2 in CNRM-CM3). The ocean model has been run twice from the beginning of 1958 to the end of 2001. The second run was initialized on the final conditions of the first run. The 20 simulated years between 1980 and 2000 of the second run were used for the comparison.

TABLE 6.2: Information about the ocean model (A) and the ocean reanalyses (B) used in this study. Here the acronyms that are referred to in the text are displayed, the full names can be found in Appendix B. The resolution is denoted in degrees longitude by degrees latitude by the number of vertical levels. The surface flux refers to the atmospheric flux that is applies on the sea surface.

A) Ocean model

Name	Resolution	Surface flux	Initial condition
NEMO-OPA 2.0	2° × 2° × 31L	CORE, ERA-40	Previous model

B) Reanalyses

Name	Resolution	Surface flux	Adjustment
ECCO-SIO 1	1° × 1° × 23L	NCEP rean.	Initialization, flux
SODA 1.4.2	0.5° × 0.5° × 40L	ERA-40	Ocean properties

Finally, data from two ocean reanalyses (Table 6.2B) were analyzed. These reanalysis data were obtained from the Estimating the Circulation and Climate of the Oceans project (ECCO SIO version 1, from http://www.ecco-group.org) and the Simple Ocean Data Assimilation project (SODA version 1.4.2, downloaded from http://apdrc.soest.hawaii.edu/w_data/ocean3.htm), and consist of 11 and 20 years of monthly data respectively (Table 1). The reanalysis data represents the "best possible" fit of a CCM to basin scale observations, meaning that one should not expect the eight CCMs or the ocean model to perform better than the reanalysis. The ECCO and SODA ocean reanalyses both use an atmospheric reanalyses as surface forcing for the ocean general circulation model, albeit from different origins (Table 6.2B). Both reanalyses do not include sea-ice models. The simulated ocean properties are adjusted to match observed values from hydrographic and satellite data sets as closely as possible. The

ECCO model uses an iteration of model runs, adjusting the initial state and surface forcing after every model run, until a best fit to the observations is obtained (Kohl *et al.* (2003)). The SODA model adjusts the simulated ocean properties to the observed values during the model run, resulting in a best fit after a single model run (Carton & Giese (2005)).

6.3 The observed hydrography

This section serves as a short summary of the various water masses observed in the Labrador and Irminger Seas, their character in terms of salinity and temperature and main causes of variability. For a more thorough description of the local water masses we refer to the selection of papers referenced in this section. The observed hydrographic series are illustrated by time-pressure sections of salinity and potential temperature showing the hydrographic structure and variability over the last few decades (Figure 6.2). The surface waters in the Labrador Sea originate from the West Greenland Current, the Labrador Current and Davis Strait through flow. These relatively cold and fresh surface waters are brought to the centre of the basin by baroclinic eddies (Lilly *et al.* (2003) and Katsman *et al.* (2004)). Relatively cold and fresh surface waters at the western border of the Irminger Sea originate from the East Greenland Current (Holliday *et al.* (2007)) and only rarely reach the centre of this basin. The variability in the surface waters is caused by air-sea interaction, melt water from sea-ice and changes in advective patterns. Between the surface water and the base of the winter mixed layer resides the Subpolar Mode Water or *SPMW* (McCartney & Talley (1982) and Brambilla & Talley (2008)). The *SPMW* is formed by air-sea interaction in branches that originate in the North Atlantic Current and thus has a relatively warm and saline character (Brambilla *et al.* (2008)). Presumably the *SPMW* is modified in the Irminger Sea by convection (Pickart *et al.* (2003), Bacon *et al.* (2003) and Pickart *et al.* (2008)). The Irminger Current transports the *SPMW* around the southern tip of Greenland to the Labrador Sea.

Intense surface cooling over the Labrador Sea initiates deep convection, which reaches down to between 500 and 2400 m depending on preconditioning and surface forcing (Marshall & Schott (1999), Haine *et al.* (2008) and Yashayaev *et al.* (2008)). During periods of strong convection, like the early 90s, the Labrador Sea Water (*LSW*) forms a large volume of homogeneous water, which is relatively cold and fresh due to the incorporation of fresh, strongly cooled surface waters (Yashayaev *et al.* (2007)). The volume of *LSW* is drained by advection southward in the upper layer of the Deep Western Boundary Current and eastward to the Irminger Sea (which takes 1 to 2 years), the Iceland Basin and Rockall Through.

Between 2000 and 3200 dbar a high salinity core with well developed temperature stratification is observed in the Irminger Sea and the Labrador Sea. This water mass is the North East Atlantic Deep Water (*NEADW*). Its salinity is influenced by varying ratios of entrainment of relatively fresh *LSW* and relatively saline Icelandic Slope Water (van Aken & de Boer (1995) and Yashayaev *et al.* (2007)). Denmark Strait Overflow Water (*DSOW*) can be found below the *NEADW*. It is cold, due to its origin in the Greenland Sea (Tanhua *et al.* (2005)) and relatively fresh with respect to the overlying *NEADW*. Variability in *DSOW* is caused by variability in the overflow and entrainment of *SPMW* and *NEADW*.

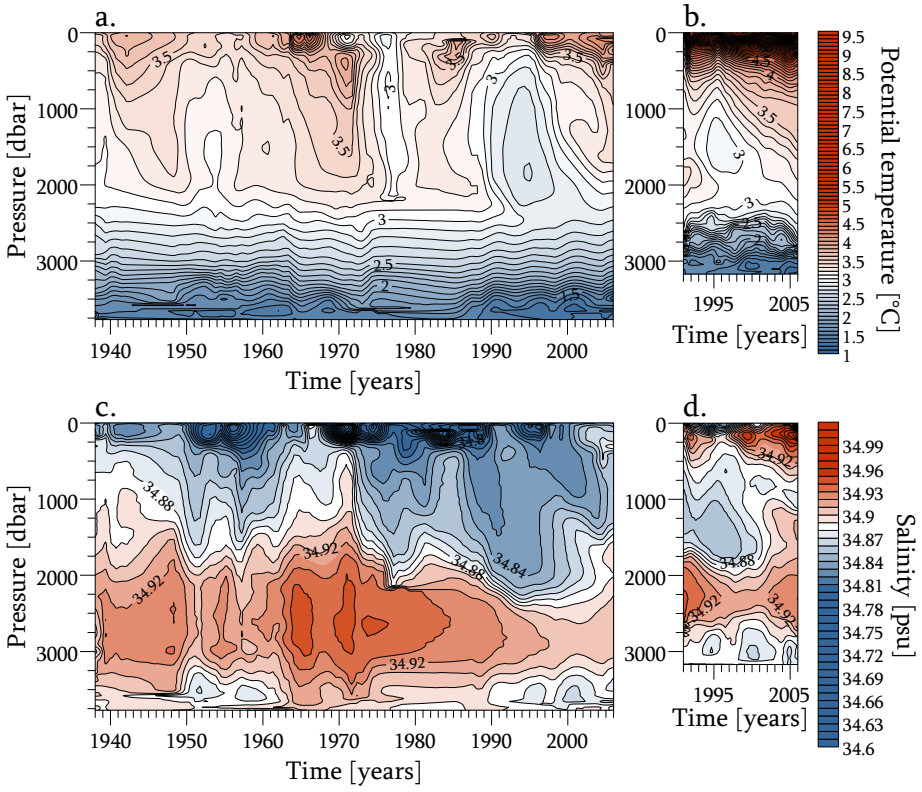

FIGURE 6.2: Observed changes over time in the hydrography of the Labrador Sea potential temperature (a) and salinity (c) and the Irminger Sea potential temperature (b) and salinity (d). Contours of potential temperature are drawn with intervals of 0.1°C, contours of salinity are drawn with intervals of 0.01 psu.

6.4 Analysis and means of comparison

The salinity and temperature volume data generated by the CCMs, the ocean-only model and the reanalyses were processed as follows. Simulated θ and S profiles at all time steps and grid points were interpolated vertically at 10 dbar intervals between the non-equidistant simulated depths. The derived hydrographic variables, the potential density and the Brunt Väisälä frequency squared (proportional to the density gradient), were calculated from the interpolated θ and S profiles. Three layer averages, for the surface layer (0 to 200 dbar), the *LSW* layer (750 to 1250 dbar), and the *NEADW* layer (2000 to 2500 dbar), were obtained by averaging horizontally between grid points and vertically between the layer boundaries. A linear fit was used to detrend the layer averages, thus removing model drift and long-term (>20 years) variations. The resulting layer averages were used to compare the 20-year mean and variability of the simulations to the observations. Time and area averaged vertical profiles of hydrographic properties were also obtained to gain insight into the vertical structure of the simulated oceans and the depth integrated properties.

TABLE 6.3: Observed hydrographic properties in the three layers in the Labrador Sea (A) and the Irminger Sea (B). The denoted values are the mean and standard deviation of the potential temperature (θ), salinity (S), potential density anomaly (σ_0) and the stratification of Brunt Väisälä frequency squared (N^2).

A) Labrador Sea

Depth [dbar]	θ [°C]	S [psu]	σ_0 [kg m^{-3}]	N^2 [10^{-6} s^{-2}]
0 to 200	3.59 ± 0.31	34.80 ± 0.05	27.67 ± 0.03	2.2 ± 2.2
750 to 1250	3.20 ± 0.17	34.86 ± 0.01	27.75 ± 0.01	0.4 ± 0.1
2000 to 2500	3.06 ± 0.11	34.91 ± 0.02	27.80 ± 0.01	1.0 ± 0.3

B) Irminger Sea

Depth [dbar]	θ [°C]	S [psu]	σ_0 [kg m^{-3}]	N^2 [10^{-6} s^{-2}]
0 to 200	6.09 ± 0.34	34.91 ± 0.02	27.46 ± 0.04	30.0 ± 6.6
750 to 1250	3.35 ± 0.09	34.88 ± 0.005	27.77 ± 0.01	0.7 ± 0.1
2000 to 2500	2.99 ± 0.05	34.92 ± 0.01	27.84 ± 0.005	1.5 ± 0.3

Layer averages from the observational time series were constructed similarly. These layer averages and standard deviations of the observational time series in the Irminger and Labrador Seas are given in Table 6.3. Although the salinity is based on a ratio of conductivity and is therefore dimensionless, we employ the practical salinity unit or psu in order to consistently report biases in hydrographic variable with their units. Note the small standard deviations in this table. It shows that the quantitative range

of variability is small compared to differences between the various water masses and similar water masses in the two basins.

As mentioned before only a few of the survey cruises were carried out in winter and spring. Therefore the observations tend to have a bias toward the late summer part of the year. For better comparison with these observations two simulated time series with a summer bias were constructed. The first summer series consists only of the simulations for the months August-September-October, in which most survey cruises took place and the sea surface temperature is at a maximum. This series will give an indication of the magnitude of the seasonal cycle. The second, more inhomogeneous summer series was constructed by randomly subsampling from each year in the original 20-year series. The timing of these subsamples is chosen by a random generator, such that it has a normal distribution around the late summer months. This last series is expected to resemble the variability of the inhomogeneously distributed observations more closely than the annual and Aug-Oct series.

The original θ and S profiles at their simulated depths were used to calculate σ_0 profiles for all time steps and grid points. From these profiles the mixed layer depth was derived using a delta criterium (Donners *et al.* (2005)) of $\Delta\sigma_0 = 0.125$ kg m^{-3}. The base of the mixed layer is defined as the depth at where the potential density difference with respect to the surface exceeds $\Delta\sigma_0$. The maximum mixed layer depth per winter is derived from the grid point with the deepest mixed layer. To reduce influences of differences in topography parameterization and horizontal resolution a fraction of convective volume was also determined. This is based on the fraction of available water column taking part in the mixed layer per grid point and the fraction of surface area within the analyzed box that the grid point represents. Summed over all grid points this gives a percentage of the volume within the analyzed box that is taking part in the mixed layer. Since the convective formation of LSW is a very important process for the local hydrography, differences in simulated mixed layer depth may explain biases found at the level of *LSW*.

To quantify the performance of the models we have assigned error scores, based on the skill scores proposed by *Schmittner et al.* (2005). The error scores are determined for each hydrographic variable, per layer per basin. They are obtained as follows. The simulation bias, or the difference between the simulated and observed mean, is normalized by dividing by the standard deviation of the observations σ_{obs}, to obtain a positive normalized root mean square error of the simulation $nrms_{mean}$:

$$nrms_{mean} = \sqrt{\frac{bias_{sim}^2}{\sigma_{obs}^2}} \qquad (6.1)$$

With these normalized root mean square errors of the model performance we define an overall error score S_k as the overall averaged $nrms_{mean}$. Thus, a high error score indicates weak model performance.

6.5 Results of the CCM-observation comparison

6.5.1 General results

Water mass analysis (as applied in Section 6.3) is often based on combinations of temperature and salinity minima or maxima seen in a temperature-salinity plot (θ,*S*-plot). The observed mean θ,*S*-profile in the Irminger Sea (Figure 6.3) shows the warm and saline Subpolar Mode Water, two salinity minima for the Labrador Sea Water density classes of 1994 and 2000, the saline North East Atlantic Water and the fresher, cold Denmark Strait Overflow Water. However, both panels of Figure 6.3 show that a description of the local simulated hydrography by using the traditional water masses is not suitable. The SODA reanalysis shows a similar θ,*S*-profile with 2 salinity maxima (resembling *SPMW* and *NEADW*) and a salinity minimum (*LSW*) albeit at higher temperatures, but gives no indication of the presence of cold *DSOW*. These water masses are not so easily recognized in the θ,*S*-profiles of the ECCO reanalysis and NEMO-OPA ocean model. The dissimilarity between the observed θ,*S*-profiles and the θ,*S*-profiles simulated by the coupled climate models (right panel of Figure 6.3) makes the comparison in terms of water masses even more difficult. We can, however, make a comparison in terms of vertical profiles of hydrographic properties.

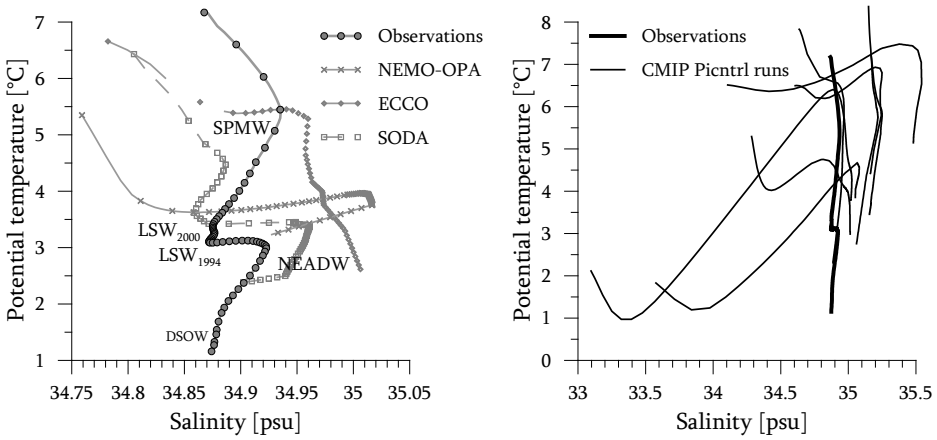

FIGURE 6.3: Potential temperature-salinity plots of the mean vertical profiles in the Irminger Sea. The left panel contains the θ,S-profiles of the observations, the ocean model and the ocean reanalyses. The local water masses are indicate in the graph. The right panel shows the θ,S-profiles of all pre-industrial runs (thin lines) and the observed profile (thick line). Note the difference in scale, especially for the salinity axis.

The time-mean vertical profiles of salinity in the Labrador Sea (Figure 6.4) illustrate the overall tendency of the coupled models to have a very low surface salinity and a high salinity beneath 500 dbar. However, the high depth-average salinity (bottom panel Figure 6.4) indicates that the low surface salinity does not compensate the saline deeper layers in most of the models. This salinity gradient over the upper 1000 dbar, which is much larger than observed, does strongly increase the stability of this layer in the models.

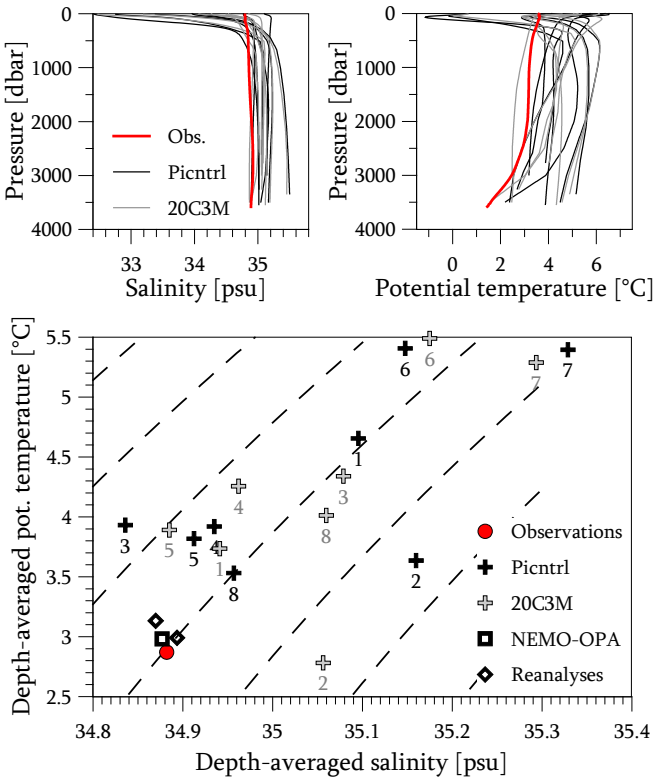

FIGURE 6.4: Vertical profiles of salinity (upper left) and potential temperature (upper right) from the observations (red line), the pre-industrial simulations (black lines) and the 20th century simulations (grey lines).

The lower panels shows the depth-average potential temperature and salinity for the observations, CCM simulation, ocean model and the reanalyses for the Labrador Sea. The numbers next to the symbols correspond to the model numbers in Figures 6.5 to 6.8. Isopycnals are drawn every 0.1 kg m^{-3} (dashed lines), with the observations on the 27.8 kg m^{-3} isopycnal.

Most of the Labrador Sea potential temperature profiles (Fig. 6.4) provide a negative contribution to the stability of the upper 1000 dbar by having cold surface water over a warm deep layer. In the next section we will show that the stabilizing effect of the salinity is much larger than the destabilizing contribution of the potential temperature profiles. The depth-average potential temperature in the pre-industrial runs of the coupled models is between 0.6 and 2.5 °C higher than observed, indicating that the local heat content is very high in these simulations.

6.5.2 PRE-INDUSTRIAL RUN VERSUS 20TH CENTURY CONTROL RUN

Both the pre-industrial (Picntrl) runs and 20th century (20C3M) runs show a very similar tendency of the depth-averaged salinity and potential temperature in the Labrador Sea (Figure 6.4). All of the coupled models have a too high depth-averaged potential temperature in the Picntrl runs. Three of the coupled models shows decrease in potential temperature over a large part of the deeper water column in the 20C3M run, with one of them (GFDL-CM2.0) simulating lower than observed temperatures within a large part of the deeper water column. Five of the models show an increase in the depth-average potential temperature with respect to the pre-industrial run, thus also increasing the bias with respect to the observations.

The salinity profiles are very similar in both runs, simulating relative fresh water over a deep saline water column. Four of the models show a decrease in depth-averaged salinity in the 20C3M run compared to the Picntrl run, while the other four show an increase in salinity. The largest increase in depth-averaged salinity (0.24 psu) is exhibited by the GFDL-CM2.0 model. This coupled model had a very fresh mean surface salinity in the pre-industrial run (32.42 psu against 34.80 psu observed), but has a mean surface salinity of 34.50 psu in the 20th century run. Despite this improvement in the surface layer, the salinity profile below 250 dbar, which was already too saline in the Picntrl run, approximately doubled its bias in the 20C3M run.

In the remaining part of the discussion of the results we will focus mostly on the pre-industrial runs. Since most of the 20th century runs are initialized on the ocean state of the pre-industrial control runs, biases in the 20C3M run will include the results of existing biases in the initialization. This is contrary to the pre-industrial runs, which are mostly initialized with an ocean state very similar to our observations, namely one of the Levitus data sets. Therefore, most insight into the original simulation biases and possible causes are more likely to be gained from the comparison between the pre-industrial runs and the observations.

6.5.3 EFFECTS OF THE SEASONAL CYCLE AND INHOMOGENEOUS SAMPLING

The difference between the annual layer averages and the late summer layer averages is most pronounced in the surface layer. Due to the local atmospheric seasonal cycle, especially solar radiation, there is an increase in temperature in spring and summer. The excess in precipitation decreases salinity in summer. The effect of summer heating and freshening is most pronounced in the Aug-Oct summer series. The temperature increases over the upper 200 dbar of the Labrador and Irminger Seas are both about 0.7 °C (not shown) with respect to the annual series. The inhomogeneous

summer series shows a maximum increase of 0.4 °C when the sample distribution is centered on September. Both increases in temperature are confined to the upper layer by the stratification, differences between the annual and summer mean of the intermediate and deep layer are <0.01 °C for both summer series and are not significant. The salinity of the surface layer generally decreases by about 0.05 psu for the Aug-Oct series and 0.03 psu for the inhomogeneous summer series. Salinity changes in the intermediate layer are about 0.001 psu and are also not significant. Although most of the observations were made in summer, consideration of the simulated summer months does not improve model performance. On the contrary, the increase in temperature and decrease in salinity strengthens the biases seen in the annual averages.

6.5.4 Mean and variability of 20 years of CCM simulations

The 20-year mean values of the pre-industrial coupled model simulations for the surface, intermediate and deep layer are graphically presented in Figures 6.5, 6.6, 6.7 and 6.8 for all discussed hydrographic properties. The result for the Labrador and Irminger Seas are discussed per layer.

A. The surface layer

All four figures reveal similar model errors for the Labrador Sea and the Irminger Sea, typical for basins connected by advection pathways (Yashayaev *et al.* (2007)). Thus, simulations with too low (or high) values for the mean hydrographic parameters in the Labrador Sea generally have also too low (or high) values in the Irminger Sea. Two models, GFDL-CM2.0 and IPSL-CM4, have extremely low salinities and potential temperatures in the surface layer, between 0.7 and 1.7 psu below the mean observed salinities, and between 2.3 °C and 3.8 °C below the observed temperatures. These model biases are orders of magnitude larger than the observed range of variability (Table 6.3). The salinity and temperature biases do not compensate in density. The simulated surface density is generally much lower than observed, especially in the Labrador Sea. Overall the surface density is too low for all but one CCM simulation, related to the lower than observed surface salinities. The low surface density causes a higher simulated stability or density gradient over the surface layer in the Labrador Sea, expressed by the Brunt-Väisälä frequency squared or N^2. In the Irminger Sea, the stability of the surface layer in the model simulations is close to the observations.

B. The intermediate layer

The intermediate layer from 750 to 1250 dbar is representative for the *LSW* in the Labrador and Irminger Seas. In most model simulations this layer is much too warm

and saline, with biases up to 2.8 °C and 0.5 psu in the Labrador Sea and 4.0 °C and 0.7 psu in the Irminger Sea. This suggests that in most models the formation of *LSW* in winter is not well represented. Both the salinity and temperature difference between the surface and intermediate layer and between intermediate properties in the Labrador and Irminger Seas is much larger than observed. The very high intermediate temperatures in the MIROC3.2 medium resolution (medres) model and the UKMO-HadCM3 models suggest that in these models the intermediate layers have the properties of *SPMW*, rather than *LSW*. Two models from the same institutes, but with higher resolution, MIROC3.2 hires and UKMO-HadGEM1, perform better. In general, the model errors in temperature and salinity of the intermediate layer seem to compensate in density, leading to a mixed behavior of the intermediate density, resulting in 65% of the models with a too high and 35% with a too low intermediate density. Similar to the surface layer, the stability of the intermediate part of the water column is systematically too high, an indication of low convective activity, with larger errors in the Labrador Sea than in the Irminger Sea.

C. The deep layer

The model results from the deep *NEADW* layer between 2000 and 2500 dbar show mixed results. While a few CCM simulations show realistic *NEADW* temperatures, most CCMs generate relatively high deep temperatures, up to 2.7 °C too high. Apart from the MIROC3.2 high resolution model, the CCMs have a higher than observed salinity in the *NEADW* layer. Also for this layer, temperature and salinity errors compensate in density for several models, but not for all. Especially the CNRM-CM3 and UKMO-HadCM3 model have considerably higher *NEADW* densities, both in the Labrador Sea and in the Irminger Sea. The relative error in N^2 in the *NEADW* layer is small compared with the shallower layers.

The quantitative results of the analysis are compiled in Table 6.4, which contains the "error score" per variable summed over the three layers. In the Irminger Sea the largest contribution (50-60% averaged over all models) to the error score is by the intermediate layer. This layer represents the core of the water formed in the Labrador Sea. The surface layer contributes 10-20% and the deep layer 20-30%. In the Labrador Sea the contribution of the layers to the final error score is not the same for all variables. Nearly 70% of the error score of N^2 is contained in the surface layer, due to the high simulated stability. The other 30% is distributed over the intermediate (20%) and deep layer (10%). Temperature skills scores are distributed equally over all layers. Salinity and density have their largest error scores in respectively the intermediate (40%) and deep layer (45%).

Labrador Sea S (left column) and θ (right column).

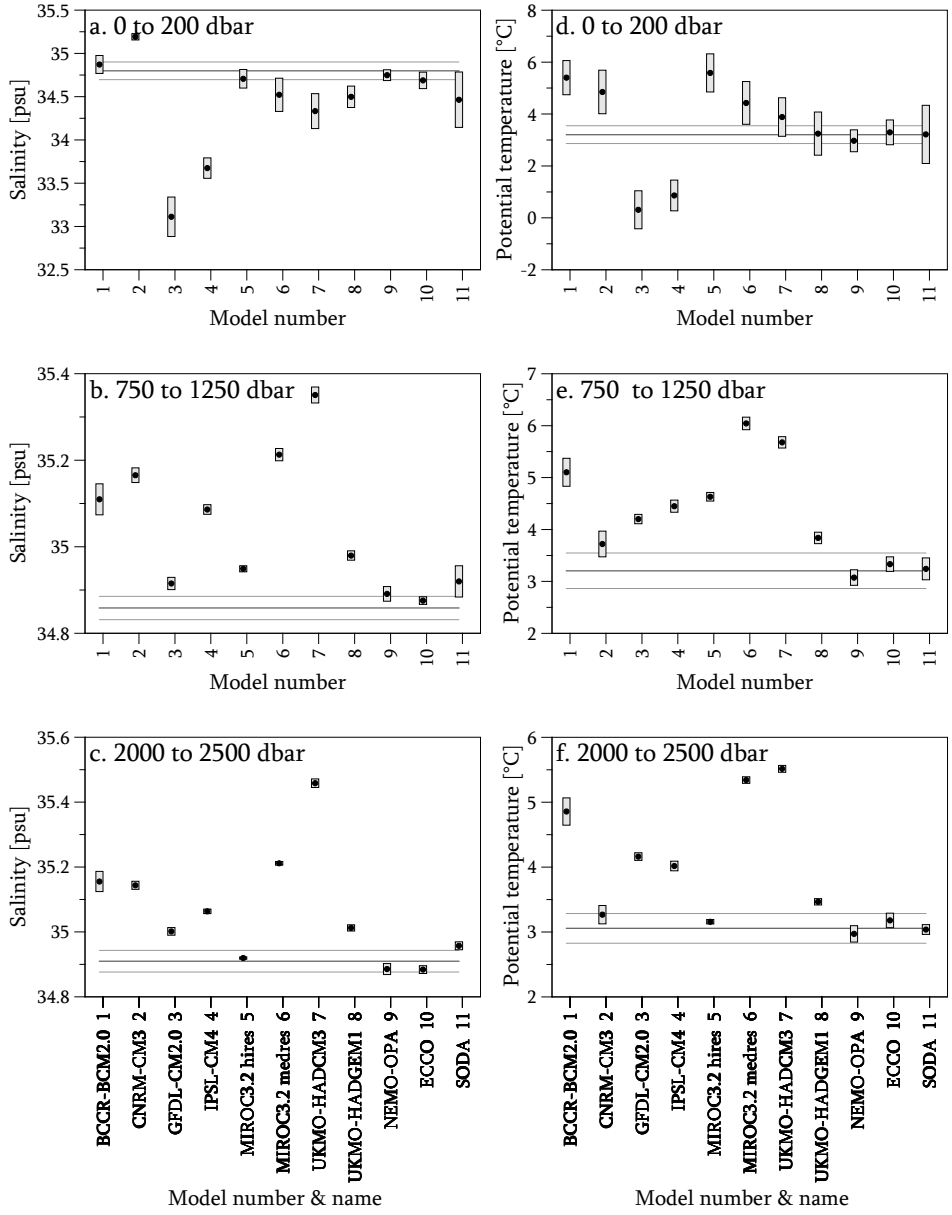

FIGURE 6.5: Labrador Sea salinity (a)-(c) and potential temperature (d)-(f). Layer averages are shown for the surface layer in (a) and (d), for the intermediate layer in (b) and (e) and for the deep layer in (c) and (f). The means (black dots) ± one standard deviations (enclosed by the rectangles) of the simulations are shown here as well as the mean of the observation (dark grey horizontal lines) ± two standard deviations (light grey lines).

Labrador Sea σ_0 (left column) and N^2 (right column).

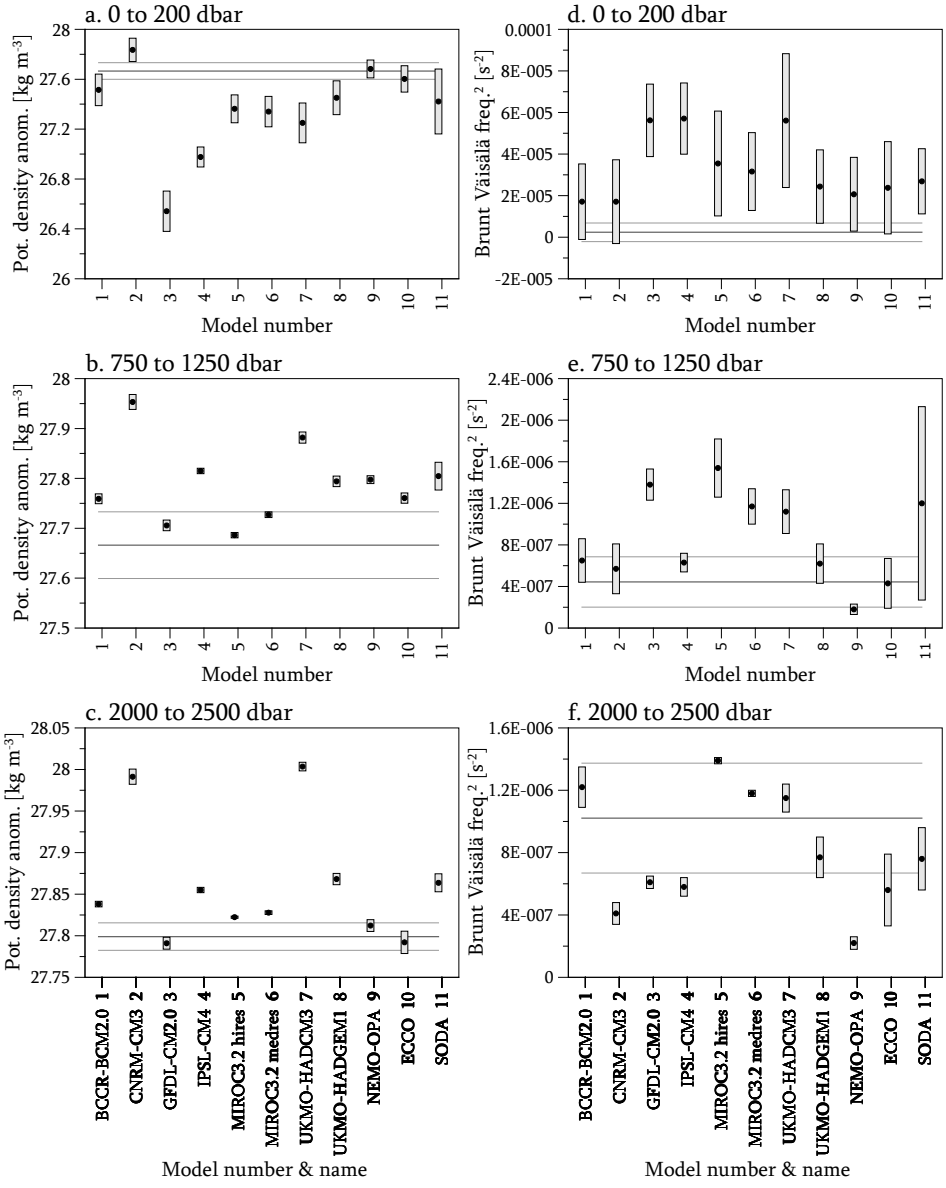

FIGURE 6.6: Labrador Sea potential density anomaly σ_0 (a)-(c) and Brunt Väisälä frequency squared (d)-(f). Layer averages are shown for the surface layer in (a) and (d), for the intermediate layer in (b) and (e) and for the deep layer in (c) and (f). The means (black dots) ± one standard deviations (enclosed by the rectangles) of the simulations and the mean of the observation (dark grey horizontal lines) ± two standard deviations (light grey lines) are shown.

Irminger Sea S (left column) and θ (right column).

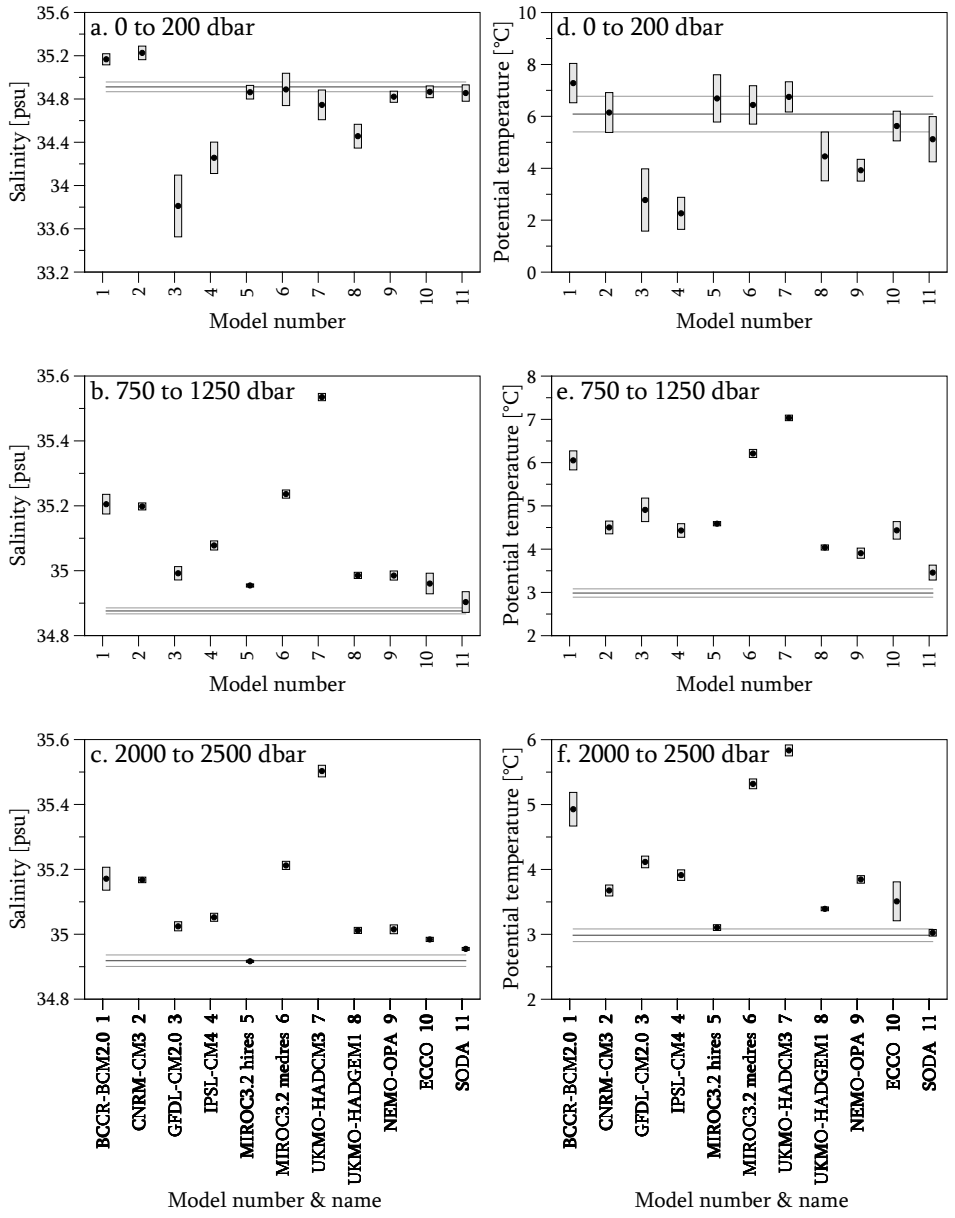

FIGURE 6.7: Irminger Sea salinity (a)-(c) and potential temperature (d)-(f). Layer averages are shown for the surface layer in (a) and (d), for the intermediate layer in (b) and (e) and for the deep layer in (c) and (f). The means (black dots) ± one standard deviations (enclosed by the rectangles) of the simulations are shown here as well as the mean of the observation (dark grey horizontal lines) ± two standard deviations (light grey lines).

Irminger Sea σ_0 (left column) and N^2 (right column).

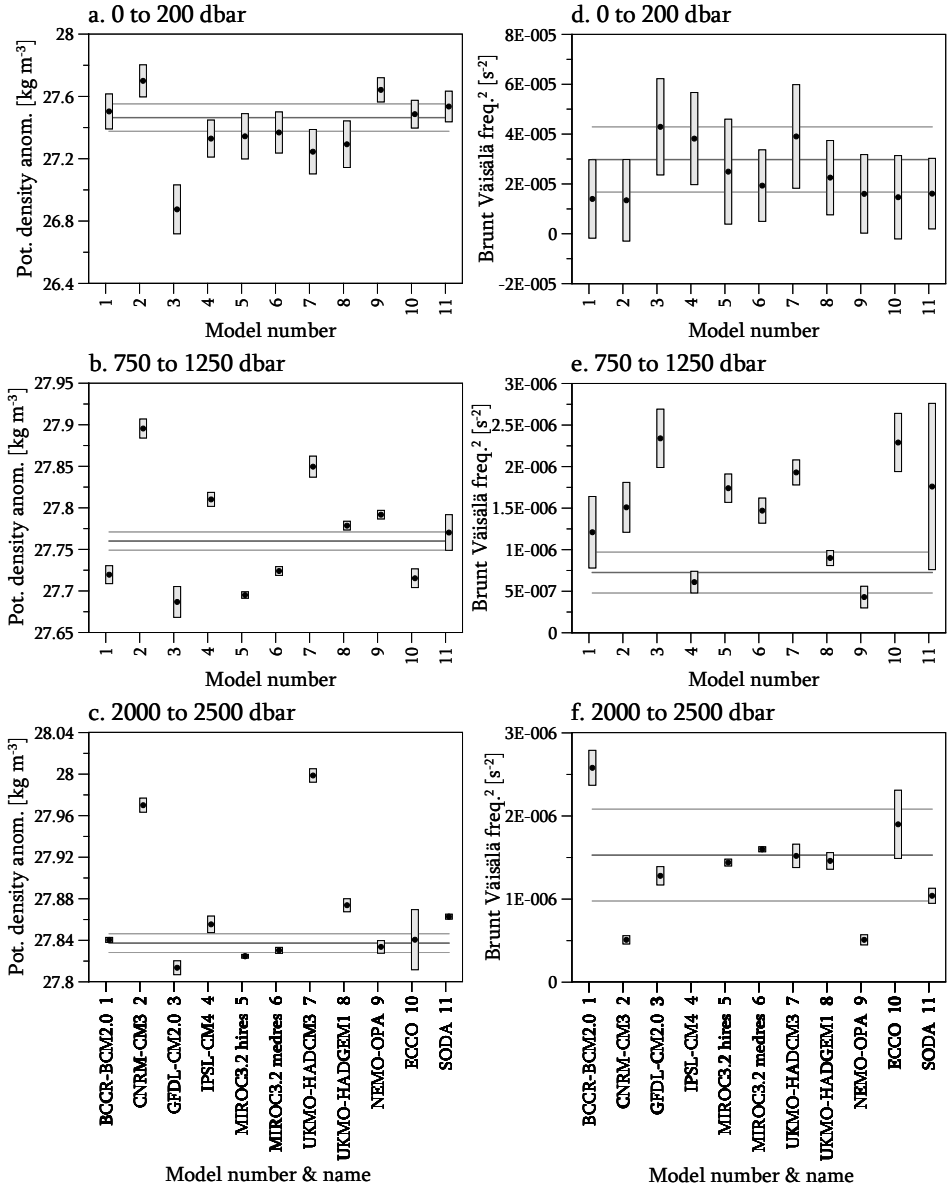

FIGURE 6.8: Irminger Sea potential density anomaly σ_0 (a)-(c) and Brunt Väisälä frequency squared (d)-(f). Layer averages are shown for the surface layer in (a) and (d), for the intermediate layer in (b) and (e) and for the deep layer in (c) and (f). The means (black dots) ± one standard deviations (enclosed by the rectangles) of the simulations and the mean of the observation (dark grey horizontal lines) ± two standard deviations (light grey lines) are shown.

TABLE 6.4: Normalized RMSEs, or the simulation bias normalized by the standard deviation of the observations, for the simulated 20-year mean hydrography in the Labrador and Irminger Seas. The error values for each variable are the means over the three analyzed layers. Total error scores (S_k) over all variables and both basins are shown in the rightmost column.

	Labrador Sea				Irminger Sea				Total
Model	S	θ	σ_0	N^2	S	θ	σ_0	N^2	S_k
BCCR-BCM2.0	12	13	4	3	38	36	3	3	14
CNRM-CM3	15	5	12	4	38	15	20	4	14
GFDL-CM2.0	14	11	12	11	29	24	11	5	15
IPSL-CM4	16	10	11	10	30	20	5	3	13
MIROC3.2 (hires)	3	8	4	9	7	12	6	3	6
MIROC3.2 (medres)	17	15	5	7	38	39	3	3	16
UKMO HadCM3	26	13	15	10	73	48	19	4	26
UKMO HadGEM1	7	3	6	4	18	12	5	1	7
NEMO-OPA 2.0	2	1	2	5	13	14	4	3	5
ECCO SIO 1	2	1	2	4	9	14	3	5	5
SODA 1.4.2	5	0	6	6	4	4	3	4	4

D. Variability

Figure 6.9 shows the relative magnitude of the variability in the simulated hydrographic properties in the Labrador Sea. The lengths of the vertical bars represent the standard deviation of the inhomogeneous summer series, normalized by the standard deviation of the observations. The standard deviation of the inhomogeneous series is independent of the summer month on which this series normal distribution is centred. Its magnitude over all layers is about 97% of the standard deviation of the annual series for all hydrographic variables. The largest decrease in variability is in the surface layer, the standard deviation of the inhomogeneous series is approximately 90% of the standard deviation of the annual series. Since the variability in the intermediate and deep layer is mostly inter-annual, the difference in variability in the two time series is small at these depths.

The potential temperature, salinity, potential density anomaly and stratification exhibit a similar behaviour in the three layers (Figure 6.9). The variability in the surface layer is too large for nearly all models. The models exhibit a mixed behaviour for the variability in the intermediate layer, with temperature variations mostly underestimated. In the deepest layer the coupled models show too low variability for all hydrographic variables. The combination of too high surface variability and low in-

termediate and deep variability suggests that the direct ocean response to the local atmospheric variability is confined to a relatively thin upper layer due to the too strong stratification. Consequently, the variability in the deeper layers is underestimated.

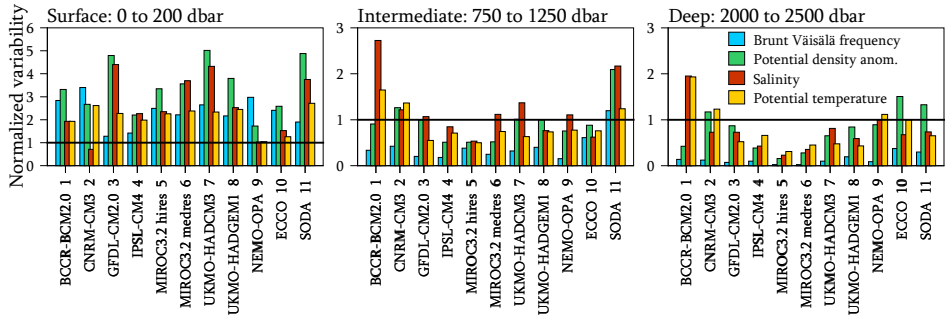

FIGURE 6.9: Normalized variability of the hydrographic properties in the Labrador Sea for the surface layer (left panel), the intermediate layer (middle panel) and the deep layer (right panel). The vertical bars represent the standard deviation of the inhomogeneous series derived from the simulations, divided by the standard deviation of the observations. The horizontal bars represent the value at which the simulated variability is equal to the observed variability.

6.5.5 Mean and variability of 200 years of CCM simulations

Two 200-year model simulations were used in order to investigate the influence of longer term variability, such as the variability caused by decadal oscillations of the North Atlantic Oscillation (Hurrell (1995)), on the 20-year mean values. The two models selected (from the group of 8 models in Table 6.1) for this analysis are CNRM-CM3 and IPSL-CM4, which both include an ocean model based on NEMO (Section 6.1) and run at the same resolution. These ocean models are coupled to different atmosphere and sea-ice models. The two models exhibited quite different results in the simulation of the Labrador and Irminger Seas (Figures 6.5 to 6.8). The variability in the 200-year simulated time series is compared to the observational data set from the Labrador Sea. The processing of the 200-year data sets is identical to the processing of the 20 year data sets, which was explained before. The mean and standard deviation of the 20-year and 200-year time series of the hydrographic variables are very similar (less than 10% difference). Also, the variability in the time series is mostly seasonal and interannual to decadal, not multi-decadal, thus explaining the relatively small difference between the standard deviations of the 20 and 200-year series. The simulated hydrographic properties do not improve significantly by extending the data set, thus we conclude that the weak performance of the IPSL-CM4 model is not due to an unlucky selection of the relatively short segment of simulated data. It can be expected that this is also true for the other model simulations.

6.6 The CCM-reanalysis and ocean model comparison

As expected, the reanalysis models and the NEMO-OPA ocean model perform much better than the coupled climate models in simulating both the depth-averaged properties (Figure 6.3) and the layer average of hydrographic parameters (Figures 6.5, 6.6, 6.7 and 6.8). This is expressed in low error scores in Table 6.4. The error scores obtained in the Labrador Sea are better than those obtained in the Irminger Sea. The potential temperature and salinity of the intermediate (*LSW*) layer and the deep (*NEADW*) layer in the Irminger Sea seem to be subject to problems similar as in the CCMs. Both the reanalyses and the NEMO-OPA model display a somewhat too high Labrador Sea surface stratification, but the NEMO-OPA ocean model performs slightly better than the reanalyses for the intermediate layer stratification (Figure 6.8). The overflow waters are restricted to a shallow layer above the bottom and are not as cold as observed. The differences between the *LSW* in the Labrador Sea and the homogeneous water mass in the Irminger Sea are larger than observed, up to 1.1 °C and 0.1 psu, but smaller than those of the coupled models. It is interesting to note that the ocean only model performs equally well as the reanalyses, despite its low resolution. The 2° by 2° resolution of the ocean model does not allow eddies to exist. ECCO (1° by 1°) and SODA (0.5° by 0.5°) have better resolutions, but are still not eddy permitting (which is reached at 0.25° by 0.25° or better). This suggests that the eddy-fluxes are not the main cause for the bias at coarse resolution. The rather large surface variability in the reanalyses could be the result of fitting ocean properties to (high temporal resolution) satellite data. The NEMO-OPA ocean model has a somewhat smaller variability. This could be related to the intensity of deep convection in the ocean model that will be discussed in the next section.

6.7. Discussion

The overall results of the coupled ocean-atmosphere climate simulations, for either 20 or 200 years, are not satisfying, with model biases strongly exceeding the observed ranges of variability. In this section we discuss some possible causes for the model biases.

6.7.1 Effect of long spin up time

We have noted that the magnitude of the model biases is related to the duration of the spin up time of the model run. The three CCMs with the longest spin up periods also obtained the highest error scores for the mean hydrography for the Labrador Sea. Considering the 5 models initialized on a Levitus data set, the correlation (R^2) between Labrador Sea overall error scores and spin up time is 0.7. During the spin up

period the initial ocean state, which was originally based on observed values and thus would have presumably scored reasonably well in our study, is adjusted to equilibrium with the simulated atmosphere. Both the compensation of a "large" initial imbalance with the atmosphere and the accumulation of small numerical errors, by e.g. spurious diapycnal diffusion, drive the final ocean simulation away from the observations. Models with a larger initial imbalance usually require longer spin up periods for stabilization.

6.7.2 MIXED LAYER DEPTH AND INTENSITY

As mentioned before, convection is a very important process in the northwestern North Atlantic, but also a very difficult process to include in low resolution models. The much stronger than observed surface layer stratification in several models and large simulation biases in the intermediate and deep layer suggest that the simulated convection is insufficient. The mixed layer depth, obtained as described in Section 6.4, is used to investigate the convective activity of the models in the study area. The mean of the 20-year maximum mixed layer depth series for the Labrador Sea are displayed against the mean maximum convective volume within the analyzed box (Figure 6.10). The maximum mixed layer depth gives an indication of the depth to which the hydrographic properties are directly affected by local convection. The maximum convective volume gives an indication of the intensity of the convection and the amount of

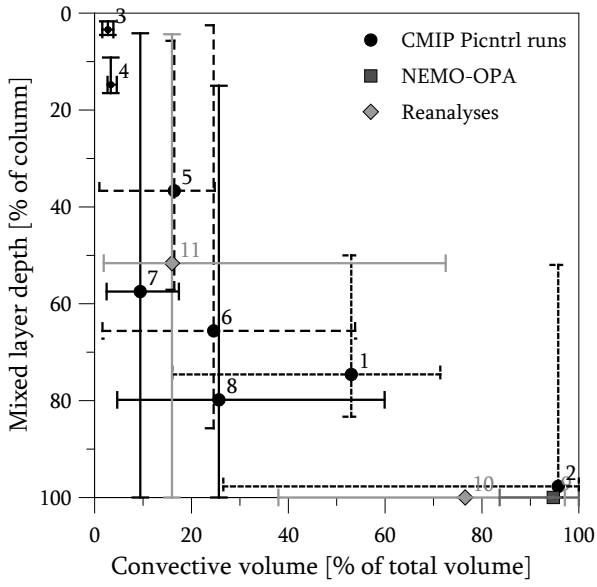

FIGURE 6.10: Mean maximum mixed layer depth vs mean convective volume in the Labrador Sea. Shown are the CMIP coupled model simulations, the NEMO-OPA model and the ocean reanalyses. The symbols represent the means, the error bars represent the ranges of annual maximum mixed layer depth in the 20-year simulations. The number next to the symbols correspond to the model numbers and names in Figure 6.9.

convectively formed water. The range of reached convection depths is denoted by the bars, giving some indication of the magnitude of the variability. Winter mixed layers in the Labrador Sea are about 500 m in years of weak convection, while the maximum observed convection depths is 2400 m or 70% of the water column (Yashayaev *et al.* (2008)). Convective volumes are very difficult to estimate from observations as is explained by *Haines et al.* (2008).

The two extremes of convective regimes in the Labrador Sea stand out in the results. Firstly, both coupled models which simulated very low surface salinities and temperatures, GFDL-CM2.0 and IPSL-CM4, exhibit very shallow convection (< 600 dbar) combined with a low convective volume. Thus, the improvement in surface salinity in the 20th century simulation of GFDL-CM2.0, as described in Section 6.5, is most likely related to the large increase in mixed layer depth (Table 6.5). Secondly, very deep mixed layers filling a large part of the volume of the basin, as seen in the CNRM-CM3 simulations, correspond to high overall salinity and potential density. In these simulations the dense and saline deep waters (such as *NEADW*) are mixed into the entire water column, thus increasing density/salinity and decreasing stratification over all layers.

Table 6.5: Mean of the 20-year maximum mixed layer depth series in fraction (%) of the water column. Values are shown for the pre-industrial run (Picntrl) and the 20th century run (20C3M) in the Labrador Sea and the Irminger Sea. the ocean model, NEMO-OPA 2.0, and the reanalyses, ECCO SIO 1 and SODA 1.4.2, are based om 20th century ocean observations and atmospheric forcing and therefore have no values for the pre-industrial period.

	Labrador Sea		Irminger Sea	
	Picntrl	20C3M	Picntrl	20C3M
BCCR-BCM2.0	75	69	98	95
CNRM-CM3	98	97	99	91
GFDL CM2.0	3	96	29	74
IPSL CM4	15	14	61	38
MIROC3.2 (hires)	37	44	35	38
MIROC3.2 (medres)	66	65	60	64
UKMO HadCM3	57	43	63	56
UKMO HadGEM1	80	90	28	45
NEMO-OPA 2.0	-	100	-	100
ECCO SIO 1	-	100	-	89
SODA 1.4.2	-	52	-	76

The reanalyses and ocean model also show a large range of convective activity. Convection in SODA reaches down to 1700 m on average, but displays a large variability. This is closer to the observed convection than the bottom reaching convection of ECCO and NEMO-OPA. This may explain why the θ,S-profiles of SODA corresponded more closely to the observed profiles.

Five of the coupled models exhibit stronger convection in the Irminger Sea, with respect to the Labrador Sea, in the pre-industrial run. In the 20th century run this is only seen in three of the coupled models. From the observations it is not quite so obvious that the convection in the Irminger Sea should be so strong, although some studies have shown that deep convection is possible in the southwestern Irminger Basin (Bacon *et al.* (2003), Pickart *et al.* (2003) and Pickart *et al.* (2008)). But it is not uncommon for models to compensate shallow Labrador convection by convective formation of intermediate water in the Irminger Sea and in the central Subpolar Gyre (e.g. Drijfhout *et al.* (2007)). Strong local adjustment of water masses that entered the Irminger Sea may explain the larger than observed differences between hydrographic properties of Labrador and Irminger water masses. Interestingly, the IPSL-CM4 model exhibits much too low surface salinity in the Irminger Sea despite the fact that the simulated convection is quite strong and the stratification is closer to the observed values.

6.7.3 Surface fluxes & coupling to atmospheric or sea-ice model

Convective mixing depths in the Labrador and Irminger Seas can only partially explain the biases of the coupled models. IPSL-CM4 shows similar salinity biases over the Labrador and Irminger Seas despite the large difference in convection strength. This suggests that the shallow Labrador convection is the result of the too strong surface stratification rather than the too strong stratification being the result of shallow convection. Important contributors to surface stratification are air-sea surface fluxes. The small biases observed in the NEMO-OPA simulations suggest that the surface fluxes are very important. The final error score of NEMO-OPA is comparable to those of the ocean reanalyses, without incorporating ocean observations like these reanalyses. The large gap between observed and modelled depth averaged salinity and temperature (Figure 6.4) thus seem to be closed by the employment of close-to-observed surface fluxes. The low surface salinity seen in many of the models indicates that the hydrological cycle may be the leading contributor among the surface fluxes. *Josey & Marsh* (2005) and *Myers et al.* (2007) showed that positive anomalies in precipitation-evaporation play a significant role in the freshening of both the eastern Subpolar Gyre and the Labrador Sea. However, both the analysis of precipitation over the two basins and

of the zonal mean precipitation between 40° N en 70° N showed that simulations with a too fresh surface layer do not have too much precipitation over the North Atlantic. Possibly a too small amount of evaporation, advection of fresh waters or too much melting sea-ice is causing the surface salinity bias. Due to limited resources these processes fall outside the scope of this study. The exact cause for the observed salinity bias in CCMs is left as an interesting subject for future research.

6.8 Conclusions

This study aims to assess the performance of coupled climate models in simulating the local hydrography of two basins in the North Atlantic Ocean, the Labrador and Irminger Seas. Many of the constituents of *NADW*, which forms the southward deep branch of the MOC, are either formed or adjusted in these basins. Some of the local processes, e.g. deep convection and entrainment over the overflows, cannot yet be explicitly represented in ocean models and have been parameterized. Although Coupled Climate Models are by their definition meant to simulate the global climate as accurately as possible and not merely a relatively small area such as the north western North Atlantic Ocean, it is nevertheless an important area for the heat and freshwater transport in the MOC and the climate in the North Atlantic region.

The reported biases in both the pre-industrial and 20th century simulations strongly exceed the ranges of observed hydrographic properties. Vertical profiles of salinity and potential temperature show that the water column below 500 dbar is generally too warm and too saline. Especially in the Labrador Sea, the surface layers are characterized by low salinity, leading to a too strong surface stratification. In some of the models this situation is not unlike a permanent "Great Salinity Anomaly" as was seen circulating the North Atlantic in the 1960s and 1970s (Dickson *et al.* (1988)), which arrested convection in the Labrador Sea. Due to the strong stratification, communication of atmospheric variability to deeper ocean layers is inhibited and surface variability is strengthened. The analysis of two 200-year simulated data sets show that the previous results are not an artefact of the arbitrary selection of a 20-year segment from a time series containing multi-decadal oscillations. Both the mean and the variability of the simulated hydrographic properties change only minimally when the analyzed time series are extended from 20 to 200 years. It is expected that this is also true for the other models.

The size of the biases in the simulations is related to the length of the spin up time of the model and most likely to the initial imbalance between model components. During the spin up the simulated ocean state is slowly pushed away from the initial (observed) ocean state and small numerical errors are accumulated.

Also, a large range of convective regimes can be found in the coupled model simulations. Very shallow convective regimes are related to large negative salinity biases in the surface layer. In contrast, deep and strong convective regimes are related to high salinity and density over the entire water column. In between these extremes the correlation of convective depth with hydrographic biases is ambiguous. Possibly the deep saline and warm layer observed in the simulations is formed by convection in the Irminger Sea, which is stronger than expected in the simulations. Low surface salinities and the reasonably good performance of the ocean model NEMO-OPA, which uses observed ocean fluxes, suggest that biases in sea surface fluxes are also contributing to the ocean simulation biases. Sensitivity studies regarding the full hydrological cycle and sea-ice are needed to improve the freshwater balance in the northwestern North Atlantic Ocean.

CHAPTER 7

Conclusions & outlook

7.1 Introduction

This thesis deals with the hydrography of the northwestern North Atlantic Ocean, in particular with the hydrography of the Irminger Sea. The chapters of this thesis describe the general circulation and hydrography, the variability on decadal to daily time scales, the sensitivity of the convection depth to the atmospheric forcing and ocean preconditioning and the ability of state-of-the-art coupled climate models to simulate the mean and variable parts of the hydrography. To what extent do these chapters answer the questions that were asked in the introduction? These were:

- How large is the inter-annual variability in the northwestern North Atlantic?
- Which water masses and/or physical processes add to the variability?
- What does the variability look like on shorter time scales?
- What role does deep convective mixing play in the Irminger Sea?
- How well does the current generation of coupled climate models simulate the ocean state and variability of the northwestern North Atlantic?

The variability of the northwestern North Atlantic is relatively large as Munk (2002) suggested. Not only are the mean currents highly variable, of the order of 1 ± 10 cm s^{-1}, the water mass characteristics also show a large variability at a range of time scales. We will conclude our results concerning this variability, and the responsible processes, with a view on the questions listed above.

7.2 Conclusions

Various types, or scales, of variability are seen in the data sets used in this study. On the longest time scale, the length of the extended hydrographic series, we see an oscillation in temperature and salinity with a period of about 50 years (Chapter 3). This oscillation is visible in the upper 2000 dbar in the centres of the Labrador Sea and the Irminger Sea as a maximum in temperature (and salinity) around 1970 followed by a minimum in temperature (and salinity) in the late 1980s and early 1990s. This variability with a time scale of about 50 year is also seen over the entire northwestern

North Atlantic Ocean in sea surface temperature data. The signal is strongest in the upper 500 dbar, where it follows the minimum sea surface temperatures of the previous winter, indicating that the subsurface temperatures are set by convective mixing. In the deeper parts of the water column, between 500 and 2000 dbar, the amplitude of the signal is somewhat smaller, about 0.8 °C in the Irminger Sea (1.0 °C in the Labrador Sea) and 0.1 psu in both the Labrador and Irminger Seas. Since this change in thermohaline properties is found over such a substantial part of the water column it has a large effect on the total heat and salt content of the water column.

Several theories exist about the forcing, driving this multi-decadal (seeming) oscillation. Both basins are subject to annual net cooling by the atmosphere, therefore advection of warmer water is needed to create the warming branch of the temperature oscillation. In this balance lie the two main candidates, responsible for the forcing. The atmospheric heat flux, which cools, and the wind stress curl, which warms through driving the gyre advection, both show a similar multi-decadal signal. This is not coincidental, since the heat flux depends strongly on the strength of the local winds. The heat flux and the wind stress curl were at a minimum in the late 1960s, coinciding with high Labrador and Irminger temperatures, and were at a maximum around 1990, coinciding with low Labrador and Irminger temperatures. Both were highly correlated with the North Atlantic Oscillation (NAO) index. Several studies attribute the changes in temperature and salinity to the changes in wind stress forcing over the Subpolar Gyre (Flatau *et al.* (2003), Häkkinen & Rhines (2004) and Hátún *et al.* (2005)). The high wind stress curl conditions of the 1990s induced a spin up of the gyre and modulated the shape of the gyre, shifting the position of the North Atlantic Current (*NAC*). The latter effect is assumed to change the fraction of warm water from the *NAC* that enters the Subpolar Gyre circulation and thereby has a direct influence on the temperature and salinity in the northwestern North Atlantic Ocean.

However, the former effect, the spin up of the gyre, seems to work counter intuitively. Intuitively, an increase in the wind stress curl speeds up the gyre and thereby increases advection. Since warm, saline water is advected towards the Irminger and Labrador Seas, this stronger advection will lead to an increase in temperature. Thus, high temperature and salinity follow high wind stress curl (with some time lag). However, the observations show a minimum in temperature and salinity during high wind stress curl conditions. This would require a time lag of over 20 years, which is much longer than one would expect based on the current velocities. Also, this theory does not take in account the variability in temperature due to changes in the heat loss to the atmosphere.

To investigate the possibility of a faster mechanism, and without ignoring the strong correlation to the variability in the heat fluxes, we attempted to construct the multi-decadal temperature signal from the variability in the atmospheric heat fluxes only, using a simple model. This assumed that the mean temperature in the upper 2000 dbar is determined by the surface heat flux to the atmosphere and a constant advective warming. The advection term is estimated from the mean atmospheric heat flux over the 50-year record and the change in temperature during this period. The modelled Labrador Sea temperature series matches the observed temperature series quite closely. Only after 1990, during the proposed modulation of the North Atlantic Current inflow, a substantial amount of warming is missed by the modelled temperature record. No salinity changes due to atmospheric fluxes were included in the model, since a significant multi-decadal signal was not found in the atmospheric freshwater flux. Changes in advection of fresh water in the surface boundary currents are more likely to be dominant for the salinity changes. It seems obvious that a combination of the wind forcing and the heat fluxes is responsible for the multi-decadal thermohaline variability, but the relative importance of each is not yet clear.

Deep convective mixing is essential to distribute sea-to-air heat loss over a considerable part of the water column. Although this is a relatively rare process in the ocean, it is one of the main processes that sets the characteristic hydrography of the Labrador Sea. Weakly stratified Labrador Sea Water (*LSW*) is formed by deep convective mixing in the centre of this basin. The minimum in temperature and salinity of the multi-decadal signal, which occurs in the 1990s, coincides with the formation of a Labrador Sea Water class with a large volume (LSW_{94}, Yashayeav et al. (2008)), but is not necessarily caused by this event. Cooling of the *LSW* already started after the warm period around 1970. The convective formation of *LSW* does have a large effect on the dissolved oxygen content and the stability (measured either as the Brunt Väisälä frequency or as the potential vorticity). About every 10 year, the oxygen content peaks and the stability reaches a minimum, typical for convective ventilation events. Three major, deep reaching, ventilation events, in the 1970s, 1980s and 1990s, coincide with periods of strong surface cooling during successive winters. During the earlier events the surface heat loss was smaller and the ventilation reached less deep. Also, these older, shallower *LSW* classes were not characterized by the fresh and cold signature that was typical for the more recent *LSW* classes like LSW_{94} and LSW_{2000} (Yashayeav *et al.* (2008)). The more saline properties of the upper layer of the ocean, combined with less cooling, created *LSW* classes that mainly could be recognized by the increased oxygen concentration and reduced stability.

Through advection, the formation of *LSW* in the Labrador Sea has a large influence on the hydrography of the Irminger Sea and the Iceland Basin. Since the hydrographic properties are more or less conserved during spreading of the water mass, the *LSW* strongly determines the characteristics of the water column at its characteristic density level. The *LSW* reaches the Irminger Sea in ~2 year and the Iceland Basin in about 5 year. The World Ocean Circulation Experiment and Climate Variability and Predictability hydrographic programs sampled these basins from 1990 to present. During this period the arrival of *LSW* meant a freshening and cooling of the local intermediate hydrography.

While the *LSW* supplied the relatively cold and fresh water for the decrease in temperature and salinity from 1970 onwards, the observed warming and salinification after the early 1990s is caused by the decay of *LSW* and its replacement by warmer and more saline waters at this density level. There are several saline water masses in the northwestern North Atlantic that can add to the increase in salinity observed in the inter-annual variability. The most prominent deep and intermediate saline water masses in these basins are: Iceland Scotland Overflow Water (*ISOW*) and Icelandic Slope Water (*IcSW*) over the eastern slope of the Reykjanes Ridge, *IcSW* and North East Atlantic Deep Water (*NEADW*) over the western slope of the Reykjanes Ridge and the combined flow of relatively saline waters (mostly *NEADW*) which continues along the Greenland slope into the Labrador Sea. All these water masses are formed at or near the shallow overflow between Iceland and Scotland, where the cold, dense overflow water mixes with the saline North Atlantic Water. The saline cores of these waters are found over the deep basin boundaries, while their saline signals spread to the centre of the basins by lateral (isopycnal) mixing. Of these deep saline waters, the somewhat warmer *IcSW* is closest to the density of *LSW*, and is thus the most likely candidate for the gradual increase in salinity and temperature of the *LSW*. In its turn, the variability in the *LSW* influences the properties of the other saline water, the *NEADW*. The *NEADW*, found in the Irminger Sea, contains (varying) fractions of *ISOW* and Lower Deep Water (both found in the Iceland Basin) which entrain *LSW* in the Charlie-Gibbs Fracture Zone (the northernmost deep passage between these basins). Thus the low temperature and salinity signal of the *LSW* returns in the *NEADW* in the eastern Irminger Sea, with a delay of 2 year. This low salinity signal travels around the Irminger Sea cyclonically and is encountered in the western Irminger Sea again about 2 years later. Subsequently, since 1990 all these water types show a gradual decrease of temperature and salinity followed by a gradual increase, with different time lags of the minima (between 2 and 5 years).

The densest, deepest waters, Denmark Strait Overflow Water (*DSOW*) in the Irminger Sea and Lower Deep Water (*LDW*) in the Iceland Basin exhibit a very different variability. The *LDW*, which is the northernmost exponent of the Antarctic Bottom Water (*AABW*), shows no significant variability. This water mass is much older, and has entrained many small mixing fractions of other water types along its way north, so that all variability originating from the *AABW* is damped by mixing and diffusion. On the other hand, the *DSOW* (an overflow water originating from the Greenland-Iceland Ridge) is highly variable on inter-annual time scales. The fast variability in temperature and salinity (seeming oscillations with a period of the order of a few years) described by Dickson *et al.* (2003) continues in the more recent surveys of the AR7E section included here. The freshening trend of -15 ppm per decade (~0.015 psu / 10 years), observed in the *DSOW* between 1965 and 2000 (Dickson *et al.* (2003)), did not continue. In fact, the *DSOW* salinity increased by 0.04 psu between 2001 and 2008 in the surveys studied here.

However, the inter-annual hydrographic variability of Irminger bottom waters in the AR7E surveys is small with respect to the variability observed by moored instruments (Chapter 4). Continuously sampling instruments were moored near the bottom, at the lower Greenland slope (at 39 °W) and near the Reykjanes Ridge (at 36 °W) as a part of the Long-term Ocean Climate Observation (LOCO) program. The five year long records of these moorings give a much more detailed insight into the variability of the waters at 3000 dbar depth in the Irminger Sea. The temperature and salinity record from the westernmost mooring shows salinity variations that indicate the presence (or alternation) of two types of *DSOW*, one fresh and the other more saline. A peak of fresh *DSOW* was seen in 2004 as a drop in salinity of 0.05 psu over the course of little more than a month. The gradual return of the *DSOW* salinity to its previous, more saline state lasted over the next two years, occasionally interrupted by smaller drops in salinity. *Dickson et al.* (2008) saw similar, although larger and longer lasting, drops in salinity upstream in Denmark Strait in the winters of 1999 and 2004 and attributed these changes to strengthening of the freshwater feed of the East Greenland Current to the overflow. This is assumed to be forced by an increase in the north wind component just North of Denmark Strait. Apparently this signal is advected to the mooring location in approximately half a year and also decreased in strength by a factor 2. Another signal seen in the *DSOW* is a non-linear (saw tooth) annual cycle in temperature. This cycle shows a sharp drop in temperature in summer, of which one coincides with a drop in salinity, namely the large drop in salinity in 2004. After each drop in temperature, the temperature increases slowly over the rest of the year until the next summer. Since the salinity does not covary with temperature in this signal, leading to slight increases in density each summer followed by a gradual decrease

during the rest of the year. The 1 per year frequency suggest that the forcing lies in an atmospheric seasonal cycle over the overflow in Denmark Strait.

The second mooring, located further east, recorded temperature, salinity, and density signals that suggested a rapid alternation between two water types. The dense water type exhibits the characteristics of *DSOW*, with temperature and salinity signals that closely resemble the *DSOW* found at the western mooring location. The lighter water type approaches the properties of the *NEADW* as observed further east in the AR7E surveys. The alternations between cold, dense *DSOW*-like water and lighter, warmer *NEADW*-like water are rapid and occur several times (large peaks about 3 to 4) per year throughout the record. Various mixing fractions are found in between. Notably, the salinity variability at the eastern mooring reflect the salinity changes observed at the western mooring. Thus the dense, cold *DSOW*-like peaks are also somewhat fresher in 2004. The alternations in water mass properties itself could not be related to local advective patterns. The bottom flow observed at the mooring location is strongly driven by topography due to the presence of a deep canyon nearby. Therefore it is likely that the temperature and salinity variability depends on the direction or strength of the flow near the entrance of the canyon.

Fast, high-amplitude variability was observed at intermediate levels of the water column. The water column between 200 and 2400 dbar was observed with autonomous profilers which recorded daily profiles of temperature and salinity at the mooring locations. The magnitude of the day-to-day variability, observed in the profiles, exceeds that of the inter-annual variability as recorded during the AR7E surveys, even when averaged over a substantial vertical interval. The day-to-day variability is thought to be caused by interleaving (intrusions) from neighbouring water masses. This type of variability aliases the spatial gradients into the time domain. It is largely isopycnal in nature and can support lateral and vertical mixing between neighbouring water masses (Joyce (1977)). A calculation based on the length scales of the density overturns, which are the result of double diffusion in intrusions, estimated a value of the order of 10^{-2} m^2 s^{-1} for the vertical eddy diffusion coefficient, K_z, in the weakly stratified intermediate layer. This high mixing coefficient facilitates the transformation of the intermediate, fresh and cool Labrador Sea Water to its older, more saline and warmer form by lateral mixing with Icelandic Slope Water described before.

Large intrusions are also found in the upper layers, but there are some additional processes that cause the variability here. The first process (or type of variability), is the occurrence of meso-scale eddies, which pass by the two mooring locations. These eddies are relatively warm and saline and therefore probably originate from the

Irminger Current located at the east of the Irminger Sea. The eddies themselves were not a subject of this study. They mostly had a temporarily effect, strengthening the observed stratification, especially in spring.

The second process has the opposite effect. This is convective mixing, which removes the stratification. The daily measurements with the profiling instruments in the moorings show the occurrence of convective mixing in winter in the Irminger Sea. The mixed layers occur in small cells (~ 3 km, close to the local Rossby radius of deformation) which circulate in the Irminger gyre. The convective cells are encountered at both moorings. Therefore the convective area is probably at least 180 km wide in the East-West direction. The deepest mixed layers were observed during the cold winter of 2007-2008, reaching down to about 1000 dbar. During the same winter deep convection also returned to the Labrador Sea (Våge *et al.* (2009), Yashayaev & Loder (2009)). Surprisingly, the deepest mixed layers in the Irminger Sea were observed at the eastern side of the basin. Here the background stratification is relatively strong and mixed layers were generally shallower than those observed further west, during previous winters. Possibly, convective mixing inside a weakly stratified centre of an eddy facilitated deep mixing in this less favourable environment. However, deeper mixed layers may well have been present near the western location although they were not observed there. The chances of observing small, randomly occurring and moving convective cells by a moored profiler (recording only 4 hours per day) are not so high. The fact that both moorings have recorded convective mixing exceeding 500 dbar repeatedly in each of the 5 winters suggests that these convective cells are quite abundant.

Although deep mixed layers were observed during each of the five winters in the mooring deployment, their long-term effect on the local hydrography is unclear. This is partly caused by the quick restratification by surface water from the boundary currents. This restratification is aided by warm, saline meso-scale eddies (Katsman *et al.* (2004)), which quickly replace the homogeneous upper layers. A second difficulty is the unknown volume of water affected by the mixing in the Irminger Sea. The abundance and lifetime of the convective cells, and thereby the affected volume of water, cannot be established by snapshots of convective cells at two remote locations. We consider the main effect on the hydrography to be the modification, or preconditioning, of the Subpolar Mode Water (*SPMW*) in the upper 500 dbar of the central Irminger Sea. The modified, cooled and freshened, *SPMW* is advected towards the Labrador Sea by the Subpolar Gyre. There the *SPMW* is one of the main constituent of LSW. This idea is not unlike the scheme proposed by *McCartney & Talley* in 1984, but does not support the idea of a specific convective water mass, formed in the Irminger Sea as *Pickart et al.* (2003) have proposed.

In order for a recognizable water mass, formed by local deep convection in the Irminger Sea, to be observed in the (late summer) surveys, the convection must reach below the layer affected by restratification. This layer is substantially thicker than its counterpart in the Labrador Sea due to the amount of relatively light water available in the boundary currents. The Labrador Sea is a semi-enclosed basin and its reservoir of light water for restratification is determined by the width of the boundary currents and the import of water around the southern tip of Greenland and through Davis Strait. In contrast, the Irminger Sea seems to have a nearly infinite supply of relatively light water in its eastern boundary currents, which branches from the North Atlantic Current. During the period 2003-2008, only one winter was observed with moored instruments in which the convective mixing reached below the layer affected by restratification, the winter of 2008. Even so, this deep convection lasted only for a short period and was not able to form a substantial volume of easily recognizable homogeneous water in the Irminger Sea.

A model study, using a one dimensional mixed layer (or encroachment) model, showed that in order to have deep reaching convection in the Irminger Sea the preconditioning must be very favourable, more so than in the Labrador Sea (Chapter 5). This is due to the stronger mean stratification over the upper 500 dbar and the lower mean winter heat fluxes for the Irminger Sea. A large part (~75% in average conditions) of the heat loss in winter is utilized to remove the stratification over the upper 500 dbar. Only during very cold and long-lasting winters will the mixed layer reach deep below this level.

Another type of model study, in which we compared the ocean simulations used for the IPCC AR4 report (Meehl *et al.* (2007)) with observations, showed that most coupled models have difficulty in representing the mean hydrographic state of the northwestern North Atlantic Ocean (Chapter 6). In this study the pre-industrial and 20th century runs of Coupled Climate Models (CCMs) were compared with the 50-year record of near-annual hydrographic observations from the Labrador and Irminger Seas. The described difficulties express themselves in various forms, reversed vertical temperature gradients, (due to) salinity gradients that dominate the density stratifications and generally a too high ocean heat and salt content. Since most of the (pre-industrial) runs are initialized on an observed ocean state, part of the problems seem to be the drift of the oceanographic state away from the initialization during the spin up period of the model. This would be caused by the imbalance between the initial ocean state and the atmosphere. Also, large differences are observed between the simulated and observed mixing regimes. Extremely deep, basin wide convection takes place annually in some of the CCMs, while nearly no mixing occurs in other models due to the

large salinity gradient. Neither regime resembles the observed intermittent mixing in the centres of the studied basins. Other known model problems, such as numerical diffusion, might also contribute to the described model biases.

7.3 Remaining problems

This study showed that the variability in the northwestern North Atlantic, particularly the Irminger Sea, has two characteristic aspects. First, the range of time scales found in the variability equals the time range of the observations. The longest period (~50 years, if it is a return period) equals the approximate length of the hydrographic record in this region. On the other hand, we still find hydrographic variability at the time scales of the sampling intervals of the moored instruments. Secondly, the amplitude of the variability on intra-annual times scale exceeds the inter-annual variability at all depths. The drop in salinity over 1 month in 2004 found in the *DSOW*, for example, was as large as the total range of the inter-annual variability of *DSOW* in the AR7E section between 1991 and 2008.

The combination of both characteristics causes the true variability, of which we have been able to sample a small part with the moored instruments, to be underrepresented in the record of near-annual hydrographic surveys of the AR7E section. This offers a challenge to the interpretation of the data collected by these surveys, as the high frequency variability is either aliased onto the inter-annual variability or missed completely (such as the switching of water mass properties between *DSOW* and *NEADW* at the eastern mooring). This challenge is less important for changes that are estimated to be slow, such as the transport of a water mass from one basin to another over the course of a few years (like the *LSW*). Also, the effects of the small-scale intrusions may not cause a large problem. These intrusions, recorded here by the moored instrumentation but also observed in shipboard hydrographic surveys, are related to the large scale lateral gradients between water masses. These large-scale gradients are sampled adequately by the surveys. Also, the intrusions work towards a reduction of this gradient and their integrated effect may be seen by studying the transformation of water masses in subsequent surveys. Nevertheless, both the fast variability of the *DSOW* and the convective mixing and restratification in the Irminger Sea are not captured (well enough) by the near-annual surveys. Faster sampling here is not only essential for a complete description of the variability, but also to figure out the driving forces behind this variability. This is even more important since they are likely related to even more variable atmospheric changes.

On multi-decadal time scales, for which we assume the resolution provided by the near-annual surveys is adequate, we are also left with an important issue. Again, the period of the multi-decadal oscillation, described here, nearly equals the length of the observational time series. This implies that we do not know whether this is indeed a recurring oscillation or that our estimate for the period is biased towards the length of the record. However, there is enough available evidence in the form of surveys and satellite data to show that this multi-decadal variability was present during the last 60 years. The problem that remains is the mechanism behind these large scale, multi-decadal changes in temperature, salinity and overall stratification. There are several atmospheric parameters that are excellent candidates because of their high correlation with the observed ocean changes. The wind stress curl, air-to-sea heat flux and the North Atlantic Oscillation index are three such parameters that are referred to by this study, but possibly there are more. But we cannot explain ocean changes by correlation alone. One or more processes that satisfactory explain the observed changes are necessary to fully understand the variability of the northwestern North Atlantic Ocean, especially with possible future climate changes in mind.

7.4 Future challenges

Naturally, the remaining problems mentioned in the previous section are some of the future challenges. But I would like to take this opportunity to bring forward some more practical challenges. One of these practical challenges is to maintain the present observatories in the northwestern North Atlantic Ocean, such as the LOCO, CIS and NOC moorings in the Irminger Sea. These moorings already have contributed to an impressive data collection, but the period in which these data have been collected has been a relatively calm, or warm, one. A period consisting of several cold winters during a persisting high NAO index, has yet to be recorded in high temporal resolution. Both the cold and the warm atmospheric state has to be observed to understand the fast variability, especially deep convection, better.

Although already a cold phase (in the 1990s) and a warm phase (in the 2000s) have been observed by the AR7 surveys this does not mean that this particular record is complete. At present, serious concerns are held by oceanographers studying this area about the continuation of AR7 surveys in the coming years. Programs including this area are coming to an end and focus is shifting to other areas and processes. However, if we want to find out more about multi-decadal changes and possible changes of the Meridional Overturning Circulation in the future we need to maintain a regular occupation of the northern North Atlantic WOCE sections.

The influence of meso-scale eddies should also be studied in more detail. Eddies in the Labrador Sea have been studied using moorings, gliders and floats. Coherent cold core eddies were shown to be created by Labrador Sea convection (Lilly & Rhines (2002)), a phenomenon which also may explain the deep convection observed in the stable eastern part of the Irminger Sea in the winter of 2007-2008. Warm eddies, which restratify the central Labrador Sea, were shown to originate from the Irminger Water in the West Greenland Current (Katsman *et al.* (2004)). The precise origin of meso-scale eddies in the Irminger Sea and their contribution to the heat and salt balance still remains unknown.

In order to understand (and ideally predict) future changes, the ocean models and coupled climate models need to be improved. The mismatch between the observed and the modelled oceans creates a large separation between the observational and modelling world. The observational record lengths have reached the point where they can be used to assess the skill of models in simulating both the mean state and the variability up to decadal time scales. On the other hand the newer generations of models have a much improved resolution and realism compared to the first slab ocean models. Also, there are some interesting model studies that find multi-decadal oscillation in the North Atlantic Ocean, with time scales similar to those found in our observations (Frankcombe *et al.* (in press 2010)). It could prove most interesting to compare these (observed and modelled) types of variability. More interaction between both disciplines can lead to large steps in understanding the oceans.

As a final remark I can state here that studies like the one presented in this thesis are only possible with an adequately functioning international data management system and oceanographers willing to supply their data to data centres.

Appendix A

List of acronyms

Water masses

AABW	Antarctic Bottom Water
DSOW	Denmark Strait Overflow Water
IcSW	Icelandic Slope Water
ISOW	Iceland Scotland Overflow Water
LDW	Lower Deep Water
LSW	Labrador Sea Water
(M)NAW	(Modified) North Atlantic Water
NADW	North Atlantic Deep Water
NEADW	North East Atlantic Deep Water
SPMW	Subpolar Mode Water

Currents

DWBC	Deep Western Boundary Current
EGC	East Greenland Current
EGCC	East Greenland Coastal Current
ERRC	East Reykjanus Ridge Current
ESC	European Slope Current
IC	Irminger Current
NAC	North Atlantic Current
NC	Norwegian Current
NIC	North Iceland Irminger Current
WGC	West Greenland Current

Topography

CGFZ	Charlie-Gibbs Fracture Zone
DS	Denmark Strait
FBC	Faroe Bank Channel
GB	Grand Banks
MAR	Mid Atlantic Ridge
RHB	Rockall-Hatton Bank
RR	Reykjanus Ridge

Data sets and institutes

AR7E	WOCE section (southeast Greenland - Ireland)
AR7W	WOCE section (Newfoundland, Canada - southwest Greenland)
CLIVAR	Climate Variability and Predictability program
ICES	International Council for the Exploration of the Sea
ICOADS	International Comprehensive Ocean-Atmosphere Data Set
ICSU	International Council for Science
IfMk	Institute für Meerskunde, Kiel
IfMh	Institute für Meerskunde, Hamburg
IOC	Intergovernmental Oceanographic Commission
LOCO	Long-term Ocean Climate Observations
NCEP	National Centers for Environmental Prediction
NIOZ	Royal Netherlands Institute for Sea Research
NOAA	National Oceanographic and Atmospheric Administration
NOC	National Oceanography Center, Southampton
UNESCO	United Nations Educational, Scientific and Cultural Organization
WHOI	Woods Hole Oceanographic Institute
WMO	World Meteorological Organization
WOCE	World Ocean Circulation Experiment

Data and instruments

ADCP	Acoustic Doppler Current Profiler
CFC	Chlorofluorocarbon
CTD	Conductivity Temperature Depth (sensor)
LOCO 2-x	Western (39° W) LOCO mooring - year of deployment
LOCO 3-x	Eastern (36° W) LOCO mooring - year of deployment
MMP	McLane Moored Profiler (CTD profiler)
M2	semi-diurnal lunar tidal cycle
SBE 37-SM	Sea Bird Electronics Microcat (CTD sensor)
SST	Sea Surface Temperature
S2	semi-diurnal solar tidal cycle

Appendix B

Coupled climate models and ocean reanalyses

Explanation of the model acronyms and model references for the models used in Chapter 6. The full name refers to the institute of origin of the model and to the model version.

Acronym	Full name	Reference
BCCM-BCM2.0	Bjerknes Centre for Climate Research Bergen Climate Model version 2.0	Furevik *et al.* (2003)
CNRM-CM3	Centre National de Recherches Météorologiques Coupled Global Climate Model version 3	Salas-Mélia *et al.* (2005)
GFDL-CM2.0	Geophysical Fluid Dynamics Laboratory Climate Model version 2.0	Delworth *et al.* (2006)
IPSL-CM4	L'Institut Pierre-Simon Laplace Coupled Model version 4	Marti *et al.* (2005)
MIROC3.2 (hires & medres)	Center for Climate System Research, University of Tokyo / National Institute for Environmental Studies / Frontier Research Center for Global Chance, Japan Agency for Marine-Earth Science and Technology Model for Interdisciplinary Research on Climate 3.2	Hasumi & Emori (2004)
UKMO HadCM3	UK Met Office Hadley Centre Third Coupled Ocean-Atmosphere GCM	Gordon *et al.* (2000)
UKMO HadGEM1	UK Met Office Hadley Centre Global Environmental Model version 1	Johns *et al.* (2004)
NEMO-OPA 2.0	Nucleus for European Modelling of the Ocean Océan Parallélisé 2° resolution version	Madec (2008)
ECCO SIO 1	Estimating the Circulation and Climate of the Ocean Scripps Institute of Oceanography version 1	Köhl *et al.* (2003)
SODA 1.4.2	Simple Ocean Data Assimilation version 1.4.2	Carton *et al.* (2005)

References

Amante, C. & B. W. Eakins (2009). ETOPO1 1 Arc-Minute Global Relief Model: Procedures, Data Sources and Analysis. *NOAA Technical Memorandum NESDIS NGDC-24, 19 pp.*

Bacon, S., G. Reverdin, I. G. Rigor, & H. M. Snaith (2002). A freshwater jet on the east Greenland shelf. *Journal of Geophysical Research*, 107 (C7), doi:10.1029/2001JC000935.

Bacon, S., W. J. Gould & Y. Jia (2003). Open-ocean convection in the Irminger Sea. *Geophysical Research Letters*, 30, 1246, doi:10.1029/2002GL016271.

Bakalian, F., S. Hameed, & R. Pickart (2007). Influence of the Icelandic Low latitude on the frequency of Greenland tip jet events: Implications for Irminger Sea convection. *Journal of Geophysical Research*, 112 (C04020), doi:10.1029/2006JC003807.

Bersch, M., J. Meincke & A. Sy (1999). Interannual thermohaline changes in the northern North Atlantic 1991-1996. *Deep-Sea Research II*, 46, 55–75, doi:10.1016/S0967-0645(98)00114-3.

Brambilla, E., & L. D. Talley (2008). Subpolar Mode Water in the northeastern Atlantic: 1. Averaged properties and mean circulation. *Journal of Geophysical Research*, 113, C04025, doi:10.1029/2006JC004062.

Brambilla, E., L. D. Talley & P. E. Robbins (2008). Subpolar Mode Water in the northeastern Atlantic: 2. Origin and transformation. *Journal of Geophysical Research*, 113, C04026, doi: 10.1029/2006JC004063.

Bumke, K., U. Karger & K. Uhlig (2002). Measurements of turbulent fluxes of momentum and sensible heat over the Labrador Sea. *Journal of Physical Oceanography*, 32, 401–410, doi: 10.1175/1520-0485(2002)032<0401:MOTFOM>2.0.CO;2.

Carton, J. A. and B. S. Giese (2005). SODA: A reanalysis of ocean climate. Online at: http://www.atmos.umd.edu/~carton/pdfs/carton&giese05.pdf.

Curry, R. G., & M. S. McCartney (2001). Ocean gyre circulation changes associated with the North Atlantic Oscillation. *Journal of Physical Oceanography*, 31, 3374-3400, doi: 10.1175/1520-0485(2001)031<3374:OGCCAW>2.0.CO;2.

Delworth, T.L., A. J. Broccoli, A. Rosati, R. J. Stouffer, V. Balaji, J. A. Beesley, W. F. Cooke, K. W. Dixon, J. Dunne, K. A. Dunne, J. W. Durachta, K. L. Findell, P. Ginoux, A. Gnanadesikan, C. T. Gordon, S. M. Griffies, R. Gudgel, M. J. Harrison, I. M. Held, R. S. Hemler, L. W. Horowitz, S. A. Klein, T. R. Knutson, P. J. Kushner, A. R. Langenhorst, H. C. Lee, S. J. Linl, J. Lu, S. L. Malyshev, P. C. D. Milly, V. Ramaswamy, J. Russell, M. D. Schwarzkopf, E. Shevliakova, J. J. Sirutis, M. J. Spelman, W. F. Stern, M. Winton, A. T. Wittenberg, B. Wyman, F. Zeng & R. Zhang (2006). GFDLs CM2 global coupled climate models - Part 1: Formulation and simulation characteristics, *Journal of Climate*, 19 (5), 643–674, doi: 10.1175/JCLI3629.1.

Dickson, R., R. Meincke, S. A. Malmberg and J. J. Lee (1988). The Great Salinity Anomaly in the northern North Atlantic 1968-1982, *Progress in Oceanography*, 20 (2), 103–151, doi: 10.1016/0079-6611(88)90049-3.

Dickson, R., J. Lazier, J. Meincke, P. Rhines & J. Swift (1996). Long-term coordinated changes in the convective activity of the North Atlantic. *Progress in Oceanography*, 38 (3), 241–295, doi: 10.1016/S0079-6611(97)00002-5.

Dickson, R., J. Meincke, I. Vassie, J. Jungclaus & S. Østerhus (1999). Possible predictability in overflow from the Denmark Strait. *Nature*, 397, 243–246, doi: 10.1038/16680.

Dickson, R., R. Curry & I. Yashayaev (2003). Recent changes in the North Atlantic. *Philosophical Transactions: Mathematical, Physical and Engineering Sciences*, 361 (1810), 1917–1934.

Dickson, B., S. Dye, S. Jónsson, A. Köhl, A. Macrander, M. Marnela, J. Meincke, S. Olsen, B. Rudels, H. Valdimarsson & G. Voet (2008). The Overflow Flux West of Iceland: Variability, Origins and Forcing. In: *Arctic-Subarctic Ocean Fluxes*, Springer Dordrecht, the Netherlands, Eds. R. R. Dickson, J. Meincke & P. Rhines. 19, 443–474.

Donners, J., S. Drijfhout & W. Hazeleger (2005). Water mass transformation and subduction in the South Atlantic, *Journal of Physical Oceanography*, 35 (10), 1841–1860, doi:10.1175/JPO2782.1

Doyle, J. D., & M. A. Shapiro (1999). Flow response to large-scale topography: the Greenland tip jet. *Tellus A*, 51, 728–748, doi: 10.1034/j.1600-0870.1996.00014.x.

Drakkar Group (2007). Eddy-permitting ocean circulation hindcasts of past decades, *CLIVAR Exchanges*, 12 (3), 8–10.

Drijfhout, S. S., W. Hazeleger, F. Selten & R. Haarsma (2008), Future changes in internal Atlantic Meridional Overturning Circulation variability. *Climate Dynamics*, 30 (4), 407-419, doi:10.1007/s00382-007-0297-y.

Dronkers, J. J. (1964). *Tidal Computations in Rivers and Coastal Waters*. North-Holland Publishing Company, Amsterdam, the Netherlands.

Eden, C. & J. Willebrand (2000). Mechanism of interannual to decadal variability of the North Atlantic Circulation. *Journal of Climate*, 14 (10), 2266–2278, doi: 10.1175/1520-0442(2001)014<2266:MOITDV>2.0.CO;2.

Flatau, M. K., L. Talley & P. P. Niiler (2003). The North Atlantic Oscillation, surface current velocities, and SST changes in the subpolar North Atlantic. *Journal of Climate*, 16 (14), 2355-2369, doi: 10.1175/2787.1.

Frankcombe, L. M., A. von der Heydt & H. A. Dijkstra (in press 2010). North Atlantic Multidecadal Climate Variability: An investigation of dominant time scales and processes. *Journal of Climate,* doi: 10.1175/2010JCLI3471.1.

Furevik, T., M. Bentsen, H. Drange, I. K. T. Kindem, N. G. Kvamsto & A. Sorteberg (2003). Description and evaluation of the Bergen climate model: ARPEGE coupled with MICOM, *Climate Dynamics*, 21 (1), 27–51, doi: 10.1007/s00382-003-0317-5.

Gill, A. E. (1982). Atmosphere-Ocean Dynamics. *International Geophysics Series Vol.30*, Academic Press, New York, USA.

Gordon, C., C. Cooper, C. A. Senior, H. Banks, J. M. Gregory, T. C. Johns, J. F. B. Mitchell & R. A. Woods (2000). The simulation of SST, sea ice extents and ocean heat transport in a version of the Hadley Centre coupled model without flux adjustments, *Climate Dynamics*, 16, 147–168, doi: 10.1007/s003820050010.

Haine, T., C. Böning, P. Brandt, J. Fischer, A. Funk, D. Kieke, E. Kvaleberg, M. Rhein & M. Visbeck (2008). North Atlantic Deep Water formation in the Labrador Sea, recirculation through the Subpolar Gyre, and discharge to the Subtropics. In: *Arctic-Subarctic Ocean Fluxes*, Springer Dordrecht, the Netherlands, Eds. R. R. Dickson, J. Meincke & P. Rhines. 27, 653-701.

Häkkinen, S., & P. B. Rhines (2004). Decline of Subpolar North Atlantic Circulation during the 1990s. *Science*, 304, 555-559, doi: 10.1126/science.1094917.

Hansen, B., & S. Østerhus (2007). Faroe Bank Channel overflow 1995-2001. *Progress in Oceanography*, 75 (4), 817-856, doi: 10.1016/j.physletb.2003.10.071.

Hátún, H., A. B. Sandø & H. Drange (2005). Influence of the Atlantic Subpolar Gyre on the thermohaline circulation. *Science*, 309, 1841-1844, doi: 10.1126/science.1114777.

Hátún, H., C. C. Eriksen & P. B. Rhines (2007). Buoyant eddies entering the Labrador Sea observed with gliders and altimetry. *Journal of Physical Oceanography*, 37, 2838–2854, doi: 10.1175/2007JPO3567.1.

Hendry, R. M., H. M. van Aken & I. Yashayaev (2007). Monitoring the ventilation of the Irminger and Labrador Seas, *Clivar Exchanges*, 12 (1), 25–27.

Holliday, N. P., A. Meyer, S. Bacon, S. G. Alderson & B. de Cuevas (2007). Retroflection of part of the East Greenland Current at Cape Farewell. *Geophysical Research Letters*, 34, doi:10.1029/2006GL02985.

Holliday, N. P., S. L. Hughes, S. Bacon, A. Beszczynska-Möller, B. Hansen, A. Lavín, H. Loeng, K. A. Mork, S. Østerhus, T. Sherwin & W. Walczowski (2008). Reversal of the 1960s to 1990s freshening trend in the northeast North Atlantic and Nordic Seas. *Geophysical Research Letters*, 35, L03614, doi:10.1029/2007GL032675.

Hurrell, J.W. (1995). Decadal trends in the North Atlantic Oscillation regional temperatures and precipitation. *Science*, 269, 676–679, doi: 10.1126/science.269.5224.676.

IPCC (2007). *Climate Change 2007: The Physical Science Basis. Contribution of Working Group I to the Fourth Assessment Report of the Intergovernmental Panel on Climate Change,* Cambridge University Press, Cambridge, United Kingdom and New York, NY, USA.

Jeffreys, H. (1925). On fluid motions produced by differences of temperature and humidity. *Quarterly Journal of the Royal Meteorological Society*, 51, 347-356.

Johns, T., C. Durman, H. Banks, M. Roberts, A. McLaren, J. Ridley, C. Senior, K. Williams, A. Jones, A. Keen, G. Rickard, S. Cusack, M. Joshi, M. Ringer, B. Dong, H. Spencer, R. Hill, J. Gregory, A. Pardaens, J. Lowe, A. Bodas-Salcedo, S. Stark & Y. Searl (2004). HadGEM1-Model description and analysis of preliminary experiments for the IPCC Fourth Assessment Report, *Hadley Centre technical note*, 55,Met Office Hadley Centre, UK.

Josey, S.A., & R. Marsh (2005). Surface freshwater flux variability and recent freshening of the North Atlantic in the eastern subpolar gyre, *Journal of Geophysical Research*, 110, doi:10.1029/2004JC002521.

K-1 model developers (2004). K-1 coupled model (MIROC) description. *Technical Report*, 1, Center for Climate System Research, University of Tokyo, Japan.

Katsman, C. A., M. A. Spall & R. S. Pickart (2004). Boundary current eddies and their role in the restratification of the Labrador Sea. *Journal of Physical Oceanography*, 34, 1967–1983, doi: 10.1175/1520-0485(2004)034<1967:BCEATR>2.0.CO;2.

Knutsen, Ø., H. Svendsen, S. Østerhus, T. Rossby & B. Hansen (2005). Direct measurements of the mean flow and eddy kinetic energy structure of the upper ocean circulation in the NE Atlantic. *Geophysical Research Letters*, 32, L14604, doi:10.1029/2005GL023615.

Kohl, A., D. Stammer, B. Cornuelle, E. Remy, Y. Lu, P. Heinbach & C. Wunsch (2003). The Global WOCE 1° Synthesis: 1992-2001, *The ECCO Report Series*, 20.

Krauss, W. (1995). Currents and mixing in the Irminger Sea and in the Iceland Basin. *Journal of Geophysical Research*, 100 (C6), 10851-10871, doi:10.1029/95JC00423.

Lab Sea Group, The. (1998). The Labrador Sea deep convection experiment. *Bulletin of the American Meteorological Society*, 79, 2033–2058.

Lavender, K. L., R. E. Davis & W. B. Owens (2000). Mid-depth recirculation observed in the interior Labrador and Irminger seas by direct velocity measurements. *Nature*, 407, 66-69, doi: 10.1038/35024048.

Lazier, J. (1994). Observations in the Northwest Corner of the North Atlantic Current. *Journal of Physical Oceanography*, 24, 1449–1463, doi: 10.1175/1520-0485(1994)024<1449:OITNCO>2.0.CO;2.

Lazier, J., R. Hendry, A. Clarke, I. Yashayaev & P. B. Rhines (2002). Convection and restratification in the Labrador Sea, 1990-2000. *Deep-Sea Research I*, 49 (10), 1819–1835, doi: 10.1016/S0967-0637(02)00064-X.

Levitus, S. & T.P. Boyer (1994). World Ocean Atlas 1994 Volume 4: Temperature, *NOAA Atlas NESDIS 4,* U.S. Government Printing Office, Washington, DC, USA.

Levitus, S., R. Burgett & T.P. Boyer (1994). World Ocean Atlas 1994 Volume 3: Salinity, *NOAA Atlas NESDIS 3,* U.S. Government Printing Office, Washington, DC, USA.

Levitus, S., et al. (1998). World Ocean Database Volume 1: Introduction, *NOAA Atlas NESDIS 18*, U.S. Government Printing Office, Washington, DC, USA.

Lherminier, P., J.-C. Gascard & D. Quadfasel (1999). The Greenland Sea in Winter 1993 and 1994: preconditioning for deep convection. *Deep-Sea Research II*, 46, 1199-1235, doi: 10.1016/S0967-0645(99)00020-X.

Lilly, J. M., P. B. Rhines, M. Visbeck, R. Davis, J. R. N. Lazier, F. Schott & D. Farmer (1999). Observing Deep Convection in the Labrador Sea during Winter 1994/95. *Journal of Physical Oceanography*, 29, 2065-2098, doi: 10.1175/1520-0485(1999)029<2065:ODCITL>2.0.CO;2.

Lilly, J. M., P. B. Rhines, F. Schott, K. Lavender, J. Lazier, U. Send & E. D'Asaro (2003). Observations of the Labrador Sea eddy field. *Progress in Oceanography*, 59 (1), 75–176, doi: 10.1016/j.pocean.2003.08.013.

Macrander, A., U. Send, H. Valdimarsson, S. Jónsson & R. H. Käse (2005). Interannual changes in the overflow from the Nordic Seas into the Atlantic Ocean through Denmark Strait. *Geophysical Research Letters*, 32, L06606, doi:10.1029/2004GL021463.

Madec, G. (2008). NEMO reference manual, ocean dynamics component: NEMO-OPA. Preliminary version, *Note du Pôle de Modélisation*, 27, Institute Pierre-Simon Laplace, France.

Manabe, S., & K. Bryan (1969). Climate calculations with a combined ocean-atmosphere model. *Journal of the Atmospheric Sciences*, 26, 786-789.

Marotzke, J. & J. R. Scott (1999). Convective mixing and the thermohaline circulation. *Journal of Physical Oceanography*, 29, 2962-2970, doi: 10.1175/1520-0485(1999)029<2962:CMATTC>2.0.CO;2.

Marshall, J.& F. Schott (1999). Open-ocean convection: Observations, theory and models. *Reviews of Geophysics*, 37, 1-64, doi:10.1029/98RG02739.

Marshall, J., Y. Kushnir, D. Battisti, P. Chang, A. Czaja, R. Dickson, J. Hurrell, M. McCartney, R. Saravanan, & M. Visbeck (2001). North Atlantic climate variability: phenomena, impacts and mechanisms. *International Journal of Climatology*, 21 (15), 1863–1898. doi: 10.1002/joc.693

Marti, O., P. Braconnot, J. Bellier, R. Benshila, S. Bony, P. Brockmann, P. Cadule, A. Caubel, S. Denvil, J.-L. Dufresne, L. Fairhead, M.-A. Foujols, T. Fichefet, P. Friedlingstein, H. Gosse, J.-Y. Grandpeix, F. Hourdin, G. Krinner, C. Levy, G. Madec, I. Musat, N. de Noblet, J. Polcher & C. Talandier (2005). The new IPSL climate system model: IPSL-CM4. *Note du Pôle de Modélisation*, 26, Institute Pierre-Simon Laplace, France.

McCartney, M. S., & L. D. Talley (1982). The Subpolar Mode Water of the North Atlantic. *Journal of Physical Oceanography*, 12, 1169–1188, doi: 10.1175/1520-0485(1982)012<1169:TSMWOT>2.0.CO;2.

McCartney, M. S., & L. D. Talley (1984). Warm-to-cold water conversion in the northern North Atlantic Ocean. *Journal of Physical Oceanography*, 14, 922–935, doi: 10.1175/1520-0485(1984)014<0922:WTCWCI>2.0.CO;2.

Meehl, G. A., C. Covey, T. Delworth, M. Latif, B. McAvaney, J. F. B. Mitchell, R. J. Stouffer & K. E. Taylor (2007). The WCRP CMIP3 multimodel dataset. *Bulletin of the American Meteorological Society, 88 (9), 1383–1394.*

Meincke, J. (1983). The modern current regime across the Greenland-Scotland Ridge. In: *Structure and development of the Greenland-Scotland Ridge*. Eds. M. H. P. Bott, S. Sakov, M. Talwani, J. Thiede, Plenum, 637–650.

Moore, G. W. K., & I. A. Renfrew (2005). Tip jets and barrier winds: A quikSCAT climatology of high wind speed events around Greenland. *Journal of Climate*, 18 (18), 3713–3725, doi: 10.1175/JCLI3455.1.

Morozov, E.G., A. N. Demidov & R. Y. Tarakanov (2008). Transport of Antarctic waters in the deep channels of the Atlantic Ocean. *Doklady Earth Sciences*, 423 (8), 1286–1289.

Munk, W. (1966). Abyssal recipes. *Deep Sea Research*, 13, 707-730.

Munk, W., & C. Wunsch (1998). Abyssal recipes II: Energetics of tidal and wind mixing. *Deep Sea Research I*, 45, 1977-2010, doi: 10.1016/S0967-0637(98)00070-3.

Munk, W. (2002). The evolution of physical oceanography in the last hundred years. *Oceanography*, 15 (1), 135-141.

Myers, P. G., S. A. Josey, B. Wheler & N. Kulan (2007). Interdecadal variability in Labrador Sea precipitation minus evaporation and salinity. *Progress in Oceanography*, 73, 341–357, doi:10.1016/j.pocean.2006.06.003.

Nansen, F. (1912). Das Bodenwasser und die Abkuhlung des Meeres. *Internationale Revue der Gesamten Hydorbiologie und Hydrographie Band V* (1), 1-42.

Østerhus, S., W. R. Turrell, S. Jónsson & B. Hansen (2005). Measured volume, heat, and salt fluxes from the Atlantic to the Arctic Mediterranean. *Geophysical Research Letters*, 32, doi:10.1029/2004GL022188.

Pickart, R. S., F. Straneo & G. W. K. Moore (2003). Is Labrador Sea Water formed in the Irminger Basin? *Deep Sea Research I*, 50 (1), 23-52, doi: 10.1016/S0967-0637(02)00134-6.

Pickart, R. S. & M. A. Spall (2007). Impact of Labrador Sea convection on the North Atlantic meridional overturning circulation. *Journal of Physical Oceanography*, 37, 2207-2227, doi: 10.1175/JPO3178.1.

Pickart, R. S., K. Våge, G. W. K. Moore, I. A. Renfrew, M. H. Ribergaard & H. C. Davies (2008). Convection in the western North Atlantic Sub-Polar Gyre: do small scale wind events matter? In: *Arctic-Subarctic Ocean Fluxes*, Springer Dordrecht, the Netherlands, Eds. R. R. Dickson, J. Meincke & P. Rhines. 26, 629-652.

Pond, S., & G. L. Pickard (1983). *Introductory dynamical oceanography, 2nd edition.* Elsevier Butterworth-Heinemann, Oxford, Great Britain, 329 pp.

Price, J. F., & M. O'Neal Baringer (1994). Outflows and deep water production by marginal seas. *Progress in Oceanography*, 33, 161-200, doi: 10.1016/0079-6611(94)90027-2.

Read, J. F., & W. J. Gould (1992). Cooling and freshening of the subpolar North Atlantic Ocean since the 1960s. *Nature*, 360, 55–57, doi: 10.1038/360055a0.

Renfrew, I. A., G. W. K. Moore, P. S. Guest & K. Bumke (2002). A Comparison of Surface Layer and Surface Turbulent Flux Observations over the Labrador Sea with ECMWF Analyses and NCEP Reanalyses. *Journal of Physical Oceanography*, 32, 383-400, doi: 10.1175/1520-0485(2002)032<0383:ACOSLA>2.0.CO;2.

Rhein, M., D. Kieke & R. Steinfeldt (2007). Ventilation of the Upper Labrador Sea Water, 2003-2005. *Geophysical Research Letters*, 34, L06603, doi:10.1029/2006GL028540.

Ruddick, B., & O. Kerr (2003). Oceanic thermohaline intrusions: theory. *Progress in Oceanography*, 56, 483-497, doi: 10.1016/S0079-6611(03)00029-6.

Rudels, B., D. Quadfasel, H. Friedrich & M.-N. Houssias (1989). Greenland Sea convection in the winter of 1987–1988. *Journal of Geophysical Research*, 94 (C3), 3223–3227, doi: 10.1029/JC094iC03p03223.

Rogers, J. C. (1997). North Atlantic storm track variability and its association to the North Atlantic Oscillation and climate variability of northern Europe. *Journal of Climate*, 10 (7), 1635–1647, doi: 10.1175/1520-0442(1997)010<1635:NASTVA>2.0.CO;2.

Ross, C. K. (1984). Temperature-salinity characteristics of the "overflow" water in Denmark Strait during "Overflow '73". *Rapp. P.-v. Fisheries. Réun. Cons. int. Explor. Mer.* 185, 111-119.

Salas-Melia, D., F. Chauvin, M. Denque, H. Douville, J. F. Gueremy, P. Marquet, S. Planton, J. F. Royer & S. Tyteca (2005). Description and validation of the CNRM-CM3 global coupled model. *CNRM working note*, 103, Centre National de Recherches Météorologiques, France.

Sandström, J. W. (1908). Dynamische Versuche mit Meerwasser. *Ann. Hydrogr. Mar. Meteorol.*, 36, 6-23.

Sarafanov, A., A. Falina, A. Sokov & A. Demidov (2008). Intense warming and salinification of intermediate waters of southern origin in the eastern subpolar North Atlantic in the 1990s to mid-2000s. *Journal of Geophysical Research*, 113, C12022, doi:10.1029/2008JC004975.

Sathiyamoorthy, S., & G. W. K. Moore (2002). Buoyancy flux at ocean weather station Bravo. *Journal of Physical Oceanography*, 32, 458–474, doi: 10.1175/1520-0485(2002)032<0458:BFAOWS>2.0.CO;2.

Schmittner, A., M. Latif & B. Schneider (2005). Model projection of the North Atlantic thermohaline circulation for the 21st century assessed by observations. *Geophysical Research Letters*, 32, doi:10.1029/2005GL024368.

Seager, R., D. S. Battisti, J. Yin, N. Gordon, N. Naik, A. C. Clement & M. A. Cane (2002). Is the Gulf Stream responsible for Europe's mild winters? *Quarterly Journal of the Royal Meteorological Soc*iety, 128.

Sloyan, B. M., & I. V. Kamenkovick (2007). Simulation of Subantarctic Mode and Antarctic Intermediate Waters in climate models. *Journal of Climate*, 20 (20), 5061–5080, doi: 10.1175/JCLI4295.1.

Straneo, F. (2006). Heat and Freshwater Transport through the Central Labrador Sea. *Journal of Physical Oceanography*, 36, 606-628, doi: 10.1175/JPO2875.1.

Sverdrup, H. U., M. W. Johnson & R. H. Fleming (1942). *The Oceans: Their Physics, Chemistry, and General Biology*. Englewood Cliffs, New Jersey: Prentice-Hall, Inc. USA.

Talley, L. D., & M. S. McCartney (1982). Distribution and circulation of Labrador Sea Water. *Journal of Physical Oceanography*, 12, 1189–1205, doi: 10.1175/1520-0485(1982)012<1189:DACOLS>2.0.CO;2.

Tanhua, T., K. Bulsewicz & M. Rhein (2005). Spreading of overflow water from the Greenland to the Labrador Sea. *Geophysical Research Letters*, 32, doi: 10.1029/2005GL022700.

Turner, J. S. (1978). Double-diffusive intrusions into a density gradient. *Journal of Geophysical Research*, 83 (C6), 2887-2901, doi:10.1029/JC083iC06p02887.

Turrell, W. R., G. Slesser, R. D. Adams, R. Payne & P. A. Gillebrand (1999). Decadal variability in the composition of Faroe Shetland Channel bottom water. *Deep-Sea Research I*, 46, 1–25, doi: 10.1016/S0967-0637(98)00067-3.

Våge, K., R. S. Pickart, V. Thierry, G. Reverdin, C. M. Lee, B. Petrie, T. A. Agnew, A. Wong & M. H. Ribergaard (2008). Surprising return of deep convection to the subpolar North Atlantic Ocean in winter 2007-2008. *Nature Geoscience*, 382, doi:10.1038.

Valdimarsson, H., & S. A. Malmberg (1999). Near-surface circulation in Icelandic waters derived from satellite-tracked drifters. *Rit Fiskideildar*, 16, 23–29.

van Aken, H. M. (1995). Hydrographic variability in the bottom layer of the Iceland Basin. *Journal of Physical Oceanography*, 25, 1716–1722, doi: 10.1175/1520-0485(1995)025<1716:HVITBL>2.0.CO;2.

van Aken, H. M., & C. J. de Boer (1995). On the synoptic hydrography of intermediate and deep water masses in the Iceland Basin. *Deep-Sea Research I*, 42, 165–189, doi: 10.1016/0967-0637(94)00042-Q.

van Aken, H. M., & G. Becker (1996). Hydrography and through-flow in the north-eastern North Atlantic Ocean: the NANSEN project. *Progress in Oceanography*, 38, 297–346, doi: 10.1016/S0079-6611(97)00005-0.

van Aken, H. M. (2002). Surface currents in the Bay of Biscay as observed with drifters between 1995 and 1999. *Deep-Sea Research I*, 49, 1071–1086, doi: 10.1016/S0967-0637(02)00017-1.

van Aken, H. M. 2007. The Oceanic Thermohaline Circulation: An Introduction. *Springer Science + Business Media*, New York, USA., pp. 326.

Volkov, D. L. (2004). Monitoring the variability of sea level and surface circulation with satellite altimetry. *Ph.D. Thesis*, Utrecht University, the Netherlands.

Volkov, D. L. (2005). Interannual variability of the Altimetry-derived eddy field and surface circulation in the extratropical north atlantic ocean in 1993-2001. *Journal of Physical Oceanography*, 34 (4), 405–426. doi: 10.1175/JPO2683.1.

Watson, A. J., M.-J. Messias, E. Fogelqvist, K. A. Van Scoy, T. Johannessen, K. I. C. Oliver, D. P. Stevens, F. Rey, T. Tanhua, K. A. Olsson, F. Carse, K. Simonsen, J. R. Ledwell, E. Jansen, D. J. Cooper, J. A. Kruepke & E. Guilyardi (1999). Mixing and convection in the Greenland Sea from atracer-release experiment. *Nature*, 401, 902-904, doi: 10.1038/44807.

Wüst, G. (1935). Schichtung und Zirkulation des Atlantischen Ozeans. Die Stratosphäre. *Wisschenschaftliche Ergebnisse der Deutsche Atlantische Expedition auf dem Forschungs- und Vermessungsschiff "Meteor" 1925-1927*, VI, 1 (2), 109-288.

Yashayaev, I. (2007). Hydrographic changes in the Labrador Sea, 1960-2005. *Progress in Oceanography*, 73, 242–276, doi: 10.1016/j.pocean.2007.04.015.

Yashayaev, I., M. Bersch & H. M. van Aken (2007). Spreading of the Labrador Sea Water to the Irminger and Iceland basins. *Geophysical Research Letters*, 34, L10602, doi: 10.1029/2006GL028999.

Yashayaev, I., N. P. Holliday, M. Bersch & H. M. van Aken (2008). The history of the Labrador Sea Water: Production, spreading, transformation and loss. In: *Arctic-Subarctic Ocean Fluxes*, Springer Dordrecht, the Netherlands, Eds. R. R. Dickson, J. Meincke & P. Rhines. 24, 569–612.

Yashayaev, I., & J. W. Loder (2009), Enhanced production of Labrador Sea Water in 2008, *Geophysical Research Letters*, 36, L01606, doi:10.1029/2008GL036162.

Yelland, M., & P. K. Taylor (1996). Wind stress measurements from the open ocean. *Journal of Physical Oceanography*, 4, 541–558, doi: 10.1175/1520-0485(1996)026<0541:WSMFTO>2.0.CO;2.

Financial support

This research received financial support from the CS1 project, part of the Dutch "Climate changes spatial planning" programme, and from the European Community's 7th framework programme (FP7/2007-2013) under grant agreement No. GA212643 (THOR: "Thermohaline Overturning – at Risk", 2008-2012).

Data acknowledgments

The author kindly thanks I. Yashayaev who provided the data set containing the hydrographic profiles from the Labrador Sea and J. Meincke, D. Quadfasel and M. Bersch who made the non-public data from the Irminger Sea available.

ICOADS and NCEP reanalysis provided by the NOAA/OAR/ESRL PSD, Boulder, Colorado, USA, from their Web site at http://www.esrl.noaa.gov/psd/.

The author acknowledges the modelling groups for making their simulations available for analysis, the Program for Climate Model Diagnosis and Intercomparison (PCMDI) for collecting and archiving the CMIP3 model output, and the WCRP's Working Group on Coupled Modelling (WCCM) for organizing the model data analysis activity. The WCRP CMIP3 multi-model dataset is supported by the Office of Science, U.S. Department of Energy.

The ECCO state estimates were provided by the Consortium for Estimating the Circulation and Climate of the Ocean funded by the National Oceanographic Partnership Program (NOPP). The SODA estimates were obtained from the data served at the Asia-Pacific Data-Research Center via their site at http://apdrc.soest.hawaii.edu/.

Dankwoord

Dan komt nu de pagina die ik het langst heb vermeden. Niet omdat ik niet dankbaar ben aan alle mensen die op de een of andere manier hebben bijgedragen aan dit proefschrift, maar omdat je er altijd wel 1 of 2 onbedoeld vergeet.

De mensen die ik uiteraard niet kan vergeten zijn mijn dagelijkse begeleider en co-promotor Hendrik en mijn promotor Sjef. Gelukkig had ik na mijn afstudeer project bij Hendrik enige ervaring in het filteren van de hoeveelheid informatie die men gebruikelijk van hem krijgt. Van handige tips over het aanpakken van de data tot en met het wel en wee van zijn kinderen. Alle informatie was even welkom, maar niet alles was direct bruikbaar in het onderzoek. Al heeft dat laatste stukje informatie nu toch nog zijn plek gekregen. Bedankt ook voor het vertrouwen dat het uiteindelijk wel goed zou komen, ook in tijden dat het even niet mee zat. Sjef moet ik vooral bedanken voor de bergen leeswerk die hij aan het einde van het traject heeft verzet. Daar kwamen zeker nuttige opmerkingen uit voort en hebben de tekst hier en daar behoorlijk aangescherpt. De leescommissie, Henk, Herman, Huib, Leo en Will, wil ik ook bedanken voor de laatste nuttige opmerkingen en ontdekte spelfouten.

Er zijn een aantal mensen die dit proefschrift mogelijk hebben gemaakt door mee te helpen met het inzamelen en verwerken van de data. Theo en Sven, jullie hebben top instrumenten geleverd voor de verankeringen, samen met de nodige uitleg hoe ik ze nu zelf moet uitzetten. Margriet, bedankt voor de lesjes zoutmeten en de latere assistentie hierbij. Frans, Jan, Ronald en Taco, jullie staan altijd klaar om te helpen met computer- en datazaken. Verder moet ik iedereen bedanken die aan boord heeft bijgedragen aan het succes van de vaartochten. Hendrik, Kees en Geert-Jan (de vaartochtleiders), Karel, Evaline en Santiago (voor de nutriënten- en zuurstofmetingen), Ruud en Sander (instrumenten), Leon, Lorendz, Marcel en Yvo (technisch verankeringswerk), de bemanning van de Pelagia en alle anderen die mee waren en voor de goede sfeer gezorgd hebben. *Also thanks to the crew of the Discovery, and PI Sheldon Bacon, for your hospitality and contribution to this thesis. Thanks to the researchers outside of NIOZ who contributed via data exchange and interesting email conversations. Especially, Igor Yashayeav, Robert Pickart and Kjetil Våge.*

De klimaatafdeling van het KNMI bedank ik voor hun gastvrijheid en hulp bij het vergelijken van de gekoppelde modellen. Vooral Wilco Hazeleger, Sybren Drijfhout en Camiel Severijns hebben hieraan bijgedragen.

Mijn afdelings- en koffiegenoten van Fysica en DMG wil ik bedanken voor de koffiegesprekken elke morgen. Dit was (en is nog steeds) een ontspannen manier om de dag te beginnen en jullie te leren kennen. Ik pik er een paar uit om het kort te houden. Kees, bedankt voor je vele verhalen. Leo, bedankt voor de introductie in de badmintonclub. Taco, herinner me om 3 uur nog even aan de middagpauze. En Theo; nee, m'n Fiat is nog steeds niet te koop. Verder moet ik zeggen dat iedereen die de afgelopen 2 jaar de gemiddelde leeftijd van de afdeling omlaag heeft gebracht (Anna, Carola, Janine, Jenny, Jeroen, Jordy en Sjoerd) erg welkom en een leuke afleiding was.

Verder zijn er nog een aantal mensen die tot grote steun zijn geweest buiten het NIOZ en het onderzoek. Natuurlijk iedereen op de zeilschool, eerst geleid door Jan Cees en Margreet en nu door Ebel en Reinder. Zonder de vele weekendjes uitwaaien in Friesland had ik het niet volgehouden. Jan Cees, jammer dat je toendertijd dat meetstation in de Irmingerzee (OWS Alpha) niet wat naar het zuiden hebt verlegd.

En natuurlijk als laatste mijn ouders, die achter al mijn keuzes staan en altijd klaar staan om me een weekend op te vangen. Mijn broertje, een oneindige bron van software en droge opmerkingen. En mijn vriend Ebel (Boe!), die een onvoorwaardelijke steun is. Bedankt voor alle warme stralen.

Curriculum Vitae

Femke de Jong is geboren op 2 januari 1980 te Valkenswaard. Daar behaalde zij in 1998 haar VWO diploma op het Hertog Jan College, wat na een paar jaar de SG Were Di werd. Van kleins af aan werden zij en haar broer door haar ouders meegenomen op zeilbootjes. Eerst in Friesland en later op de Waddenzee en de Noordzee. Sinds het eindexamenjaar van het VWO is zij zelf ook zeilinstructeur in Friesland en daar is zij nu nog regelmatig te vinden. Door het zeilen en het bestuderen van getijdetabellen en stromingskaarten raakte zij geïnteresseerd in de oceanografie. Daarom ging zij in Utrecht de studie Meteorologie en Fysische Oceanografie volgen. Tijdens deze studie heeft zij, samen met 6 studiegenootjes, ook een half jaar lang vakken aan de School of Meteorology aan de Universiteit van Oklahoma, in de USA, gevolgd. Na een vaartocht op het onderzoeksschip Pelagia, in het kader van een prakticum oceanografie, besloot zij haar afstudeeronderzoek bij het Koninklijk Nederlands Instituut voor Zeeonderzoek (NIOZ) te doen. In september 2004 rondde zij haar studie af met een diploma van de Universiteit Utrecht. Een klein half jaar later was zij weer terug op het NIOZ voor een promotieonderzoek in het kader van het Klimaat voor Ruimte programma. Dit project, waarvan het resultaat voor u ligt, behelsde het monitoren van de Noord Atlantische Oceaan. Het Europese THOR programma, waar zij nu als postdoc aan werkt, is een voortzetting van dit programma.

Femke de Jong was born in Valkenswaard on Januari 2nd 1980. There she attended the Hertog Jan College, which became the combined school Were Di. From a young age she went sailing with her parents and her brother. First on the Frisian lakes and later on the Wadden and North Seas. From the spring of 1998 until present she has been active as a sailing instructor. Through sailing, and the hours spent on tide tables and current atlasses, she became interested in physical oceanography. That is why she went to study Meteorology and Physical Oceanography at the University of Utrecht in the fall of 1998. During this study she also spend a semester at the School of Meteorology of the University of Oklahoma, USA, together with 6 fellow students from Utrecht. After joining a cruise on the research vessel Pelagia she decided to do her master thesis at the Royal Netherlands Institute for Sea Research (NIOZ). She graduated from the University of Utrecht in September 2004. Five months later she was back at NIOZ for a PhD research project within the Dutch Space for Climate program. This project, of which you see the end result here, concerned the monitoring of the North Atlantic Ocean. This research is continued in the Europese THOR project, on which Femke is now working as a postdoc.

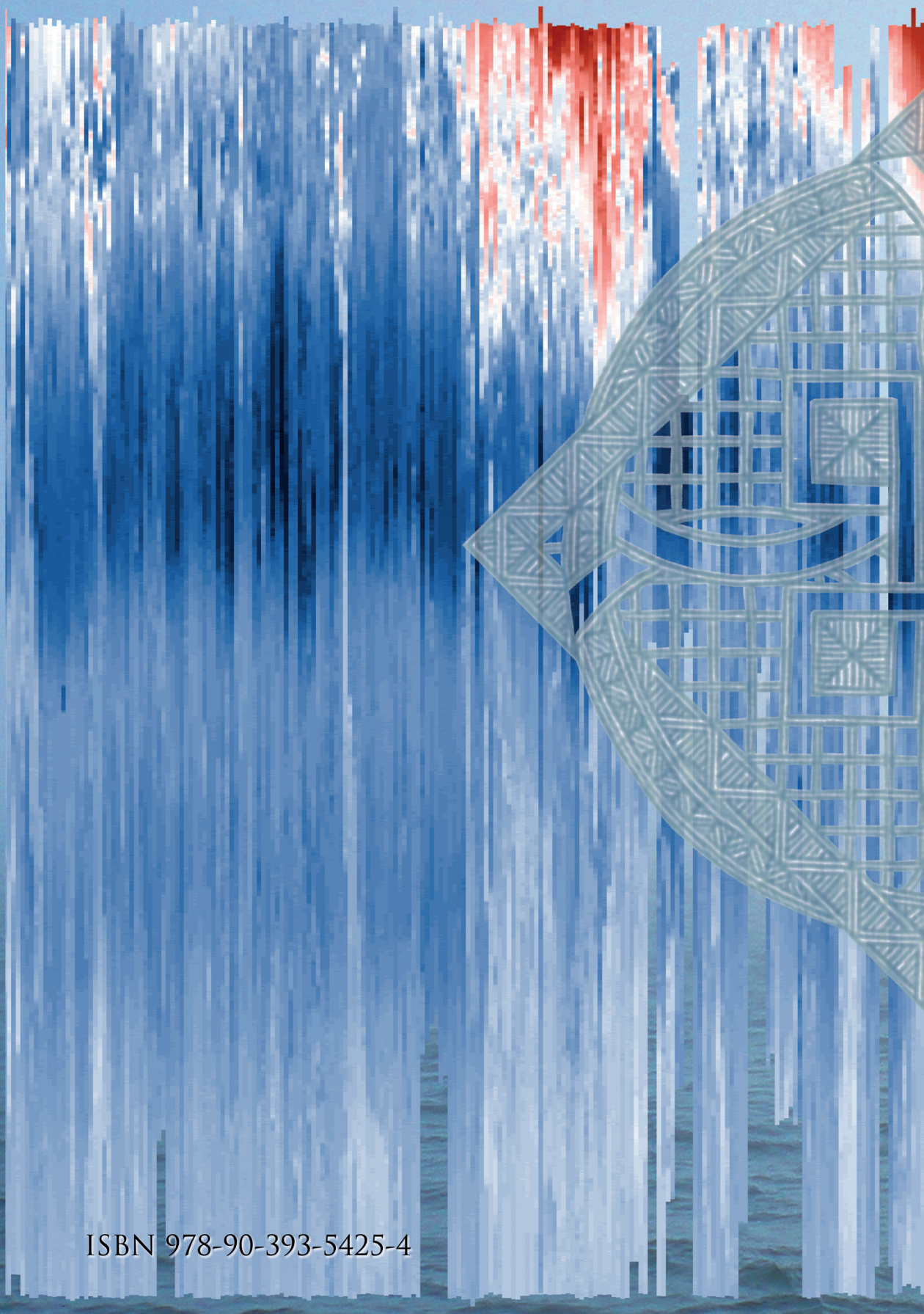

ISBN 978-90-393-5425-4